AD-A172 814 FLUID DYNAMIC MECHANISMS AND INTERACTIONS WITHIN SEPARATED FLOWS (U) ILLINOIS UNIV AT URBANA DEPT OF MECHANICAL AND INDUSTRIAL ENG A L ADDY ET AL JUL 86 1/3

UNCLASSIFIED UILU-ENG-86-4006 ARO-19823 19-EG F/G 20/4 NL

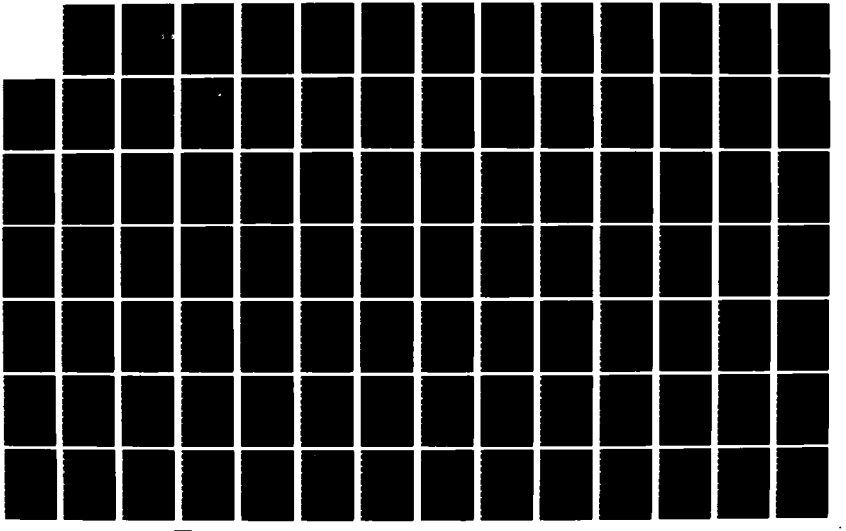

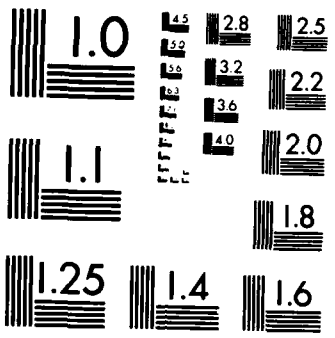

MECHANICAL ENGINEERING LABORATORY
UILU ENG 86-4006
DEPARTMENT OF MECHANICAL
AND INDUSTRIAL ENGINEERING
UNIVERSITY OF ILLINOIS AT URBANA-CHAMPAIGN
URBANA, ILLINOIS 61801

(2)

FINAL TECHNICAL REPORT

FLUID DYNAMIC MECHANISMS AND INTERACTIONS WITHIN SEPARATED FLOWS

by

A. L. Addy
W. L. Chow
J. C. Dutton
H. H. Korst
R. A. White

JULY 1986

Supported by
U.S. Army Research Office
Research Contract DAAG 29-83-K-0043
and the
Department of Mechanical and Industrial Engineering

UNCLASSIFIED
SECURITY CLASSIFICATION OF THIS PAGE (When Data Entered)

REPORT DOCUMENTATION PAGE		READ INSTRUCTIONS BEFORE COMPLETING FORM
1. REPORT NUMBER: ARO 19823.19-EG	2. GOVT ACCESSION NO.: AD-A172 814 N/A	3. RECIPIENT'S CATALOG NUMBER: N/A
4. TITLE (and Subtitle): FLUID DYNAMIC MECHANISMS AND INTERACTIONS WITHIN SEPARATED FLOWS		5. TYPE OF REPORT & PERIOD COVERED: Final Technical Report 1983-1986
		6. PERFORMING ORG. REPORT NUMBER: UILU ENG 86-4006
7. AUTHOR(s): A. L. Addy, W. L. Chow, J. C. Dutton, H. H. Korst, and R. A. White		8. CONTRACT OR GRANT NUMBER(s): DAAG 29-83-K-0043
9. PERFORMING ORGANIZATION NAME AND ADDRESS: Dept. of Mechanical and Industrial Engineering, University of Illinois at Urbana-Champaign, Urbana, Illinois 61801		10. PROGRAM ELEMENT, PROJECT, TASK AREA & WORK UNIT NUMBERS: ---
11. CONTROLLING OFFICE NAME AND ADDRESS: U. S. Army Research Office, Post Office Box 12211, Research Triangle Park, NC 27709		12. REPORT DATE: July 1986
		13. NUMBER OF PAGES: 258
14. MONITORING AGENCY NAME & ADDRESS (if different from Controlling Office)		15. SECURITY CLASS. (of this report): Unclassified
		15a. DECLASSIFICATION/DOWNGRADING SCHEDULE: N/A

16. DISTRIBUTION STATEMENT (of this Report)

Approved for public release; distribution unlimited.

17. DISTRIBUTION STATEMENT (of the abstract entered in Block 20, if different from Report)

NA

18. SUPPLEMENTARY NOTES

The view, opinions, and/or findings contained in this report are those of the author(s) and should not be construed as an official Department of the Army position, policy, or decision, unless so designated by other documentation.

19. KEY WORDS (Continue on reverse side if necessary and identify by block number)

Base flows
Component method
Laser Doppler velocimetry
Missile aerodynamics
Projectile flight

20. ABSTRACT (Continue on reverse side if necessary and identify by block number)

The significant data and results of a joint research effort investigating the fluid dynamic mechanisms and interactions within separated flows are presented in detail. The results were obtained through analytical, experimental, and computational investigations of base flow-related configurations conducted by the Gas Dynamics Group at the University of Illinois at Urbana-Champaign. The objectives of the research program focus on understanding the component mechanisms and interactions which establish and maintain high-speed separated flow regions. Flow

DD FORM 1 JAN 73 1473 EDITION OF 1 NOV 65 IS OBSOLETE

UNCLASSIFIED
SECURITY CLASSIFICATION OF THIS PAGE (When Data Entered)

models and theoretical analyses have been developed to describe the base flowfield and LDV experiments have provided new flowfield data. The research program approach has been to conduct extensive small-scale experiments on base flow configurations and to analyze these flows by component models and finite-difference techniques. The modeling of base flow of missiles (both unpowered and powered) for the transonic flight regime has been successful by component models based on the equivalent body approach. The development and use of a state-of-the-art laser Doppler velocimeter system for experiments with two-dimensional small-scale models in supersonic flows have provided quality, well-documented velocity data. The LDV experiments have yielded mean and turbulence information for a variety of near-wake flow mechanisms such as initial shear layer development, recompression/reattachment/redevelopment processes, shock wave-boundary layer interactions, and propulsive jet/freestream interactions. Correlation between the LDV data and component method mixing analysis has yielded results of interest. The research on plume effects and plume modeling has defined the pertinent variables for effective wind tunnel simulation of propulsive nozzle plumes. Many of the research efforts are described in detail and the results were presented at appropriate conferences and published in the literature. The future research activities of primary interest are indicated to be small-scale experiments on two-dimensional and axisymmetric separated flow configurations emphasizing LDV as the primary measurement tool, continuation and refinement of component modeling of base flow in the transonic flight regime, and full-scale numerical computation of base flows through improvement of existing computer codes.

FLUID DYNAMIC MECHANISMS AND INTERACTIONS WITHIN SEPARATED FLOWS

Final Technical Report

by

A. L. Addy[†]
W. L. Chow[††]
J. C. Dutton[†††]
H. H. Korst[††††]
R. A. White[††]

July 1986

Supported by

U.S. Army Research Office
Research Contract DAAG 29-83-K-0043

and the

Department of Mechanical and Industrial Engineering
University of Illinois at Urbana-Champaign
Urbana, Illinois 61801

Approved for Public Release; Distribution Unlimited

[†] Professor and Associate Head of Mechanical Engineering
[††] Professor of Mechanical Engineering
[†††] Associate Professor of Mechanical Engineering
[††††] Emeritus Professor of Mechanical Engineering

Section B.8 entitled: "A Study of Compressible Turbulent Reattaching Free Shear Layers" is deleted because of pages that are cut off. Per Ms. Sylvia Hall, Army Research Office

ABSTRACT

The significant data and results of a joint research effort investigating the fluid dynamic mechanisms and interactions within separated flows are presented in detail. The results were obtained through analytical, experimental, and computational investigations of base flow-related configurations conducted by the Gas Dynamics Group at the University of Illinois at Urbana-Champaign. The objectives of the research program focus on understanding the component mechanisms and interactions which establish and maintain high-speed separated flow regions. Flow models and theoretical analyses have been developed to describe the base flowfield and LDV experiments have provided new flowfield data. The research program approach has been to conduct extensive small-scale experiments on base flow configurations and to analyze these flows by component models and finite-difference techniques. The modeling of base flow of missiles (both unpowered and powered) for the transonic flight regime has been successful by component models based on the equivalent body approach. The development and use of a state-of-the-art laser Doppler velocimeter system for experiments with two-dimensional small-scale models in supersonic flows have provided quality, well-documented velocity data. The LDV experiments have yielded mean and turbulence information for a variety of near-wake flow mechanisms such as initial shear layer development, recompression/reattachment/redevelopment processes, shock wave-boundary layer interactions, and propulsive jet/freestream interactions. Correlation between the LDV data and component method mixing analysis has yielded results of interest. The research on plume effects and plume modeling has defined the pertinent variables for effective wind tunnel simulation of propulsive nozzle plumes. Many of the research efforts are described in detail and the results were presented

at appropriate conferences and published in the literature. The future research activities of primary interest are indicated to be small-scale experiments on two-dimensional and axisymmetric separated flow configurations emphasizing LDV as the primary measurement tool, continuation and refinement of component modeling of base flow in the transonic flight regime, and full-scale numerical computation of base flows through improvement of existing computer codes.

ACKNOWLEDGMENT

The members of the Research Group wish to recognize Vincent A. Amatucci, Graduate Research Assistant, for extending his endeavors beyond his own research activities to encompass major contributions to technical reports/papers and this final report.

TABLE OF CONTENTS

Page

LIST OF APPENDICES

INTRODUCTION

An ongoing research effort has been funded by the U.S. Army Research Office to investigate the fluid dynamic mechanisms and interactions within separated flows with particular attention to the base flow problem. The overall effort has incorporated analytical, experimental, and computational investigations aimed at gaining a more insightful understanding of the fundamental fluid dynamic mechanisms existing in the near-wake flowfield. The investigations of separated flow problems have been focused on missile afterbody flows and more importantly the interactions between the base and body flows.

The Gas Dynamics Group at the University of Illinois has conducted successful experiments on base flow configurations utilizing a laser Doppler velocimeter system in order to obtain mean and fluctuating information about the flowfield. Analytical predictions based on component methods have been refined and improved while finite-difference computational techniques have also been implemented and tested. This unique collaboration between researchers using experiments, component method analyses, and computations has led to a logical and systematic approach to the base flow problem and yielded valuable insight regarding the fundamental interactions.

The approach of this final technical report will be to present in detail the significant data, results, and extensions for the near-wake base flow problem and related problems which have been obtained under the sponsorship of the U.S. Army Research Office through Research Contract DAAG 29-83-K-0043. Since much of the group's research results have been presented and published by the individual researchers, this report will highlight their work and results and include the appropriate publication. In all cases where the analytical, experimental, and computational efforts have yielded significant

or new results, the information has been presented at professional meetings and published in the public literature. In some instances direct comparison was possible between analyses and actual base flow configuration experiments within the research group.

Problem Statement

Since the early 1950's an extensive amount of research effort has studied the separated flow region at the base of a missile for turbulent supersonic approach flow boundary layers. The analyses attempt to describe the complex interactions between the freestream flow, shear layers, and the recirculating region in order to predict such flow characteristics as base pressure, base temperature, heat transfer quantities, entrainment rates, and afterbody flow separation. The more successful models or methods, judged by their ability to predict base flow conditions in reasonable agreement with experiment, are all combinations of theoretical and empirical components which have been combined to model this complex flow region [1-7]‡. Most research efforts are based on the Chapman-Korst component model where the turbulent base flowfield is divided into distinct regions which are each analyzed individually subject to the appropriate assumptions and boundary conditions.

The flexibility and adaptability of the component model has been demonstrated by the many extensions and modifications of the component approach utilized to treat the two-dimensional and axisymmetric base flow problem with and without an inner exhaust jet. However, further details concerning the fundamental fluid dynamic interactions are still somewhat lacking and insight into the interaction mechanisms could enhance the prediction techniques. The

---

‡Numbers in brackets refer to entries in **REFERENCES.**

complexity of the separated base flowfield leads researchers to investigate each mechanism in simple, controlled analyses and experiments in an attempt to isolate, identify, and predict each individual process and then join them into an entire flowfield prediction scheme.

The base flowfield is characterized by the separation of a supersonic turbulent boundary layer as it approaches the geometric corner of the missile afterbody. The flow undergoes an expansion/compression process at the geometric corner in which a free shear layer is formed and enhances interaction between the freestream flow and the recirculating flow. The shear layer eventually recompresses, reattaches, and redevelops in a way such as to produce closure for the base region. In each of these regions questions exist concerning the fundamental fluid dynamics and further examination of these mechanisms is warranted.

The flow mechanisms investigated during the current research effort are illustrated in Figure 1 and briefly described as follows:

- Geometric separation of a boundary layer to form a free shear layer. Localized expansions or compressions at the separation point are important factors affecting initial shear layer development, turbulence intensity, shear layer growth, and initialization of the flow approaching reattachment and recompression;

- Free shear layer growth and development. Shear layer growth rate, entrainment rate, and general turbulence characteristics determine the effectiveness and influence of the shear layer on mixing;

- Recirculating flow strength and influence. The velocity field of the recirculating region, normally considered to be quiescent, affects shear layer development and base pressure;

- Recompression, reattachment, and redevelopment of the shear flow in the presence of the external and internal flows; and

- Shock wave or aerodynamically induced separation of the afterbody turbulent boundary layer prior to actual geometric separation.

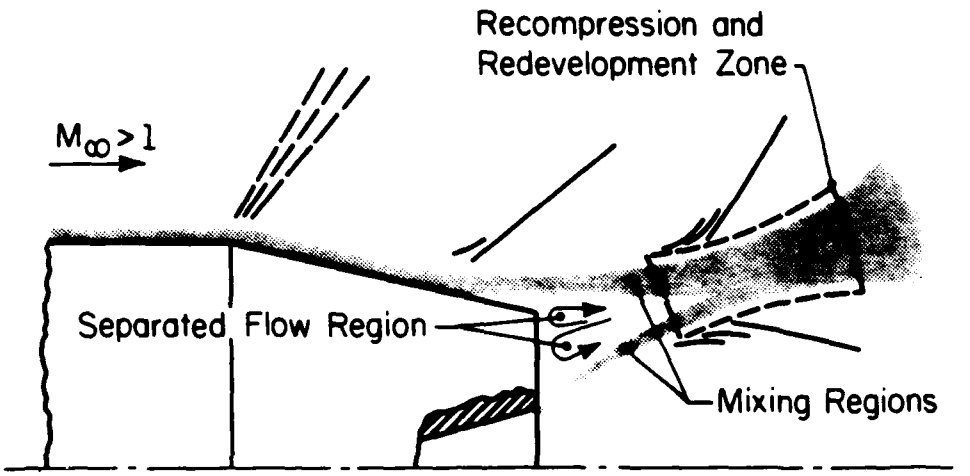

● Power-On Supersonic Base Flowfield

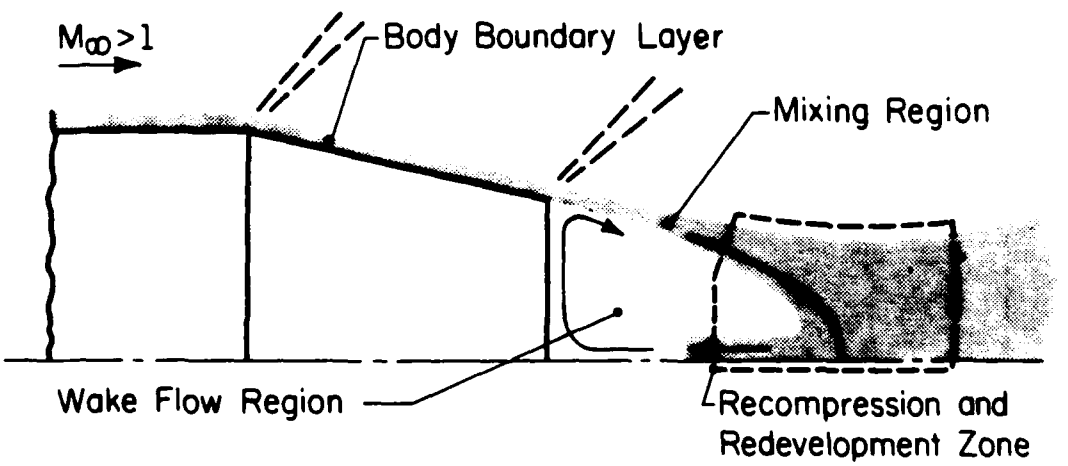

● Power-Off Supersonic Base Flowfield

● BASE FLOWS

Figure 1 Typical base flow configurations indicating the important flow regions.

These mechanisms of the base flowfield have been the focus of many investigations and theses during the tenure of this three-year Army Research Office-sponsored research program. The concentrated effort has joined a variety of analytical, experimental, and computational investigations such that many significant conclusions and important results have been found.

Research Objectives

The research philosophy maintained throughout the duration of this three-year contract has been to unify analytical, experimental, and computational investigations in a way which produces an enhanced predictive capability for the base flow problem. The eventual goal has been to develop a predictive level of expertise which affords straightforward prediction of base flowfield characteristics and parameters without an unwieldy amount of empirical information being required. The predictive capability should become developed enough to handle a wide range of geometric configurations and all possible flight regimes.

In an effort to begin and continue work towards this predictive capability, specific objectives can be identified on a more fundamental level concentrating on simple flow mechanisms. These specific objectives are as follows:

(1) To investigate the fundamental flow mechanisms and interactions which establish and maintain separated flow regions;

(2) To develop flow models and theoretical analyses which incorporate a minimum number of empirical components to describe the fundamental separated flow mechanisms;

(3) To conduct quality small-scale experiments using specific base flow configurations and a laser Doppler velocimeter to make velocity measurements in separated flows and thus providing well-documented mean and turbulence data for a wide variety of configurations;

(4) To develop a level of expertise in making velocity measurements using a state-of-the-art two-component laser Doppler velocimeter system; as well as to maintain and upgrade the LDV system and associated computers to keep this unique facility current;

(5) To utilize and incorporate the data which results from the LDV experiments into the simultaneous analytical and computational efforts; and

(6) To combine the theoretical and experimental efforts into a unified predictive capability.

These research objectives provide the guidelines and motivations for all of the research investigations described in this Final Technical Report. An implicit objective of each participating researcher has been to make the investigations and results available in the literature since much of it is quite significant and new.

Research Approach and Group Organization

The research approach has been to conduct extensive small-scale experiments related to the basic flow mechanisms encountered in these flows and t. analyze these flows based on component models and finite-difference techniques. The experiments examined relatively simple base flow configurations and made LDV measurements, static pressure measurements, and flow visualization studies of the flowfield generated in a small-scale wind tunnel. The theoretical analyses emphasized the interactive nature of the various flow mechanisms and tested improvements to the predictive capability.

The Gas Dynamics research Group is comprised of five faculty members (A. L. Addy, W. L. Chow, J. C. Dutton, H. H. Korst, and R. A. White) bringing to the investigation of the base flow problem many years of experience and many varied interests. The group supervises a large number of capable and inquisitive graduate students both on the masters and doctoral level. The interests of the five faculty members as well as their graduate students span the entire

spectrum from predominantly theoretical-numerical analyses to experimental investigations.

Final Technical Report Organization

The overall organization of this report attempts to detail the major accomplishments of the research group during the three-year period of ARO sponsorship in a fashion which illustrates the three-pronged effort: analytical, experimental, and computational. Each research investigation is categorized and described in brief detail and the associated published literature is included in an appendix. The inclusion of a copy of the published literature is intended to ease the burden on the reader for obtaining symposium proceedings and other publications which tend to be difficult to obtain.

The relatively brief "text" of this final technical report has been outlined and organized to provide quick reference to a particular topic of interest. Most of the research results have been made available through organized meetings and publications of the American Institute of Aeronautics and Astronautics (AIAA) and the American Society of Mechanical Engineers (ASME). In those instances when a detailed paper is available, only a brief description is given and the reader is referred to the appropriate appendix for further details.

The research results are treated for analytical topics in Section 1, experimental efforts in Section 2, and computational work in Section 3. The remaining sections describe the research efforts in crossover and related areas concerning separated and base flows.

Once the research topics have been discussed, the continuing and future research activities of the research group are described. The strong commitment of this research group towards an understanding of the base flow problem

is evidenced by the multi-year development and assembly of advanced experimental equipment which will provide well-documented data for the ongoing analytical and computational work. Lastly, some conclusions and recommendations are made concerning new information about the base flowfield and the value of a unified group research effort for this problem area.

Continuing Research Activity

Although this final technical report summarizes a three-year effort, our research group is continuing the investigations of the base flow problem and anticipates further significant contributions to the knowledge of the fundamental mechanisms and interactions of the near-wake flow. The emphasis of our ongoing research activity is focused on the following general research tasks:

(1) Power-on and power-off transonic base flow analyses based on the equivalent body concept;

(2) Small-scale wind tunnel experiments investigating the problem of supersonic turbulent base flow in the presence of an inner exhaust jet. The experiments emphasize LDV measurements of the near-wake flowfield;

(3) Unsteady aspects of flow reattachment after separation from a rearward-facing step. The experiments will emphasize fast-response pressure measurements near the reattachment point; and

(4) Planning and development of experiments to examine the characteristics and flow mechanisms involving plume-induced separation on a thin-base model.

These ongoing research tasks and the published results of the past six years are indicative of the strong commitment of the Gas Dynamics Group and their graduate students to quality and thorough research aimed at a better understanding of the mechanisms of separated flows. A large commitment of financial resources and time has been made to establish a unified research effort and efficiently utilize the computer and LDV facilities made available to this group through Army Research Office support. The level of significant results

presented in this report and the number of doctoral graduates continuing fundamental research indicates the personal interest and commitment to quality and the potential for contributions in the future.

RESEARCH TOPICS

1. COMPONENT ANALYSIS AND MODELING OF BASE FLOWS

The development and improvement of component models for the prediction of missile base flowfields have been the subject of considerable effort during the current research program. Both the transonic and supersonic flight regimes have been investigated as have the effects of nonuniform nozzle flow and afterbody boattailing. The methods employed and the significant results of these studies are summarized in the following sections.

1.1 Base Pressure of an Unpowered Projectile Within the Transonic Flight Regime

An equivalent body concept has been developed to examine the base pressure problem of transonic flow past a blunt-based projectile. In this analysis, the external inviscid flow is established by finite difference computations of the axisymmetric potential equation, and the viscous flow processes are treated on the basis of an integral approach. While the viscous flow region is attached and guided by the external inviscid flow in the sense of boundary layer concepts, the parameters which are needed to describe the equivalent body geometry for the inviscid flow are determined through viscous considerations. The strong viscid-inviscid interaction of this flow is clearly illustrated by this approach to the problem. A definition of the base pressure that is compatible with that for the supersonic flow regime has been developed for the transonic flow regime. In addition, an analysis of the asymptotic far-wake condition has been used to relate a needed parameter to the total drag experienced by the projectile.

This method has been applied to the problem of transonic flow (both subsonic and supersonic) past a six caliber secant-ogive-cylinder (SOC)

projectile. From this study, it has been learned that the base drag is always a large portion of the total drag experienced by a projectile in transonic flight. In addition, the transonic drag rise has been clearly observed in this investigation. The predicted static pressure distributions along the projectile surface have been compared to experimental data for flight Mach numbers in the range M_∞ = 0.9 - 1.2 and have been found to be in excellent agreement with the data.

The details of this research effort are described in two papers authored by Professor W. L. Chow. These papers are included as Sections A.1 and A.2 in Appendix A.

1.2 Effects of Boattailing of an Unpowered Projectile in Transonic Flow

The method described above for transonic flow past a blunt trailing edge projectile has been extended to consider the effect of boattailing the projectile. It was recognized that only the geometry of the equivalent body needed to be modified, and once this was accomplished, the earlier study became the special case of zero-degree boattail. The remaining details of the analysis are identical to those described previously for the blunt base projectile.

This technique has been used to investigate the effect of boattailing on the forebody pressure distribution and the base pressure for transonic flow past a six caliber SOC projectile. Computations for two freestream Mach numbers, M_∞ = 0.9 and 1.2, were performed for several boattail angles. Over the limited range of angles considered, it was observed that the reduction of the base drag outweighed the additional drag incurred on the boattail, thus indicating a favorable interference effect. However, it was also recognized that more precise simulation of turbulence is needed before a more accurate

evaluation of the optimum boattail configuration can be carried out. Comparison with experimental projectile surface pressure data has been done whenever possible. Reasonably good agreement in the pressure distribution on the projectile forebody has been observed over the range of parameters studied.

Further details concerning this research investigation can be found in a paper authored by Professor W. L. Chow. This paper is reproduced in Section A.3 of Appendix A.

1.3 Base Pressure of a Powered Projectile Within the Transonic Flight Regime

The capability for prediction of the base pressure of a powered projectile within the transonic flight regime has been examined in an attractive and straightforward way through component modeling of the flow. This approach, originally developed for the supersonic base pressure problem, can be extended to transonic flow regimes using the previously described equivalent body concept for separated flow problems and the computer program developed for solution of the transonic inviscid flow.

The external inviscid transonic flow is established from an equivalent axisymmetric body whose asymptotic radius at a far downstream position is determined by the final uniformly flowing jet corresponding to the jet pressure ratio. The geometry of the equivalent body is characterized by a shape factor whose value is linked to the size of the separation region and the level of the base pressure. The value of the shape factor is determined by the viscous flow processes which govern the viscid-inviscid interaction.

Once the inviscid flowfield has been established, the isoenergetic quasi-constant pressure turbulent jet mixing processes are determined which satisfy the initial conditions. The inner jet flow has as its pressure field that which is transmitted from the established transonic flowfield across the wake.

The inviscid supersonic stream has been established by the method of characteristics. This process is continued until the region of lowest pressure is reached and the recompression process occurs. The calculation of the recompression process itself is governed by a recompression parameter and a solution is reached when the mass entrainment from the freestream matches the mass extraction by the inner jet.

Reasonable results have been obtained from this straightforward component approach and further questions or suggestions about this method can be directed to Professor W. L. Chow.

1.4 Effects of Nonuniform Throat Flow on Base Pressure at Supersonic Flight Speeds

The effects on base pressure at supersonic flight speeds of nonuniform propulsive nozzle flow have been investigated. The nozzle flowfield is computed by using the transonic throat flow series solution of Dutton and Addy [8] to initiate method of characteristics calculations for the nozzle divergence section. The Chapman-Korst component flow model is then used to compute the missile base flowfield.

This technique has been used to investigate nonuniform nozzle flow effects on base pressure for a cylindrical boattail configuration at a flight Mach number of $M_E = 2.0$ with a circular arc throat/conical expansion section propulsion nozzle. The parametric values considered for the dimensionless nozzle throat wall radius of curvature were $R_{CW}/R_T = 0.75$, 1.0, 1.5, 2.0, 4.0, and 8.0 and for the nozzle gas specific heat ratio were $\gamma_I = 1.25$ and 1.4. For $\gamma_I = 1.4$, nonuniform nozzle flow effects result in a maximum increase in base pressure of approximately 6% over the ideal conical nozzle baseline case. For $\gamma_I = 1.25$ the maximum increase is about 7%. Since the component model with nonuniform nozzle flow effects included generally predicts a higher base

pressure than the ideal conical flow baseline case while the experimental measurements fall 13-14% below this same baseline, it is readily concluded that these effects are not the primary source of disagreement between the original component model and experiments. In fact, these results point out that there must be other, larger factors not accounted for in the original theory which act in the opposite direction to bring the base pressure down to the measured level. Such factors include the afterbody and nozzle wall boundary layers and inadequate modeling of the shear layer mixing, recompression, and redevelopment processes.

The methods and results of this study are discussed in detail in the two papers contained in Sections A.4 and A.5 of Appendix A. These papers were written by Professors A. L. Addy and J. C. Dutton and Mr. V. A. Amatucci.

2. SMALL-SCALE EXPERIMENTS OF SEPARATED FLOW CONFIGURATIONS UTILIZING A LASER DOPPLER VELOCIMETER

A major focus of research effort has been the development of a state-of-the-art two-color, two-component laser Doppler velocimeter (LDV) system for making mean and turbulence measurements in separated flow experiments. Startup and development of the LDV system has been the concern of Professor A. L. Addy and four of his doctoral-level graduate students over more than six years. This group has investigated high-speed flow configurations characterized by embedded separated regions in small-scale wind tunnel experiments aimed at gathering insight into the fundamental flow mechanisms involved. The non-intrusive nature of the LDV system makes it of special value in supersonic separated flows in providing mean and turbulence data with no artificial disturbance of the flowfield.

The research effort towards making LDV measurements of the base flow region is motivated by the following research objectives:

- To develop facilities and expertise for making LDV measurements in high-speed flows with embedded separated flow regions;
- To investigate separated flow mechanisms in plane, two-dimensional configurations; and
- To identify and investigate the techniques and problems associated with the use of an LDV system in high-speed compressible flows.

The intent of each research topic which utilizes the LDV system is to provide new, extensive, and well-documented data and also to study the capability of laser Doppler velocimetry as an experimental measurement tool.

The sections which follow describe the particular research efforts of Professor Addy's four doctoral students and the significant results and observations that result from their work. In all cases the experiments involve test models of base flow configurations in small-scale blowdown wind tunnels where the data included Schlieren photographs, pressure measurements, and velocity measurements utilizing the LDV system.

2.1 Initial Development of Turbulent Compressible Free Shear Layers

An experimental investigation was conducted to examine the nature of compressible, two-dimensional planar, turbulent free shear layers formed by the separation of a Mach 2.43 flow over a backward facing step. Two different wind tunnel test sections were used to achieve a constant pressure separation of the shear layer at the backstep corner so that the developing free shear layer was unaffected by pressure gradient effects. The objective was to gain some detailed knowledge of the mean flow and turbulence characteristics of the developing free shear layer in the absence of an initial expansion or compression process.

The study made use of sidewall static pressure measurements, surface oil flow visualization, Schlieren photographs, and two-component coincident laser

Doppler velocimeter measurements. The constant pressure initial shear layer development was achieved in one case by forcing reattachment onto an adjustable ramp located downstream of the step and in the second case by using a porous plate assembly to inject mass bleed into the recirculating region. The boundary layer and flowfield velocity measurements provided details regarding the physics of the flow not available in prior research efforts.

The results showed streamwise component turbulence intensities comparable to incompressible mixing layer values. Transverse velocity component turbulence intensities, turbulence shear stresses, shear layer growth rates, and shear layer entrainment rates were all significantly smaller than incompressible mixing layer values. Free shear layer turbulent stresses and mass flow entrainment rates were increased as a result of flow recirculation. LDV statistical velocity bias was experimentally confirmed and a two-dimensional velocity inverse weighting factor was found to correct for the bias reasonably well.

The research effort on initial free shear layer development was conducted by Dr. H. L. Petrie and the details can be found in his doctoral thesis [9]. In addition two papers have been authored by Dr. Petrie, Dr. M. Samimy, and Professor Addy and include further details of this work. These papers are included in this report as Sections B.1 and B.2 in Appendix B and give more specific details of the experiments and results.

2.2 Reattachment and Redevelopment of Compressible Turbulent Free Shear Layers

An experimental study was conducted using small-scale wind tunnel configurations to examine the base flowfield with particular focus on the recompression, reattachment, and redevelopment process. The free shear layers and resulting near-wake flowfields were produced in three different ways,

namely:

(1) Geometric separation of a Mach 2.46 flow with a turbulent boundary layer without any expansion or compression at the corner, with subsequent reattachment onto an adjustable ramp;

(2) Geometric separation of a Mach 2.07 flow with a turbulent boundary layer from a traditional backstep with reattachment on the wind tunnel floor; and

(3) Two supersonic streams of Mach 2.07 and 1.50 separating from a 25.4 mm base with impingement and interaction downstream.

The experiments investigated the fundamental features of the reattachment and redevelopment process onto solid walls and compliant boundaries.

The experiments emphasized data collected using a two-color, two-component laser Doppler velocimeter system in coincident mode but also included Schlieren photographs and detailed static pressure measurements. The differences between reattachment on a solid wall and reattachment on a compliant boundary (such as existed in the two-stream case) were examined as well as the effects of the corner expansion process. Again the objective of the research effort was to gain some basic knowledge about high velocity separated flows and the fundamentals of the recompression and reattachment process.

A significant amount of new results was found relating to the expansion and recompression process. In the single stream cases, the distortion of the turbulence field resulting from the boundary layer expansion at the step was found to produce a strong anisotropy which continued throughout the shear layer and was enhanced in the reattachment region. In contrast to incompressible reattaching free shear layers, significant increases in the turbulence level, shear stress, and turbulent triple products were observed within the reattachment region. Large turbulence structure and enhanced mixing were observed in the redeveloping region. For the two-stream case, both streams

show general features similar to those of compressible reattachment onto a solid surface.

The research effort concerning reattachment and redevelopment was the work of Dr. M. Samimy's doctoral thesis [10]. The details of these experiments are available in Dr. Samimy's Ph.D. thesis and also in a number of publications and papers co-authored with Dr. Petrie and Professor Addy and included in this final technical report as Sections B.3 through B.8 of Appendix B.

2.3 Turbulent Boundary Layer Properties Downstream of a Shock Wave-Boundary Layer Interaction

An experimental investigation was conducted to study the interaction between a shock wave and a turbulent boundary layer. The boundary layer was formed on the floor of a wind tunnel operating with a freestream Mach number of 2.94. Compression corner models, or ramps, mounted on the wind tunnel floor were used to generate the oblique shock wave. Ramp angles of 8, 12, 16, 20, and 24 degrees were used to produce the full range of possible flowfields, including flow with no separation, flow with incipient separation, and flow with a significant amount of separation.

Measurement techniques used in this investigation included Schlieren photography, surface static pressure measurement, surface streak pattern measurement, and laser Doppler velocimetry. The LDV system was used to make two-component coincident velocity measurements within the redeveloping boundary layer downstream of the interaction.

The results of the LDV measurements indicated that the boundary layer was significantly altered by the interaction. The mean streamwise velocity profiles downstream of the separated compression corners were very wake-like in nature, and the boundary layer profiles downstream of all the interactions

showed an acceleration of the flow nearest the wall as the boundary layers began to return to equilibrium conditions. The streamwise turbulence intensity and the Reynolds stress within the redeveloping boundary layers were increased by the interaction, with the amount of increase directly related to ramp angle. Both quantities reached maximum values in the central regions of the boundary layers. Several features of the redeveloping flow, including high rates of boundary layer growth, large Reynolds stress values, and large turbulent triple product values, indicated the presence of large scale turbulent structures within the turbulent boundary layers downstream of the shock wave-boundary layer interactions.

This research effort on the shock wave-boundary layer problem was conducted by Dr. D. W. Kuntz for his Ph.D. thesis [11]. Further details of these experiments can be found in the thesis and also in publications co-authored by Dr. Kuntz, Mr. V. A. Amatucci, and Professor Addy. Two of these publications are included in this final technical report as Sections B.9 and B.10 of Appendix B.

2.4 Turbulent Compressible Base Flow in the Presence of an Inner Exhaust Jet

An ongoing experimental research effort is investigating the turbulent base flow problem in the presence of an inner propulsive jet. A small-scale wind tunnel facility is being utilized to produce two compressible turbulent supersonic streams which separate from a finite thickness base and interact in a traditional base flowfield. The mechanisms of expansion, shear layer mixing, recompression, reattachment, and redevelopment are all present to produce the fundamental flow mechanisms associated with a typical flow region behind a powered missile.

The experiments are examining the fundamental flow processes in terms of how they are affected by variation in inner jet Mach numbers and jet-to-freestream pressure ratio. The models used in these experiments produce a freestream Mach number of 2.55 and inner jet Mach numbers of 2.05 and 2.55. The jet-to-freestream static pressure ratio values will be 1.0, 1.3, and 2.1 and in all cases the boundary layers at separation will undergo strong expansions and subsequent mixing.

The flowfield measurements include Schlieren photographs, sidewall static pressure data, and laser Doppler velocimeter data. The LDV system is being used in a forward scatter two-component coincident mode in order to extract mean and turbulence information from the instantaneous velocity data. The flowfield quantities of interest are mean flow velocity components, turbulence intensities, kinematic Reynolds stresses, turbulent kinetic energy, higher order moments including triple products and skewness and flatness factors, and the turbulence production, apparent eddy viscosity, and mixing length scale. The measurements are concentrated in the regions of the separation points, shear layer growth, and recompression and redevelopment.

This ongoing research effort on the turbulent base flow problem with an inner exhaust jet is the doctoral work of Mr. V. A. Amatucci. The details will be available in his Ph.D. thesis in January of 1987.

3. COMPUTATIONAL ANALYSIS OF RELATED RESEARCH TOPICS

In addition to the development of component base flow models described in Section 1 and the small-scale LDV separated flow experiments described in Section 2, continuing progress has also been made in the area of computational analysis of related high-speed separated flows. Included in this category are thin-layer Navier-Stokes computations for transonic flow past a powered

projectile and analysis of laminar flow past a projectile using viscid-inviscid interaction techniques. The results of these studies are summarized in the following sections.

3.1 Turbulent Base Pressure of a Projectile in Transonic Flight Condition--Thin-Layer Navier-Stokes Computations

An effort has recently been directed toward numerical computations of a base flowfield on the basis of the thin-layer Navier-Stokes equations with algebraic turbulence modeling. Attempts have been made to improve the results of these computations for the case of transonic, power-on base flow for a cylindrical boattail geometry. A thin-layer time-dependent Navier-Stokes base flow code has been employed in these computations. This code uses the Beam and Warming [12] approximate factorization scheme in its solution algorithm together with the algebraic turbulence model of Baldwin and Lomax [13]. To improve the capability of the computer program, the streamwise diffusion of momentum terms were included, so that the full Navier-Stokes equations were employed rather than the thin-layer approximate forms. Also, because of the difficulty in applying the Baldwin-Lomax turbulence model for the jet mixing process along the jet boundary, an attempt at improving the estimation of the turbulent eddy viscosity was made based on the simple exchange coefficient concept.

Once these changes were implemented in the code, the base flowfield was computed for a cylindrical boattail geometry at a flight Mach number of M_∞ = 1.4 and a nozzle Mach number of M_n = 2.75. The results for this centered power-on case indicate that the base pressure is increased as compared to the original calculations, but that it is still low when compared with the experimental data. On the other hand, the magnitude of the maximum reverse flow velocity within the separated region is reduced to a reasonable level so that

the pressure variation across the base is acceptable. The results of this computation are compared with other approaches and experimental data in the figure contained in Appendix C.

This research was conducted by Professor W. L. Chow.

3.2 Numerical Analysis of Laminar Flow Past a Projectile Using Viscous-Inviscid Interaction

A viscid-inviscid interaction technique has been developed to predict flows with separation. The outer inviscid flow is calculated from the potential equation while the viscous flow regions are computed on the basis of boundary layer equations. A modification of the viscous momentum equation was necessary in order to continue marching in the streamwise direction through separated flow regions. This modification, known as the FLARE approximation, suppresses the streamwise convection term when the streamwise velocity component is negative.

This interaction method has been used to compute laminar flow through an asymmetric expansion in a two-dimensional channel and laminar flow past an axisymmetric secant-ogive-cylinder projectile. The results of these calculations suggest that this viscid-inviscid interaction technique can provide reasonable predictions of separated flows provided the reverse flow velocities remain below approximately 15 percent of the freestream velocity. When applied to the case of an asymmetric expansion in a two-dimensional channel, the results agree favorably with experimental results. However, the FLARE approximation has been demonstrated to be mathematically unsound for several of the axisymmetric flow cases considered.

The results of this research study are discussed in the M.S. thesis of Mr. E. L. Gruber [14] who worked under the direction of Professor W. L. Chow.

4. CORRELATION OF EXPERIMENTAL RESULTS FOR TURBULENT EXCHANGE MECHANISMS IN SUPERSONIC, COMPRESSIBLE FREE SHEAR LAYERS

A research effort was undertaken to investigate the behavior of the turbulent exchange mechanisms for supersonic compressible free shear layers by evaluating recent experimental results obtained through application of laser Doppler velocimetry and hot-wire anemometry. The purpose was to describe the mechanisms which control both flow separation and wake flow, with particular emphasis on the shear layer mixing region.

The analytical approach to prediction of the shear layer properties was based on a two-layer component method treatment of the mixing region. The two-layer model was developed specifically for flowfields experiencing expansion at separation and treats the shear layer as being composed of an inner viscid-dissipative layer and an outer inviscid-rotational layer. The model is applicable to regions near the point of geometric separation and is applicable to flowfields with finite approaching boundary layer thicknesses. This convenient theory is used to help interpret and correlate newly obtained free shear layer data.

Empirical information is extracted from the mean flow and turbulent data of four experimental efforts concerned with the traditional backstep configuration. The analysis uses the kinematic, dynamic, and thermodynamic exchange characteristics of the free shear layer as a basis for comparison. By evaluating the available experimental data and comparing the results with the corresponding two-layer model solution, information was obtained concerning the two-layer model's ability to interpret such experimental results.

The two-layer model adequately predicted the behavior of the turbulent exchange mechanisms although it had difficulty with the expansion at geometric separation. Transition in the shear layer and the shear layer velocity

profiles and spread rate parameters correlated well between the two-layer analysis and experimental data.

The details of this correlation research effort can be found in the M.S. thesis of Mr. J. A. Moorehouse [15] prepared under the guidance of his advisor, Professor H. H. Korst.

5. MODELING OF PROPULSIVE JET PLUMES AND THE EFFECTS ON AFTERBODY AND BASE FLOWS

The operation of propulsive nozzles at pressure ratios high enough to cause plume-induced separation on the afterbody suggests appropriate initial efforts to predict the flowfield. The research attempts to predict afterbody flowfields having gross amounts of separation upstream of the geometric corner usually require quality data obtained in wind tunnel simulations. Thus a considerable research effort has been focused on proper modeling and simulation of propulsive jets in wind tunnels, and that work is described below.

5.1 Wind Tunnel Simulations of Propulsive Jets and Their Modeling By Congruent Plumes

An ongoing research effort by Professor R. A. White of the University of Illinois and Drs. Agrell and Nyberg of the Aeronautical Research Institute of Sweden (FFA) has been examining the effects of aerodynamic interference caused by plume-induced separation from propulsive afterbodies. In particular, they have conducted wind tunnel experiments using Freon and air to evaluate the merits and potential of a methodology for plume simulation by congruent plumes with gases of dissimilar specific heat ratios.

The generation of jet plumes in wind tunnel investigations must account for all of the factors affecting the induced flowfield, such as plume shape, plume deflection, mass entrainment along the shear layers, wake closure, viscous and dynamic effects, temperature, and specific heat ratio. Since all

these parameters cannot be simulated simultaneously in a wind tunnel, their relative importance must be determined. Analytical concepts have pointed to plume geometry, pliability, and entrainment characteristics as factors of highest concern and wind tunnel tests at facilities of the FFA have been conducted to evaluate a new plume simulation methodology.

The new methodology correctly stresses jet plume geometry in terms of the initial expansion angle of the jet, but goes further. This technique allows matching of both the initial deflection angle and the plume shape through its local radius of curvature. The local pressure rise at impingement of the plume and external flow is also satisfied.

Experiments using compressed air and Freon-22 tested the applicability and limits of this methodology for a broad range of wind tunnel test conditions. The results demonstrated good correlation between base pressure and flow separation near the vicinity of the base although some minor discrepancies between the Freon and air cases require further study. The methodology also produced satisfactory results when operated 25 percent off of the design pressure and at high angles of attack.

The details of this plume simulation research effort were published in the literature, and the publications have been made available here as Sections D.1 and D.2 of Appendix D.

5.2 Modeling of Propulsive Jet Plumes Utilizing Wall Curvature Effects

A second research effort examining the modeling of jet plumes in wind tunnels has used the unique approach of designing model nozzles with converging-diverging-converging cross sections. The analysis satisfies the plume simulation requirements for geometry by not only duplicating the initial plume angle but in particular by choosing the initial radius of curvature to

adequately define the plume shape bordering the near wake. Plume surface pliability is modeled to satisfy both the inviscid and viscid interaction mechanisms of plume-slipstream confluence at the end of the wake.

Experiments using these converging-diverging-converging model nozzles were conducted in an effort to determine the validity of this type of nozzle modeling in wind tunnels. The results demonstrated general agreement between predicted and experimentally determined flowfield parameters.

Further details regarding this research effort are provided in the M.S. thesis of Mr. S. E. Doerr [16].

5.3 Mechanisms Controlling Non-Steady Plume-Wall Interactions

An extension of jet plume simulation has been done in an effort to observe, analyze, and explain the flowfield arising from the interaction between a supersonic exhaust plume and nearby walls. The phenomenon is characterized by large-scale separation and irreversibility and the development of strong, non-steady pressure waves.

The research effort analyzes the plume-wall interaction in terms of the different flow components and regions and attempts to determine system parameters such as cycle times, shock strength, and base pressure limits. The analysis calculates the primary nozzle flow, secondary nozzle flow, and shock wave system development in a component method fashion.

The details of this research effort on observations and analysis of plume-wall interactions can be obtained in the doctoral thesis of Dr. M. J. Marongiu [17] conducted under the guidance of Professors H. H. Korst and R. A. White.

CONTINUING AND FUTURE RESEARCH ACTIVITIES

Much of the research conducted during this contract focuses on the base flow problem and related analytical, computational, and experimental interests. The complex nature of the near-wake flowfield indicates that many fundamental and interesting questions have still been unanswered. The five principal investigators, as well as many of the doctoral graduate students, have a strong commitment and interest in continuing the research effort associated with the investigation of the fundamental mechanisms which occur during missile flight.

The research activities which are considered of primary interest and warrant continuing and future emphasis can be generally described as follows:

(1) Small-scale, planar, two-dimensional experiments of fundamental supersonic separated flows related to base flow configurations and emphasizing laser Doppler velocimetry as the measurement tool;

(2) Initiation of axisymmetric, supersonic, small-scale experiments to obtain detailed flowfield measurements for the power-on and power-off cases for configurations more closely approximating actual missile or projectile applications;

(3) Continuation and refinement of component modeling of base flow in the transonic flight regime; and

(4) Investigation of methodologies to improve and/or use existing computer codes for numerical computation of base flows.

Small-Scale, Two-Dimensional Experiments Related to Near-Wake Flows

In the general description of the near-wake flowfield, the separation of a boundary layer to form a free shear layer, the development of the free shear layer in the presence of a recirculating flow, and the recompression/reattachment of a free shear layer were identified as fundamental flow mechanisms for which detailed experimental data are needed. If analytical and computational models are to be improved and refined, reliable and well-documented data are a

necessity. As a consequence, three separate but related series of experiments are underway which should provide new insight and data concerning these basic flow mechanisms. The two-dimensional experiments can be briefly categorized as follows:

(1) An investigation of separation, recompression, and redevelopment in supersonic two-stream flows;

(2) An investigation of flow-induced separation and recompression in supersonic two-stream flows; and

(3) An investigation of the effects of base geometry on base flowfields in supersonic flow.

The small-scale, two-dimensional experiments will focus on extensive laser Doppler velocimeter measurements and static pressure surveys of the fundamental mechanisms in the near-wake region.

The significant amount of time, energy, and finances expended to assemble and operate a two-component, two-color LDV system has resulted in the collection, processing, and presentation of mean and turbulence data for base flow experiments. The widespread acceptance of LDV data produced by this research group for backstep and shock wave-boundary layer experiments illustrates the need for such data and the ability of these researchers to make careful, reliable, and well-documented measurements with an LDV system in supersonic separated flows. Further improvements to the LDV system such as additional electronic and optical components, a new DEC PDP-11/73 data acquisition computer, a new HP-9000 laboratory based super mini-computer, and a computer controlled traversing system ensure the availability of precision test facilities for state-of-the-art data measurement on small-scale wind tunnel models. The experiments conducted by the doctoral graduate students of Professors Addy and Dutton using these types of research tools will continue to provide relevant and insightful base flow data.

Initiation of Small-Scale Axisymmetric Experiments Related to Near-Wake Flows

Since the geometry in actual missile applications is axisymmetric, a series of small-scale experiments will extend the research group's expertise and experience into making velocity and pressure measurements for geometries more closely approximating actual missile flight. The axisymmetric power-off and power-on base flow experiments will utilize an annular nozzle apparatus where the center sting is supported upstream in a plenum chamber. The sting will be hollow to allow for the introduction of the jet flow which is accelerated through a converging-diverging nozzle. The outer surface of the sting is cylindrical and acts as a centerbody for the outer nozzle.

The experimental measurements to be obtained in this investigation will again consist of Schlieren/shadowgraph photography, and afterbody and base static pressure distributions, but with primary emphasis on LDV velocity measurements from which can be extracted mean and turbulence quantities. The overriding objective of this study is to define the flow mechanisms occurring and to obtain quantitative detailed flow data for axisymmetric power-off and power-on base flows.

Component Modeling of Base Flow in the Transonic Flight Regime

In the majority of external flow problems, a large portion of the flow away from the body and the wake is essentially inviscid, while the region adjacent to the body and wake is predominantly viscous. As previously discussed, the equivalent body concept for the treatment of a six caliber secant-ogive-cylinder projectile in transonic flow has been developed with excellent agreement with data for surface pressure distribution and base drag for zero or small boattail angles. Shortcomings in the treatment of larger boattail

angles demonstrate the need for more sophisticated treatment of the viscous flow processes.

Therefore, a research effort will be directed at developing a method which solves the inviscid region using a potential flow analysis and solves the viscous regions, including the wake, using the Navier-Stokes equations with improved turbulence modeling. This represents an intermediate approach between utilizing the simplified integral analysis for the viscous regions on the one hand and using the Navier-Stokes technique for the entire flowfield on the other.

Numerical Computation of Base Flows

A recently started and continuing effort will investigate the large-scale Navier-Stokes computation of base flowfields and is aimed at developing methodologies to improve and/or implement existing computer codes. Once a basic scheme for computing the overall base flowfield has been developed, several problems of interest can be investigated. Some of these problems include plume-induced separation, alterations of the base geometry, introduction of base bleed, and initiation of wake combustion. Utilizing the computational resources at the University of Illinois to make large-scale Navier-Stokes calculations, taken together with our ability to make detailed LDV flowfield measurements, we are making progress in understanding the complex flow processes occurring in high-speed separated flows. The experimental data should aid in the development of better computational models, and the calculations should also help to define better experiments in terms of which regions of the flowfield and which flow quantities are of primary interest.

CONCLUSIONS AND RECOMMENDATIONS

The research effort directed at an understanding of the fundamental fluid dynamic mechanisms of separated flows has produced a significant amount of new information and provided new insight into the base flow problem. The support of this research contract has served to unify the efforts of the five principal investigators and their graduate research assistants and to provide a balanced analytical, computational, and experimental investigation of the near-wake flowfield and related fluid dynamic mechanisms. The strong representation of the work of this research group in the available literature and at conferences is a testimony to the contributions made towards an understanding of missile base flow and is also an indication of the strong commitment of interest, time, and effort towards maintaining a strong technical expertise at the University of Illinois in the base flow area of research.

From the research conducted over the past three years, the following conclusions can be drawn:

(1) The research group has successfully assembled and used a state-of-the-art laser Doppler velocimeter system for making velocity measurements in small-scale near-wake flowfields. The two-color, two-component LDV system has demonstrated its usefulness as a measurement tool in wind tunnel model simulations of base flow configurations.

(2) Significant LDV data has been obtained and presented which details the mean and turbulence characteristics of the fluid dynamic mechanisms encountered in the typical expansion and separation-type processes of the base flowfield. Detailed velocity information has been and is being gathered using the LDV system for such base flow mechanisms as initial shear layer development, recompression/reattachment, shock wave-boundary layer interaction, and plume/freestream interaction.

(3) Significant progress and insight have been gained in the component method analysis of the flowfield about an unpowered projectile in the transonic flight regime. The equivalent body concept has been improved and the pressure

distribution and base drag predicted by this technique are in excellent agreement with available experimental data.

(4) An analysis which incorporates the effects of nonuniform nozzle flow on base pressure was developed and showed these effects to be minor in comparison with larger factors not accounted for in the original component model.

(5) Successful correlation was made between the research group's LDV experimental results and a two-layer analytical model for description of the shear layer mixing region.

(6) Success was obtained in developing analyses and modeling theories for jet plume effects on afterbodies and base flows. The ability to predict proper wind tunnel simulation of rocket or jet plumes strongly depends upon appropriate matching of the initial plume deflection angle, plume radius of curvature, and plume pliability.

Numerous other specific conclusions may be drawn from the research work which has been completed and are indicated in each separate instance throughout this technical report.

In addition, the research which has been conducted over the past three years has identified the following items for recommendation:

(1) The further development and application of the LDV system for small-scale base flow experiments is strongly recommended in light of its ability to provide mean and turbulence data and its suitability to separated flowfields. The doctoral-level graduate students who have used and are using the LDV system demonstrate a commitment to maintaining and improving the system as a state-of-the-art tool and are breaking new ground in the operational use of an LDV system in supersonic separated flow applications.

(2) Further small-scale experiments of base flow configurations are recommended with emphasis on LDV measurements of two-stream interactions. An eventual transition from two-dimensional planar wind tunnel models to axisymmetric flow configurations is suggested.

(3) The continued investigation and refinement of analytical component model approaches to the description of the base flowfield is recommended. Incorporation of the component method approach with Navier-Stokes solutions, coupled in regions of the base flowfield where appropriate, is a logical next step in handling any attempt at prediction of the

complex viscid-inviscid processes occurring in the near-wake.

(4) Investigation of methodologies and techniques to improve and use existing Navier-Stokes computer codes for full-scale numerical computations of the base flowfield is also strongly recommended. The great potential for linking between the ongoing LDV experiments and the computational capability and its possible benefits motivate this recommendation.

As indicated throughout this technical report, much new information has been obtained and published through this U.S. Army Research Office-sponsored research effort, but many questions about fundamental mechanisms remain still unanswered. Through the unified effort of analysis, computation, and experimentation, the research group at the University of Illinois will continue to provide new information and new ideas about the fluid dynamic mechanisms and potential solution techniques for the base flow problem.

REFERENCES

1. Korst, H. H., Page, R. H., and Childs, M. E., "A Theory for Base Pressures in Transonic and Supersonic Flows," University of Illinois at Urbana-Champaign, ME-TN-392-2, March 1955.

2. Korst, H. H., "A Theory for Base Pressures in Transonic and Supersonic Flow," Journal of Applied Mechanics, December 1956, pp. 593-600.

3. Carpenter, P. W. and Tabakoff, W., "Survey and Evaluation of Supersonic Base Flow Theories," NASA CR-97129, August 1965.

4. Addy, A. L., "Detailed Analyses for the Base Pressure Programs (TSABPP-1,2)," Report No. RD-TN-69-7, U.S. Army Missile Command, Redstone Arsenal, Huntsville, Alabama, August 1969.

5. Addy, A. L., "Analysis of the Axisymmetric Base-Pressure and Base-Temperature Problem with Supersonic Interacting Freestream-Nozzle Flows Based on the Flow Model of Korst, et al., Part III: A Computer Program and Representative Results for Cylindrical, Boattailed, or Flared Afterbodies," Report No. RD-TR-69-14, U.S. Army Missile Command, Redstone Arsenal, Huntsville, Alabama, February 1970.

6. Addy, A. L., Korst, H. H., White, R. A., and Walker, B. J., "A Study of Flow Separation in the Base Region and Its Effects During Powered Flight," AGARD Conference on Aerodynamic Drag, AGARD-CPP-124, April 1973.

7. Page, R. H., "A Review of Component Analysis of Base Pressure for Supersonic Turbulent Flow," Proceedings of the Tenth International Symposium on Space Technology and Science, Tokyo, Japan, 1973, pp. 459-469.

8. Dutton, J. C. and Addy, A. L., "Transonic Flow in the Throat Region of Axisymmetric Nozzles," AIAA Journal, Volume 19, Number 6, June 1981, pp. 801-804.

9. Petrie, H. L., "A Study of Compressible Turbulent Free Shear Layers Using Laser Doppler Velocimetry," Ph.D. Thesis, Department of Mechanical and Industrial Engineering, University of Illinois at Urbana-Champaign, Urbana, Illinois, 1984.

10. Samimy, M., "An Experimental Study of Compressible Turbulent Reattaching Free Shear Layers," Ph.D. Thesis, Department of Mechanical and Industrial Engineering, University of Illinois at Urbana-Champaign, Urbana, Illinois, 1984.

11. Kuntz, D. W., "An Experimental Investigation of the Shock Wave-Turbulent Boundary Layer Interaction," Ph.D. Thesis, Department of Mechanical and Industrial Engineering, University of Illinois at Urbana-Champaign, Urbana, Illinois, 1985.

12. Beam, R. M. and Warming, R. F., "An Implicit Factored Scheme for the Compressible Navier-Stokes Equations," AIAA Paper No. 77-645, June 1977.

13. Baldwin, B. S. and Lomax, H., "Thin-Layer Approximation and Algebraic Model for Separated Turbulent Flows," AIAA Paper No. 78-257, 1978.

14. Gruber, E. L., "Numerical Analysis of Laminar Flow Past a Projectile Using Viscous-Inviscid Interaction," M.S. Thesis, Department of Mechanical and Industrial Engineering, University of Illinois at Urbana-Champaign, Urbana, Illinois, 1985.

15. Moorehouse, J. A., "Correlation of Experimental Results for Turbulent Exchange Mechanisms in Supersonic, Compressible Free Shear Layers Based on a Transitional Two-Layer Model," M.S. Thesis, Department of Mechanical and Industrial Engineering, University of Illinois at Urbana-Champaign, Urbana, Illinois, 1985.

16. Doerr, S. E., "Modeling of Propulsive Jet Plumes--Extension of Modeling Capabilities By Utilizing Wall Curvature Effects," M.S. Thesis, Department of Mechanical and Industrial Engineering, University of Illinois at Urbana-Champaign, Urbana, Illinois, 1984.

17. Marongiu, M. J., "Mechanisms Controlling Non-Steady Plume-Wall Interactions in Rocket Launch Tubes," Ph.D. Thesis, Department of Mechanical and Industrial Engineering, University of Illinois at Urbana-Champaign, Urbana, Illinois, 1985.

APPENDIX A

COMPONENT ANALYSIS AND MODELING OF BASE FLOWS

SECTION A.1

BASE PRESSURE OF A PROJECTILE WITHIN THE TRANSONIC FLIGHT REGIME

Paper No. AIAA-84-0230

Presented at the AIAA 22nd Aerospace Sciences Meeting

Reno, Nevada

January 9-12, 1984

by

W. L. Chow

AIAA'84

AIAA-84-0230

Base Pressure of a Projectile Within the Transonic Flight Regime

W.L. Chow, Univ. of Illinois, Urbana, IL

AIAA 22nd Aerospace Sciences Meeting

January 9-12, 1984/Reno, Nevada

BASE PRESSURE OF A PROJECTILE WITHIN THE TRANSONIC FLIGHT REGIME

W. L. Chow*

University of Illinois at Urbana-Champaign
Urbana, IL 61801

ABSTRACT

An equivalent body concept is developed to examine the base pressure problem of a transonic flow past a blunt-based projectile. The inviscid flow is established by finite difference computations of the axisymmetric potential equation where the displacement effect of the attached turbulent boundary layer on the body is also accounted for. The viscous flow processes behind the base such as turbulent jet mixing, recompression, reattachment, and redevelopment are treated through integral formulations. The strong viscid-inviscid interaction is clearly illustrated from the method of approach to the problem. A definition of the base pressure, compatible with that for the supersonic flow regime has been developed which is necessary for the transonic flow regime. An analysis of the asymptotic far wake condition would relate a needed parameter to the total drag experienced by the projectile. Results are obtained for transonic (both subsonic and supersonic) approaching flow conditions. Comparisons with available experimental data are also presented. Extension to cases with small angles of incidence is also discussed.

INTRODUCTION

Despite the prevailing popularity of solving fluid dynamic problems through large-scaled numerical computations of the Navier-Stokes equation, study of the base pressure problem from the conventional approach provides a unique opportunity to illustrate vividly the flow mechanisms governing the phenomenon of these problems. It is well known that the viscous flow plays an equally important role as the external inviscid flow in the establishment of the overall flow pattern. This feature has been classified as a strong viscid-inviscid interaction. Since the viscous flow is always located along the edge of the inviscid flow region, the viscous flow is thus guided by the inviscid flow in the sense of the boundary layer concept. On the other hand, in direct association with the inviscid flow field, the geometry of the wake as well as the pressure level and distribution within the wake are dependent upon the viscous flow processes of jet mixing, recompression, reattachment, and redevelopment behind the base. This mutual dependency between the inviscid and viscous flows was pointed out by Crocco and Lees.[1] Much work on base pressure has been carried out since that time. Some of them are listed here.[2-16] It should be noted that all these investigations were restricted to problems with supersonic external flows. Other than the limited few exceptions[15,16], none of these analyses considered the process of redevelopment after reattachment.

In a more detailed examination of the recompression-reattachment process of a turbulent free shear layer[14], it was learned that this same integral analysis can be applied to study the base presssure problems in any other flow regime. An examination of base pressure problems of incompressible wedge flow was later carried out.[17-19] The elliptic inviscid flow is established from conformal mapping. The viscous flow was guided by the established inviscid flow while the characteristic parameters describing the inviscid flow were determined from viscous flow processes. This method of analysis also led to the study of the base pressure problem for the transonic flow past a backward facing step in the two-dimensional or axisymmetric configuration.[20-23] Indeed, since the pressure field is established from the inviscid flow, it would be appropriate to simulate the pressure field including that behind the body on the basis of an "equivalent body" concept. The solution of the transonic inviscid flow was established from the finite difference calculations of the potential equation. It was learned that the point of reattachment behaved as a saddle point singularity of the system of equations describing the isoenergetic viscous flow recompression. Furthermore, the pressure at the step cannot be taken as the base pressure within the transonic flow regime. It is obvious that the step pressure coefficient increases toward zero as the free stream Mach number increases toward unity, meanwhile the base pressure coefficient decreases toward more negative values. It was also recognized that the study carried out up to this point constituted only the first approximation to the problem, since the resulting equivalent body established from the viscous flow analysis was not yet compatible with the original equivalent body selected to establish the inviscid flow.

Additional study has been carried out on the transonic base pressure problem. Specifically the base pressure of a six-caliber secant-ogive-cylinder projectile immersed in a transonic flow has been examined. The flow condition on the forebody including the attached turbulent boundary layer, together with the processes of mixing, recompression, reattachment, and redevelopment behind the base, must be included in the considerations. It will be shown that the equivalent body for this problem can be described with the help of two characteristic parameters. It will also be demonstrated that the point of reattachment is a saddle point singularity for the system of equations describing the viscous flow recompression. Continued computation after reattachment will reveal that the fully developed wake flow state is also a saddle point singularity of the system of equations describing the viscous flow redevelopment. However, with additional analysis of the

*Professor of Mechanical Engineering, Dept. of Mech. and Ind. Eng.; also, Associate Fellow, AIAA.

asymptotic state of fully developed flow, one parameter can be directly related to the total drag of the body, and the problem can be reduced to a problem of Reynolds number matching from the analysis of recompression. Extension to the case of flow with a small angle of attack will also be suggested and discussed.

ANALYTICAL CONSIDERATIONS

For an external flow past a body, the surface pressure distribution is the item of utmost concern which supplies the basic information for the lift, drag calculations. Inasmuch as the boundary layer concept is applicable, the pressure distribution is entirely determined from the inviscid flow geometry. For the present problem of flow past a projectile, the equivalent body geometry must be established before any viscous flow processes can be examined and studied.

The Equivalent Body

For a transonic flow past a projectile, whose typical configuration is shown in Fig. 1, it is expected that after the flow separates from the base, usually a turbulent jet mixing process occurs along the wake boundary. The dividing streamline is thus energized, preparing itself for the subsequent recompression and reattachment at the end of the near wake. After reattachment, additional compression of the shear layer occurs in the early part of the redevelopment before the pressure field decays toward that of the free stream. Based on the displacement concept of the boundary layer, the equivalent inviscid body boundary would be located away from the viscous dividing streamline by a distance of the displacement thickness, δ^*, of the viscous layer above the dividing streamline. This reasoning leads to the specification of the equivalent body $R_b(z)$ for the present problem by:

$$R_b(z) = 0 \qquad \text{for } z \leq 0 \qquad (1a)$$

$$R_b(z) = R_{og} + \delta^*(z) \qquad \text{for } 0 \leq z \leq z_T \qquad (1b)$$

$$R_b(z) = R_{cyl} + \delta^*(z) \qquad \text{for } z_T \leq z \leq z_G \qquad (1c)$$

$$R_b(z) = \delta^*_{asy} + (R_{cyl} + \delta^*_b - \delta^*_{asy})\, e^{\left(-\frac{\Delta 2}{1-\Delta}\right)} \qquad \text{for } z_G \leq z \leq z_R \qquad (1e)$$

where $\Delta = (z-z_G)/(z_R-z_G)$

$$R_b(z) = \delta^*_{asy} \qquad \text{for } z_R \leq z \qquad (1f)$$

The schematic sketch of the equivalent body of a projectile is shown in Fig. 2. It will be recognized that the parameters characterizing the equivalent body geometry are z_R and δ^*_{asy} for this specific projectile. It is also worthwhile to note that Δ varies from zero to unity when z is between points G and R and the second power employed in Eq. (1d) assures the slope continuity of the profile at the base. Furthermore, it can be shown that under the far-wake condition, the displacement thickness of the viscous layer approaches a finite value even when the viscous layer thickness approaches infinity at far downstream locations.

The Inviscid Flow Field

Once the equivalent body is specified for a transonic approaching flow Mach number, the inviscid flow is established from relaxative finite difference calculations of the full potential equation. In fact it follows precisely a procedure described in the study of transonic flow past a boattailed afterbody.[24-25] This is briefly discussed here. At first, a transformation is introducd to transform the infinite physical region of concern into a finite region of computation. A specific finite difference form of the transformed potential equation is written which depends upon whether the flow is locally supersonic or locally subsonic. A row of grid is added below the body surface so that the tangent flow condition on the surface can be obeyed. When the finite difference equations are written for all grid points at a certain stream-wise location, a tri-diagonal system of equations is obtained. Values of the potential function are found by solving the system of equations. This new information is immediately employed to update the corresponding value of the grid below the body surface in satisfying the local boundary condition. This procedure is then repeated for the next stream-wise location. This line-by-line sweeping of the computational plane from upstream toward downstream directions is carried out until the change in the value of the potential function is less than an arbitrarily small number for all grid points throughout the domain of computation. A convergent solution of the potential function has been obtained. In the midst of computations of the

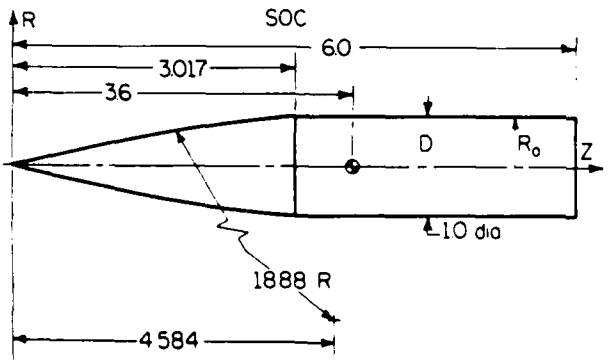

Fig. 1 A 6 Caliber Secant-Ogive-Cylinder Projectile

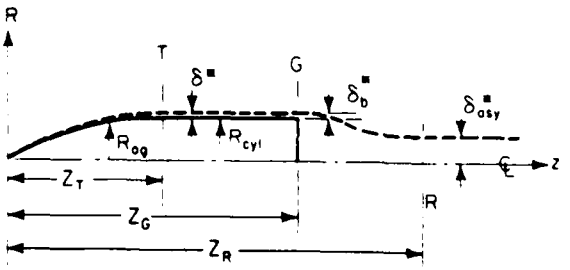

Fig. 2 Equivalent Body Configuration

potential function the turbulent boundary layer growth with prevalent pressure gradient on the body surface has also been estimated from an integral approach. The equivalent body geometry is correspondingly modified to account for the displacement effect of the turbulent boundary layer growth. Thus the boundary layer thickness, momentum thickness and the displacement thickness of the viscous layer at the base are known as soon as the inviscid flowfield is established.

Turbulent Jet Mixing, Recompression, and Reattachment

The integral analysis of these flow processes precisely follows the early study of a flow past a backward facing step.[23] Only a brief description of these considerations is given here. Again, an isoenergetic flow condition is assumed throughout all viscous flow regions.

Immediately behind the base, a turbulent jet mixing process occurs along the wake boundary. As one would observe later, the pressure also decreases significantly along the path of mixing in the transonic regime. Nevertheless, the mixing process can be treated on the basis of a quasi-constant pressure analysis.[26] At each location, the velocity profile is derived from a constant local pressure calculation with the same initial boundary layer profile. A linear velocity profile with the local slope given by

$$\frac{\partial u}{\partial r} = \frac{\sigma u_e}{\pi^{1/2} x} \tag{2a}$$

is assumed. The eddy diffusivity, ε, for this region is given by

$$\varepsilon = \frac{1}{4\sigma^2} x u_e \tag{2b}$$

where x is the distance along the path of mixing measured from the origin of mixing, u_e is the local free stream velocity and σ, the spread rate parameter assumes the value of 12 throughout this series of study. The turbulent boundary layer at the step provides the initial condition, and the dividing streamline velocity, the shear layer thicknesses above and below the dividing streamline, as well as the shear stress along the dividing streamline, can be determined at each section along the mixing region. This mixing analysis is carried out until the section of lowest pressure along the wake is reached. The flow properties here also provide the initial conditions for the subsequent recompression process.

Prior to consideration of recompression, an average base pressure can be determined from the momentum principle. One observes from Fig. 3 that the momentum principle, when applied between the base and section m, the end of the mixing region, readily yields

$$p_b \pi R_o^2 = \int_{R_{dm}}^{R_o} p_d \, 2\pi r dr + \pi R_{dm}^2 p_m - \int_o^{\lim} \tau_d 2\pi r dz + \int_o^{\delta_b} 2\pi r \rho u^2 dr + \int_o^{h_b} 2\pi r \rho u^2 dr \tag{3}$$

where the forward flow momentum is evaluated from the linear mixing profile and the backward flow momentum is evaluated from the reverse flow velocity profile for the following recompression process. An average base pressure ratio, p_b/p_∞, may be solved from the above equation. In supersonic external flows, there is practically no pressure

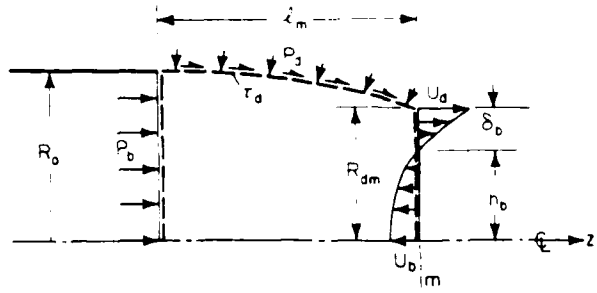

Fig. 3 Average Base Pressure Defined from the Momentum Principle

variation prior to recompression. Under this condition, the shear stress integral in Eq. (3) balances with the forward flow momentum, and the backward flow momentum is usually negligible. Thus the base pressure from Eq. (3) would be equal to the uniform pressure prevailing within the wake for the supersonic flow condition. In transonic flow, the pressure variation immediately behind the base is so severe that the above expression is needed to give a more realistic estimation of the average base pressure and the base drag.

Recompression essentially follows what has been developed previously.[23] At each section the dimensionless velocity of the flow has a profile of

$$\phi = \frac{u}{ue} = \phi_d + s\zeta_a + (3(1-\phi_d) - 2s)\zeta_a^2 + [s-2(1-\phi_d)]\zeta_a^3 \qquad 0 \le \zeta_a \le 1 \tag{4a}$$

above the dividing streamline, a linear profile of

$$\phi = \frac{u}{u_e} = \phi_d \zeta_\ell \qquad (0 \le \zeta_\ell \le 1) \tag{4b}$$

below the dividing streamline for the forward wake flow, and a cosine profile of

$$\phi = \frac{u}{u_e} = -\phi_b \cos\frac{\pi}{2}\zeta_b \qquad (0 \le \zeta_b \le 1) \tag{4c}$$

for the back wake flow, where

$$\phi_d = \frac{u_d}{u_e},\ \phi_b = \frac{u_b}{u_e},\ \zeta_a = \frac{r-R_d}{\delta_a},\ \zeta_\ell = \frac{r-R_d+\delta_b}{\delta_b},\ \zeta_b = \frac{r}{h_b},\ \delta_a = R_e - R_d,\ \delta_b = R_d - h_b. \tag{4d}$$

The slope parameter, s, in Eq. (4a) is linearly coupled to ϕ_d, and the proportional constant is evaluated at the initial section of the recompression region. This manipulation assures the fact that both ϕ_d and s vanish together at the section of reattachment. A locally triangular geometry was also assumed for the wake flow so that the wake centerline, which divides the forward flow from the back flow, shall also pass through the point of reattachment as it should.

A system of five ordinary differential equations was obtained to describe the process of recompression. They are given by

$$A_i \frac{dR_e}{dz} + B_i \frac{dR_d}{dz} + C_i \frac{d\phi_d}{dz} + D_i \frac{dh_b}{dz} + E_i \frac{d\phi_b}{dz}$$

$$= F_i \frac{dC_e}{dz} + G_i \qquad (i = 1 \ldots 5) \qquad (5)$$

The first two equations were obtained from the continuity principle for the viscous layers above and below the dividing streamline, respectively. The next two were the momentum relations for the two layers and the last was derived from the condition of local triangular wake geometry. Coefficients A_i, $B_i \ldots G_i$ (see Ref. (23) for expressions of these functions) are complicated functions of flow properties and conditions. Equation (5) describes the variation of the locations of the edge of shear layer R_e; the dividing streamline R_d and its velocity u_d together with the back flow height h_b and velocity u_b throughout the recompression region. C_e is the Crocco number of the adjacent free-stream. The turbulent shear stress along the dividing streamline, which appears in terms G_3 and G_4, is evaluated through an eddy diffusivity which is related to that at the initial section of recompression by

$$\frac{\varepsilon}{\varepsilon_m} = \frac{u_e}{u_{e_m}} \left(\frac{\delta_a}{\delta_{a_m}}\right) \left(\frac{\ell_m + x_r}{\ell_m}\right) \qquad (6)$$

where δ_a refers to the shear layer thickness above the dividing streamline, and x_r refers to the distance along the recompression region. Perhaps it is worthwhile to note that with an integral analysis for the turbulent mixing and recompression process, only the emperical information of the eddy diffusivity along the dividing streamline is needed throughout these regions.

From the recompression calculation by integrating the system of equations, it was learned that the point of reattachment behaves as a saddle-point singularity for the system of equations describing the flow. For slightly different z_R values, which, of course, correspond to the different inviscid flow field, the dividing streamline velocity would either decrease to negative values during recompression, before the point of reattachment on the centerline of the wake is reached, or eventually break away from the trend of continuous reduction and start to increase. In the actual calculation, since the establishment of the inviscid flow field is time consuming, the value of z_R was kept fixed, and the saddle point behavior is observed from the fact that slightly different initial boundary layer thicknesses before mixing would lead to widely different results toward the end of recompression. Figure 4 shows a typical set of results of calculations showing the different trends of the normalized dividing streamline velocity, ϕ_d. To keep the computational effort within a reasonable level, one must attempt to reach the point of reattachment through extrapolation at the end of recompression when the initial boundary layer thicknesses of two divergent trends are within a small margin.

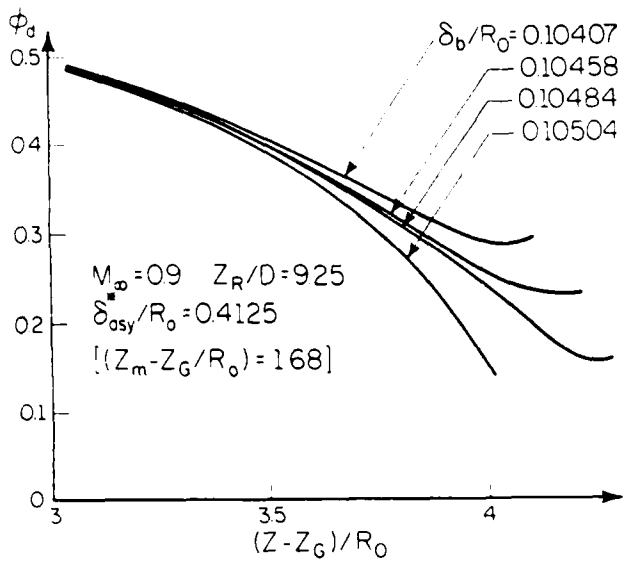

Fig. 4 Saddle Point Behavior of Recompression Process

Redevelopment of Flow

At the point of reattachment, the velocity profile has the shape of $\phi = 3\zeta^2 - 2\zeta^3$ according to Eq. (4a). It is now assumed that throughout the region of redevelopment, the velocity has the profile of

$$\phi = \phi_w + (1-\phi_w)(3\zeta^2 - 2\zeta^3) \qquad (7)$$

where ϕ_w is the centerline wake velocity and $\zeta = r/\delta_e$; δ_e being the thickness of the viscous layer within the region of redevelopment.

The continuity equation and the equation of motion within the boundary layer formulation are

$$\frac{\partial(\rho u r)}{\partial z} + \frac{\partial(\rho v r)}{\partial r} = 0 \qquad (8a)$$

$$\frac{\partial(\rho u^2 r)}{\partial z} + \frac{\partial(\rho u v r)}{\partial r} = -r\frac{dp}{dz} + \frac{\partial(\tau r)}{\partial r} \qquad (8b)$$

Upon integrating across the viscous layer, Eq. (8) readily yields

$$[1-2(1-C_e^2)I_1]\frac{d\delta_e}{dz} - (1-C_e^2)\delta_e I_4 \frac{d\phi_w}{dz} = \tan\beta_e$$

$$+ \left[\frac{\delta_e I_1}{C_e}(1-C_e^2\frac{3\gamma-1}{\gamma-1}) + 2C_e\delta_e I_3(1-C_e^2)\right]\frac{dC_e}{dz} \qquad (9a)$$

$$\frac{2I_2(1-C_e^2)}{\delta_e}\frac{d\delta_e}{dz} + (1-C_e^2)I_6\frac{d\phi_w}{dz} =$$

$$-\frac{dC_e}{dz}\left[\frac{2I_2}{C_e}(1-C_e^2\frac{2\gamma-1}{\gamma-1}) + 2C_e(1-C_e^2)I_5\right.$$

$$\left. + \frac{1}{2C_e}(1-2(1-C_e^2)I_1)\right] \qquad (9b)$$

where

$$I_1 = \int_0^1 \frac{\phi\zeta d\zeta}{1-C_e^2\phi^2}, \quad I_2 = \int_0^1 \frac{\phi(1-\phi)\zeta d\zeta}{1-C_e^2\phi^2}$$

$$I_3 = \int_0^1 \frac{\phi^3\zeta d\zeta}{(1-C_e^2\phi^2)^2}, \quad I_4 = \int_0^1 \frac{1+C_e^2\phi^2}{(1-C_e^2\phi^2)^2}\Gamma\zeta d\zeta$$

$$I_5 = \int_0^1 \frac{\phi^3(1-\phi)\zeta d\zeta}{(1-C_e^2\phi^2)^2}, \quad I_6 = \int_0^1 \frac{1-2\phi+C_e^2\phi^2}{(1-C_e^2\phi^2)} \Gamma\zeta d\zeta$$

$$\Gamma = \frac{\partial\phi}{\partial\phi_w} = 1-3\zeta^2+2\zeta^3 \tag{10}$$

C_e is the Crocco number of the free stream, which is related to the Mach number M_e by

$$C_e^2 = \frac{M_e^2}{\frac{2}{\gamma-1}+M_e^2} \tag{11}$$

θ_e is the streamline angle at the edge of the shear layer, and all integrals, I_1 through I_6, are only functions of C_e and ϕ_w. It is to be noted that this integral analysis is equally valid for laminar or turbulent flows since the shear stress vanishes at both limits of integration. Indeed, the far-wake condition of

$$\delta_e(1-\phi_w)^{1/2} = \text{const} \tag{12}$$

is satisfied by both laminar or turbulent flows. It may be shown that the system of equations given by Eq. (9) with the assumed velocity profile is compatible with this condition.

The right-hand side of Eq. (9) contains the pressure gradient term which is implicitly linked with the spread of the viscous layer into the already established inviscid flow region. This situation has already been encountered in the upstream recompressive flow described by Eq. (5). Iterative solution procedures must be relied upon at each step of the numerical integration if accurate results are expected.

It has been learned from this approach of the problem that the fully developed flow condition presents itself also as a saddle-point singularity of the system of equations describing the flow. For a fixed z_r but with slightly different δ^*_{asy} values, the redevelopment flow after the reattachment (after the point of reattachment has been obtained from extrapolation) will lead either to positive and ever increasingly large $d\delta_e/dz$ or to smaller and eventually negative $d\delta_e/dz$ value. Negative $d\delta_e/dz$ also invariably leads to negative $d\phi_w/dz$, resulting in a reduction of wake centerline velocity. An example to illustrate this phenomenon is shown in Fig. 5. Both these behaviors are physically unrealistic and the correct value of δ^*_{asy} lies in between. This, of course, is the typical behavior of a saddle-point.

It is now worthwhile to note that with z_r and δ^*_{asy} as the characteristic parameters needed to establish the corresponding inviscid flow, two-saddle-point singularities provide two discriminating criteria for the determination of their correct values under the given flow conditions. However, two-saddle points in sequence is mathematically "unstable", especially when the first saddle point can only be determined from extrapolation. Numerical consistency for a system of nonlinear ordinary differential equations cannot be easily achieved. For the present problem, the numerical

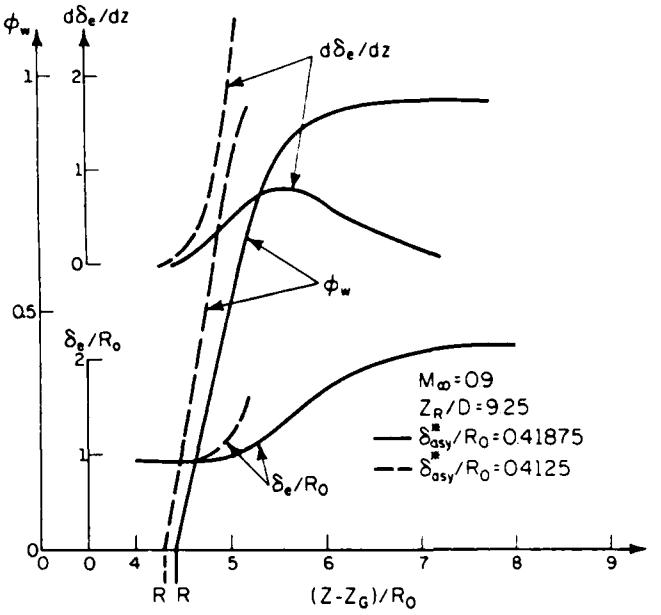

Fig. 5 Saddle Point Behavior of Redevelopment Process

error generated from the finite difference computation of the potential equation may also have important influences on this phase of the computations. Fortunately, an analysis of the asymptotic wake flow would relate δ^*_{asy} to the total drag experienced by the projectile, and the integration against two-saddle-point singularities in sequence is conveniently avoided.

Asymptotic Wake Flow Condition

It is stipulated that under the asymptotic far wake flow situation, the approaching free stream external flow condition is restored. The velocity profile within the wake still obeys Eq. (7), but with $(1-\phi_w)$ as a small quantity, so that higher orders of this quantity can be ignored. According to the definition of the displacement thickness given by

$$\rho_\infty u_\infty(\delta_e^2 - \delta^{*2}_{asy}) = 2\int_0^{\delta_e} \rho u r\, dr \tag{13}$$

and the drag-momentum relationship for the far wake flow given by

$$D_t = 2\pi\int_0^{\delta_e} \rho u(u_\infty - u) r dr \tag{14}$$

where D_t is the total drag experienced by the projectile, it may be shown from Eqs. (13) and (14) that

$$\left(\frac{\delta^*_{asy}}{R_o}\right) = \left[\frac{C_{Dt}}{2}\frac{1+C_\infty^2}{1-C_\infty^2}\right]^{1/2} \tag{15}$$

where

$$C_{Dt} = D_t \Big/ \frac{\rho_\infty V_\infty^2}{2} R_o^2.$$

The total drag, D_t, is the sum of the form drag, skin friction drag on the forebody, and the base drag on the base.

METHOD OF CALCULATIONS AND RESULTS

With the introduction of the relationship given by Eq. (15), calculation procedures become greatly simplified. For a given free stream Mach number, M_∞, a pair of values of $z_{R/D}$ and δ^*_{asy}/R_o are selected. The potential flow solution for this geometric configuration is subsequently established. After the turbulent jet mixing process behind the base has been analyzed, the total drag coefficient can be evaluated, and the δ^*_{asy}/R_o is immediately adjusted according to Eq. (15). Since the effect of δ^*_{asy}/R_o on the total drag is very minor, the correct value of δ^*_{asy}/R_o can be determined usually within three iterations. Once this condition is satisfied, viscous recompression can be determined by integrating the system of Eq. (5). The dimensionless dividing streamline velocity will either be reduced to a negative value before the centerline is reached or will break away from the continuous pattern of reduction and start to increase--the saddle point behavior. This phenomenum demands the adjustment of $z_{R/D}$ value accordingly. Once this adjustment is within a small margin ($\Delta z_{R/D} < 0.0025$ for the present series of calculations), the solution is reached even if the detailed wake flow pattern has not yet been satisfactorily established. It is entirely possible to continue these detailed calculations including the redevelopment after reattachment. Early results obtained from such efforts[27] are shown in Figs. 6 and 7, where the overall pressure field realized, the reproduced equivalent body, and the path of the dividing streamline within the wake are shown. The reproduced equivalent body, was obtained by adding the displacement thickness of the viscous layer above the dividing streamline onto the path of the dividing streamline. However, all these calculations are not necessary if only the information on base drag and the total drag are desired. Calculations have been carried out for all the transonic Mach numbers where wind tunnel pressure data on this projectile are available.[28] The unit Reynolds number employed was also compatible with the wind tunnel test condition (Rey/ft = 4×10^6). Figure 8 shows the pressure distribution on the equivalent body along with the experimental data on the forebody. The corresponding average base pressure coefficient and the base pressure ratio are also labeled in the figures. Under some subsonic Mach number conditions, the agreement of pressure with the data on the cylinder is less desirable, although it has no influence on the forebody form drag evaluation. The base pressure ratio obtained from this study is shown in Fig. 9. Various drag coefficients and the total drag coefficient for the transonic Mach numbers are presented in Fig. 10.

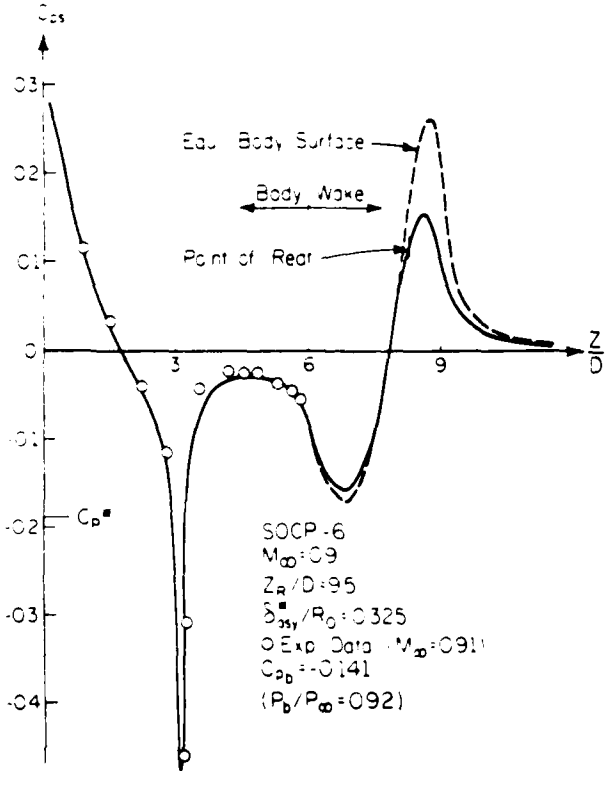

Fig. 6 Pressure Distribution Realized from Detailed Evaluations

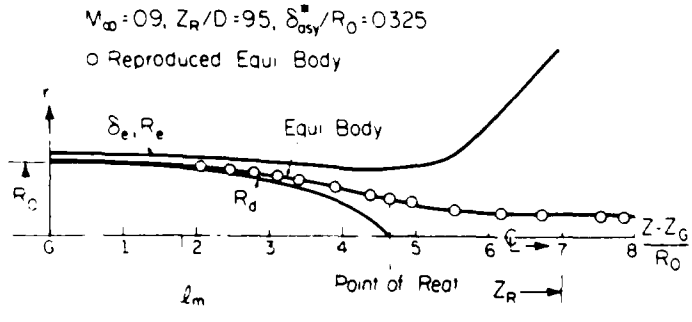

Fig. 7 Dividing Streamline, Viscous Wake, and Reproduced Equivalent Body

DISCUSSION

It should be noted that the method developed for this study should also be applicable for smaller free stream subsonic Mach number flows, including incompressible flow condition, and also for larger supersonic free stream Mach numbers. Computations of these cases have been carried out and the results are also reported in Figs. 9 and 10. Although the correctness of the base pressure ratio for $M_\infty > 1.3$ is doubtful since isentropic shocks have occurred, previous results of $P_b/P_\infty = 0.7625$ at $M_\infty = 1.5$ on supersonic flow past an axisymmetric backward facing step[29] with comparable initial boundary layer thickness seems to imply that these results are not completely unreasonable.

No computations have been carried out for the range of $0.98 < M_\infty < 1.08$. In fact, additional under-relaxation have been applied for the potential flow calculations at $M_\infty = 0.98$. Also, the calculations for the potential flow have been modified from the original scheme[25] for the supersonic approaching flows. Although it seems from Figs. 9

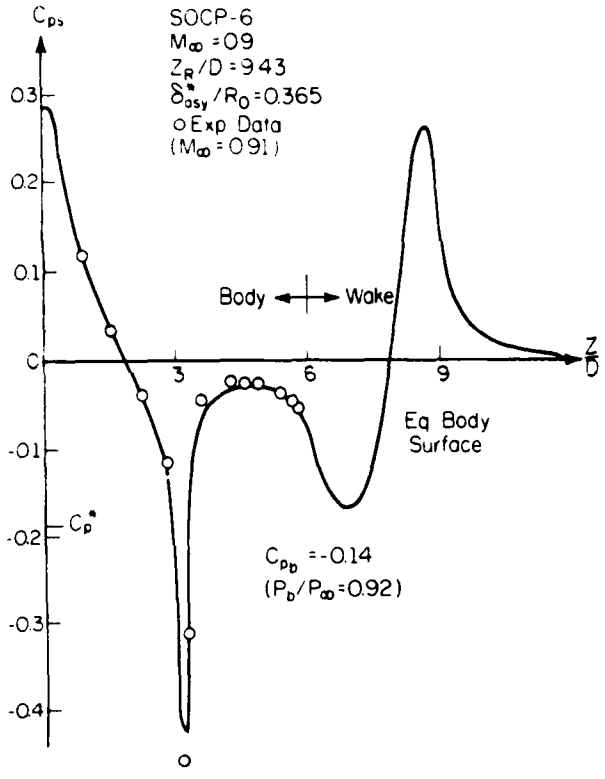

Fig. 8a Pressure Distribution on Equivalent Body
M_∞ = 0.9

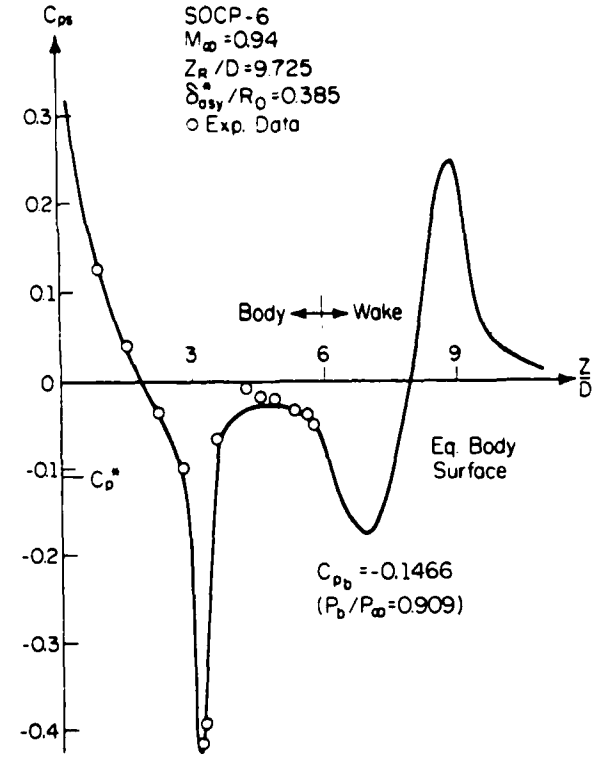

Fig. 8b Pressure Distribution on Equivalent Body
M_∞ = 0.94

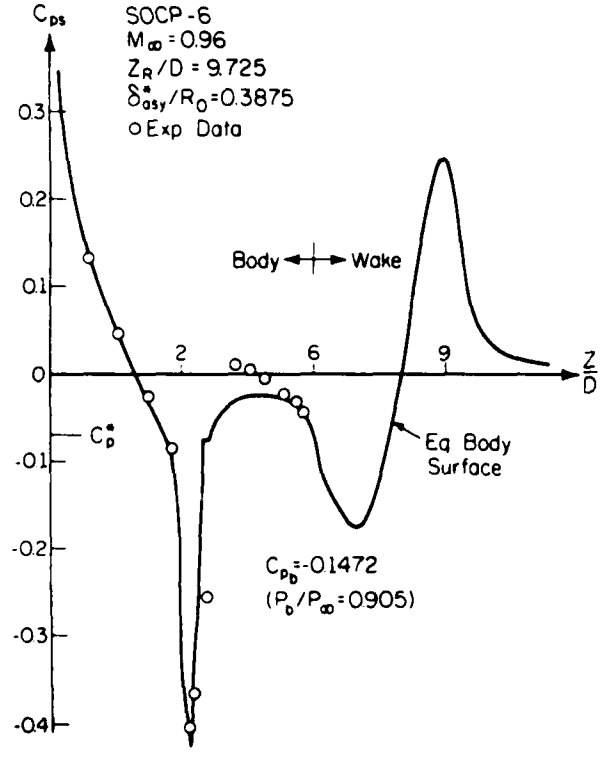

Fig. 8c Pressure Distribution on Equivalent Body
M_∞ = 0.96

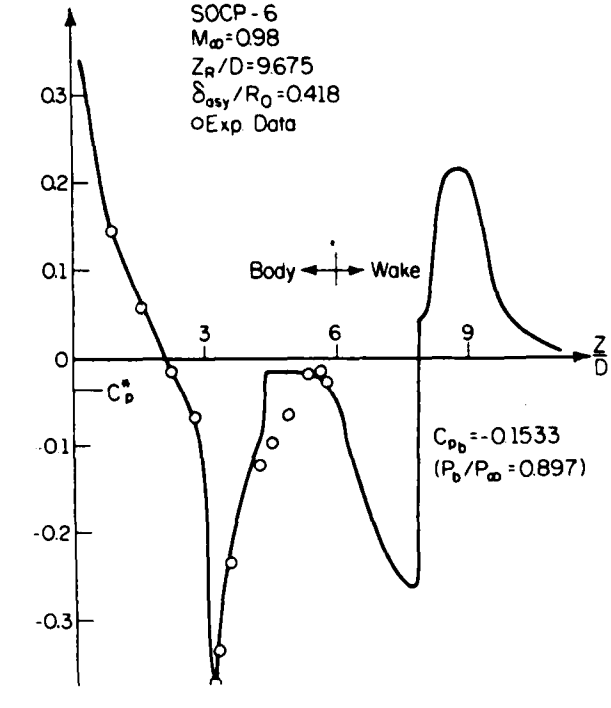

Fig. 8d Pressure Distribution Equivalent Body
M_∞ = 0.98

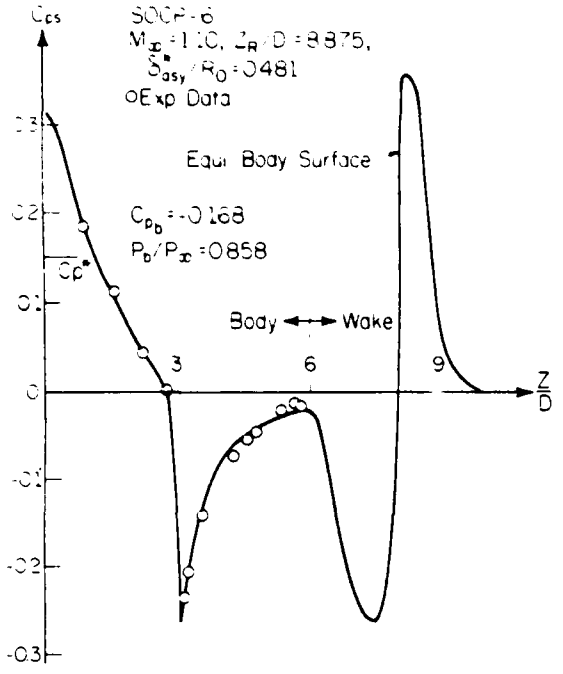

Fig. 8e Pressure Distribution on Equivalent Body M_∞ = 1.10

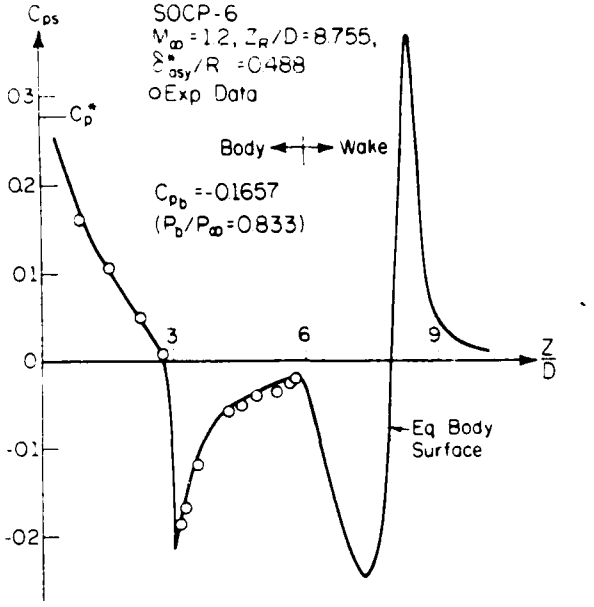

Fig. 8f Pressure Distribution on Equivalent Body M_∞ = 1.20

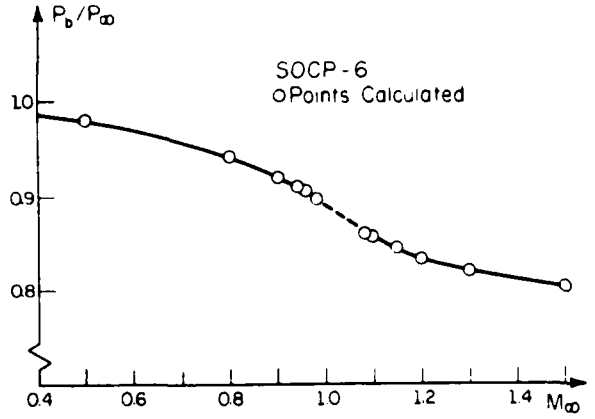

Fig. 9 Average Base Pressure within the Transonic Regime

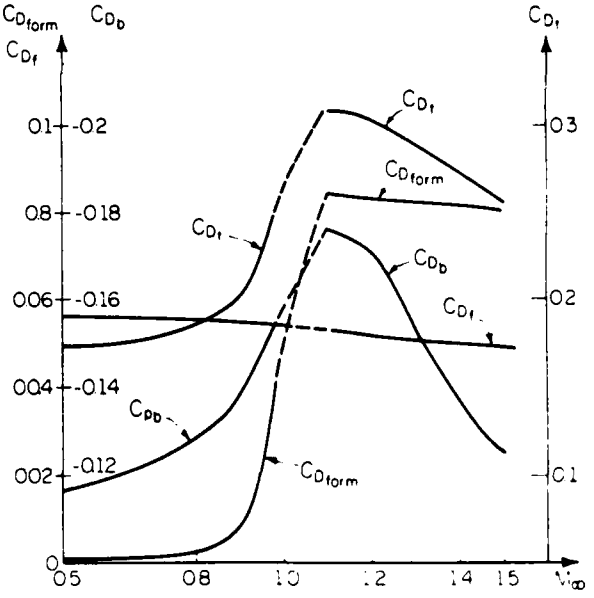

Fig. 10 Drag Coefficient within Transonic Regime

and 10, that the results are more or less bracketed for the range of $0.98 < M_\infty < 1.08$, it is by no means a simple matter to carry out these calculations. At the least, additional under-relaxations must be applied to obtain a convergent solution for the potential flow within this range of the Mach number. A considerably greater amount of computer time is also needed for these occasions.

It is obvious from this scheme of computations that the overall pressure field is produced from the characteristic parameters z_R and δ^*_{asy}. While δ^*_{asy} is directly related to the total drag experienced by the body, and z_R is determined from the recompression of the free turbulent shear layer which is nevertheless guided by the already established inviscid flow. The flow mechanisms of viscid and inviscid flows are so interwoven that they all play important roles in the establishment of the solution. With an integral analysis of the viscous flows, the important flow features are brought forth clearly so that influences of different flow components and flow mechanisms can be easily identified and appreciated.

For the analysis of turbulent jet mixing process, only the eddy diffusivity along the dividing streamline needs to be specified. The expression given by Eq. (2b) has been employed for the present problem. In addition, the eddy diffusivity for the subsequent recompression process is also estimated on a similar basis. It is well known that this expression is valid only for fully developed turbulent mixing flows. In addition, the value of σ is 12 for incompressible flow, and its value tends to increase with the Mach number. More accurate evaluation of this mixing process can be achieved from the two-equation turbulence modeling. It is believed, however, that the present simplified scheme will yield a fairly reasonable estimation of this process of turbulent transport. A more precise estimation can be included into the analysis in the future if it is proved to be necessary.

Extension to Flows with Small Angles of Incidence

The study carried out so far is for axisymmetric configurations; thereby the flow must be at the condition of zero angle of attack.

When the angle of attack is not zero, the flow problems become three-dimensional. Even under the situation of a small angle of attack, the flow condition is so complicated that it seems to be hopeless to examine this problem on a simple basis. Although the flow condition on the forebody may still be examined using the calculation of the three-dimentional potential equation[29], the viscous flows of mixing, recompression-reattachment, and redevelopment behind the body are so complicated that a clear visualization of the flow field within the wake is difficult, if not impossible. It is certain that the descriminating streamlines, which stagnate at the end of the nearwake, do not coincide with the jet boundary streamline within different meridianal planes and an open wake condition exists. A certain amount of fluid mass from the external flow is fed into the wake from the windward meridianal planes, while the same amount of fluid is pumped out from the wake along the leeward meridianal planes. A detailed study of these problems can only be relied upon using the large-scaled numerical calculations of the Navier-Stokes equation.

Since the present analysis was based on an equivalent body concept, one may assume that the effect of the small angle of attack to the viscous flow processes is small under this situation. Essentially, it is to stipulate that the angle of attack will exert its influence only on the equivalent inviscid body which is already established for the case of zero angle of attack. Hopefully, an inviscid study of the flow past this equivalent body under small angle of incidence would yield a crude estimation of the base pressure for these flow conditions.[30] The merit of such a speculation can only be ascertained when experimental data of this nature become abundantly available.

ACKNOWLEDGEMENT

This work was carried out under partial support from the U.S. Army Research Office through Contract DAAG29-83-K-0043. This effort was actually initiated while the author served as a Senior Research Associate of the National Research Council, National Academy of Science, working in the Aerodynamic Research Branch, Launch and Flight Division of the U.S. Army Ballistic Research Laboratory. Valuable discussions and help from Dr. W. B. Sturek and his group in BRL are greatly appreciated.

REFERENCES

1. Crocco, L. and Lees, L., "A Mixing Theory for the Interaction Between Dissipative Flows and Nearly Isentropic Streams," J. of the Aeronautical Sciences, Vol. 19, No. 10, Oct. 1952, pp. 649-676.
2. Korst, H. H., "A Theory for Base Pressures in Transonic and Supersonic Flow," J. of Applied Mechanics, Dec. 1956, pp. 593-600.
3. Korst, H. H., Page, R. H., and Childs, M. E., "A Theory for Base Pressures in Transonic and Supersonic Flows," University of Illinois, ME-TN-392-2, March 1955.
4. Beheim, M. A., Klann, J. L., and Yeager, R. A., "Jet Effects on Annular Base Pressure and Temperature in a Supersonic Stream," NASA TRR-125, 1962.
5. Carriere, P., and Sirieix, M., "Resultats Recents Dans L'Etude Des Problemes De Melange Et De Recollement," ONERA T. P. 165, 1964.
6. Korst, H. H., Chow, W. L., and Zumwalt, G. W., "Research on Transonic and Supersonic Flow of a Real Fluid at Abrupt Increases in Cross Section," ME Technical Report 392-5, Engineering Experiment Station University of IL, Dec. 1959.
7. Lees, L., and Reeves, B. L., "Supersonic Separated and Reattaching Laminar Flows: I. General Theory and Application to Adiabatic Boundary-Layer/Shock-Wave Interactions," AIAA J., Vol. 2, No. 11, Nov. 1964, pp. 1907-1920.
8. McDonald, H., "The Turbulent Supersonic Base Pressure Problem: A Comparison Between a Theory and Some Experimental Evidence," The Aeronautical Quarterly, Vol. 17, May 1966, pp. 105-126.
9. Weinbaum, S., "Rapid Expansion of a Supersonic Boundary Layer and Its Application to the Near Wake," AIAA J., Vol. 4, No. 2, Feb. 1966, pp. 217-226.
10. Chow, W. L., "On the Base Pressure Resulting From the Interaction of a Supersonic External Stream With a Sonic or Subsonic Jet," J. of the Aerospace Sciences, March 1959, pp. 176-180.
11. Page, R. H., "A Review of Component Analysis of Base Pressure for Supersonic Turbulent Flow," Proc. of the 10th Int. Symposium on Space Technology and Science, Tokyo, Japan, 1973, pp. 459-469.
12. Alber, I. E. and Lees, L., "Integral Theory for Supersonic Turbulent Base Flows," AIAA J., Vol. 6, No. 7, July 1968, pp. 1343-1351.
13. Addy, A. L., Korst, H. H., White, R. A., and Walker, B. J., "A Study of Flow Separation in the Base Region and Its Effects During Powered Flight," AGARD Conference on Aerodynamic Drag, AGARD-CPP-124, April 1973.

14. Chow, W. L., "Recompression of a Two-Dimensional Supersonic Turbulent Free Shear Layer," Developments in Mechanics, Vol. 6, Proc. of the 12th Midwestern Mechanics Conference, August 1971, pp. 319-332.
15. Chow, W. L., and Spring, D. J., "Viscous Interaction of Flow Redevelopment after Flow Reattachment with Supersonic External Streams," AIAA J., Vol. 13, No. 12, Dec. 1975, pp. 1576-1584.
16. Weng, C. H., and Chow, W. L., "Axisymmetric Supersonic Turbulent Base Pressures," AIAA J., Vol. 16, No. 6, June 1978, pp. 553-554.
17. Chow, W. L., and Spring, D. J., "Viscid-Inviscid Interaction of Two-Dimensional Incompressible Separated Flows," J. of Applied Mechanics, Vol. 43, Series E, No. 3, Sept. 1976, pp. 387-395.
18. Warpinski, N. R., and Chow, W. L., "Base Pressure Associated With Incompressible Flow Past Wedges at High Reynolds Numbers," J. of Applied Mechanics, Vol. 46, No. 3, Sept. 1979.
19. Warpinski, N. R., and Chow, W. L., "Viscid-Inviscid Interaction Associated with Incompressible Flow past Wedges at High Reynolds Numbers," ME-TR-395-4, UILU ENG 77-4001, Engineering Experiment Station, Dept. of Mech. and Ind. Engr., University of IL at Urbana-Champaign, Feb. 1977, also NASA CR-135246.
20. Chow, W. L., and Shih, T. S., "Transonic Flow past a Backward Facing Step," AIAA J., Vol. 15, No. 9, pp. 1342-1343, 1977.
21. Liu, J. S. K., and Chow, W. L., "Base Pressures of an Axisymmetric Transonic flow past a backward facing step," AIAA J., Vol. 17, No. 4, 1979, pp. 330-331.
22. Chow, W. L., and Shih, T. S., "The Viscid-Inviscid Interaction Associated with a Two-Dimensional Transonic Flow past a Backstep," ME-TR-395-3, UILU ENG 75-4003, Engineering Experiment Station, Dept. of Mech. and Ind. Engr., University of IL at Urbana-Champaign, Final Report prepared for the Research Grant, U.S. Army DAHC04-75-G-0041, Oct. 1975.
23. Liu, J. S. K., and Chow, W. L., "Base Pressure problems Associated with an Axisymmetric Transonic Flow past a Backward Facing Step," ME-TR-395,5, Dept. of Mech. and Ind. Engr., University of IL at Urbana-Champaign, Final Report prepared for Research Grant, U. S. Army DAAG29-76-G-0199, Nov. 1977, ADA050658.
24. Chow, W. L., Bober, L. J., and Anderson, B. H., "Strong Interaction Associated with Transonic Flow past Boattails," AIAA J., Vol. 13, No. 1, 1975, pp. 112-113.
25. Chow, W. L., Bober, L. J., and Anderson, B. H., "Numerical Calculation of Transonic Boattail Flow," NASA TN D-7984, June 1975.
26. Brink, D. F., and Chow, W. L.," Two-Dimension Jet Mixing with a Pressure Gradient," J. of Applied Mechanics, Vol. 42, Series E, No. 1, pp. 55-60, March 1975.
27. Chow, W. L., "Base Pressure of a Transonic Flow past a Projectile," Proc. of the Symposium on Rocket/Plume Fluid Dynamic Interactions, Vol. I, Base Flows, Fluid Dynamic Lab Report 83-101, College of Engineering, University of Texas at Austin, April 1983.
28. Kayser, L. D., and Whiton, F., "Surface Pressure Measurements on a Boattailed Projectile Shape at Transonic Speeds," Memorandum Report ARBRL-MR-03161, Ballistic Research Laboratory, Aberdeen Proving Ground, MD, March 1982.
29. Weng, C. H., "Base Pressure Problems Associated with Supersonic Axisymmetric External Flow Configurations," Ph.D. Thesis, Dept. of Mech. and Ind. Engr., University of IL at Urbana-Champaign, Urbana, IL, 1975.
30. Nakayama, A., and Chow, W. L., "Calculations of Transonic Boattail Flow at a Small Angle of Attack," ME-TN-395-6, Dept. of Mech. and Ind. Engr., University of Illinois at Urbana-Champaign, Report prepared for Research Grant NGL 14-005-140, April 1979. Also NASA CR-158471.

SECTION A.2

BASE PRESSURE OF A PROJECTILE WITHIN THE TRANSONIC FLIGHT REGIME

AIAA Journal

Volume 23, Number 3, March 1985

Pages 388-395

by

W. L. Chow

Base Pressure of a Projectile Within the Transonic Flight Regime

W. L. Chow*
University of Illinois at Urbana-Champaign, Urbana, Illinois

An equivalent body concept is developed to examine the base pressure problem of a transonic flow past a blunt-based projectile. The inviscid flow is established by finite difference computations of the axisymmetric potential equation. All viscous flow processes are treated through integral formulations. The strong viscid-inviscid interaction is clearly illustrated from the method of approach to the problem. A definition of the base pressure that is compatible with that for the supersonic flow regime has been developed for the transonic flow regime. An analysis of the asymptotic far-wake condition relates a needed parameter to the total drag experienced by the projectile. Results are obtained for transonic (both subsonic and supersonic) approaching flow conditions and are also compared with the available experimental data. Extension to cases with small angles of incidence is also discussed.

Nomenclature

$A_i, B_i, \ldots, G_i$ = coefficient functions
D_i, C_{Di} = total drag force, total drag coefficient of the projectile
h_b = height of reverse flow
P = pressure
R_b = equivalent body radius for inviscid flow analysis
R_d = radial coordinate of the dividing streamline
R_e = radial location of the edge of the viscous layer
R_0 = base radius of the projectile
s = velocity slope parameter for the recompression region [see Eq. (4a)]
u, v = velocity component in z, r coordinate system
x = z coordinates for the jet mixing process whose origin is located at the base
z, r = cylindrical coordinates
z_R = z location where the equivalent body radius reaches δ^*_{asy}
δ^* = displacement thickness of the shear layer
δ_a = thickness of the viscous layer above the dividing streamline in the mixing and recompression regions, $= R_e - R_d$
δ_b = thickness of the forward-flowing viscous layer below the dividing streamline in the mixing and recompression regions, $R_d - h_b$
δ_r = thickness of viscous layer in the redevelopment region
ϵ = eddy diffusivity along the dividing streamline
ζ_a = dimensionless radial coordinate for the shear layer above the dividing streamline, $(r - R_d)/\delta_a$
ζ_b = dimensional radial coordinate for the reverse flow region, r/h_b
ζ_r = dimensional radial coordinate for the forward flowing shear layer below the dividing streamline, $(r - R_d + \delta_b)/\delta_b$
ρ = density
τ = shear stress
ϕ = dimensionless velocity, u/u_e

Subscripts

asy = far-wake condition
b = reverse flow
cyl = cylinder
d = dividing streamline
e = edge of the viscous layer
G = projectile base (see Fig. 2)
m = end of the mixing region (also, beginning of recompression region)
og = ogive
R = point of reattachment
w = wake flow in the region of flow redevelopment
∞ = approaching flow condition

Received Nov. 14, 1983; presented as Paper 84-0230 at the AIAA 22nd Aerospace Sciences Meeting, Reno, Nev., Jan. 9-12, 1984; revision received March 26, 1984.

*Professor of Mechanical Engineering, Department of Mechanical and Industrial Engineering. Associate Fellow AIAA.

Introduction

DESPITE the prevailing popularity of solving fluid dynamic problems through large-scale numerical computations of the Navier-Stokes equation, study of the base pressure problem from the conventional approach provides a unique opportunity to illustrate vividly the flow mechanisms governing the phenomenon of these problems. It is well known that the viscous flow plays a role as important as the external inviscid flow in the establishment of the overall flow pattern. This feature has been classified as a strong viscid-inviscid interaction. Since the viscous flow is always located along the edge of the inviscid flow region, the viscous flow is thus guided by the inviscid flow in the sense of the boundary-layer concept. On the other hand, in direct association with the inviscid flowfield, the geometry of the wake as well as the pressure level and distribution within the wake are dependent upon the viscous flow processes of jet mixing, recompression, reattachment, and redevelopment behind the base. This mutual dependency between the inviscid and viscous flows was pointed out by Crocco and Lees.[1] Much work on base pressure has been carried out since that time.[2-16] It should be noted that all of these investigations were restricted to problems with supersonic external streams. Other than the limited few exceptions,[15,16] none of these analyses considered the process of redevelopment after reattachment.

In a more detailed examination of the recompression-reattachment process of a turbulent free shear layer,[14] it was learned that this same integral analysis can be applied to study the base pressure problems in any other flow regime. An examination of base pressure problems of incompressible wedge flow was later carried out.[17-19] The elliptic inviscid flow is established from conformal mapping. The viscous flow was guided by the established inviscid flow, while the characteristic parameters describing the inviscid flow were determined from viscous flow processes. This analysis also led to the study of the base pressure problem for the transonic flow past a backward-facing step in the two-dimensional and axisymmetric configurations.[20-23] Indeed, since the pressure field is established from the inviscid flow, it would be appropriate to simulate the pressure field on the basis of an "equivalent body." The solution of the transonic inviscid flow was established from the finite difference computations of the potential equation. It was learned that the point of reattachment behaved as a saddle-point singularity of the system of equations describing the isoenergetic viscous flow recompression. Furthermore, the pressure at the step cannot be taken as the base pressure within the transonic flow regime. It is obvious that the step pressure coefficient increases toward zero as the freestream Mach number increases toward unity; meanwhile, the base pressure coefficient decreases toward more negative values. It was also learned that studies carried out up to this point constituted only the first approximation to the problem since the resulting equivalent body established from the viscous flow analysis was not yet compatible with the equivalent body selected to establish the inviscid flow.

Additional studies have been carried out on the transonic base pressure problem. Specifically the base pressure of a six-caliber secant-ogive-cylinder projectile immersed in a transonic flow has been examined. The flow condition on the forebody, including the attached turbulent boundary together with the processes of mixing, recompression, reattachment, and redevelopment behind the base, must be included in the considerations. It will be shown that the equivalent body for this problem can be described with two characteristic parameters. It will also be demonstrated that the point of reattachment is a saddle-point singularity for the system of equations describing the viscous flow recompression. Continued computation after reattachment will reveal that the fully developed wake flow state is also a saddle-point singularity of the system of equations describing the viscous flow redevelopment. However, with additional analysis of the asymptotic state of fully developed flow, one parameter can be directly related to the total drag of the body, and the problem can be reduced to a problem of Reynolds number matching from the analysis of recompression. Extension to the case of flow with a small angle of attack will also be suggested and discussed.

Analytical Considerations

For external flow past a body, the surface pressure distribution is the item of utmost concern which supplies the basic information for the lift-drag calculations. Inasmuch as the boundary-layer concept is applicable, the pressure distribution is determined entirely from the inviscid flow geometry. For the present problem of flow past a projectile, the equivalent body geometry must be established before any viscous flow processes can be examined and studied.

The Equivalent Body

For transonic flow past a projectile, whose typical configuration is shown in Fig. 1, it is expected that after the flow separates from the base, usually a turbulent jet mixing process occurs along the wake boundary. The dividing streamline is thus energized, preparing itself for the subsequent recompression and reattachment at the end of the near wake. After reattachment, additional compression of the shear layer occurs in the early part of the redevelopment before the pressure field decays toward that of the freestream. Based on the displacement concept of the boundary layer, the equivalent inviscid body boundary would be located away from the viscous dividing streamline by a distance of the displacement thickness δ^* of the viscous layer above the dividing streamline. This reasoning leads to the specification of the equivalent body $R_b(z)$ for the present problem by

$$R_b(z) = 0 \qquad \text{for } z \le 0 \tag{1a}$$

$$= R_{og} + \delta^*(z) \qquad \text{for } 0 \le z \le z_T \tag{1b}$$

$$= R_{cyl} + \delta^*(z) \qquad \text{for } z_T \le z \le z_G \tag{1c}$$

$$= \delta^*_{asy} + (R_{cyl} + \delta^*_b - \delta^*_{asy}) e^{(-\Delta^2/1-\Delta)} \qquad \text{for } z_G \le z \le z_R \tag{1d}$$

where $\Delta = (z - z_G)/(z_R - z_G)$,

$$R_b(z) = \delta^*_{asy} \qquad \text{for } z_R \le z \tag{1e}$$

The schematic sketch of the equivalent body of projectile is shown in Fig. 2. It will be recognized that the parameters characterizing the equivalent body geometry are z_R and δ^*_{asy} for this specific projectile. It is also worthwhile to note that Δ varies from zero to unity when z is between points G and R and the second power employed in Eq. (1d) assures the slope continuity of the profile at the base. Futhermore, it can be shown that under the far-wake condition, the displacement thickness of the viscous layer approaches a finite value even when the viscous layer thickness approaches infinity at far downstream locations.

The Inviscid Flowfield

Once the equivalent body is specified for a transonic approach flow Mach number, the inviscid flow is established from relaxative finite difference calculations of the full potential equation. In fact, it follows precisely a procedure described in the study of transonic flow past a boattailed afterbody.[24,25] That procedure is discussed briefly herein. At first, a transformation is introduced to transform the infinite physical region of concern into a finite region of computation. A specific finite difference form of the transformed potential equation is written which depends upon whether the flow is locally supersonic or subsonic. A row of grid points is added below the body surface so that the tangent flow condition on the surface can be obeyed. When the finite difference equations are written for all grid points at a certain streamwise location, a tridiagonal system of equations is obtained. Values of the potential function are found by solving the system of equations. This new information is immediately employed to update the corresponding value of the grid below the body surface in satisfying the local boundary condition. This procedure is then repeated for the next streamwise location. This line-by-line sweeping of the computational plane from upstream toward downstream directions is carried out until the change in the value of the potential function is less than an arbitrarily small number for all grid points throughout the domain of computation. A convergent solution of the potential function is obtained. In the midst of computations of the potential function, the turbulent boundary-layer growth with the prevalent pressure gradient on the body surface has also been estimated from an integral approach. The equivalent body geometry is correspondingly modified to account for the displacement effect of this turbulent boundary-layer growth. Thus the boundary-layer, momentum, and displacement thicknesses of the viscous layer at the base are known as soon as the inviscid flowfield is established.

Turbulent Jet Mixing, Recompression, and Reattachment

The integral analysis of these flow processes precisely follows the early study of a flow past a backward-facing step.[23] Only a brief description of these considerations is given here. Again, an isoenergetic flow condition is assumed throughout all viscous flow regions.

Immediately behind the base, a turbulent jet mixing process occurs along the jet boundary. As one will observe later, the pressure also decreases significantly along the path of mixing in the transonic regime. Nevertheless, the mixing process can be treated on the basis of a quasi-constant pressure analysis.[26] At each location, the velocity profile is derived from a local constant pressure calculation with the same initial boundary-layer profile. A linear velocity profile with the local slope given by

$$\frac{\partial u}{\partial r} = \frac{\sigma u_e}{\pi^{1/2} x} \tag{2a}$$

is assumed, which is the inflection-point slope of an error-function mixing profile. The eddy diffusivity ϵ for this region is given by

$$\epsilon = (1/4\sigma^2)\, x u_e \tag{2b}$$

where x is the distance along the path of mixing measured from the origin of mixing, u_e the local freestream velocity, and σ, the spread-rate parameter for the turbulent mixing process, assumes the value of 12 throughout this series of study. The turbulent boundary layer at the step provides the initial condition. The dividing streamline velocity, the shear layer thicknesses above and below the dividing streamline, as well as the shear stress along the dividing streamline can be determined at each section along the mixing region. This mixing analysis is carried out until the section of lowest pressure along the wake is reached. The flow properties here also provide the initial conditions for the subsequent recompression process.

Prior to consideration of recompression, an average base pressure can be determined from the momentum principle. One observes from Fig. 3 that the momentum principle, when applied between the base and section m, the end of the mixing region, readily yields

$$p_b \pi R_0^2 = \int_{R_{dm}}^{R_0} P_d 2\pi r dr + \pi R_{dm}^2 P_m - \int_0^{t_m} \tau_d 2\pi r dz + \int_0^{\delta_b} 2\pi r \rho u^2 dr + \int_0^{h_b} 2\pi r \rho u^2 dr \tag{3}$$

where the forward flow momentum is evaluated from the linear mixing profile and the backward flow momentum is evaluated from the reverse flow velocity profile for the following recompression process. An average base pressure ratio, P_b/P_∞, may be solved from the above equation. In supersonic external flows, there is practically no pressure variation prior to recompression. Under this condition, the shear stress integral in Eq. (3) balances with the forward flow momentum, and the backward flow momentum is usually negligible. Thus, the base pressure from Eq. (3) would be equal to the uniform pressure prevailing within the wake for the supersonic flow condition. In transonic flow, the pressure variation immediately behind the base is so severe that the above expression is needed to give a more realistic estimation of the average base pressure and base drag.

Recompression essentially follows that which has been developed previously.[23] At each section the dimensionless velocity of the flow has a profile of

$$\phi = u/u_e = \phi_d + s\zeta_a + (3(1-\phi_d) - 2s)\zeta_a^2 + [s - 2(1-\phi_d)]\zeta_a^3 \quad 0 \le \zeta_a \le 1 \tag{4a}$$

above the dividing streamline, a linear profile of

$$\phi = u/u_e = \phi_d \zeta_f \qquad 0 \le \zeta_f \le 1 \tag{4b}$$

below the dividing streamline for the forward wake flow, and a cosine profile of

$$\phi = u/u_e = -\phi_b \cos(\pi/2)\,\zeta_b \quad 0 \le \zeta_b \le 1 \tag{4c}$$

for the reverse wake flow, where

$$\phi_d = \frac{u_d}{u_e}, \quad \phi_b = \frac{u_b}{u_e}, \quad \zeta_a = \frac{r - R_d}{\delta_a}, \quad \zeta_f = \frac{r - R_d + \delta_b}{\delta_b}$$
$$\zeta_b = \frac{r}{h_b}, \quad \delta_a = R_e - R_d, \quad \delta_b = R_d - h_b \tag{4d}$$

The slope parameter s in Eq. (4a) is linearly coupled to ϕ_d, and the proportional constant is evaluated at the initial section of the recompression region. This manipulation assures the fact that both ϕ_d and s vanish together at the section of reattachment. A locally triangular geometry is also assumed for the wake flow so that the wake centerline which divides the forward and reverse flow also shall pass through the point of reattachment as it should.

A system of five ordinary differential equations is obtained to describe the process of recompression. They are given by

$$A_i \frac{dR_e}{dz} + B_i \frac{dR_d}{dz} + C_i \frac{d\phi_d}{dz} + D_i \frac{dh_b}{dz} + E_i \frac{d\phi_b}{dz} = F_i \frac{dC_e}{dz} + G_i \qquad i = 1,\ldots,5 \tag{5}$$

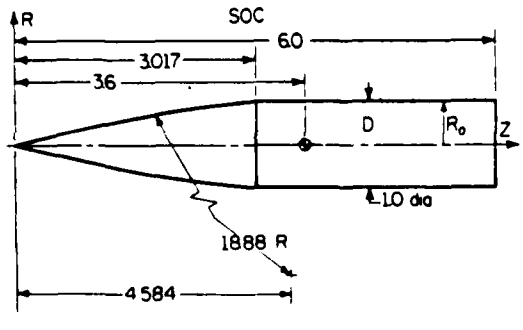

Fig. 1 A six-caliber secant-ogive-cylinder projectile.

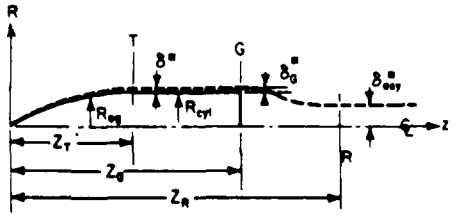

Fig. 2 Equivalent body configuration.

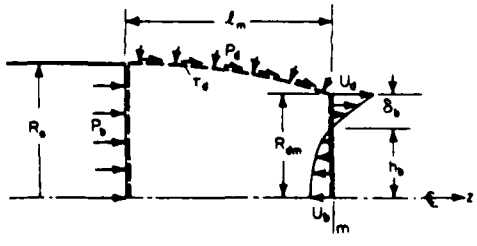

Fig. 3 Average base pressure defined from the momentum principle.

The first two equations are obtained from the continuity principle for the viscous layers above and below the dividing streamline, respectively. The next two were the momentum relations for the two layers, and the last was derived from the condition of local triangular wake geometry. Coefficients $A_1, B_1, \ldots, G_1$ (see Ref. 23 for expressions of these functions) are complicated functions of flow properties and conditions. Equation (5) describes the variation of the locations of the edge of shear layer R_e, the dividing streamline R_d, and its velocity u_d, together with the reverse flow height h_b and velocity u_b throughout the recompression region. C_e is the Crocco number of the adjacent freestream which is related to the Mach number M_e by

$$C_e^2 = \frac{M_e^2}{[2/(\gamma-1)]+M_e^2} \tag{6}$$

The turbulent shear stress along the dividing streamline, which appears in terms G_3 and G_4, is evaluated through an eddy dif usivity which is related to that at the initial section of recompression by

$$\frac{\epsilon}{\epsilon_m} = \frac{u_e}{u_{em}}\left(\frac{\delta_a}{\delta_{am}}\right)\left(\frac{\ell_m + x_r}{\ell_m}\right) \tag{7}$$

where δ_a refers to the shear layer thickness above the dividing streamline, and x_r refers to the distance along the recompression region. Perhaps it is worthwhile to note that with an integral analysis for the turbulent mixing and recompression process, only the empirical information of the eddy diffusivity along the dividing streamline is needed throughout these regions.

The right-hand side of Eq. (5) contains the pressure gradient term which is implicitly linked with the spread of the viscous layer into the already established inviscid flow region. Iterative solution procedures must be relied upon at each step of the numerical integration if accurate results are expected.

It was learned from the recompression calculation that by integrating the system of equations, the point of reattachment behaves as a saddle-point singularity for the system of equations describing the flow. For slightly different z_R values, which, of course, correspond to different inviscid flowfields, the dividing streamline velocity would either decrease to negative values during recompression, before the point of reattachment on the centerline of the wake is reached, or eventually break away from the trend of continuous reduction and start to increase. In the actual calculation, since the establishment of the inviscid flowfield is time consuming, the value of z_R was kept fixed, and the saddle-point behavior is observed from the fact that slightly different initial boundary-layer thicknesses before mixing would lead to widely different results toward the end of recompression. Figure 4 shows a typcial set of results of calculations showing the different trends of the normalized dividing streamline velocity, ϕ_d. To keep the computational effort within a reasonable level, one must attempt to reach the point of reattachment through extrapolation at the end of recompression when the initial boundary-layer thicknesses of two divergent trends are within a small margin.

Redevelopment of Flow

At the point of reattachment, the velocity profile has the shape of $\phi = 3\zeta^2 - 2\zeta^3$ according to Eq. (4a). It is now assumed that throughout the region of redevelopment, the velocity has the profile

$$\phi = \phi_w + (1-\phi_w)(3\zeta^2 - 2\zeta^3) \tag{8}$$

where ϕ_w is the centerline wake velocity and $\zeta = r/\delta_e$. δ_e is the thickness of the viscous layer within the region of redevelopment.

The continuity equation and the equation of motion under the boundary-layer formulation are

$$\frac{\partial(\rho u r)}{\partial z} + \frac{\partial(\rho v r)}{\partial r} = 0 \tag{9a}$$

$$\frac{\partial(\rho u^2 r)}{\partial z} + \frac{\partial(\rho u v r)}{\partial r} = -r\frac{dp}{dz} + \frac{\partial(\tau r)}{\partial r} \tag{9b}$$

Upon integrating across the viscous layer, Eqs. (9) readily yield

$$[1-2(1-C_e^2)I_1]\frac{d\delta_e}{dz} - (1-C_e^2)\delta_e I_4 \frac{d\phi_w}{dz} = \tan\beta_e + \left[\frac{\delta_e I}{C_e}\left(1 - C_e^2\frac{3\gamma-1}{\gamma-1}\right) + 2C_e\delta_e I_3(1-C_e^2)\right]\frac{dC_e}{dz} \tag{10a}$$

$$\frac{2I_2(1-C_e^2)}{\delta_e}\frac{d\delta_e}{dz} + (1-C_e^2)I_6\frac{d\phi_w}{dz} = -\frac{dC_e}{dz}\left[\frac{2I_2}{c_e}\left(1 - C_e^2\frac{2\gamma-1}{\gamma-1}\right) + 2C_e(1-C_e^2)I_5 + \frac{1}{2C_e}(1-2(1-C_e^2)I_1)\right] \tag{10b}$$

where

$$I_1 = \int_0^1 \frac{\phi\zeta d\zeta}{1-C_e^2\phi^2}, \qquad I_2 = \int_0^1 \frac{\phi(1-\phi)\zeta d\zeta}{1-C_e^2\phi^2}$$

$$I_3 = \int_0^1 \frac{\phi^3\zeta d\zeta}{(1-C_e^2\phi^2)^2}, \qquad I_4 = \int_0^1 \frac{1+C_e^2\phi^2}{(1-C_e^2\phi^2)^2}\Gamma\zeta d\zeta$$

$$I_5 = \int_0^1 \frac{\phi^3(1-\phi)\zeta d\zeta}{(1-C_e^2\phi^2)^2}, \qquad I_6 = \int_0^1 \frac{1-2\phi+C_e^2\phi^2}{(1-C_e^2\phi^2)}\Gamma\zeta d\zeta$$

$$\Gamma = \frac{\partial\phi}{\partial\phi_w} = 1 - 3\zeta^2 + 2\zeta^3 \tag{11}$$

β_e is the streamline angle at the edge of the shear layer and all integrals, I_1 through I_6, are only functions of C_e and ϕ_w. It is to be noted that this integral analysis is equally valid for laminar or turbulent flows since the shear stress vanishes at both limits of integration. Indeed, the far-wake condition of

$$\delta_e(1-\phi_w)^{1/2} = \text{const} \tag{12}$$

is satisfied by either laminar or turbulent flow. It may be shown that the system of equations given by Eqs. (10) with the assumed velocity profile is compatible with this condition.

It has been learned from this approach of the problem that the fully developed flow condition also presents itself as a saddle-point singularity of the system of equations describing the flow. For a fixed Z_R but with slightly different δ^*_{asy} values, the redevelopment flow after the reattachment (after the point of reattachment has been obtained from extrapolation) will lead either to positive and ever increasingly large $d\delta_e/dz$ or to a smaller and eventually negative $d\delta_e/dz$ value. Negative $d\delta_e/dz$ also invariably leads to negative $d\phi_w/dz$, resulting in a reduction of wake centerline velocity. An example illustrating this phenomenon is shown in Fig. 5. Both of these behaviors are physically unrealistic and the correct value of δ^*_{asy} lies in between. This, of course, is the typical behavior of a saddle point.

It is now worthwhile to note that with Z_R and δ^*_{asy} as the characteristic parameters [illegible] correspond-

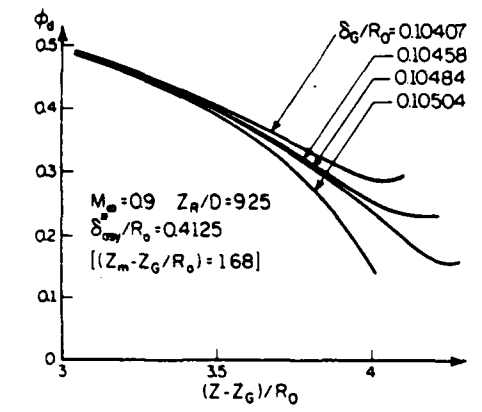

Fig. 4 Saddle-point behavior or recompression process.

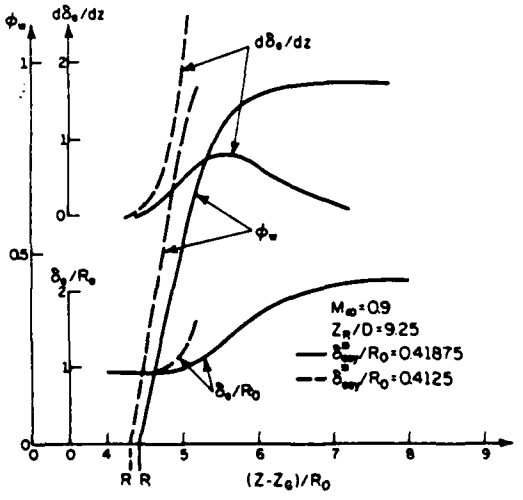

Fig. 5 Saddle-point behavior of redevelopment process.

ing inviscid flow, two saddle-point singularities provide two discriminating criteria for the determination of their correct values under the given flow conditions. However, two saddle points in sequence are mathematically "unstable," especially when the first saddle point can only be determined from extrapolation. Numerical consistency for systems of nonlinear ordinary differential equations cannot be achieved easily. For the present problem, the numerical error generated from the finite difference computation of the potential equation may also have important influences on this phase of the computations. Fortunately, an analysis of the asymptotic wake flow would relate δ^*_{asy} to the total drag experienced by the projectile, and the integration against two-saddle-point singularities in sequence is conveniently avoided.

Asymptotic Wake Flow Condition

It is stipulated that under the asymptotic far-wake flow situation, the approaching freestream external flow condition is restored. The velocity profile within the wake still obeys Eq. (8), but with $(1-\phi_w)$ as a small quantity, so that higher orders of this quantity can be ignored. According to the definition of the displacement thickness given by

$$\rho_\infty u_\infty (\delta_e^2 - \delta^{*2}_{asy}) = 2\int_0^{\delta_e} \rho u r dr \tag{13}$$

and the drag-momentum relationship for the far-wake flow given by

$$D_f = 2\pi \int^{\delta_e} \rho u (u_\infty - u) r dr \tag{14}$$

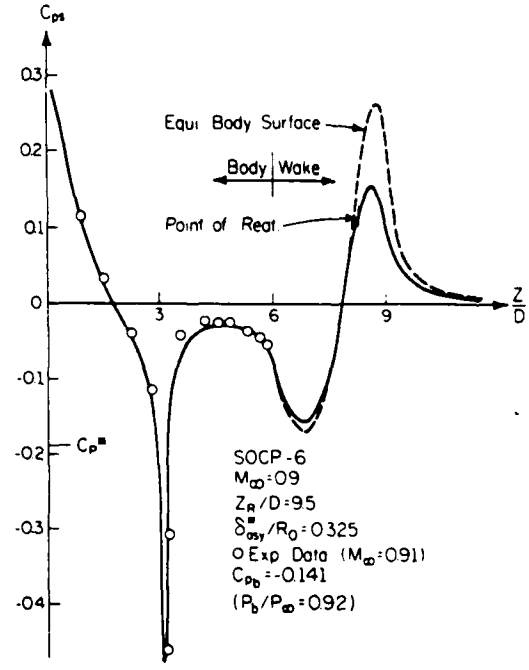

Fig. 6 Pressure distribution realized from detailed evaluations.

where D_f is the total drag experienced by the projectile, it may be shown from Eqs. (13) and (14) that

$$\left(\frac{\delta^*_{asy}}{R_0}\right) = \left[\frac{C_{Df}}{2}\frac{1+C_\infty^2}{1-C_\infty^2}\right]^{1/2} \tag{15}$$

where

$$C_{Df} = D_f \Big/ \frac{\rho_\infty V_\infty^2}{2}\pi R_0^2$$

The total drag D_f is the sum of the form drag, skin friction drag on the forebody,and the base drag on the base.

Method of Calculations and Results

With the introduction of the relationship given by Eq. (15), calculation procedures become greatly simplified. For a given freestream Mach number M_∞, a pair of values of z_R/D and δ^*_{asy}/R_0 is selected. The potential flow solution for this geometric configuration is established subsequently. After the turbulent jet mixing process behind the base has been analyzed, the total drag coefficient can be evaluated, and δ^*_{asy}/R_0 is immediately adjusted according to Eq. (15). Since the effect of δ^*_{asy}/R_0 on the total drag is minor, the correct value of δ^*_{asy}/R_0 can be determined usually within three iterations. Once this condition is satisfied, viscous recompression can be determined by integrating the system of Eq. (5). The dimensionless dividing streamline velocity will either be reduced to a negative value before the centerline is reached or will break away from the continuous pattern of reduction and start to increase—the saddle-point behavior. This phenomenon demands the adjustment of the z_R/D value accordingly. Once this adjustment is within a small margin ($\Delta z_R/D \le 0.0025$ for the present series of calculations), the solution is reached even if the detailed wake flow pattern has not yet been satisfactorily established. It is entirely possible to continue these detailed calculations including the redevelopment after reattachment. Early results obtained from such efforts[27] are shown in Figs. 6 and 7 where the realized pressure field, the reproduced equivalent body, and the path of the dividing streamline are shown. The reproduced equivalent body was obtained by adding the displacement thickness of the viscous [illegible] dividing streamline

onto the path of the dividing streamline. However, all of these calculations are not necessary if only the information on base and total drag is desired. Calculations have been carried out for all of the transonic Mach numbers where wind tunnel pressure data on this projectile are available.[28] The unit Reynolds number employed was also compatible with the wind tunnel test condition ($Rey/ft = 4 \times 10^6$). Figure 8 shows the pressure distribution on the equivalent body along with the experimental data on the forebody. The corresponding average base pressure coefficient and the base pressure ratio are also labeled in the figures. Under some subsonic Mach number conditions, the agreement of pressure with the data on the cylinder is less desirable although it has no influence on the forebody form drag evaluation. The base pressure ratio obtained from this study is shown in Fig. 9. Various drag coefficients and the total drag coefficient for the transonic Mach numbers are presented in Fig. 10.

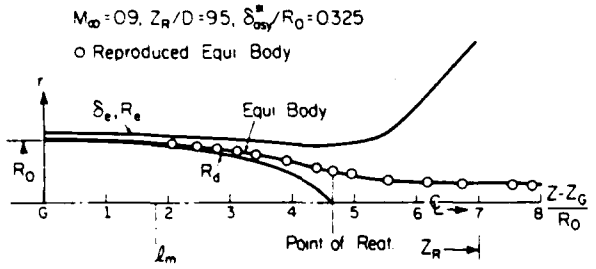

Fig. 7 Dividing streamline, viscous wake, and reproduced equivalent body.

Discussion

It should be noted that the method developed for this study should also be applicable for smaller freestream subsonic Mach number flows, including the incompressible flow condition and also for larger supersonic freestream Mach numbers. Computations of these cases have been carried out and the results are also reported in Figs. 9 and 10. Although the correctness of the base pressure ratio for $M_\infty > 1.3$ is doubtful since entropy increases from shocks may no longer be negligible, previous results of $p_b/p_\infty = 0.7625$ at $M_\infty = 1.5$ on supersonic flow past an axisymmetric backward-facing step[20] with comparable initial boundary-layer thickness seems to imply that these results are not completely unreasonable.

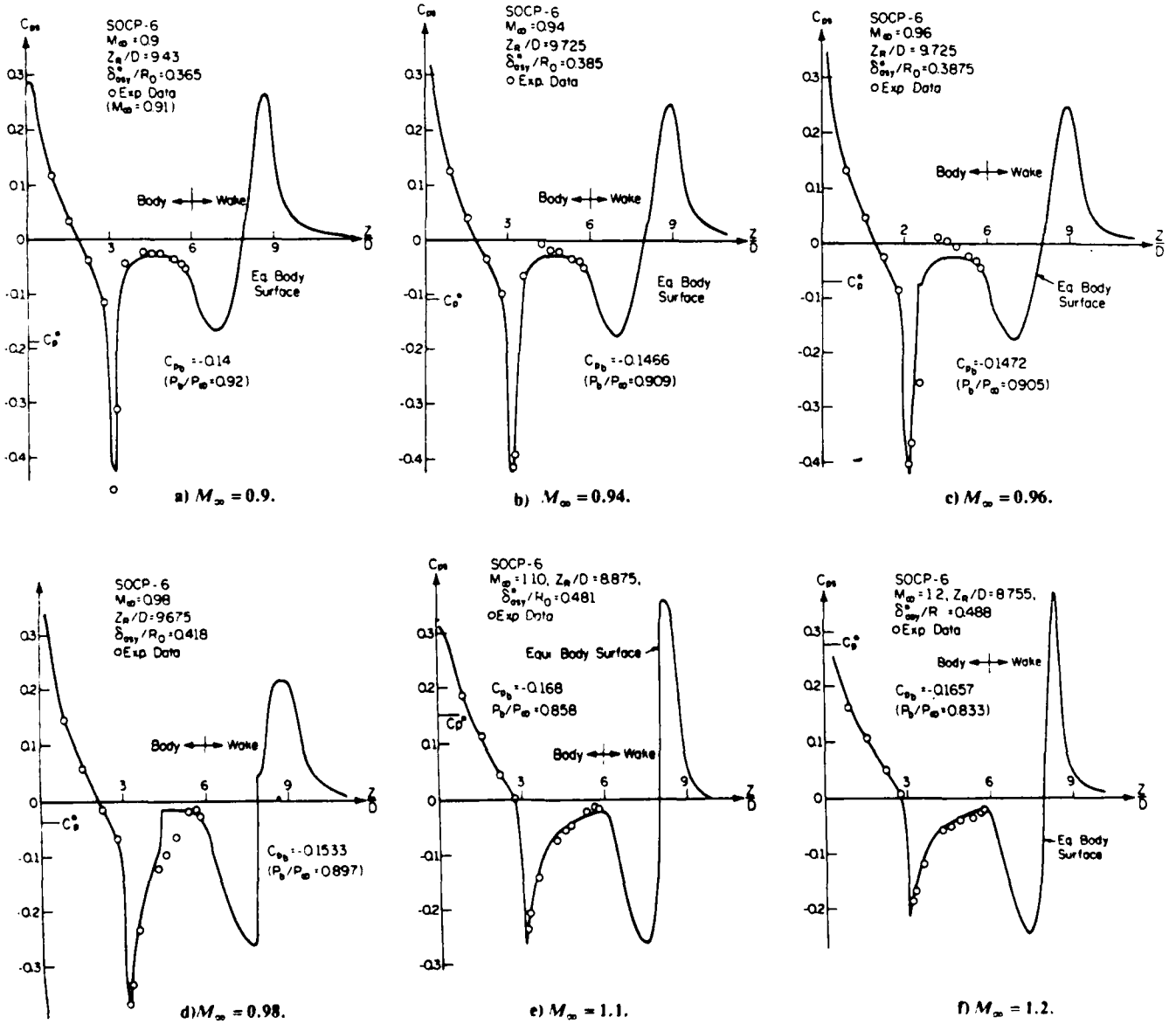

Fig. 8 Pressure ... on an equi...

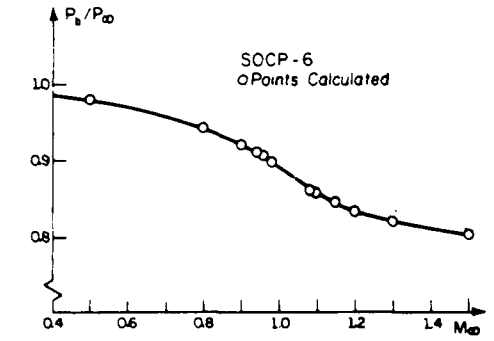

Fig. 9 Average base pressure within the transonic regime.

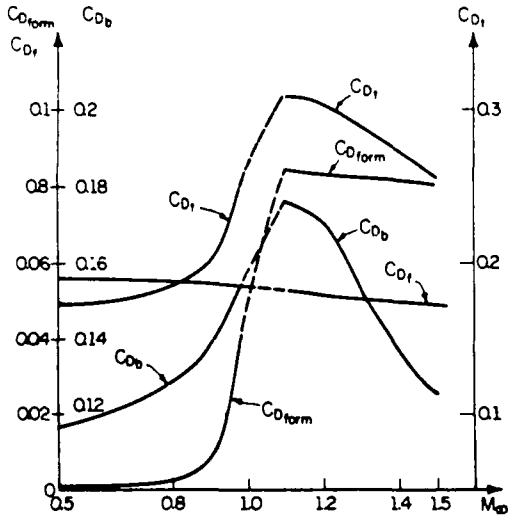

Fig. 10 Drag coefficients within transonic regime.

No computations have been carried out for the range of $0.98 < M_\infty < 1.08$. In fact, additional underrelaxation has been applied for the potential flow calculations at $M_\infty = 0.98$. Also, the calculations for the potential flow have been modified from the original scheme[25] for the supersonic approaching flows. Although it appears from Figs. 9 and 10 that base pressure results are more or less bracketed, the forebody form drag may have a peak within the range of $0.98 < M_\infty < 1.08$. Also, it is by no means a simple matter to carry out these calculations. At the least, additional underrelaxation is needed to obtain a convergent solution for the potential flow within this range of the Mach number. A considerably greater amount of computer time is also needed for these occasions.

It is obvious from this scheme of computations that the overall pressure field is produced from the characteristic parameters z_R and δ^*_{sty}. While δ^*_{sty} is directly related to the total drag experienced by the body, z_R is determined from the recompression of the free turbulent shear layer which is nevertheless guided by the already established inviscid flow. The flow mechanisms of viscid and inviscid flows are so interwoven that they all play important roles in the establishment of the solution. With an integral analysis of the viscous flows, the important flow features are brought forth clearly so that influences of different flow components and flow mechanisms can be easily identified and appreciated.

For the analysis of turbulent jet mixing process, only the empirical eddy diffusivity along the dividing streamline needs to be specified. In addition, the eddy diffusivity for the subsequent recompression process is also estimated on a similar basis. It is well known that the expression given by Eq. (2b) is valid only for constant-pressure fully developed turbulent mixing flows. In fact, the value of σ is 12 for incompressible flow, and its value tends to increase slightly with the Mach number. Perhaps more accurate evaluation of this mxing process can be obained from the two-equation turbulence modeling. It is believed, however, that the present simplified scheme will yield a fairly reasonable estimation of this process of turbulent transport. A more precise estimation can be included into the analysis in the future if it is proved necessary.

The computing time required for a complete calculation of the case of $M_\infty = 0.9$ is around 5 min on the Cyber 175 computer system. The required memory space in 21K for the computing program and 71K for its execution.

Extension to Flows with Small Angles of Incidence

The study carried out thus far is for axisymmetric configurations; thereby the flow must be at the condition of zero angle of attack.

When the angle of attack is not zero, the flow problems become three-dimensional. Even under the situation of a small angle of attack, the flow condition is so complicated that an accurate study can be based only on large-scale three-dimensional computations. Since the present analysis was based on an equivalent body concept, one may assume that the effect of the small angle of attack to the viscous flow processes is small under this situation. Essentially, it is to stipulate that the angle of attack will exert its influence only on the equivalent inviscid body which is already established for the case of zero angle of attack. It is hoped that an inviscid study of the flow past this equivalent body[30] under a small angle of incidence would yield a crude estimation of the base pressure for these flow conditions. The merit of such a speculation can be evaluated only when experimental data of this nature become abundantly available.

Acknowledgments

This work was carried out under partial support from the U.S. Army Research Office through Contract DAAG29-83-K-0043. This effort was actually initiated while the author served as a Senior Research Associate of the National Research Council, National Academy of Science, working in the Aerodynamic Research Branch, Launch and Flight Division of the U.S. Army Ballistic Research Laboratory. Valuable discussions and help from Dr. W. B. Sturek and his group in BRL are greatly appreciated.

References

[1] Crocco, L. and Lees, L., "A Mixing Theory for the Interaction Between Dissipative Flows and Nearly Isentropic Streams," *Journal of the Aeronautical Sciences*, Vol. 19, Oct. 1952, pp. 649-676.

[2] Korst, H. H., "A Theory for Base Pressures in Transonic and Supersonic Flow," *Journal of Applied Mechanics*, Vol. 22, Dec. 1956, pp. 593-600.

[3] Korst, H. H., Page, R. H., and Childs, M. E., "A Theory for Base Pressures in Transonic and Supersonic Flows," University of Illinois, Urbana, Ill., ME-TN-392-2, March 1955.

[4] Beheim, M. A., Klann, J. L., and Yeager, R. A., "Jet Effects on Annular Base Pressure and Temperature in a Supersonic Stream," NASA TR R-125, 1962.

[5] Carriere, P. and Sirieix, M., "Resultants Recent Dans L'Etude Des Problems De Melange Et De Recollement," ONERA TP 165, 1964.

[6] Korst, H. H., Chow, W. L., and Zumwalt, G. W., "Reseach on Transonic and Supersonic Flow of a Real Fluid at Abrupt Increases in Cross Section," Engineering Experiment Station, University of Illinois, Urbana, Ill., ME Tech. Rept. 392-5, Dec. 1959.

[7] Lees, L. and Reeves, B. L., "Supersonic Separated and Reattaching Laminar Flows: I. General Theory and Application to Adiabatic Boundary-Layer/Shock-Wave Interactions," *AIAA Journal*, Vol. 2, Nov. 1964, pp. 1907-1920.

[8] McDonald, H., "The Turbulent Supersonic Base Pressure Problem: A Comparison Between a Theory and Some Experimental Evidence," *The Aeronautical Quarterly*, Vol. 17, May 1966, pp. 105-126.

[9] Weinbaum, S., "Rapid Expansion of a Supersonic Boundary Layer and Its Application to the Near Wake," *AIAA Journal*, Vol. 4, Feb. 1966, pp. 217-226.

[10] Chow, W. L., "On the Base Pressure Resulting from the Interaction of a Supersonic External Stream with a Sonic or Subsonic Jet," *Journal of the Aerospace Sciences*, Vol. 26, March 1959, pp. 176-180.

[11] Page, R. H., "A Review of Component Analysis of Base Pressure for Supersonic Turbulent Flow," *Proceedings of the 10th International Symposium on Space Technology and Science*, Tokyo, Japan, 1973, pp. 459-469.

[12] Alber, I. E. and Lees, L., "Integral Theory for Supersonic Turbulent Base Flows," *AIAA Journal*, Vol. 6, July 1968, pp. 1343-1351.

[13] Addy, A. L., Korst, H. H., White, R. A., and Walker, B. J., "A Study of Flow Separation in the Base Region and Its Effects During Powered Flight," AGARD Conference on Aerodynamic Drag, AGARD-CPP-124, April 1973.

[14] Chow, W. L., "Recompression of a Two-Dimensional Supersonic Turbulent Free Shear Layer," *Developments in Mechanics, Proceedings of the 12th Midwestern Mechanics Conference*, Vol. 6, Aug. 1971, pp. 319-332.

[15] Chow, W. L. and Spring, D. J., "Viscous Interaction of Flow Redevelopment after Flow Reattachment with Supersonic External Streams," *AIAA Journal*, Vol. 13, Dec. 1975, pp. 1576-1584.

[16] Weng, C. H. and Chow, W. L., "Axisymmetric Supersonic Turbulent Base Pressures," *AIAA Journal*, Vol. 16, June 1978, pp. 553-554.

[17] Chow, W. L. and Spring, D. J., "Viscid-Inviscid Interaction of Two-Dimensional Incompressible Separated Flows," *Journal of Applied Mechanics*, Vol. 43, Ser. E, No. 3, Sept. 1976, pp. 387-395.

[18] Warpinski, N. R. and Chow, W. L., "Base Pressure Associated with Incompressible Flow Past Wedges at High Reynolds Numbers," *Journal of Applied Mechanics*, Vol. 46, No. 3, Sept. 1979, pp. 483-492.

[19] Warpinski, N. R. and Chow, W. L., "Viscid-Inviscid Interction Associated with Incompressible Flow past Wedges at High Reynolds Numbers," Engineering Experiment Station, Department of Mechanical and Industrial Engineering, University of Illinois at Urbana-Champaign, ME-TR-395-4, UILU ENG 77-4001, Feb. 1977; also, NASA CR-135246.

[20] Chow, W. L. and Shih, T. S., "Transonic Flow Past a Backward Facing Step," *AIAA Journal*, Vol. 15, Sept. 1977, pp. 1342-1343.

[21] Liu, J.S.K. and Chow, W. L., "Base Pressures of an Axisymmetric Transonic Flow Past a Backward Facing Step," *AIAA Journal*, Vol. 17, April 1979, pp. 330-331.

[22] Chow, W. L. and Shih, T. S., "The Viscid-Inviscid Interaction Associated with a Two-Dimensional Transonic Flow past a Backstep," Engineering Experiment Station, Department of Mechanical and Industrial Engineering, University of Illinois at Urbana-Champaign, ME-TR-395-3, UILU ENG 75-4003, Final Report prepared for the Research Grant, U.S. Army DAHC04-75-G-0041, Oct. 1975.

[23] Liu, J.S.K. and Chow, W. L., "Base Pressure Problems Associated with an Axisymmetric Transonic Flow past a Backward Facing Step," Department of Mechanical and Industrial Engineering, University of Illinois at Urbana-Champaign, ME-TR-395-5, Final Report prepared for Research Grant, U.S. Army DAAG29-76-G-0199, Nov. 1977 (ADA050658).

[24] Chow, W. L. Bober, L. J., and Anderson, B. H., "Strong Interaction Associated with Transonic Flow past Boattails," *AIAA Journal*, Vol. 13, Jan. 1975, pp. 112-113.

[25] Chow, W. L., Bober, L. J., and Anderson, B. H., "Numerical Calculation of Transonic Boattail Flow," NASA TN D-7984, June 1975.

[26] Brink, D. F. and Chow, W. L., "Two-Dimension Jet Mixing with a Pressure Gradient," *Journal of Applied Mechanics*, Vol. 42, Ser. E, No. 1, March 1975, pp. 55-60.

[27] Chow, W. L., "Base Pressure of a Transonic Flow past a Projectile," *Proceedings of the Symposium on Rocket/Plume Fluid Dynamic Interactions*, Vol. 1, Base Flows, Fluid Dynamic Lab., College of Engineering, University of Texas at Austin, Rept. 83-101, April 1983.

[28] Kayser, L. D. and Whiton, F., "Surface Pressure Measurements on a Boattailed Projectile Shape at Transonic Speeds," ARBRL-MR-03161, Ballistic Research Laboratory, Aberdeen Proving Ground, Md., March 1982.

[29] Weng, C. H., "Base Pressure Problems Associated with Supersonic Axisymmetric External Flow Configurations," Ph.D. Thesis, Department of Mechanical and Industrial Engineering, University of Illinois at Urbana-Champaign, 1975.

[30] Nakayama, A. and Chow, W. L., "Calculations of Transonic Boattail Flow at a Small Angle of Attack," Department of Mechanical and Industrial Engineering, University of Illinois at Urbana-Champaign, ME-TN-395-6, Report prepared for Research Grant NGL 14-005-140, April 1979; also, NASA CR-158471.

SECTION A.3

THE EFFECT OF BOATTAILING A PROJECTILE IN TRANSONIC FLOW

Proceedings of the Third Symposium On
Numerical and Physical Aspects of
Aerodynamic Flows

Long Beach, California

January 1985

Pages 9-15 through 9-22

by

W. L. Chow

THE EFFECT OF BOATTAILING OF A PROJECTILE IN TRANSONIC FLOW

Prepared for the Third Sym. on
Numerical and Physical Aspects
of Aerodynamic Flows

Proceeding of Sym.

9-15 to 9-22
Calif.State Univ.
Long Beach,Calif. Jan.1985

W. L. Chow
Professor of Mechanical Engineering
Department of Mechanical and Industrial Engineering
University of Illinois at Urbana-Champaign
1206 West Green Street
Urbana, IL 61801

ABSTRACT

The base pressure problem for a transonic flow past a blunt trailing edged projectile was continued on the basis of an equivalent body approach. Specifically, the effect of boattailing on the forebody pressure distribution and the base pressure was examined. Within the limited range of small boattail angles, it was observed that the reduction of the base drag outweighed the additional drag incurred on the boattail indicating its favorable interference. It was recognized that more precise simulation of turbulence was needed before more accurate evaluation on the optimum boattail configuration could be carried out. Computations for two freestream Mach numbers (M_∞ = 0.9 and 1.2) were performed for different boattail angles. Comparison with the experimental data is presented whenever available. Reasonably good agreement in the pressure distribution on the forebody was observed.

INTRODUCTION

It is well known that the base pressure problem provides a typical example of strong viscid-inviscid interaction. Both viscous and inviscid flows exert such strong influences on each other that solutions cannot be obtained without simultaneous consideration of both inviscid and viscous flow mechanisms. Since this special feature of separated flows was pointed out by Crocco and Lees[1], a tremendous amount of base pressure research was carried out in the supersonic flow regime. While the "critical point" approach was later pursued by Lees, et al.[2,3], Korst[4,5] introduced the "component" approach by dividing the flow events behind the base into

i. Supersonic flow expansion around the corner,

ii. Constant pressure turbulent jet mixing,

iii. Recompression, reattachment and,

iv. Redevelopment of the flow after reattachment.

Each component was delineated and analyzed, and a solution was reached by synthesizing treatments of these flow components. Many other research efforts, e.g.[6-9] were initiated along these lines. These efforts were briefly described[10] and are not reviewed here. It should be pointed out, however, that separated flow problems are elliptic in nature even though the external inviscid supersonic flow is governed by hyperbolic differential equations. Other than the limited few efforts[11-13], all the foregoing studies did not consider the process of redevelopment after reattachment.

In the transonic flow regime, the external inviscid flow is governed by elliptic differential equations. Since the viscous flow always appears along the edge of the inviscid flow, where the boundary layer concept is usually applicable, it is natural to expect that the pressure field is induced from an "equivalent body" whose geometry behind the blunt base must be determined from viscous flow considerations. Indeed this was the basic scheme introduced to study the base pressure problem in the transonic flow past a projectile[9]. The inviscid flow was established from numerical computation of the axisymmetric potential equation, while the viscous flow processes behind the base, such as turbulent jet mixing, recompression, reattachment, and redevelopment were treated from integral formulations. The turbulent boundary layer on the projectile was also calculated from an integral approach whose displacement effect was also incorporated into the equivalent body geometry. On the basis of these integral formulations, a crude description of the turbulent transport across the dividing streamline behind the base was possible by specifying merely a spread rate parameter of the viscous flow for the mixing region and by an additional empirical correlation of the eddy diffusivity throughout the recompression region. However, no empirical information on turbulent transport was needed for the process of flow redevelopment after reattachment. In fact, the flow redevelopment formulated therein was equally applicable for laminar flow process.

It was also precisely for the reason of integral formulation of the viscous flows that the equivalent body behind the base be conveniently specified with two characteristic parameters. The special feature of the strong viscid-inviscid interaction of the problem was then manifested by the fact that the viscous flow attaches itself to the established inviscid flow in the sense of the boundary layer concept where the adjacent freestream condition of the viscous layer depends upon the spread of the viscous layer, while the parameters required to establish the inviscid flow are to be determined from viscous flow considerations.

It was later found, within the scope of such a simple scheme of dealing with such problems, that the point of reattachment (point of confluence) behind the base is a saddle-point singularity for the system of equations describing the viscous flow recompression. Furthermore, upon obtaining the point of reattachment through extrapolation after sufficient narrowing down of the margin of a certain descriptive parameter for integration, it was found that the fully redeveloped flow state is also a saddle-point singularity of the system of equations describing the viscous flow redevelopment after reattachment. Although two discriminative criteria are adequate for determining the two parameters needed to establish the inviscid flow, two saddle-

point singularities in sequence do not allow consistent numerical computations of the flow.

Fortunately, later investigations on the asymptotic far-wake flow condition revealed that one of the characteristic parameters may be related to the total drag experienced by the projectile. Thus only one additional parameter was needed and was determined through the saddle-point integration toward reattachment after the turbulent jet mixing. The base pressure and the base drag can be determined without the detailed establishment of flow redevelopment other than the far-wake flow condition. It should be emphasized that the pressure above the blunt base prior to separation cannot be treated as the base pressure in the transonic flow regime. Even with a local subsonic flow there, the pressure reduction along the dividing streamline immediately behind the base is so severe that a reasonably accurate estimation of the base drag and the average base pressure can be determined only from the scheme suggested in that study.

Computations have been carried out mainly for the transonic Mach number range of 0.9 to 0.98 and 1.08 to 1.2 for a six-caliber secant-ogive-cylinder projectile. The surface pressure distribution on the projectile obtained from computations have been compared with the experimental data[14] within this range of the Mach number. Good agreement was observed. Although in principle, computations of the flow within the Mach number range of 0.98 to 1.08 can be performed, it was not carried out simply for the reason that much more computer time would be needed. In addition there was no experimental data available for this projectile within this range for comparison purpose. However, computation was extended to low subsonic Mach number ($M_\infty = 0.3$) and high transonic Mach number ($M_\infty = 1.5$) without encountering any difficulty. All results obtained from that investigation were already reported[10].

The present study examines the effect of boattailing of the same projectile from the same basic approach. It was recognized that only the geometry of the equivalent body needs to be modified. Once this was accomplished, the previous study became a special case of zero-degree boattail. However in order to discuss the problem in a more satisfactory manner for the present investigation, some of the important descriptions of this scheme are again presented in reasonable detail in the following sections.

ANALYTICAL CONSIDERATIONS

Inviscid Flow

The present study is directed to the boattailed configuration of the six-caliber secant-ogive cylinder projectile shown in Fig. 1. To produce the pressure field from an inviscid flow consideration, one may describe the equivalent body geometry for this projectile by:

$$R_b(z) = 0 \qquad \text{for } z \le 0 \qquad (1a)$$

$$R_b(z) = R_{aq}(z) + \delta^*(z) \qquad \text{for } 0 \le z \le z_T \qquad (1b)$$

$$R_b(z) = R_{cyl} + \delta^*(z) \qquad \text{for } z_T \le z \le z_Q \qquad (1c)$$

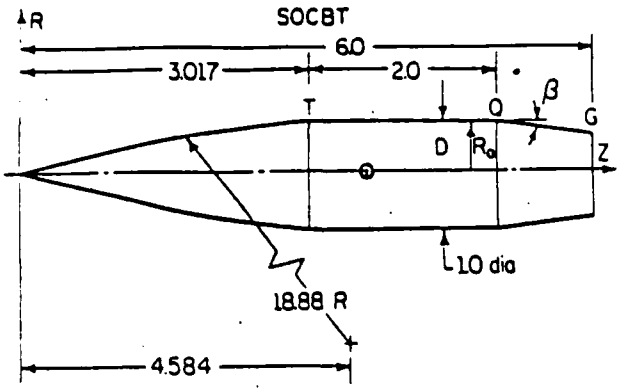

Figure 1 A 6-Caliber Secant-Ogive-Cylinder Projectile with Boattail.

$$R_b(z) = R_{cyl} - (z - z_Q)\tan\beta + \delta^*(z)$$

$$\text{for } z_Q \le z \le z_G \qquad (1d)$$

$$R_b(z) = \delta^*_{asy} + (R_G + \delta^*_G - \delta^*_{asy}) \cdot \exp\left(-\frac{s\Delta + \Delta^2}{1 - \Delta}\right) \text{ for } z_G \le z \le z_R \qquad (1e)$$

where

$$\Delta = (z - z_G)/(z_R - z_G)$$

and

$$s = \frac{\tan\beta\,(z_R - z_G)}{R_G + \delta^*_G - \delta^*_{asy}}$$

$$R_b(z) = \delta^*_{asy} \qquad \text{for } z_R \le z \qquad (1f)$$

A schematic sketch of an equivalent body is shown in Fig. 2. δ^* represents the displacement thickness of the turbulent boundary layer on the projectile. It should be noted that z_R and δ^*_{asy} are the two parameters characterizing the geometry of this body behind the projectile. Also Δ varies from zero to unity between points G and R, and the slope parameter s is inserted into the exponential term so that the equivalent body has a continuous slope at point G. The small slope modification due to the change of the displacement thickness of the boundary layer at the base was ignored. Obviously, this formulation is equally applicable to cases of conical flare (negative boattail).

Once the equivalent body was specified by selecting the two parameters z_R and δ^*_{asy} for a particular transonic approaching flow Mach number, the

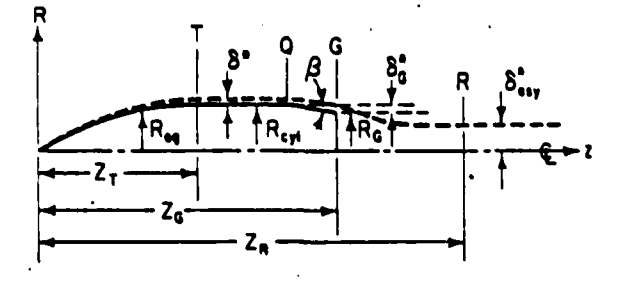

Figure 2 The Equivalent Body.

inviscid flow field was established from relaxative finite difference computations of the axisymmetric potential flow equation. In fact, it precisely followed a procedure described in early studies of the transonic flow[15]. Although description of these procedures is not repeated here, it should be noted that the turbulent boundary layer on the projectile was also estimated from an integral approach whose displacement effect was then taken into account in the midst of computations of the potential equation. Thus, when the inviscid flowfield is established, the integral boundary layer properties are also determined at the end of the boattail. It is also important to note that the turbulent boundary layer was estimated with the adiabatic wall condition and the separation criterion was set at $H_i \geq 2.5$ where H_i is the form factor of the transformed incompressible boundary layer. No separation was observed for the cases reported here.

Viscous Flow Behind the Base

a. Isoenergetic Turbulent Jet Mixing Process

Immediately after the flow leaves the boattail, a free turbulent mixing flow occurs along the jet boundary so that the dividing streamline can be energized to prepare itself for the subsequent recompression process. Since the pressure changes drastically within the region, a quasi-constant pressure mixing analysis was employed where the velocity profile along the path of the mixing region was derived from a simple locally constant pressure integral analysis with the same initial boundary layer[16,17]. The eddy diffusivity ϵ needed for the estimation of the turbulent transport across the dividing streamline was given by the simple expression of

$$\epsilon = \frac{1}{4\sigma^2} \times u_a \qquad (2)$$

where x is the distance from the point G; the point of separation, u_a is the adjacent freestream velocity; and σ is the spread rate parameter for such a mixing region. A value of twelve was employed as its value throughout this investigation. The location and the velocity of the dividing streamline, the shear layer thickness above and below it, and the shear stress along it can be determined up to the lowest pressure point behind the base. Referring to Fig. 3, an average base pressure can then be determined from the momentum equation given by

$$P_b \pi R_G^2 = \int_{R_{d_m}}^{R_G} P_d \, 2\pi r_d \, d r_d + \pi R_{d_m}^2 P_m - \int_0^{\ell_m} \tau_d \, 2\pi r_d \, dz + \int_0^{\delta_b} 2\pi r \rho u^2 \, dr + \int_0^{h_b} 2\pi r \rho u^2 \, dr \qquad (3)$$

where the subscript d refers to quantities along the diving streamline, m refers to properties at the section of minimum pressure (i.e. end of the mixing region). A linear velocity profile was adopted for the shear layer below the dividing streamline within the mixing region while the backflow at the minimum pressure section followed a profile employed for the ensuing recompression process, which necessarily satisfies the continuity principle for the wake flow at this section.

b. The Process of Viscous Flow Recompression

Since an integral analysis was employed

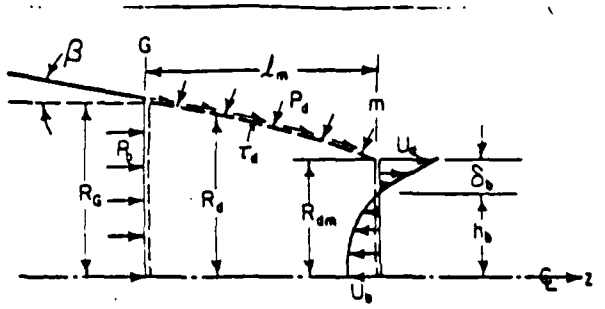

Figure 3 Definition of the Average Base Pressure.

to describe this process, velocity profiles were selected to satisfy the boundary conditions for this region. They have been described previously[16] and are not presented here. It should be pointed out that (i) the slope of the velocity profile at the dividing streamline was linearly coupled to its velocity (the proportional constant was evaluated at the end of the mixing region) and (ii) a locally triangular wake geometry (i.e. local extensions of the dividing streamline path and the centerline locations would intersect at the same point on the axis) was assumed. These manipulations assure the fact that the dividing streamline velocity and its slope vanish together at the point of attachment on the axis which is also the terminal point of the wake centerline (line of vanishing velocity within the wake) as it should. Again, isoenergetic assumption conveniently eliminated consideration of the energy equation.

Five ordinary differential equations were obtained to analyze this process. They are given by

$$A_i \frac{dR_e}{dz} + B_i \frac{dR_d}{dz} + C_i \frac{d\phi_d}{dz} + D_i \frac{dh_b}{dz} + E_i \frac{d\phi_d}{dz} = F_i \frac{dC_e}{dz} + G_i \quad (i = 1,\ldots,5) \qquad (4)$$

which describe the locations of the edge of the viscous layer, Re; the dividing streamline, R_d; the centerline of the wake, h_b; dimensionless velocities of the dividing streamline, ϕ_d; and the reverse flow along the axis ϕ_b. C_e is the dimensionless inviscid flow velocity ($C_e = u_e/V_{max}$) at the edge of the viscous layer and dC_e/dz essentially represents the pressure gradient. Coefficients $A_i, B_i, \ldots, G_i$ are very complicated functions of the flow properties and geometry of the wake[17]. Four of those equations were derived from the continuity and momentum principles for the shear layers above and below the dividing streamline while the last one was derived from the locally triangular wake geometry. The eddy diffusivity needed to estimate the shear stress along the dividing streamline was correlated with that at the end of the mixing through

$$\frac{\epsilon}{\epsilon_m} = \frac{u_e}{u_{e_m}} \left(\frac{\delta_a}{\delta_{a_m}}\right) \left(\frac{\ell_m + x_r}{\ell_m}\right) \qquad (5)$$

where δ_a is the shear layer thickness above the dividing streamline and x_r represents the distance along the recompression region. Upon integrating this system of equations with the results of mixing as the initial conditions, it was learned that the point of reattachment behaves as a saddle point of the system of equations describing the flow. For

slightly different z_R values, which of course correspond to different inviscid flow fields, the dividing streamline velocity would either decrease to negative values during recompression, before the point of reattachment on the centerline of the wake is reached, or eventually break away from the trend of continuous reduction and start to increase. In the actual calculation, since the establishment of the inviscid flow field was time consuming, the value of z_R was kept fixed, and the saddle-point behavior was observed from the fact that slightly different initial boundary layer thicknesses before mixing would lead to widely different results toward the end of recompression. Figure 4 shows a typical set of results of calculations showing the different trends of the normalized dividing streamline velocity, ϕ_d. To keep the computational effort within a reasonable level, one must attempt to reach the point of reattachment through extrapolation at the end of recompression when the initial boundary layer thicknesses of two divergent trends are within a small margin.

c. Redevelopment of Flow

Upon selecting the velocity profile to be given by

$$\phi = \phi_w + (1 - \phi_w)(3\zeta^2 - 2\zeta^3) \qquad (6)$$

for this region, where ϕ_w is the dimensionless wake centerline velocity and $\zeta = r/R_e$, the basic principles will lead to two equations of the form

$$A_i \frac{dR_e}{dz} + B_i \frac{d\phi_w}{dz} = C_i \frac{dC_e}{dz} + D_i \quad (i = 1,2) \qquad (7)$$

where again the coefficients $A_1,\ldots,D_1$, are complicated functions of the flow properties[10]. Integration of this system of equations reveals that the fully developed state is a saddle-point singularity of the equations. For a fixed z_R and slightly different δ^*_{asy} values, the redevelopment flow after the reattachment (after the point of reattachment was obtained from extrapolation) will lead either to positive and increasingly large dR_e/dz or to smaller and eventually negative dR_e/dz values. Negative dR_e/dz also invariably leads to negative $d\phi_w/dz$, resulting in a reduction of wake centerline velocity. An example to illustrate this phenomenon is shown in Fig. 5. Both these behaviors are physically unrealistic and the correct value of δ^*_{asy} lies in between. This, of course, is the typical behavior of a saddle point.

It was mentioned in the INTRODUCTION that one needs the saddle point discriminative nature to determine the correct values of z_R and δ^*_{asy} for the problem. However, consistent numerical computations cannot be carried out when they occur in sequence. Fortunately from the considerations of the asymptotic far wake flow condition, as shown in the APPENDIX, δ^*_{asy} may be related to the total drag coefficient through

$$\left(\frac{\delta^*_{asy}}{R_0}\right) = \left(\frac{C_{D_t}}{2}\,\frac{1 + C_\infty^2}{1 - C_\infty^2}\right)^{1/2} \qquad (8)$$

where $C_{D_t} = D_t/\rho_\infty V_\infty^2/2 \pi R_0^2$. The total drag, D_t, is the sum of the form drag, skin friction drag on the forebody including that on the boattail, and the base drag on the projectile base.

METHOD OF CALCULATION AND RESULTS

With the δ^*_{asy} value directly related to the total drag coefficient, computational procedures becomes greatly simplified. For a given freestream Mach number and a specific boattail angle, a pair of values for z_R/D and δ^*_{asy}/R_0 was selected. The potential flow solution for this configuration was subsequently established. After the turbulent mixing process was analyzed up to the lowest pressure section behind the base, the total drag coefficient was evaluated and the value of δ^*_{asy}/R_0 adjusted according to Eq. (8). It was learned that the influence of δ^*_{asy}/R_0 on the total drag coefficient is not very significant, and the correct value of δ^*_{asy}/R_0 could be established within a few iterations. Once this condition is satisfied,

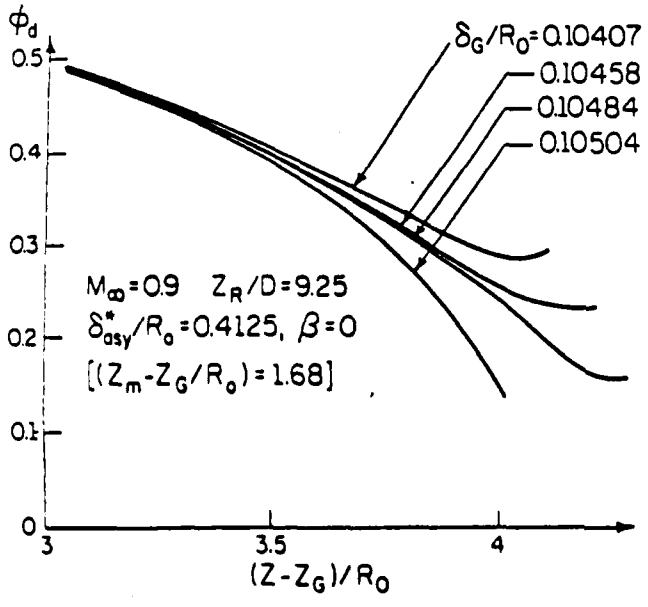

Figure 4 Saddle Point Characters of the Recompression Process.

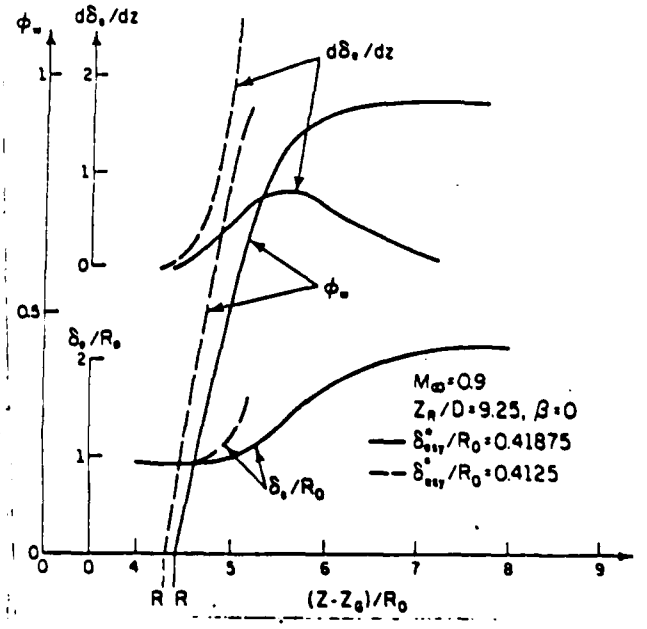

Figure 5 The Saddle Point Character of the Redevelopment Process.

integration of the system of equations (Eq. (4)) can be carried out for the recompression-reattachment analysis until the z_R/D value is narrowed down to a selected small value (e.g. 0.025). The δ^*_{asy}/R_o is of course readjusted for each new z_R/D value. The solution to the problem was reached even though the detailed wake flow pattern was not satisfactorily established. It is indeed possible to continue such detailed calculations. Results obtained from such an early effort are shown in Figs. 6 and 7 where the overall pressure distribution, the reproduced equivalent body, and the path of the dividing streamline within the wake are presented. It is obvious from Fig. 6 that the realized pressure coefficient should be less negative and less positive than that on the equivalent body in the negative and positive pressure coefficient regions ,respectively, as the result of the spread of the viscous layer.

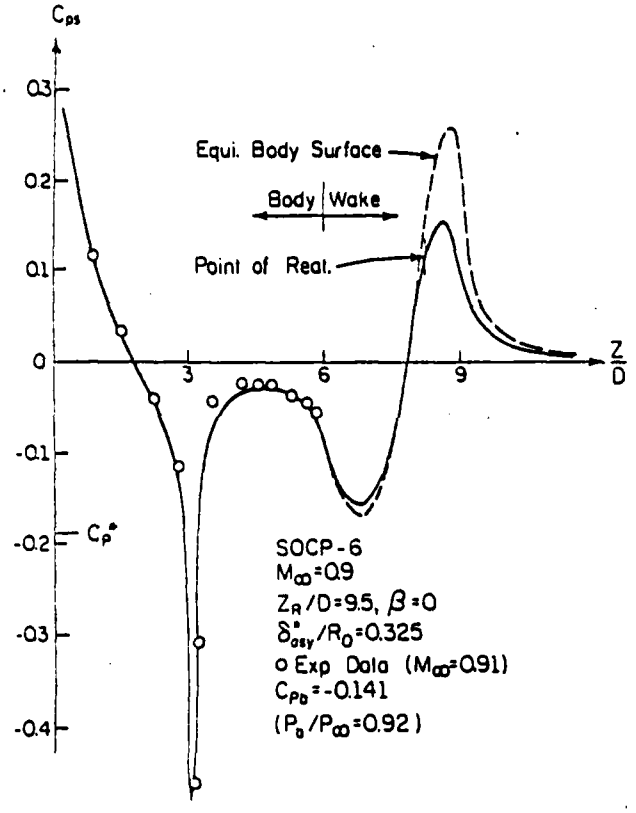

Figure 6 Established Pressure Distributions.

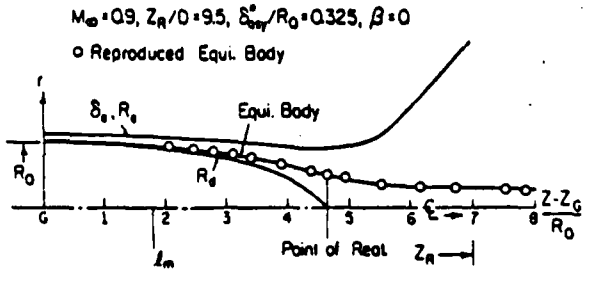

Figure 7 Established Wake Configuration Behind the Base.

Computations were carried out for $M_\infty = 0.9$ and $M_\infty = 1.2$ with increasing boattail angles. The Reynolds number per foot was set at 4×10^6. Figures 8 and 9 show the pressure distributions on the established equivalent body with the resulting base pressure ratio also reported for different boattail angles. Appropriate experimental data[11] are also plotted and compared. Figures 10 and 11 show the influences of the boattail angles on different and total drag coefficients. It can be seen that as the boattail angle increases, the base drag is reduced at the expense of increasing form

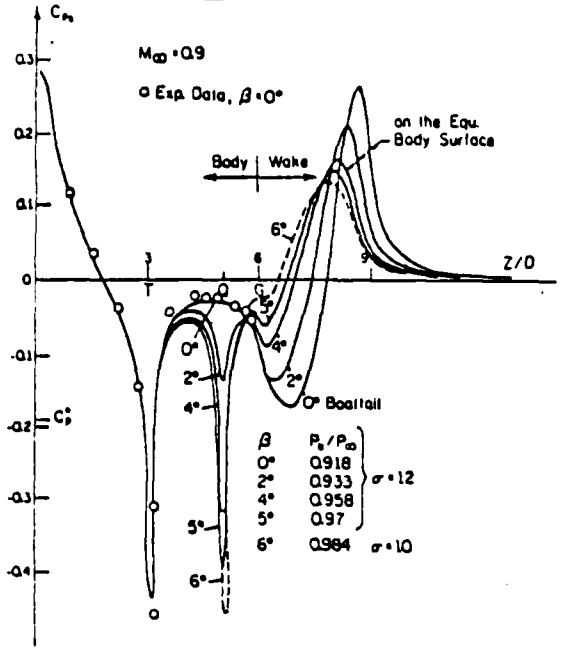

Figure 8 Surface Pressure Distribution for $M_\infty = 0.9$ at Different Boattail Angles.

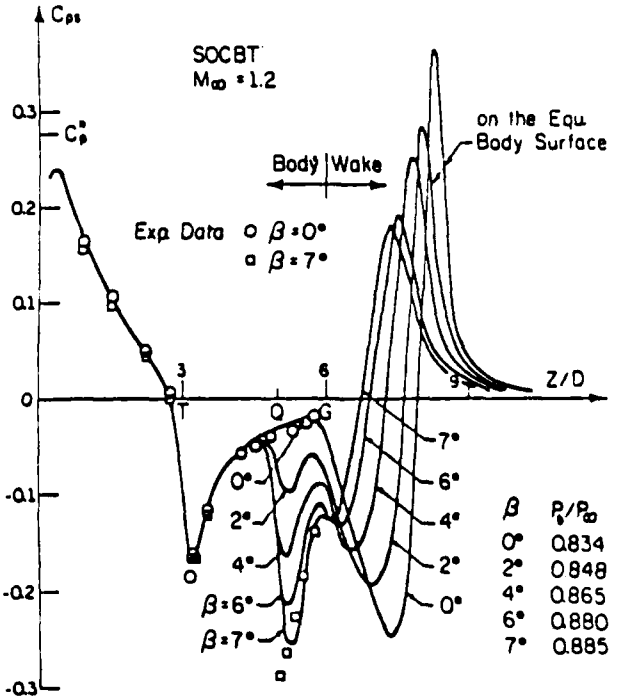

Figure 9 Surface Pressure Distribution for $M_\infty = 1.2$ at Different Boattail Angles.

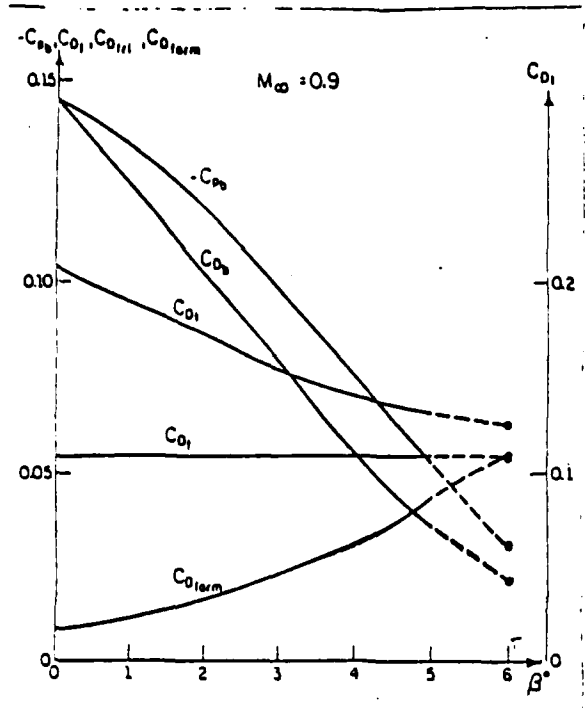

Figure 10 Drag Coefficients for $M_\infty = 0.9$.

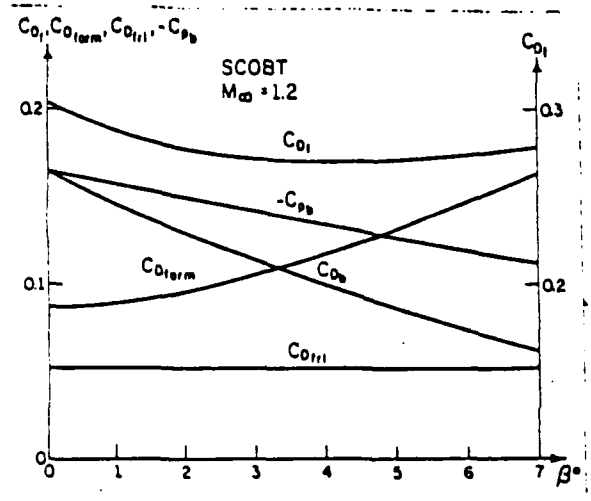

Figure 11 Drag Coefficients for $M_\infty = 1.2$.

drag. The point of minimum pressure point within the wake also shifts upstreamwise which is the basic reason for the higher base pressure ratio, since the dividing streamline is less energized through jet mixing under these conditions. Although the present computation produced results for $\beta = 7°$ at $M_\infty = 1.2$, it has not produced results for $\beta > 6°$ at $M_\infty = 0.9$. There were practically no minimum pressure points within the wake and the pressure seemed to be continuously increasing for the flow after leaving the base. The detailed turbulent flow mechanisms of mixing under increasing pressure condition held the key to the solution of the problem under these conditions. More discussion will be presented in the following section.

Since experimental data on the surface pressure on the projectile for $\beta = 7°$ at $M_\infty = 0.91$ was available[14], calculation of this case was carried out with parameters extrapolated from results for smaller boattail angles. It was also learned from these computations that the surface pressure on the forebody of projectile is not very sensitive to these parameters. The results are shown in Fig. 12. These results certainly do not agree as well with the experimental data as with zero boattail angle.

DISCUSSION

The merit of selecting a boattail configuration is to increase the base pressure ratio and to reduce the base drag even with a corresponding increment of the form drag on the forebody. This is well born out from these calculations where the base pressure increases for larger and larger boattail angles. The reduction of the base drag outweighs the corresponding increase in form drag that for small boattail angles, boattailing offers favorable interference. However for $M_\infty = 1.2$, the results seem to indicate that the minimum total drag was reached around four degree boattail angles.

For all cases where solutions have been established, the surface pressure distributions agree reasonably well with the corresponding experimental data indicating that the forebody drag coefficient is quite reliable. However, no detailed experimental data on the base pressure and the base drag

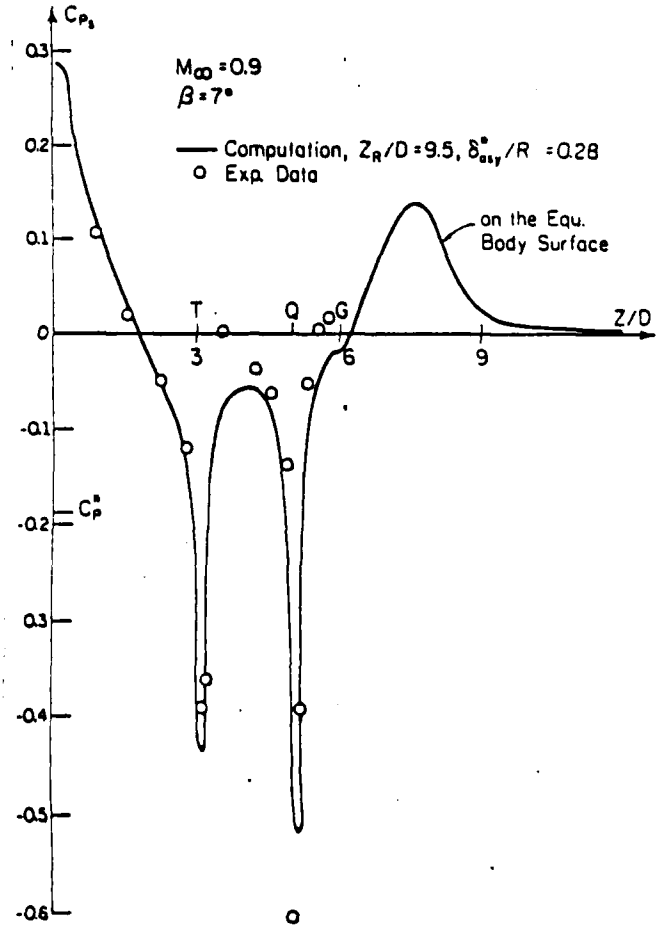

Figure 12 Surface Pressure Distributions with $\beta = 7°$, at $M_\infty = 0.9$.

are available; thus verification of these results is difficult, especially when the pressure on the base of the projectile is known to be non-uniform. The trend of the base pressure variation with the boattail angle and the Mach number seems to be reasonable. Obviously, further experimental investigation is needed in this area.

It should be noted that the original intention of choosing a crude description of turbulent transport was to avoid the detailed modeling of turbulence throughout the flow region. A simple and proper specification of the σ value, the spread rate parameter for the jet mixing process, considerably reduces the scope of the analysis. It can yield reasonably accurate results only when the mixing region is reasonably long, so that the mixing process nearly becomes fully developed under the constant pressure condition. (σ is also named as a similarity parameter for this reason.) Obviously this crude description cannot be expected to produce reliable results when the initial boundary layer is not thin, when the mixing region is short, or when a continuous increase in pressure prevails at the beginning of such a mixing region, which is precisely what is occurring under the condition of larger boattail angle ($\beta > 6°$) at $M_\infty = 0.9$. In fact, for the case of $\beta = 6°$ at $M_\infty = 0.9$, the mixing activity immediately behind the base was so low (due to the short length of mixing region) that the dividing streamline could not cope with any subsequent increase in pressure. Although the idea of origin shift by page[18] may be helpful under this situation, a σ value of ten was inserted into Eq. (2) instead of twelve for this particular condition, and the results reported in Figs. 8 and 10 were so obtained. A more precise description of the turbulent mixing process immediately behind the base under these flow conditions is needed to produce reasonable results.

Perhaps it should be emphasized that more precise simulations of the turbulent flow process are needed when one tries to explore all possible flow conditions associated with the boattail flow even with a sophisticated treatment based on the Navier-Stokes equation and two-equation turbulence modeling. It is conceivable that the flow may ignore the existence of the boattail if the boattail angle is large and the boattail is short. With reasonably long and intermediate boattail angles, the flow may even become unsteady with intermittent separation and reattachment on the boattail before the end of the boattail is reached. Obviously, an accurate description of the turbulent separation process is needed. In this sense a recent contribution by Nakayama and Koyama[19] in the study of turbulent wall flow under adverse pressure gradient on the basis of turbulence kinetic energy consideration may be useful in this aspect of the problem.

For the case of $\beta = 7°$ at $M_\infty = 0.9$, whose surface pressure distribution is presented in Fig. 11, the integral description of the boundary layer is simply not adequate to simulate the response of the turbulent viscous layer where drastic change and reversal of pressure gradient occur. Nevertheless, the present scheme of computation does offer certain interesting results, in general, for the present projectile problem within the transonic flow regime with a reasonably short computer time (approximately 5 minutes of Cyber 175 for each case). It can be predicted with confidence that similar results can be produced for higher subsonic Mach numbers and lower supersonic Mach numbers.

CONCLUSIONS

From this series of investigations, it may be concluded that the idea of an equivalent body to treat the base pressure problem within the transonic flow region leads to a useful and workable scheme. It also produced reasonably reliable results in illustrating the favorable interference through boattailing. Due to the overly simplified description of the turbulent transport, it has its shortcomings when continuous compression extends from boattail into the wake under relatively large boattail angle conditions at $M_\infty = 0.9$. More precise and accurate descriptions of turbulence modeling are needed for extensive explorations of the flow with boattails, even when carried out on the basis of the Navier-Stokes equations with turbulence modeling.

ACKNOWLEDGMENT

This research was carried out under partial support from the U.S. Army Research Office through Contract DAAG29-83-K-0043.

APPENDIX: THE ASYMPTOTIC WAKE FLOW CONDITION

It is assumed that for the redevelopment of flow, the velocity in the wake region is given by

$$\phi = \frac{u}{u_e} = \phi_w + (1 - \phi_w)(3\zeta^2 - 2\zeta^3) \qquad (A\text{-}1)$$

where ϕ_w is the dimensionless centerline velocity, and $\zeta = r/R_e$, where R_e is the radius at the edge of the viscous layer, which is also the thickness of the viscous layer δ_e within this region. For the asymptotic far wake flow, it is stipulated that the freestream approaching flow condition is restored in the external flow and $\phi_w = 1 - \epsilon$, where ϵ is a small quantity, so that higher orders of it may be ignored.

From the definition of δ^* for axisymmetric flow given by

$$\rho_e u_e (\delta_e^2 - \delta_{asy}^{*2}) = 2 \int_0^{\delta_e} \rho\, u\, r\, dr \qquad (A\text{-}2)$$

one obtains

$$\frac{\delta_{asy}^{*2}}{2\delta_e^2} = \int_0^1 \left(1 - \frac{\rho}{\rho_e}\phi\right) \zeta\, d\zeta$$

$$= \frac{1}{2} - \int_0^1 \frac{(1 - C_\infty^2)\,\phi\,\zeta\, d\zeta}{1 - C_\infty^2\,\phi^2}\,. \qquad (A\text{-}3)$$

Since $\phi_w = 1 - \epsilon$, the integral in Eq. (A-3) may be converted to

$$\int_0^1 \frac{(1 - C_\infty^2)\,\phi\,\zeta\, d\zeta}{1 - C_\infty^2\,\phi^2} = \frac{1}{2} - \frac{3}{20}\frac{1 + C_\infty^2}{1 - C_\infty^2}\,\epsilon + O(\epsilon^2) \qquad (A\text{-}4)$$

and Eq. (A-3) becomes

$$\left(\frac{\delta^*_{asy}}{R_0}\right)^2 = \frac{3}{10}\,\epsilon\,\frac{(1+C_\infty^2)}{1-C_\infty^2}\left(\frac{\delta_e}{R_0}\right)^2 . \qquad \text{(A-5)}$$

From the drag-momentum relationship given by

$$D_t = 2\pi \int_0^{\delta_e} \rho u\,(u_\infty - u)\,r\,dr \qquad \text{(A-6)}$$

one has

$$C_{D_t} \equiv \frac{D_t}{\frac{\rho_\infty u_\infty^2}{2}\pi R_0^2} = 4\left(\frac{\delta_e}{R_0}\right)^2 \int_0^1 \frac{\rho}{\rho_\infty}\,\phi(1-\phi)\,\epsilon\,d\epsilon . \qquad \text{(A-7)}$$

The integral in Eq. (A-7) may be evaluated as

$$\int_0^1 \frac{\rho}{\rho_\infty}\,\phi(1-\phi)\,\epsilon\,d\epsilon = \frac{3\epsilon}{20} + O(\epsilon^2)$$

and Eq. (A-7) becomes

$$C_{D_t} = \frac{3}{5}\frac{\delta_e^2\,\epsilon}{R_0^2} . \qquad \text{(A-8)}$$

Upon eliminating $\delta_e^2\,\epsilon$ from Eqs. (A-5) and (A-8), the equation for the asymptotic far wake flow given by

$$\left(\frac{\delta^*_{asy}}{R_0}\right)^2 = \frac{C_{D_t}}{2}\,\frac{1+C_\infty^2}{1-C_\infty^2} \qquad \text{(A-9)}$$

is established. Incidentally, Eq. (A-8) also implies that the condition given by

$$\delta_e\,(1-\phi_w)^{1/2} = \text{constant} \qquad \text{(A-10)}$$

is valid for the asymptotic wake flow whether it is compressible or incompressible, laminar or turbulent.

REFERENCES

1. Crocco, L., and Lees, L., "A Mixing Theory for the Interaction Between Dissipative Flows and Nearly Isentropic Streams," J. of the Aeronautical Sciences, Vol. 19, No. 10, Oct. 1952, pp. 649-676.
2. Lees, L., and Reeves, B. L., "Supersonic Separated and Reattaching Laminar Flows: I. General Theory and Applicaton to Adiabatic Boundary-Layer/Shock-Wave Interactions," AIAA J., Vol. 2, No. 11, Nov. 1964, pp. 1907-1920.
3. Alber, I. E., and Lees, L., "Integral Theory for Supersonic Turbulent Base Flows," AIAA J., Vol. 6, No. 7, July 1968, pp. 1343-1351.
4. Korst, H. H., "A Theory for Base Pressures in Transonic and Supersonic Flow," J. of Applied Mechanics, Dec. 1956, pp. 593-600.
5. Korst, H. H., Chow, W. L., and Zumwalt, G. W., "Research on Transonic and Supersonic Flow of a REal Fluid at Abrupt Increases in Cross Section," ME Technical Report 392-5, Engineering Experiment Station University of Illinois at Urbana-Champaign, Dec. 1959.
6. Page, R. H., "A Review of Component Analysis of Base Pressure for Supersonic Turbulent Flow," Proc. of the 10th Int. Symposium on Space Technology and Science, Tokyo, Japan, 1973, pp. 459-469.
7. Beheim, M. A., Klann, J. L., and Yeager, R. A., "Jet Effects on Annular Base Pressure and Temperature in a Supersonic Stream," NASA TRR-125, 1962.
8. Carriere, P., and Sirieix, M., "Resultats Recents Dans L-Etude Des Problemes De Melange Et De Recollement," ONERA T. P., 165, 1964.
9. McDonald, H., "The Turbulent Supersonic Base Pressure Problem: A Comparison Between a Theory and Some Experimental Evidence," The Aeronautical Quarterly, Vol. 17, May 1966, pp. 105-126.
10. Chow, W. L., "Base Pressure of a Projectile Within the Transonic Flow Regime," Paper AIAA-84-0230, presented in AIAA 22nd Aerospace Science Meeting, Jan. 1984, Reno, Nevada, to appear in AIAA Journal.
11. Chow, W. L., "Recompression of a Two-Dimensional Supersonic Turbulent Free Shear Layer," Development in Mechanics, Vol. 6, Proc. of the 12th Midwestern Mechanics Conference, August 1971, pp. 319-332.
12. Chow, W. L., and Spring, D. J., "Viscous Interaction of Flow Redevelopment after Flow Reattachment with Supersonic External Streams," AIAA J., Vol. 13, no. 12, Dec. 1975, pp. 1576-1584.
13. Weng, C. H., and Chow, W. L., "Axisymmetric Supersonic Turbulent Base Pressures," AIAA J., Vol. 16, No. 6, June 1978, pp. 553-554.
14. Kayser, L. D., and Whiton, F., "Surface Pressure Mesurements on a Boattailed projecile Shape at Transonic Speeds," Memorandum Report ARBRL-MR-03161, Ballistic Research Laboratory, Aberdeen Proving Ground, MD, March 1982.
15. Chow, W. L., Bober, L. J., and Anderson, B. H., "Numerical Calculation of Transonic Boattail Flow," NASA TN D-7984, June 1975.
16. Brink, D. F., and Chow, W. L., "Two-Dimension Jet Mixing with a Pressure Gradient," J. of Applied Mechanics, Vol. 42, Series E, No. 1, pp. 55-60, March 1975.
17. Liu, J. S. D., and Chow, W. L., "Base Pressure Problems Associated with an Axisymmetric Transonic Flow past a Backward Facing Step," ME-TR-395,5, Department of Mechanical and Industrial Engineering, University of Illinois at Urbana-Champaign, Report prepared for Research Grant, U.S. Army DAAG29-76-G-0199, Nov. 1977, ADA050658.
18. Hill, W. G., Jr., and Page, R. H., "Initial Development of Turbulent Compressible Free Shear Layers," J. Basic Engineering, Vol. 91, Series D, No. 1, March 1969, pp. 67-73.
19. Nakayama, A., and Koyama, H., "A Wall Law for Turbulent Boundary Layers in Adverse Pressure Gradients," AIAA J., Vol. 22, No. 10, Oct. 1984, pp. 1386-1389.

SECTION A.4

AN INVESTIGATION OF THE EFFECTS OF NONUNIFORM THROAT FLOW ON BASE PRESSURE AT SUPERSONIC FLIGHT SPEED

Paper No. AIAA-84-0314

Presented at the AIAA 22nd Aerospace Sciences Meeting

Reno, Nevada

January 9-12, 1984

by

A. L. Addy, V. A. Amatucci, and J. C. Dutton

AIAA'84

AIAA-84-0314

An Investigation of the Effects of Non-Uniform Throat Flow on Base Pressure at Supersonic Flight Speed

A.L. Addy and V.A. Amatucci, Univ. of Illinois at U-C, Urbana, IL; and J.C. Dutton, Texas A&M Univ., College Station, TX

AIAA 22nd Aerospace Sciences Meeting

January 9-12, 1984/Reno, Nevada

AN INVESTIGATION OF THE EFFECTS OF NON-UNIFORM THROAT FLOW ON BASE PRESSURE AT SUPERSONIC FLIGHT SPEEDS

A. L. Addy* and V. A. Amatucci**
University of Illinois at Urbana-Champaign
Urbana, Illinois

J. C. Dutton†
Texas A&M University
College Station, Texas

Abstract

The effects on base pressure at supersonic flight speeds of non-uniform propulsive nozzle flow were investigated. The Chapman-Korst component model for base flow during powered supersonic flight served as the basis for the evaluation of these effects. The base pressures were compared for ideal conical nozzles and for conical nozzles with circular arc throats. These comparisons were made for parametric variations in the radius of curvature of the nozzle throat and the specific heat ratio for the propulsive nozzle flow. For the cases presented, the non-uniform nozzle flow resulted in a maximum predicted increase in base pressure of approximately 5-8%. On the other hand, an earlier empirical modification to the base flow model, which improves agreement with experiment, decreases the predicted base pressure by approximately 14%.

Nomenclature

M_E, M_I	Freestream and nozzle exit Mach numbers
P_B	Base pressure
P_E, P_I	Freestream and nozzle static pressures at the base plane
R	Radial coordinate
R_{CW}	Radius of curvature of the wall at the nozzle throat
R_T, R_I	Nozzle throat and exit radii
r	Empirical recompression coefficient in base flow model
X	Axial coordinate
β_I	Conical nozzle half angle
Δ	Percentage deviation of the base pressure from the baseline case
γ_E, γ_I	Freestream and nozzle specific heat ratios

Introduction

Investigations of base flow during powered flight at supersonic speeds are principally based on one of the computer implementations of the theoretical Chapman-Korst component flow model and on experiments using small-scale models. The overall objective is to develop a computer-based approach whereby the influence of the many geometric and flow variables on the base flow can be rapidly predicted with a reasonable degree of accuracy and confidence.‡ To improve agreement with experiments, empirical modifications to the component flow model are often made based on small-scale experimental results. In the theoretical component model, the propulsive nozzle is usually represented as an ideal nozzle which produces either uniform or conical flow at the nozzle exit. However, many of the small- and full-scale base flow experiments have been conducted with conical nozzle geometries which typically have a small radius of curvature of the throat wall, a conical expansion section with a relatively large divergence angle, and/or a truncated expansion section. These nozzles would be expected to produce non-uniform and non-conical flow at the nozzle exit and to affect the plume expansion into the base region. These effects and their significance on base flow have not been systematically investigated. The purpose of this paper is to describe an investigation of these non-uniform nozzle flow effects on base pressure, to present comparisons between predicted and experimental results, and to establish levels of significance of non-uniform nozzle flow through parametric results.

Analysis

Brief descriptions of the Chapman-Korst model and the conical nozzle flow analysis of the current investigation follow.

Base Flow Model[2]

The base flow configuration under consideration is shown in Fig. 1. In this analysis, the freestream and nozzle Mach numbers at the base plane are assumed to be supersonic. The freestream and nozzle flows expand or compress, as the case may be, to a common base pressure, P_B. Downstream of the base plane, a recompression shock system forms at the confluence of the separated freestream and nozzle flows.

Inviscid Flowfield Component. In the Chapman-Korst model, the separated flow boundaries are approximated by inviscid constant-pressure

---

* Professor and Associate Head, Department of Mechanical and Industrial Engineering. Associate Fellow AIAA.

**Graduate Research Assistant, Department of Mechanical and Industrial Engineering. Student Member AIAA.

† Assistant Professor, Department of Mechanical Engineering. Member AIAA.

‡ As an example, an extensive computer simulation of base flow parameters was conducted for the space shuttle by Roberts, Wallace, and Sims.[1]

nozzle flows expanding and/or compressing from the freestream and nozzle static pressures, P_F and P_I, respectively, to the base pressure, P_B. The Mach numbers along the constant-pressure freestream and nozzle flow boundaries and the local flow angles at the confluence of these flows defines the oblique recompression shock system.

In one of the earlier computer implementations[3,4] of the Chapman-Korst flow model, a uniform freestream flow was assumed to approach a cylindrical, boattailed, or flared afterbody which terminates at the base plane. The inviscid freestream constant-pressure boundary is calculated by the method of characteristics from the local freestream flow conditions at the base plane and the assumed value of P_B. Similarly, the nozzle flow is assumed to be from either an ideal uniform flow or conical flow nozzle. The inviscid nozzle flow constant-pressure boundary is calculated by the method of characteristics from the local nozzle flow conditions at the base plane and the assumed value of P_B.

In the current investigation, the nozzle flow conditions at the base plane were generalized to include flow from a conical nozzle with a circular arc throat section. In order to determine the nozzle exit plane flowfield, a supersonic start line is determined at the nozzle throat from an approximate series solution. The remainder of the nozzle flowfield is determined by the method of characteristics. The local nozzle flowfield data at the base plane and the assumed value of P_B are used to determine the inviscid constant-pressure nozzle flow boundary. More details on the conical nozzle flow analysis are provided in the following section.

In the Chapman-Korst model, the solution value of P_B is determined by linking the inviscid and mixing components by a suitable recompression criterion at the confluence of the separated freestream and nozzle flows.

Turbulent Mixing Component. An approximate constant-pressure mixing analysis is used to analyze the mixing region and results in an error function velocity profile. This mixing profile is superimposed on each of the inviscid boundaries and is localized relative to these inviscid boundaries by momentum considerations. Once the mixing profiles have been located relative to the inviscid boundaries, two important streamlines within each mixing region can then be determined. The first is the jet-boundary (j) streamline which separates the separated freestream or nozzle flow and the recirculating base flow. The second is the discriminating (d) streamline in each mixing region which has just sufficient energy, based on a recompression criterion, to match the recompression pressure rise at the confluence of the separated flows.

Recompression Component. The discriminating streamline in each mixing profile is assumed to stagnate through essentially an isentropic process to the static pressure maintained by the oblique shock system downstream of the confluence of the inviscid boundaries. The recompression process in the base flow analysis is an important component which significantly affects the resulting base flow solution.

Since the recompression process is not well understood, empirical representations or modifications to the recompression are often presented.[5,6] In this investigation, the empirical recompression coefficient which was developed in the correlation of many sets of experimental data with the Chapman-Korst model is used.[6] This correlation provides little insight into the recompression process; rather, it simply improves the agreement between experimental results and theoretical predictions. As a consequence, this approach provides a useful engineering analysis tool for estimating base flow conditions.

Conservation of Mass and Energy. Once the j- and d-streamlines have been identified in each mixing region, conservation of mass and energy in the base region provide the criteria for determining the solution values of the base pressure and temperature.

Conical Nozzle Flow

Configuration. The conical nozzle which was incorporated into the base flow analysis during this investigation is shown in Fig. 2. The nozzle consists of a circular arc throat section which is joined at the tangency point J to a straight line diverging section. The nozzle configuration is specified by the dimensionless throat wall radius of curvature ratio, R_{CW}/R_T; by the nozzle exit radius ratio, R_I/R_T; and by the nozzle divergence angle, θ_I.

Methodology. The nozzle flowfield was predicted using an approximate throat flow solution to establish a start line for a method of characteristics calculation of the supersonic flow in the nozzle diverging section. The throat flow analysis employed in this study is a series expansion solution due to Dutton and Addy.[7] The solution method used in reference 7 is similar to that employed originally by Hall[8] in that it is obtained from the full irrotationality and gas dynamic equations together with the appropriate boundary conditions and order-of-magnitude estimates. However, by utilizing the generalized expansion variable, $\epsilon = 1/(R_C+n)$ where $R_C = R_{CW}/R_T$ is the dimensionless throat wall radius of curvature ratio and the parameter n can take on arbitrary values, the analysis of reference 7 can be extended to the technologically important case of nozzles with sharply curved throat wall contours.

The start line for the method of characteristics computations was obtained from the TRANNOZ computer code[9] which is based on the analysis of reference 7. The start line used is the contour line of zero transverse velocity, $V(X,R) = 0$, which originates from the throat wall location, (X_T,R_T), and terminates on the nozzle axis. Along this start line, the local Mach number is supersonic at the wall and is selected to be slightly supersonic at the axis. Using this start line, nozzles with a dimensionless throat wall radius of curvature as small as approximately $R_C = 0.5$ can be analyzed and, in this case, $n = 1$ is recommended. It is to be noted that the solution of reference 7 has been compared to experimental data[7,10] and has been found to be in good agreement through a surprisingly wide region of the nozzle throat. In addition, Fujii and Kutler[11]

have used it to initiate their finite difference nozzle flow calculations and have found good agreement between their computations and single phase experimental data. It should also be mentioned that as a closed-form series, the numerical implementation of this solution is extremely fast as compared, for example, to the time-dependent method. This feature makes the approximate series solution particularly appealing for parametric studies such as the present one.

As shown in Fig. 3, the nozzle flowfield is calculated by the method of characteristics from the non-characteristic start line to the characteristic line through the throat wall. The flowfield is next calculated for the remainder of the circular arc throat section and then for the straight line diverging section. In this latter section, wave coalescence occurs within the flowfield and intensifies near the axis. This wave coalescence leads to the formation of shock waves within the nozzle flowfield. Since these waves are weak, they can be treated approximately as the coalescence of reversible compression waves.

Results

Conical Nozzle Flow

For purposes of comparison, the nozzle flowfield was calculated for the same conical nozzle analyzed by Fujii and Kutler[11] for single phase flow; this nozzle has $R_{CW}/R_T = 0.625$, $\theta_I = 15°$, and $X_T/R_T = 6.0$. This particular nozzle configuration has also been analyzed by Serra[12] and experimentally investigated by Back and Cuffel.[13] The wall and axis Mach number distributions due to Fujii and Kutler, Serra, and Back and Cuffel are presented in Fig. 2 of reference 11. The results predicted by the present approximate nozzle analysis are generally in good agreement with these presented in Fig. 2 of reference 11. The present analysis predicts the onset of the compression on the axis and predicts a Mach number decrease along the axis which is essentially in agreement with the predictions of Serra.[12] These results differ from the experimental data of Back and Cuffel and the calculations of Fujii and Kutler for which a rather steep decrease in the Mach number occurs after the onset of the compression on the axis. The Mach number distribution along the wall predicted by the present analysis is in good agreement with the theoretical predictions of Fujii and Kutler and the experimental results of Back and Cuffel. Since this nozzle configuration represents an extreme nozzle geometry and the present analysis provides good agreement with other prediction methods and experimental data, the present approximate analysis is considered to be adequate for the current base flow investigation.

For the base flow investigation, conical nozzle throat flows were predicted for parametric variations in dimensionless throat wall radius of curvature ratio:

$$R_{CW}/R_T = 0.75,\ 1.0,\ 1.5,\ 2.0,\ 4.0,\ 8.0$$

and specific heat ratio:

$$\gamma_I = 1.25,\ 1.4\ .$$

The approximate series solutions for the nozzle throat start lines, $V(X,R) = 0$, are presented in Figs. 4 and 5 for these parametric values. These start lines were then used to predict the flowfields through a family of conical flow nozzles with the following fixed geometric parameters: $R_I/R_T = 1.6239$ and $\theta_I = 15°$. As a result, the length ratio of this nozzle varies with the dimensionless throat wall radius of curvature ratio.

Base Flow

The nozzle exit flowfield data were input to the base flow program as outlined earlier and base pressure solutions were obtained for the configuration shown in Fig. 1. For purposes of comparison with earlier parametric results with ideal conical nozzles, the following base flow configuration parameters were selected for the freestream:

$$\gamma_E = 1.4, \quad M_E = 2.0$$

and for the nozzle flow:

$$\gamma_I = 1.4,\ R_I/R_E = 0.6,\ M_I = 2.5 \text{ (nominal)}$$

or

$$\gamma_I = 1.25,\ R_I/R_E = 0.6,\ M_I = 2.343 \text{ (nominal)}.$$

For ideal conical nozzles, the base pressure ratio, P_B/P_E, is presented in Fig. 6 as a function of the operating pressure ratio, P_I/P_E. In this figure, the base flow solutions are presented for $\gamma_I = 1.25$ and 1.4. In addition, the results are presented for recompression coefficient values of $r = 1.0$ and 0.88. For $r = 1.0$, this is the unmodified base flow model. For $r = 0.88$, this value of the recompression coefficient was determined from the correlation developed to improve the agreement between experimental and theoretical results for cylindrical afterbodies.[6] Note that the empirical recompression coefficient decreases the value of the predicted base pressure by approximately 14%.

The unmodified case with $r = 1.0$ was selected as the baseline case for the purpose of comparing the base pressure results between the different conical nozzle geometries and the ideal conical nozzle geometry.

For $\gamma_I = 1.25$ and 1.4, the variations in predicted base pressure for the various nozzle geometries are presented in Figs. 7 and 8. These variations are presented relative to the respective baseline cases; these data are presented as

$$\Delta(\%) = \frac{100 \cdot \left[(P_B/P_E) - (P_B/P_E)_{Baseline}\right]}{(P_B/P_E)_{Baseline}}$$

versus the operating pressure ratio, P_I/P_E, for parametric values of R_{CW}/R_T and γ_I.

From Fig. 7 for $\gamma_I = 1.4$, the nozzle geometry results in an approximate increase in $\Delta = 6\%$ for $R_{CW}/R_T = 1.5$. With increasing values of R_{CW}/R_T, the deviation from the baseline case approaches

zero. Surprisingly, the deviation from the baseline case is also small for the smallest value of R_{CW}/R_T considered in this investigation.

From Fig. 8 for $\gamma_I = 1.25$, similar results are observed. In this case, an approximate increase of $\Delta = 7\%$ occurred for a value of $R_{CW}/R_T = 1.0$.

In both figures, the empirically correlated values of the base pressure ratio are significantly less, on the order of 13-15%.

Conclusions

The detailed investigation of the effects of non-uniform nozzle flow on the base flow region has yielded valuable information concerning prediction of flowfield parameters. The implications and conclusions from this investigation are as follows:

1. The data for the range of cases which were investigated show that the non-uniform nozzle flow effects resulted in an increase of predicted base pressure of approximately 5-8%. The increase in predicted P_B/P_E was dependent upon the ratio of the nozzle throat wall radius of curvature to the throat radius.

2. The incorporation of the approximate series solution for the transonic throat analysis and the method of characteristics conical nozzle flowfield calculation into the component model base pressure analysis provides an efficient means for quickly analyzing the effects of many parameters, including nozzle geometry, on the base pressure. The appropriate trends for properties in the base flow region are predicted. A typical nozzle and base flow solution requires approximately 2 seconds of execution time on a CDC Cyber 175.

3. The Chapman-Korst model with ideal nozzle flow tends to predict base pressures which are higher than the corresponding experimental values. Inclusion of non-uniform nozzle flow effects into the base flow analysis tends to increase the difference between predicted and experimental values. For the worse cases, this difference is on the order of 20-25% as determined from the use of an empirical recompression coefficient with the Chapman-Korst model. This empirical correlation has been shown to provide good agreement between predicted and experimental values.

Acknowledgment

This research was sponsored by the U.S. Army Research Office under contract DAAG 29-79-C-0184 and the Department of Mechanical and Industrial Engineering.

References

[1]Roberts, B. B., Wallace, R. O., and Sims, J. L., "Plume Base Flow Simulation Technology," NASA CP-2283, Part 1, March 1983.

[2]Addy, A. L., "Detailed Analyses for the Base-Pressure Programs (TSABPP-1,2)," Report No. RD-TN-69-7, U.S. Army Missile Command, Redstone Arsenal, Alabama, August 1969.

[3]Addy, A. L., "Analysis of the Axisymmetric Base-Pressure and Base-Temperature Problem with Supersonic Interacting Freestream-Nozzle Flows Based on the Flow Model of Korst, et al., Part I: A Computer Program and Representative Results for Cylindrical Afterbodies," Report No. RD-TR-69-12, U.S. Army Missile Command, Redstone Arsenal, Alabama, July 1969.

[4]Addy, A. L., "Analysis of the Axisymmetric Base-Pressure and Base-Temperature Problem with Supersonic Interacting Freestream-Nozzle Flows Based on the Flow Model of Korst, et al., Part III: A Computer Program and Representative Results for Cylindrical, Boattailed, or Flared Afterbodies," Report No. RD-TR-69-14, U.S. Army Missile Command, Redstone Arsenal, Alabama, February 1970.

[5]Carriere, P. and Sirieix, M., "Resultats Recents Dans L'Etude Des Problemes De Melange Et De Recollement," ONERA T. P. 165, 1964.

[6]Addy, A. L., "Experimental-Theoretical Correlation of Supersonic Jet-on Base Pressure for Cylindrical Afterbodies," Journal of Aircraft, Vol. 7, No. 5, September-October 1970, pp. 474-477.

[7]Dutton, J. C. and Addy, A. L., "Transonic Flow in the Throat Region of Axisymmetric Nozzles," AIAA Journal, Vol. 19, June 1981, pp. 801-804.

[8]Hall, I. M., "Transonic Flow in Two-Dimensional and Axially-Symmetric Nozzles," Quarterly Journal of Mechanics and Applied Mathematics, Vol. XV, Pt. 4, 1962, pp. 487-508.

[9]Dutton, J. C. and Addy, A. L., "TRANNOZ: A Computer Program for Analysis of Transonic Throat Flow in Axisymmetric, Planar, and Annular Supersonic Nozzles," Report No. UILU-ENG-80-4005, Department of Mechanical and Industrial Engineering, University of Illinois at Urbana-Champaign, April 1980.

[10]Dutton, J. C. and Addy, A. L., "Transonic Flow in the Throat Region of Annular Supersonic Nozzles," AIAA Journal, Vol. 20, No. 9, September 1982, pp. 1236-1243.

[11]Fujii, K. and Kutler, P., "Computations of Two-Phase Supersonic Nozzle Flows by a Space-Marching Method," AIAA Paper No. 83-0041, January 1983.

[12]Serra, R. A., "Determination of Internal Gas Flows by a Transient Numerical Technique," AIAA Journal, Vol. 10, No. 5, May 1972, pp. 603-611.

[13]Back, L. H. and Cuffel, R. F., "Detection of Oblique Shocks in a Conical Nozzle with a Circular-Arc Throat," AIAA Journal, Vol. 4, No. 12, December 1966, pp. 2219-2220.

Figures

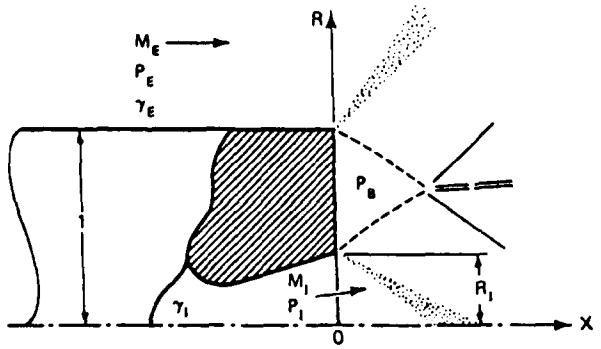

Fig. 1 Base flow configuration and notation.

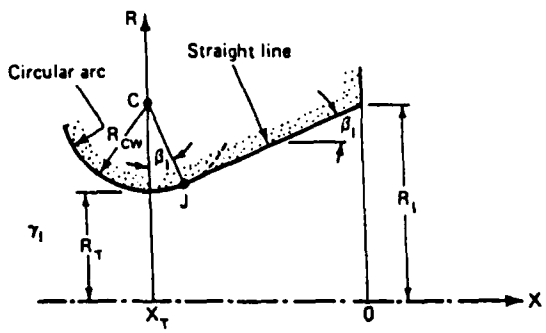

Fig. 2 Conical nozzle geometry and notation.

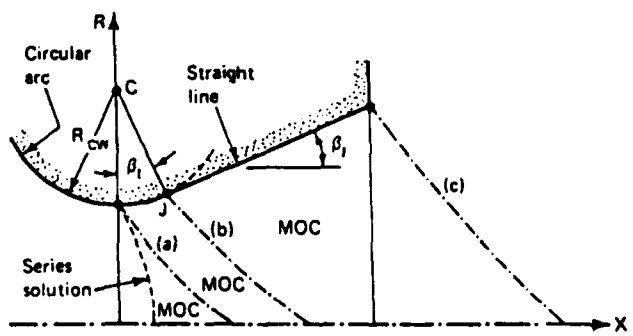

----- Non-characteristic start line

-·-·- Characteristic lines:

(a) Throat

(b) Junction between circular arc and straight line segments

(c) Nozzle exit

Fig. 3 Conical nozzle flowfield calculation sequence.

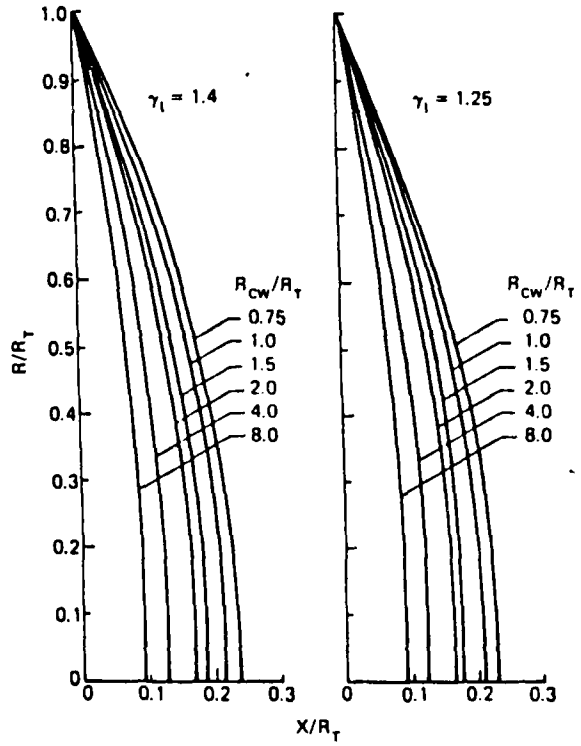

Fig. 4 Nozzle throat start lines for V(X,R) = 0 from TRANNOZ.

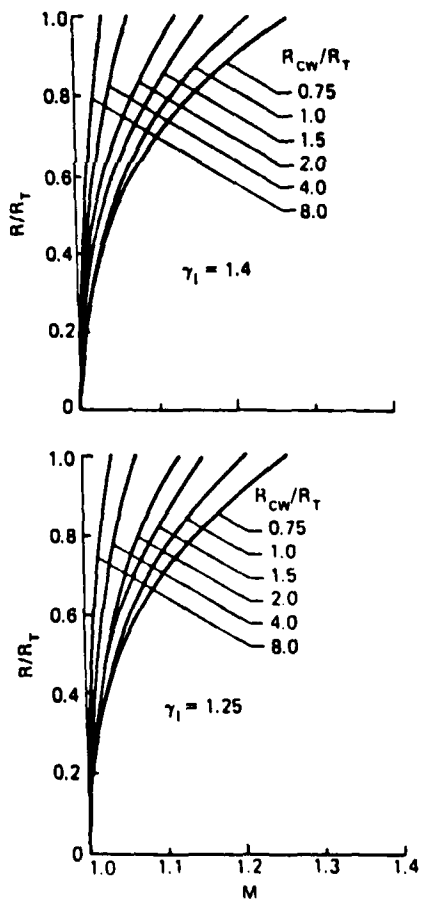

Fig. 5 Mach number distributions on the nozzle start line where V(X,R) = 0.

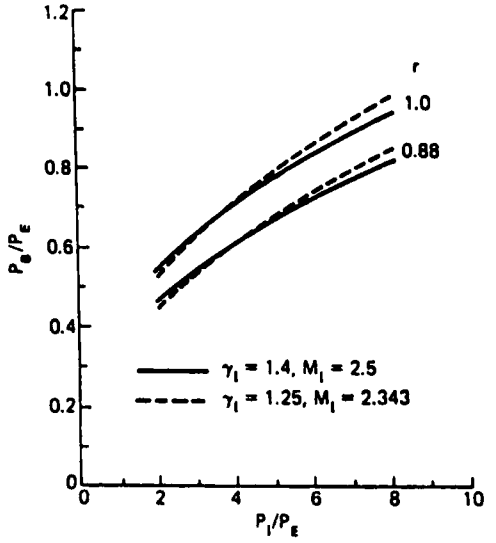

Fig. 6 Base pressure ratio for baseline cases with an ideal conical nozzle and different specific heat ratios ($M_E = 2.0$, $R_I/R_E = 0.6$, $\beta_I = 15°$, $R_T/R_E = 0.3695$).

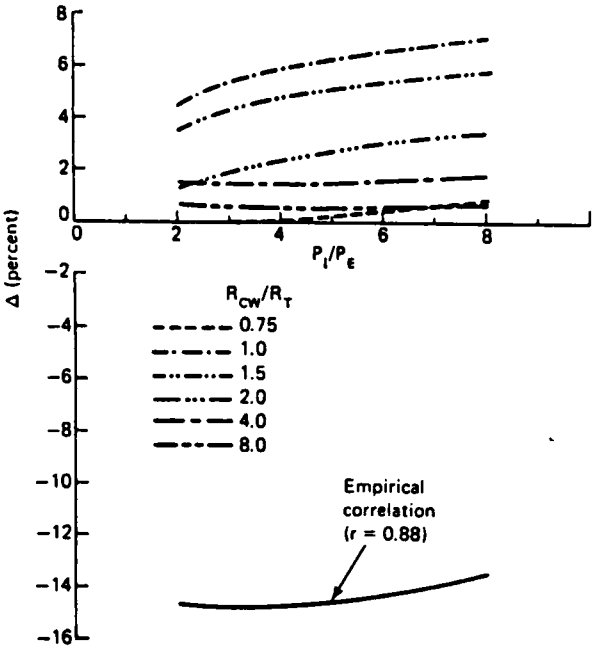

Fig. 8 Variation of the base pressure ratio from the baseline case for different values of the conical nozzle throat wall radius of curvature ratio and an empirical correlation ($\gamma_I = 1.25$).

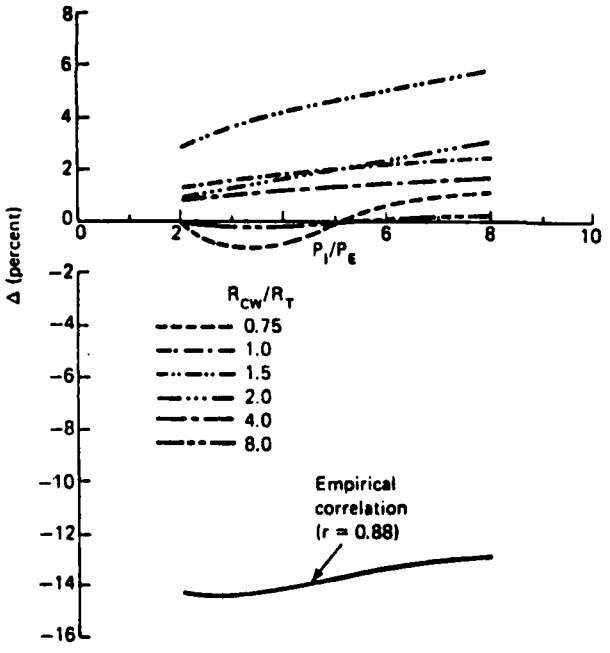

Fig. 7 Variation of the base pressure ratio from the baseline case for different values of the conical nozzle throat wall radius of curvature ratio and an empirical correlation ($\gamma_I = 1.4$).

SECTION A.5

NONUNIFORM NOZZLE FLOW EFFECTS ON BASE PRESSURE AT SUPERSONIC FLIGHT SPEEDS

AIAA Journal

Volume 24, Number 7, July 1986

Pages 1209-1212

by

A. L. Addy, J. C. Dutton, and V. A. Amatucci

AIAA Journal

VOLUME 24, NUMBER 7 JULY 1986

Nonuniform Nozzle Flow Effects on Base Pressure at Supersonic Flight Speeds

A. L. Addy,* J. C. Dutton,† and V. A. Amatucci‡
University of Illinois at Urbana-Champaign
Urbana, Illinois

Introduction

ANALYTICAL investigations of missile base flow during powered flight at supersonic speeds are principally based on one of the computer implementations of the Chapman-Korst component flow model.[1-3] To improve agreement with experiments, empirical modifications of this analysis are usually used based on small-scale experimental results. In the component model, the propulsive nozzle is generally represented as an ideal nozzle which produces either uniform or conical flow at the nozzle exit. However, many of the small-scale experiments and full-scale prototypes employ nozzle geometries which have a small radius of curvature of the throat wall, a conical expansion section with a relatively large divergence angle, and/or a truncated expansion section. These nozzles would be expected to produce nonuniform and non-conical flow at the exit, thereby affecting the plume expansion into the base region. These effects have often been hypothesized as some of the possible causes of the disagreement between the component model predictions and experimental results, although no systematic investigation of their significance on base flow has been reported. The purpose of this paper is to present parametric results of nonuniform nozzle flow effects on base pressure for typical conical nozzle geometries in order to determine their expected magnitudes and to test the hypothesis stated.

Method of Analysis

The missile base configuration under consideration is shown in Fig. 1. The internal nozzle flow expands through a conical nozzle with a circular arc throat to supersonic conditions at the exit. The nozzle geometry is completely specified by the dimensionless throat wall radius of curvature R_{CW}/R_T, by the nozzle exit radius ratio R_1/R_T, and by the divergence half-angle β_1. The external freestream flow is also assumed to be supersonic, and for the cylindrical afterbody considered, the only pertinent geometric variable is the base radius ratio R_1/R_B. The freestream and nozzle flows separate at the base and expand or compress, as the case may be, to a common base pressure P_B. A recompression

Received July 29, 1985.

*Professor and Associate Head, Department of Mechanical and Industrial Engineering. Associate Fellow AIAA.

†Associate Professor, Department of Mechanical and Industrial Engineering. Member AIAA.

‡Graduate Research Assistant, Department of Mechanical and Industrial Engineering. Student Member AIAA.

shock system forms downstream at the confluence of the separated freestream and nozzle flows.

As opposed to earlier implementations[2,3] of the Chapman-Korst flow model, which assume ideal uniform or conical nozzle flow, the present method predicts the actual nonuniform flowfield of the nozzle in Fig. 1. The approximate throat flow series solution of Ref. 4 is used to establish an initial value line for a method of characteristics calculation of the flow in the nozzle diverging section. The analysis of Ref. 4 has been compared to experimental data[4,5] and has been found to be in good agreement through a wide region of the nozzle throat. In addition, Fujii and Kutler[6] have used it to initiate finite difference nozzle flow calculations which agree well with single-phase experimental data. The start line employed here was obtained from the TRANNOZ computer code,[7] where the line used is the contour of zero radial velocity, $V(X,R)=0$. This noncharacteristic curve originates from the throat wall location, $(0,R_T)$, where the flow is supersonic and terminates on the nozzle axis at a location selected such that the local Mach number is slightly supersonic. With this technique, nozzles with a dimensionless throat wall radius of curvature as small as approximately $R_{CW}/R_T=0.5$ can be analyzed.

As shown in Fig. 1, the nozzle flowfield is calculated by the method of characteristics from the noncharacteristic starting curve to the right-running characteristic through the throat wall location. Next the flowfield is calculated for the remainder of the circular arc throat section and then for the conical diverging section. In this latter region, wave coalescence occurs and intensifies near the axis. This coalescence leads to the formation of oblique shock waves within the nozzle flowfield. Since these waves are weak, however, they can be treated approximately as the coalescence of reversible compression waves.

The base flow is predicted with the widely used TSABPP[1-3] computer implementation of the Chapman-Korst component model. In this investigation, a uniform freestream flow is assumed to approach a cylindrical afterbody, where it separates at the base. The resulting inviscid freestream constant-pressure boundary is calculated by the method of characteristics from the local freestream flow conditions M_E and P_E at the base plane and the assumed value of P_B. Similarly, the separated nozzle flow constant-pressure boundary is calculated by the method of characteristics from the local flow conditions along the nozzle exit lip characteristic c in Fig. 1 and the assumed value of P_B. The conditions along this characteristic are obtained from the nozzle flow analysis discussed previously.

In the Chapman-Korst model, the solution value of P_B is determined by linking these inviscid components to mixing components through a suitable recompression criterion at the confluence of the separated freestream and nozzle flows. The turbulent mixing layers are analyzed by means of an approximate constant-pressure mixing theory resulting in an error function velocity profile. This profile is superimposed on each of the inviscid boundaries and is localized relative to these boundaries by momentum considerations. Once the mixing profiles have been located, two important streamlines within each mixing region are determined. The first is the jet boundary streamline, which divides the separated freestream or nozzle flow from the recirculating base flow. The second is the discriminating streamline in each mixing region, which has sufficient energy, based on a recompression criterion, to match the recompression pressure rise at the confluence of the separated flows.

The recompression criterion assumes that the discriminating streamline in each mixing profile stagnates through essentially an isentropic process to the static pressure maintained by the oblique shock system downstream of the confluence of the inviscid boundaries. The recompression process in the base flow analysis is an important component which significantly affects the resulting base flow solution. However, since it is poorly understood, empirical modifications to the recompression model are often used to bring the simplified component model predictions into better agreement with experimental measurements. Once the jet boundary and discriminating streamlines have been identified in each mixing region, conservation of mass and energy in the base region provide the criteria for determining the solution values of the base pressure and temperature.

The foregoing series solution-method of characteristics-component model methodology is computationally efficient, thereby providing a means for quickly analyzing the effect of many parameters, including nozzle geometry, on the base pressure. A typical nozzle flow and base flow solution requires approximately 5 s of execution time on a CDC Cyber 175 computer.

Results and Discussion

For purposes of comparison, the nozzle flowfield was calculated for the same conical nozzle analyzed by Fujii and Kutler[6] for single-phase flow; this nozzle has $R_{CW}/R_T=0.625$, $R_I/R_T=2.625$, and $\beta_I=15$ deg. This configuration has also been analyzed by Serra[8] and experimentally investigated by Back and Cuffel.[9] The wall and axis Mach number distributions due to Fujii and Kutler, Serra, and Back and Cuffel (taken from Fig. 2 of Ref. 6) are compared to the results of the present nozzle analysis in Fig. 2. The present method agrees quite well with both the measurements and the results of Fujii and Kutler for the wall Mach number distribution. All three analytical techniques also predict the axis Mach number profile reasonably well up to the point where the steep decrease in the Mach number occurs after

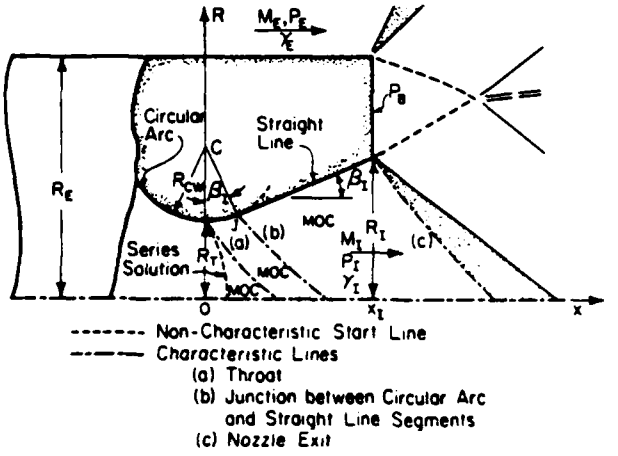

Fig. 1 Missile base configuration and nomenclature.

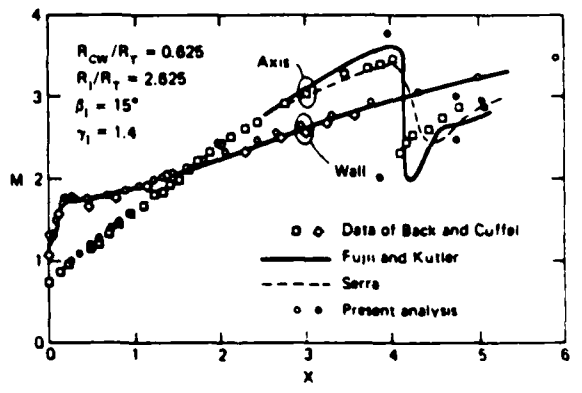

Fig. 2 Comparison of the present conical nozzle flowfield analysis with the analyses and experiments of others.

the onset of compression on the axis. At this point the various analyses and data diverge somewhat, although it appears that the present technique predicts the axis Mach numbers at least as well as the two finite-difference methods. Since this nozzle configuration represents an extreme geometry and the present analysis provides generally good agreement with other prediction methods and experimental data, the present method is considered to be adequate for the current study.

For the base flow investigation, the conical nozzle exit radius ratio and divergence half-angle were fixed at $R_J/R_T = 1.6239$ and $\beta_J = 15$ deg, respectively. The parametric values considered for the dimensionless throat wall radius of curvature were $R_{CW}/R_T = 0.75$, 1.0, 1.5, 2.0, 4.0, and 8.0 and for the nozzle gas specific heat ratio were $\gamma_J = 1.25$ and 1.4. Since R_{CW}/R_T was varied but R_J/R_T was held constant, the dimensionless length of the nozzle varies directly with the throat wall radius of curvature ratio. Also, the exit radius ratio value corresponds to a nominal exit Mach number of $M_J = 2.343$ for $\gamma_J = 1.25$ and $M_J = 2.5$ for $\gamma_J = 1.4$. The base thickness radius ratio was taken as $R_J/R_E = 0.6$ and, for purposes of comparison with earlier parametric results with ideal conical nozzles,[3] the freestream flow parameters were also fixed at $M_E = 2.0$ and $\gamma_E = 1.4$.

Figure 3 presents the base pressure results for $\gamma_J = 1.4$ over the operating pressure ratio range $2 \le P_J/P_E \le 8$. The top line in Fig. 3 gives the base pressure ratio P_B/P_E over this range as predicted by the original Chapman-Korst component flow model assuming ideal conical nozzle flow and without any of the empirical modifications which are used to bring the theory and experimental measurements into closer agreement. The calculations embodied in this line serve as the baseline case for determining whether or not nonuniform nozzle flow effects are a major source of the discrepancy between the original theory and experiments and what the magnitudes of these effects are. The percent deviations Δ from the baseline case are plotted in the central portion of Fig. 3 for each of the parametric values of R_{CW}/R_T, where

$$\Delta \text{ (percent)} = \frac{100[(P_B/P_E) - (P_B/P_E)_{\text{baseline}}]}{(P_B/P_E)_{\text{baseline}}}$$

As can be seen, nonuniform nozzle flow effects result in a maximum *increase* in base pressure of approximately 6%, and, interestingly, this maximum deviation occurs at the intermediate radius of curvature ratio $R_{CW}/R_T = 1.5$. This latter result can be explained as follows. For $R_{CW}/R_T = 8.0$, the nozzle flowfield nonuniformities introduced by the throat geometry are small so that the base pressure deviation from the ideal conical case is also small. As R_{CW}/R_T is decreased, the throat flow nonuniformities become more pronounced and Δ increases as a result. However, as R_{CW}/R_T is reduced further, a competing effect appears. Since the exit radius R_J/R_E is constant, the conical divergent section of the nozzle (point J to the exit in Fig. 1) is longer for these smaller values of R_{CW}/R_T. Therefore, even though larger flowfield nonuniformities are introduced by these sharp throat curvatures, the flow has a larger distance over which to relax back toward ideal conical conditions. As a result, Δ decreases again. The base pressure results for $\gamma_J = 1.25$ (not shown) are qualitatively similar to those for the $\gamma_J = 1.4$ case presented in Fig. 3. However, the maximum deviation is approximately 7% and occurs for $R_{CW}/R_T = 1.0$.

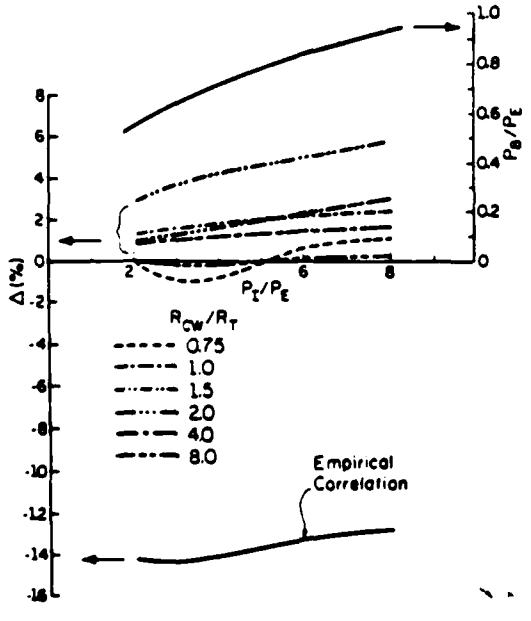

Fig. 3 Base pressure results for $\gamma_J = 1.4$.

Also shown in Fig. 3 are component model calculations which utilize the empirical recompression criterion proposed in Ref. 10. However, for the purposes of the present discussion, this line may be considered simply as an empirical correlation of the approximately 150 experimental data sets which form the basis of this criterion. Since the component model with nonuniform nozzle flow effects included generally predicts a *higher* base pressure than the ideal conical flow baseline case while the experimental measurements fall 13-14% *below* this same baseline, it is readily concluded that these effects are *not* the primary source of the disagreement between the original unmodified component model and experiments. In fact, these results point out that there must be other, larger factors not accounted for in the original theory which act in the opposite direction to bring the base pressure down to the measured level. Such factors include the afterbody and nozzle wall boundary layers and inadequate modeling of the mixing, recompression, and redevelopment processes. In addition, since experimental and prototype hardware often have nozzle geometries for which the present analysis predicts significant nonuniform nozzle flow effects on the base flow, these effects should be included in the development of more advanced component models or in Navier-Stokes flowfield calculations. Only when all pertinent mechanisms are understood and properly treated will a unified, nonempirical base flow theory be realized.

Acknowledgments

This research was sponsored in part by the U. S. Army Research Office under Contract DAAG 29-79-C-0184 and the Department of Mechanical and Industrial Engineering.

References

[1] Addy, A. L., "Detailed Analyses for the Base-Pressure Programs (TSABPP-1,2)," U. S. Army Missile Command, Redstone Arsenal, AL, Rept. RD-TN-69-7, Aug. 1969.

[2] Addy, A. L., "Analysis of the Axisymmetric Base-Pressure and Base-Temperature Problem with Supersonic Interacting Freestream-Nozzle Flows Based on the Flow Model of Korst, et al., Part I: A Computer Program and Representative Results for Cylindrical Afterbodies," U. S. Army Missile Command, Redstone Arsenal, AL, Rept. RD-TR-69-12, July 1969.

[3] Addy, A. L., "Analysis of the Axisymmetric Base-Pressure and Base-Temperature Problem with Supersonic Interacting Freestream-Nozzle Flows Based on the Flow Model of Korst, et al., Part III: A Computer Program and Representative Results for Cylindrical, Boattailed, or Flared Afterbodies," U. S. Army Missile Command, Redstone Arsenal, AL, Rept. RD-TR-69-14, Feb. 1970.

[4] Dutton, J. C. and Addy, A. L., "Transonic Flow in the Throat Region of Axisymmetric Nozzles," *AIAA Journal*, Vol. 19, June 1981, pp. 801-804.

[5] Dutton, J. C. and Addy, A. L., "Transonic Flow in the Throat Region of Annular Supersonic Nozzles," *AIAA Journal*, Vol. 20, Sept. 1982, pp. 1236-1243.

[6]Fujii, K. and Kutler, P., "Computations of Two-Phase Supersonic Nozzle Flows by a Space-Marching Method," AIAA Paper No. 83-0041, Jan. 1983.

[7]Dutton, J. C. and Addy, A. L., "TRANNOZ: A Computer Program for Analysis of Transonic Throat Flow in Axisymmetric, Planar, and Annular Supersonic Nozzles," Department of Mechanical and Industrial Engineering, University of Illinois at Urbana-Champaign, Rept. UILU-ENG-80-4005, April 1980.

[8]Serra, R. A., "Determination of Internal Gas Flows by a Transient Numerical Technique," *AIAA Journal*, Vol. 10, May 1972, pp. 603-611.

[9]Back, L. H. and Cuffel, R. F., "Detection of Oblique Shocks in a Conical Nozzle with a Circular-Arc Throat," *AIAA Journal*, Vol. 4, Dec. 1966, pp. 2219-2220.

[10]Addy, A. L., "Experimental-Theoretical Correlation of Supersonic Jet-On Base Pressure for Cylindrical Afterbodies," *Journal of Aircraft*, Vol. 7, Sept.-Oct. 1970, pp. 474-477.

APPENDIX B

SMALL-SCALE EXPERIMENTS OF SEPARATED FLOW CONFIGURATIONS UTILIZING A LASER DOPPLER VELOCIMETER

SECTION B.1

A STUDY OF COMPRESSIBLE FREE SHEAR LAYERS USING LASER DOPPLER VELOCIMETRY

Paper No. AIAA-85-0177

Presented at the AIAA 23rd Aerospace Sciences Meeting

Reno, Nevada

January 14-17, 1985

by

H. L. Petrie, M. Samimy, and A. L. Addy

AIAA'85

AIAA-85-0177

A Study of Compressible Turbulent Free Shear Layers Using Laser Doppler Velocimetry

H. L. Petrie, U.S. Army Missile Lab., Redstone Arsenal, AL; and M. Samimy and A. L. Addy, Univ. of Illinois at Urbana-Champaign, Urbana, IL

AIAA 23rd Aerospace Sciences Meeting

January 14-17, 1985/Reno, Nevada

A STUDY OF COMPRESSIBLE TURBULENT FREE SHEAR LAYERS USING LASER DOPPLER VELOCIMETRY

H. L. Petrie
National Research Council Associate
U.S. Army Missile Laboratory
Redstone Arsenal, Alabama 35897

M. Samimy
University of Illinois
at Urbana-Champaign
Urbana, Illinois 61801

A. L. Addy
University of Illinois at Urbana-Champaign
Urbana, Illinois 61801

Abstract

An experimental investigation of two-dimensional planar turbulent free shear layers with supersonic freestream Mach numbers is discussed. Three backward facing step flow configurations were investigated in order to gain a detailed knowledge of the mean flow and turbulent field in developing free shear layers with and without an adjacent recirculating flow and a constant pressure separation. Two channel coincident laser Doppler velocimeter (LDV) measurements, surface static pressure measurements, Schlieren flow visualization, and surface oil flow visualization were used to study these flows.

Introduction

The near wake base region of blunt based missile type bodies at supersonic freestream Mach numbers presents difficult problems to the experimentalist, the analytic modeler, and the computationalist alike, see Fig. 1. Although modeling methods like the Chapman-Korst component theory, see Chapman[1], Korst[2], and Korst, et al.[3], or Carpenter and Tabakoff[4], have seen extensive attention and development and Navier-Stokes computer codes have been[5,6] applied to these flowfields, see Hasen[5], Fox[6] or Horstman, et al.[7], an accurate and general predictive capability does not exist. Knowledge of the physics of these flows gained through simple model experiments has served to guide the development of component theory but these past experimental efforts have provided very little turbulent field or recirculating flow region information. The extensive use of LDV in the present study of turbulent free shear layers via simple model experiments is a step beyond these past efforts in providing such information. The evaluation and development of Navier-Stokes codes and the turbulence models they incorporate for the study of missile base region flows should be facilitated by such experimental information.

Experimental Program

A series of small-scale cold air flow experiments were conducted in blowdown wind tunnel facilities. Further details, data, discussion, and aspects of this investigation not discussed below are presented by Petrie[8].

Experimental Configurations

The three backward facing step configurations used are shown in Fig. 2. Constant pressure separation was achieved with the ramp configuration, Fig. 2(a), by adjusting the reattachment ramp angle. The flowrate of the mass bleed through the porous plate, the wind tunnel floor in Fig. 2(b), was matched to the shear layer entrainment rate in order to achieve a constant pressure separation. These two configurations allowed study of the developing turbulent mixing layer without complicating separation shock wave or expansion fan effects. Also, the purpose of the porous plate mass bleed was to remove the recirculating flow and its possible effects on the shear layer and to simulate a quiescent semi-infinite fluid boundary condition in a small wind tunnel. The ramp configuration flow was examined previously at M_∞ = 2.92 by Settles, et al.[9], primarily to study mixing[10] layer reattachment[11] and redevelopment. Ikawa[10] and Ikawa and Kubota[11] studied the porous plate flow configuration at M_∞ = 2.47. Pressure probes and hot-wires were used in these two previous studies. The simple backstep configuration, Fig. 2(c), was examined primarily to detail the recompression and redevelopment zone but useful mixing layer and recirculating flow data were obtained for the present study. The emphasis of this paper is discussion of the ramp configuration results and is entirely limited to the approach flow, mixing layers prior to the recompression zone, and the adjacent freestream and recirculating flow.

The ramp and porous plate experiments were conducted in a 101.6 mm span wind tunnel while the simple backstep experiments were in a 50.8 mm span wind tunnel. Step heights were 25.4 mm for the ramp and simple backstep and 44.45 mm for the porous plate. The porous plate itself had an open length of 240 mm. The approach flow to the ramp and porous plate was at M_∞ = 2.43 with T_0 = 298°K and P_0 = 551.6 kPa. This resulted in U_∞ = 570 m/s with a unit Reynolds number of 5.57×10^7 /m. The simple backstep data were taken for a M_∞ = 2.07 approach flow which expanded to Mach 2.74 adjacent to the separated shear layer with P_0 = 528.1 kPa and T_0 = 293°K. The freestream velocity adjacent to the simple backstep mixing layer was U_∞ = 594.59 m/s after the expansion; $Re/m = 6.69 \times 10^7$ /m.

The ramp angle and porous plate mass bleed flowrate were adjusted for constant pressure separation by viewing the flow with the Schlieren

system. A 19.4° ramp angle was used. The ramp mixing layer reattached onto the ramp 4.5 mm below the level of the approach flow step height, see Fig. 3. Although the reattachment line was straight and horizontal, the flow was not two-dimensional in the reattachment region. However, measurements made 19.05 mm off of the wind tunnel center plane indicated a nearly two-dimensional core existed.

The Laser Doppler System

A commercial two color, two channel coincident, frequency shifted LDV system with a 5 Watt argon ion laser was used in this study. Forward scatter, 10° off axis light collection with a 250 mm focal length lens was always used. The focusing optics used in the ramp and porous plate experiments provided a measurement volume with fringe spacings of 5.779 μm for λ = 488 nm and 6.092 μm for λ = 514.5 nm and approximately 21 fringes. The backstep experiments used optics producing 13.56 μm and 14.30 μm fringe spacings. The larger fringe spacings were desired because of the high turbulent intensities expected in supersonic regions of the recompression zone and the possible fringe bias problems that may have resulted with a two channel coincident LDV, see Whiffen[12], Whiffen, et al.[13], Buchave[14], and Dimotakis[15]. A detailed discussion of fringe bias in highly turbulent high speed flows is presented by Petrie[8].

The small scale of the experiments and large velocity gradients across the shear layers could have led to errors due to poor spatial resolution. Estimates of the effects of the spatial resolution in the presence of flow gradients[16], after Karpuk and Tiedermann, demonstrated that there was sufficient resolving power for accurate results in all cases.

Frequency shifting at 40 MHz with the fringes oriented at ± 45° to the approach flow direction was done in all cases except some of the approach boundary layer data. One channel unshifted data were taken in the boundary layer near to the wall where the beam blockage became a problem.

TSI, Inc. Model 1990A digital frequency counters processed the Doppler signals. Frequencies were based on 8 Doppler cycles using a 4-to-8 cycle frequency comparison with a 3.9% agreement required. The ± 1 ns clock count resolution resulted in an apparent turbulent intensity of 1.23% at the 570 m/s freestream velocity of the ramp configuration.

Seeding was accomplished with 6 jet atomizers manufactured by TSI using a 50 cP silicone oil. The wind tunnel plenum and the porous plate mass bleed flow were seeded. Experiments were conducted to estimate mean particle diameters by measuring the velocity lag of particles downstream of an oblique shock wave formed at a 15° compression ramp with a Mach 2.58 approach flow. Comparison with calculations using the empirical particle drag coefficient by Walsh[1] indicated 1 μm mean diameter particles were seen by the LDV.

The Approach Boundary Layer

The 99% and momentum thicknesses of the approach boundary layer were δ = 3.71 mm and θ_0 = .28 mm in the Mach 2.43 wind tunnel. These LDV results agree within 2 to 2.5% with the pressure probe results of Hampton and White[18] taken in the same wind tunnel under similar flow conditions. θ_0/δ = .0754 was approximately 12% larger than the results of Maise and McDonald's[19] formulation.

The power law

$$U/U_\infty = (y/\delta)^{.1667}$$

fit the ramp wind tunnel approach boundary layer streamwise velocity profile very well. A modified logrithmic law of the wall, see Maise and McDonald[19], Mathews, et al.,[20] and Baronti and Libby[21],[22] with Coles[23] wake function and Van Driest's[24] compressibility transformation was fitted to the velocity profile. This allowed estimation of the skin friction coefficient, C_f = .00142, and wall shear stress, τ_w = 214.6 Pa, for the ramp and porous plate flows.

The streamwise boundary layer turbulence intensity profile results of the present study generally agree with the results of others[24], see Fig. 4[25]. The LDV data of Johnson[26] and Dimotakis, et al.[27], and the hot-wire data of Kistler[28] and Rose[29] are shown. Later LDV and hot-wire data, not shown, by Johnson and Rose[29] follow along Klebanoff's[30] incompressible result but fall above the curve as do the Mach 3 results of Yanta and Lee[30]. Similar agreement was observed with the boundary layer Reynold's stress fluctuations, $-\langle u'v'\rangle$, and the results of Johnson[25], see Petrie[8].

The U component flatness and skewness factors peaked sharply at the outer edge of the boundary layer and then declined rapidly in magnitude to y/δ = .6 after which the decline was very gradual. Peak skewness factors were as large or larger than those of Yanta and Lee[30] and peak flatness[30] factors were noticeably larger. Yanta and Lee[30] excluded data more than ± 3σ from the mean, which should lead to discarding good data for the highly flat and skewed velocity distributions in the outer boundary layer. This was definitely the case, as determined by examination of the velocity histograms, when the ± 3σ criterion was applied to the data of this study. Flatness factors were underpredicted by 25% and the streamwise turbulence intensity by as much as 10.1% for these skewed distributions when this was done in the current study. The current results are similar to those of Hayakawa, et al.[31] at Mach 2.85, which were obtained with a hot-wire anemometer.

The Mean Flow

The mean streamwise velocity profiles for the ramp configuration shear layer are shown in Fig. 5. X is the streamwise distance from the step and y is the transverse coordinate. The mixing layer has spread across the boundary layer dominant by X/θ_0 = 178.77. The ramp streamwise velocity profiles were noticeably fuller for y < 0 and X/θ_0 > 178.77 than the porous plate

AD-A172 814 FLUID DYNAMIC MECHANISMS AND INTERACTIONS WITHIN SEPARATED FLOWS (U) ILLINOIS UNIV AT URBANA DEPT OF MECHANICAL AND INDUSTRIAL ENG A L ADDY ET AL JUL 86 2/3

UNCLASSIFIED UILU-ENG-86-4006 ARO-19823 19-EG F/G 20/4 NL

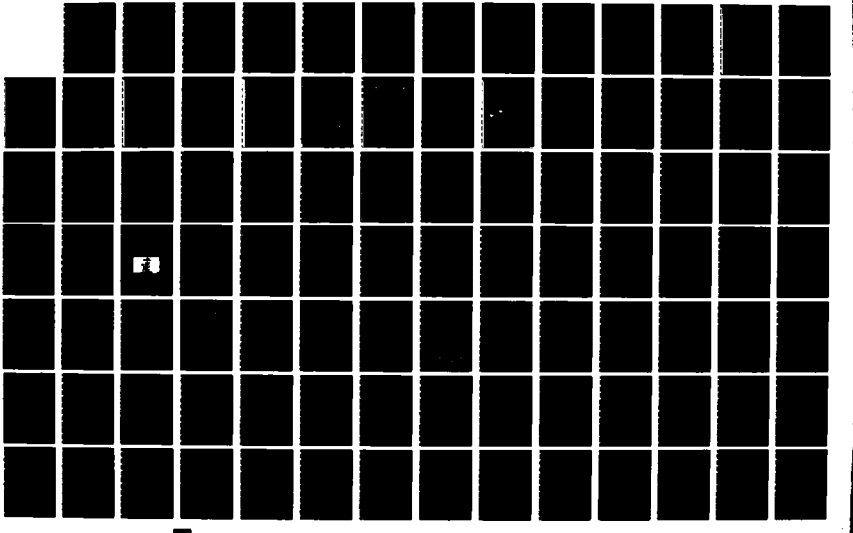

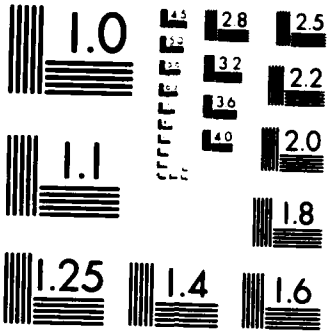

profiles indicating more flow has been entrained into the ramp mixing layer.

The y coordinate has been scaled by the local shear layer momentum thickness, θ, in Fig. 6 and y* is the distance from the $U/U_\infty = .5$ location. Mean profile self-similarity for $X/\theta_0 \geq 250$ or $X/\delta \geq 18.8$ seems to be the case. Ikawa[16] observed mean similarity for $X/\theta_0 \geq 275$ at $M_\infty = 2.47$ and Settles, et al.[8] observed similarity for $X/\delta \geq 18$ at $M_\infty = 2.92$.

The shear layer width, b, defined as the distance between the $U/U_\infty = .9$ and .1 locations and the local shear layer momentum thickness, θ, grew in a near linear fashion soon after separation. Growth rate estimates for the ramp shear layer are $db/dx = .078$ and $d\theta/dx = .009$. Ikawa[16] observed $db/dx = .064$ and $d\theta/dx = .0073$ which are similar to current porous plate estimates. Typical incompressible growth rates[32] are $db/dx = .19$, see Champagne, et al.[32], and Liepmann and Laufer[33] found $d\theta/dx = .035$. Since

$$\frac{d\theta}{dx} = \frac{d}{dx}\int_{-\infty}^{y_j} \frac{\rho U}{\rho_\infty U_\infty}\, dy$$

where y_j is the location of the dividing streamline, see Petrie[8], then mixing layer entrainment at these freestream Mach numbers is reduced by nearly a factor of five with respect to incompressible flows. The current results indicate an increase in growth and entrainment due to a recirculating flow in excess of 20%.

The ramp configuration recirculating flow mean velocity vectors are shown in Fig. 7. The maximum reverse flow velocity magnitude was .19 U_∞. The simple backstep reverse velocities had a larger maximum, .26 U_∞. The directed nature of the recirculating flow towards the step separation point may lead to the onset of plume induced separation on missile afterbodies. Separation on afterbodies has been observed to occur as soon as the base pressure exceeds the afterbody surface static pressure, see White and Agrell[34,35].

Static pressure variations of 4% and 6% were seen in the backstep and ramp recirculating flows, respectively. Minimum pressures occur where the recirculating velocities are high; near the base of the ramp in Fig. 7 and at X/H = 1 for the simple backstep. The static pressures in the mixing layer were slightly higher than in the recirculating flow except near the backstep where the recirculating flow stagnates and the pressure rose to the mixing layer level.

The Turbulent Field

A qualitative knowledge of the turbulent field was obtained by observation of the velocity probability distribution functions. Figure 8 shows streamwise component distributions at various locations across the flow for the ramp configuration at $X/\theta_0 = 268.15$. The velocity biased distributions were obtained by adding a 1 to the bin accumulator if the velocity of the i^{th} data point fell within the range of the bin and were normalized with the total number of data points. The velocity bias corrected distributions were obtained by adding $1/V_{Ti}$, where $V_{Ti}^2 = U_i^2 + V_i^2$ to the bin accumulator and normalizing with the sum of all $1/V_{Ti}$. The vertical lines in the distributions locate the mean values on the abscissa and the horizontal lines locate the ordinate. The two arrows mark the Mach 1.2 location, or the normal Mach number below which hot-wires become Mach number sensitive, see Smits, et al.[36] and Wagner[37]. Since the mean V velocity is small, a drop in the PDF centered at U = 0 is expected if a velocity bias exists. This dip at U = 0 was observed in all of the data and the $1/V_T$ correction generally produced more reasonable looking distributions than the bi-model biased distributions. A small coincidence time window may lead to a similar PDF dip. The effects of the time window size were examined and were not a factor, see Petrie[8].

The velocity probability distributions skew significantly at the high speed edge of the shear layer, developing a long tail on the low speed side of the distribution. The dynamic range of velocity distribution increased to a maximum near the $y^*/\theta = 0$ location. This is the $U/U_\infty = .5$ location and is slightly below the sonic line. The mode of the velocity distribution is centered in the distribution, which is nearly Gaussian, in the central region of the mixing layer. The velocity distributions skew again at the low speed side of the mixing layer but this is not as pronounced as on the freestream side. These features are seen in the skewness and kurtosis factor results discussed below.

All of the data presented below have been corrected for velocity bias using the $1/V_T$ correction. Figures 9 and 10 show the relative magnitude of the correction versus the local turbulent intensity for the streamwise component mean velocity and turbulent intensity, respectively. The[38,39] curve in Fig. 9 is Erdmann and Tropea's low turbulent intensity free running processor result; the bias of the mean equals the intensity squared. Johnson, et. al.[40,41] obtained similar results in a low speed two stream mixing layer. Behavior similar to the U component turbulence intensity in Fig. 10 was observed by Buchave[14] when the one-dimensional McLaughlin and Tiedermann[42] correction was applied to simulated three-dimensional Gaussian turbulence field under certain conditions. The biased and uncorrected U component standard deviation, σ_u, differ by less than 10% in most of the flow. The difference between the corrected and biased streamwise turbulent intensity based on the local mean velocity increase monotonically and asymptotically with the turbulent intensity to 30%; the two-dimensional corrected intensity being the larger of the two.

Ramp configuration U and V component turbulence intensity results are shown in Figs. 11 and 12. These data did not collapse together as the mean flow did in Fig. 6. Scaling with the local maximum intensity did collapse the data at downstream locations but on the high speed side of the mixing layer only. Turbulence intensities at the three most downstream locations on the low speed side of the mixing layer, $y^*/\theta < 0$, were noticeably higher for the ramp than the porous plate.

Streamwise component turbulence intensities based on the local velocity magnitude increased dramatically for $y^*/\theta < 0$. Values peaked at 170% to 450% where the local mean was nearly zero. Intensities near the sonic line were 30% to 40%.

The maximum turbulence intensities, based on the freestream velocity, versus X/θ_0 for the ramp are shown in Fig. 13. Both ramp and porous plate streamwise intensities increased and then leveled off at approximately 14.6% after separation. Ramp intensity levels increased to 17.2% downstream of $X/\theta_0 > 125.14$. The V component intensity underwent a more gradual increase after separation. The maximum $-\langle u'v'\rangle$ term increased sharply after separation, however. The correlation coefficient maximmum was initially very high, $R_{uv} > .7$, for $X/\theta_0 = 21.45$. The ramp configuration V component intensity reached 8.2% at $X/\theta_0 = 357.54$. The porous plate streamwise intensity increased slightly with X reaching 15.6% at $X/\theta_0 = 357.54$. Porous plate end effects due to the diffuser inlet pressure rise were the cause. Porous plate V component maximum intensities were quite similar to the ramp results.

The simple backstep streamwise component maximum turbulence intensities increased from 15.0% to 25% prior to the pressure rise. Transverse component maximum intensities ranged from 4.7% after separation to 7.3% prior to recompression.

Incompressible mixing layers have similar magnitude maximum streamwise turbulence intensities but larger transverse component intensities. Champagne, et al.[32] observed 17.1% and 11.7% values for the U and V component maximum turbulence intensities, respectively. The compressible mixing layer transverse intensity were 1/2 to 1/3 of the streamwise values while this ratio is 2/3 for incompressible flows.

The available hot-wire streamwise intensity results differ substantially from the current results. Wagner[37] did not make measurements in the transonic core of a $M_\infty = 5$ mixing layer due to the Mach number dependence of the hot-wire but did extrapolate to estimate a 9% maximum streamwise turbulence intensity. Ikawa[10,11] observed a 5 to 6% maximum, or less than the approach boundary layer values. Ikawa[10,11] also observed maximum streamwise turbulence intensities based on the local velocity of only 9% which occurred on the supersonic side of the mixing layer. This seems to be an unlikely result. These results may indicate calibration or frequency response problems and/or significant pressure fluctuations and the breakdown of Morkovin's[43] hypothesis as suggested by Bradshaw[44] and indicated by results of Brown and Roshko[45] and Roshko[45]

Reynolds' shear stress values for the ramp mixing layer are shown in Fig. 14. Downstream maximum values compare well with the value Ikawa[11] estimated from the mean streamwise velocity profile, $\tau/\rho_\infty U_\infty^2 = .0028$. Current results also fit the trends of the data at higher and lower Mach numbers by Sirieix and Solignac[46] and Maydew and Reed[2]. Wygnanski and Fiedler[48] observed $\tau/\rho_\infty U_\infty = .0092$ and Patel[49] obtained a maximum of .0104 in incompressible mixing layers. Half of the difference between the current and incompressible results was due to the factor of 2.2 decrease in the mean density from the high to low velocity side of the ramp and porous plate mixing layers; approximately 85% of this change has occurred above $y^*/\theta = 0$. The decline with respect to incompressible results of the V or transverse fluctuations appears primarily responsible for the smaller $-\langle u'v'\rangle$ values. Brown and Roshko's[44] order of magnitude arguments suggests both $\langle v'^2\rangle$ and $-\langle u'v'\rangle$ are inversely proportional to Mach number. The correlation coefficient, $R_{uv} = -\langle u'v'\rangle/\sigma_u\sigma_v$ at downstream locations ranged from .5 to .58 across the mixing layers in the current study which is similar to the .54 incompressible value of Patel[49] and .57 of Liepmann[2] and Laufer[33]. The backstep maximum $-\langle u'v'\rangle/U_\infty$ values were similar to the ramp values after separation but increased to values exceeding incompressible levels prior to recompression.

The apparent kinematic eddy viscosity, $-\langle u'v'\rangle/(\partial\bar{U}/\partial y)$, increased dramatically on the low speed side of the mixing layer, see Fig. 15. Average values of the eddy viscosity for $-4 < y^*/\theta < 4$ increased almost linearly with X.

The mixing length, $L = |u'v'|^{1/2}/(\partial\bar{U}/\partial y)$, in Fig. 16 also grew linearly with X as the scaling with θ indicates. For the ramp shear layer, $b \approx 8\theta$, so the mixing length ranges from $1/32 < L/b < 1/16$ across the mixing layer. The minimum mixing length occurs near the maximum Reynold's shear stress term location.

U component skewness and kurtosis factor results differ from those observed in incompressible mixing layers, see Wygnanski and Fiedler[48] and Champagne, et al.[32] Larger magnitudes occurred on the high speed side of the mixing layer and smaller ones on the low speed side opposite the incompressible results, see Figs. 17 and 18. The smaller low speed side kurtosis factors in the compressible mixing layer may indicate a less convoluted potential flow/turbulent flow interface with smaller ejections and entraining motions compared to the incompressible case. The observed low entrainment rates support that such a difference is plausible. Other differences between compressible and incompressible mixing layers is a shift from the high to low velocity side, that is from $y^* > 0$ to $y^* < 0$, of the location of the maximum shear stress, maximum transverse component turbulent intensity, and the point where the skewness factor goes through zero.

Conclusions

An experimental study of compressible turbulent free shear layers using a two channel LDV and three backward facing step flow configurations was conducted. Although mixing layer growth rates and entrainment rates are much smaller than those of incompressible flows, streamwise turbulence intensity levels were comparable. Transverse component turbulence intensities and Reynolds shear stress values were significantly smaller than in incompressible mixing layers, however. The results indicate structural differences between the incompressible and

compressible mixing layers. The recirculating flow noticeably effected the mixing layers in a number of ways. The assumption of constant eddy viscosity appears to be particularly poor in the presence of a recirculating flow. Statistical velocity bias of the LDV data was observed and a two-dimensional velocity inverse correction worked reasonably well.

Acknowledgment

This research was supported by the U.S. Army Research Office under contracts DAAG 29-79-C-0184 and DAAG 29-83-K-0043.

References

[1] Chapman, D. R., "An Analysis of Base Pressure at Supersonic Velocities and Comparison with Experiment," NACA TN 2137, 1950.

[2] Korst, H. H., Page, R. H., and Childs, M. E., "A Theory for Base Pressures in Transonic and Supersonic Flows," University of Illinois at Urbana-Champaign, ME-TN-392-2, 1955.

[3] Korst, H. H., "A Theory for Base Pressures in Transonic and Supersonic Flow," Journal of Applied Mechanics, 593, 1956.

[4] Carpenter, P. W. and Tabakoff, W., "Survey and Evaluation of Supersonic Base Flow Theories," NASA CR-97129, 1965.

[5] Hasen, G. A., "Navier-Stokes Solutions For An Axisymmetric Nozzle in a Supersonic External Stream," Wright Aeronautical Laboratories, Report AFWAL-TR-81-3161, March 1982.

[6] Fox, J. H., "Predicting Plume-Induced Separation on Bluff Base Bodies," AIAA Paper No. 84-0315, AIAA 22nd Aerospace Sciences Meeting, Reno, Nevada, January 9-12, 1984.

[7] Horstmann, C. C., Settles, G. S., Bogdonoff, S. M., and Williams, D. R., 1982, "A Reattaching Free Shear Layer in Compressible Turbulent Flow - A Comparison of Numerical and Experimental Results," AIAA Journal, Vol. 20, No. 1, January 1984, pp. 79-85.

[8] Petrie, H. L., "A Study of Compressible Turbulent Free Shear Layers Using Laser Doppler Velocimetry," Ph.D. Thesis, University of Illinois at Urbana-Champaign, Department of Mechanical and Industrial Engineering, April 1984.

[9] Settles, G. S., Baca, B. K., Williams, D. R., and Bogdonoff, S. M., "A Study of Reattachment of a Free Shear Layer in Compressible Turbulent Flow," AIAA Journal, Vol. 20, No. 1, January 1984, pp. 60-67.

[10] Ikawa, H. and Kubota, T., "Investigation of Supersonic Turbulent Mixing Layer with Zero Pressure Gradient," AIAA Journal, 13, 566, 1975.

[11] Ikawa, H., "Turbulent Mixing Layer Experiment in Supersonic Flow," Ph.D. Thesis, Aeronautical Engineering Department, California Institute of Technology, Vol. 13, No. 5, May 1975, pp. 566-572.

[12] Whiffen, M. C., "Polar Response of an LV Measurement Volume," Proceedings of the Minnesota Symposium on Laser Velocimetry," University of Minnesota, 1975, pp. 589-590.

[13] Whiffen, M. C., Lau, J. C., and Smith, M. D., "Design of LV Experiments for Turbulence Measurements," Rev. Sci. Instr., Vol. 48, No. 7, July 1977, pp. 197-207.

[14] Buchave, P., "Biasing Errors in Individual Particle Measurements with the LDA-Counter Signal Processor," The Accuracy of Flow Measurements by Laser Doppler Methods, Proceedings of the LDA Symposium, Copenhagen, Denmark, Hemisphere Publishing Co., New York, 1976, pp. 258-278.

[15] Dimotakis, P. E., "Single Scattering Particle Laser Doppler Measurements of Turbulence," AGARD CP-193, Non-Intrusive Flow Measurements, 1976, pp. 10-1-10-14.

[16] Karpuk, M. E. and Tiederman, W. G., Jr., "Effect of Finite Size Probe Volume upon Laser Doppler Anemometer Measurements," AIAA Journal, Vol. 14, No. 8, August 1976, pp. 1099-1105.

[17] Walsh, M. J., "Influence of Particle Drag Coefficient on Particle Motion in High-Speed Flow with Typical Laser Velocimetry Applications," NASA TN D 8120, 1976.

[18] Hampton, L. P. and White, R. A., "The Effect of Sudden Expansions and Compressions on Turbulent Boundary Layer Momentum Thickness in Supersonic Flow," University of Illinois at Urbana-Champaign, Urbana, Illinois, Report No. UILU-ENG-83-4004, 1983.

[19] Maise, G. and McDonald, H., "Mixing Length and Kinematic Eddy Viscosity in a Compressible Boundary Layer," AIAA Journal, Vol. 6, No. 1, January 1968, pp. 73-80.

[20] Mathews, D. C., Childs, M. E., and Paynter, G. C., "Use of Coles' Universal Wake Function for Compressible Turbulent Boundary Layers," Journal of Aircraft, Vol. 7, No. 2, February 1970, pp. 137-140.

[21] Baronti, P. O. and Libby, P. A., "Velocity Profiles in Turbulent Compressible Boundary Layers," AIAA Journal, Vol. 4, No. 2, February 1966, pp. 193-202.

[22] Coles, D., "The Law of the Wake in the Turbulent Boundary Layer," Journal of Fluid Mechanics, Vol. 1, Part 2, 1956, pp. 191-226.

[23] Van Driest, E. R., "Turbulent Boundary Layer in Compressible Fluids," Journal of the Aeronautical Sci., Vol. 18, No. 3, March 1951, pp. 145-160.

[24] Johnson, D. A., "Turbulence Measurements in a Mach 2.9 Boundary Layer Using Laser Velocimetry," AIAA Journal, Vol. 12, No. 5, May 1974, pp. 711-714.

[25] Dimotakis, P. E., Collins, D. J., and Lang, D. B., "Laser Doppler Velocity Measurements in Subsonic, Transonic, and Supersonic Turbulent Boundary Layers," Laser Velocimetry and Particle Sizing, Thompson, H. D. and Stevenson, W. H. editors, Hemisphere Publishing Co., New York, 1979, pp. 208-219.

[26] Kistler, A. L., "Fluctuation Measurements in a Supersonic Turbulent Boundary Layer," The Physics of Fluids, Vol. 2, No. 3, March 1959, pp. 290-297.

[27] Rose, W. C., "Turbulence Measurements in a Compressible Boundary Layer Subject to a Shock-Wave Induced Adverse Pressure Gradient," AIAA Paper No. 73-167, 1973.

[28] Johnson, D. A. and Rose, W. C., "Laser Velocimeter and Hot-Wire Anemometer Comparison in a Supersonic Boundary Layer," AIAA Journal, Vol. 13, No. 4, April 1975, pp. 512-515.

[29] Klebanoff, D. S., "Characteristics of Turbulence in a Boundary Layer with Zero Pressure Gradient," NACA Report No. 1247, 1955.

[30] Yanta, W. J. and Lee, R. E., "Measurements of Mach 3 Turbulence Transport Properties on a Nozzle Wall," AIAA Journal, Vol. 14, No. 6, June 1976, pp. 725-729.

[31] Hayakawa, K., Smits, A. J., and Bogdonoff, S. M., "Hot-Wire Investigation of an Unseparated Shock-Wave/Turbulent Boundary-Layer Interaction," AIAA Journal, Vol. 22, No. 5, May 1984, pp. 579-585.

[32] Champagne, F. H., Pao, Y. H., and Wygnanski, I J., "On the Two-Dimensional Mixing Region," Journal of Fluid Mechanics, Vol. 74, Part 2, 1976, pp. 209-250.

[33] Liepmann, H. W. and Laufer, J., "Investigations of Free Turbulent Mixing," NACA TN 1257, 1947.

[34] White, R. A. and Agrell, J., "An Experimental Investigation of Supersonic Axisymmetric Flow over Boattails Containing a Centered Propulsive Jet," The Aeronautical Research Institute of Sweden (FFA), Technical Note AU-913, 1974.

[35] White, R. A. and Agrell, J., "Boattail and Base Pressure Prediction Including Flow Separation for Afterbodies with a Centered Propulsive Jet and Supersonic External Flow at Small Angles of Attack," AIAA/SAE 13th Propulsion Conference, Paper No. 77-958, Orlando, Florida, 1977.

[36] Smits, A. J., Hayakawa, K., and Muck, K. C., "Constant Temperature Hot-Wire Anemometer Practice in Supersonic Flows - Part 1 - The Normal Wire," Paper No. 83-0050, AIAA 21st Aerospace Sciences Meeting, Reno, Nevada, 1983.

[37] Wagner, R. D., "Mean Flow and Turbulence Measurements in a Mach 5 Free Shear Layer," NASA TN-D7366, 1973.

[38] Erdmann, J. C. and Tropea, C., "Turbulence Induced Statistical Bias in Laser Anemometry," Proceedings of the Seventh Symposium on Turbulence, University of Missouri-Rolla, September 1981, pp. 129-138.

[39] Erdmann, J. C. and Tropea, C., "Statistical Bias of the Velocity Distribution Function in Laser Anemometry," International Symposium on Applications of Laser Doppler Anemometry to Fluid Mechanics, Lisbon, Portugal, July 1982, Paper 16.2.

[40] Johnson, D. A., Modarress, D., and Owen, F. K., "An Experimental Verification of Laser-Velocimeter Sampling Bias and its Correction," Engineering Applications of Laser Velocimetry, ASME, New York, 1982, pp. 153-162.

[41] Johnson, D. A., Modarress, D., and Owen, F. K., "An Experimental Verification of Laser Velocimeter Sampling Bias and Its Correction," J. of Fluid Engineering, Vol. 106, No. 1, March 1984, pp. 5-12.

[42] McLaughlin, D. K. and Tiederman, W. G., Jr., "Biasing Correction for Individual Realization of Laser Anemometer Measurements in Turbulent Flow," The Physics of Fluids, Vol. 16, No. 12, December 1973, pp. 2082-2088.

[43] Bradshaw, P., "Compressible Turbulent Shear Layers," Annual Review of Fluid Mechanics, Vol. 9, Annual Reviews, Inc., Palo Alto, 1977, pp. 33-54.

[44] Brown, G. L. and Roshko, A., "On Density Effects and Large Structure in Turbulent Mixing Layers," Journal of Fluid Mechanics, Vol. 64, Part 4, 1974, pp. 775-816.

[45] Roshko, A., "Structure of Turbulent Shear Flows: A New Look," AIAA Journal, Vol. 14, No. 10, October 1976, pp. 1349-1357.

[46] Sirieix, M. and Solignac, J. L., "Contribution a l'etude experimentale de la couche de melange turbulent isobare d'un ecoulement supersonique," AGARD CP-4, Separated Flows, 1966.

[47] Maydew, R. C. and Reed, J. F., "Turbulent Mixing of Axisymmetric Compressible Jets (In the Half-Jet Region) with Quiescent Air," Sandia Corporation, Research Report SC-4764, 1963.

[48] Wygnanski, I. and Fiedler, H. E., "The Two-Dimensional Mixing Region," Journal of Fluid Mechanics, Vol. 41, 1970, pp. 327-361.

[49] Patel, R. P., "An Experimental Study of a Plane Mixing Layer," AIAA Journal, Vol. 11, No. 1, January 1973, pp. 67-71.

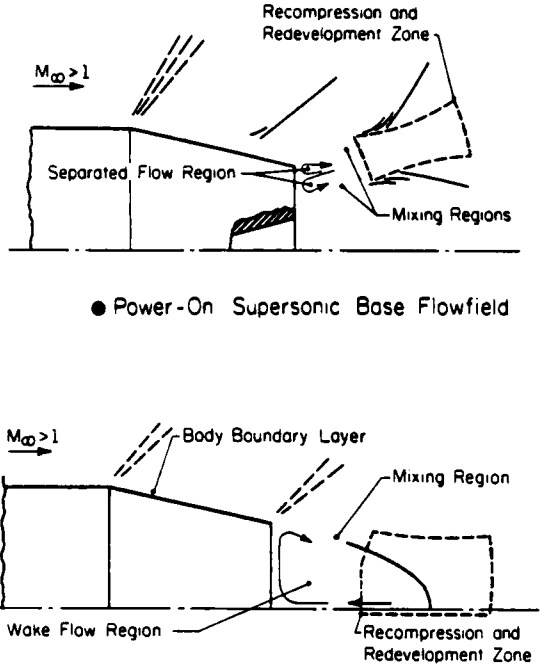

Fig. 1 Supersonic missile base flowfields with boattailed afterbodies.

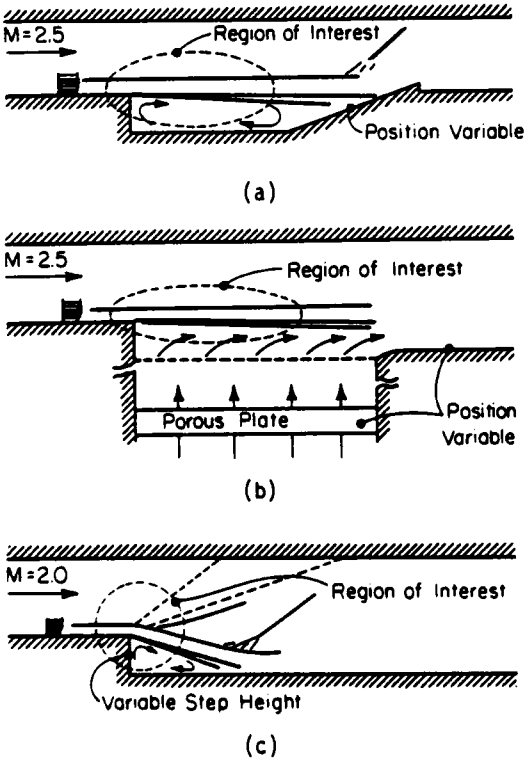

Fig. 2 Test models.

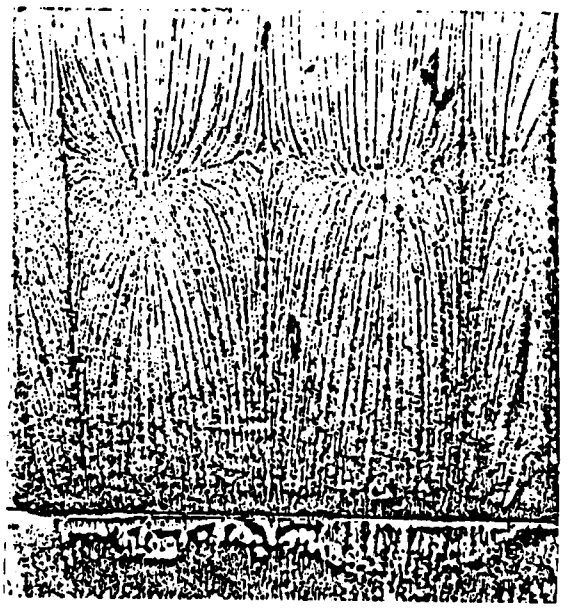

Fig. 3 Surface oil flow visualization of free shear layer reattachment onto ramp. The free-stream flow moves bottom to top.

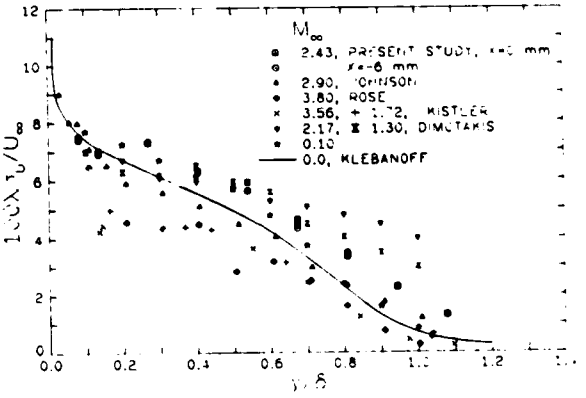

Fig. 4 U velocity component boundary layer turbulence intensity values.

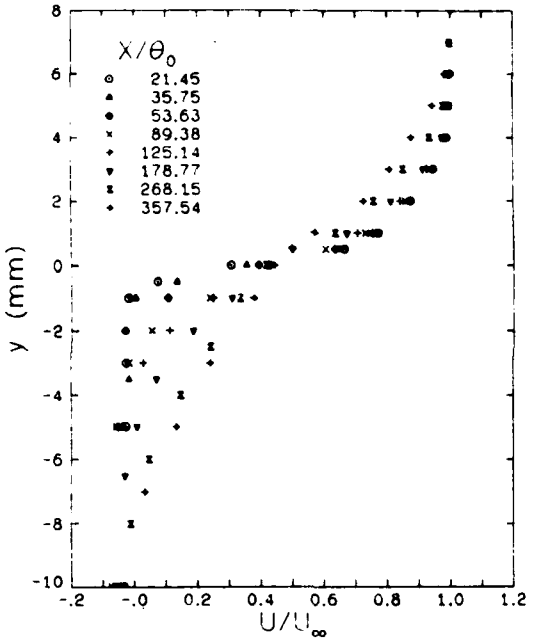

Fig. 5 Mean streamwise component free shear layer velocity profiles for the ramp configuration.

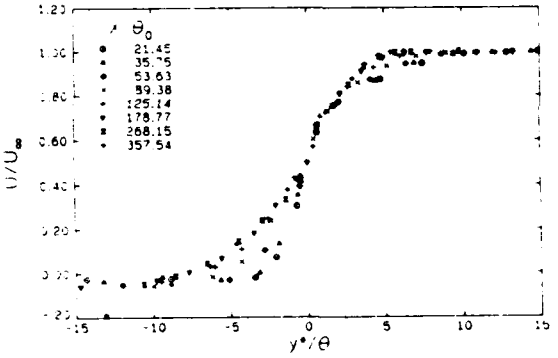

Fig. 6 Streamwise component shear layer velocity profiles for the ramp configuration.

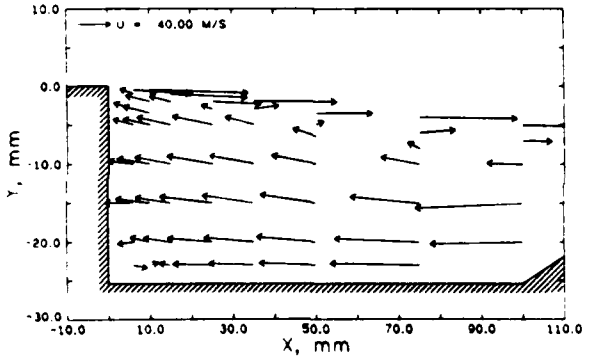

Fig. 7 The ramp configurations recirculating flow mean velocity vectors. The vector scale is indicated in the upper left corner, $U_\infty \approx 570$ m/s.

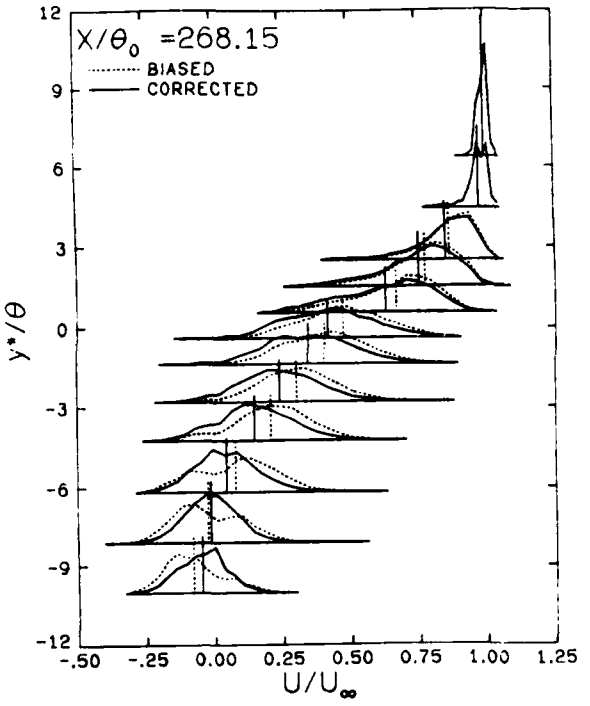

Fig. 8 Streamwise component velocity probability distributions for the ramp configuration, X = 75 mm.

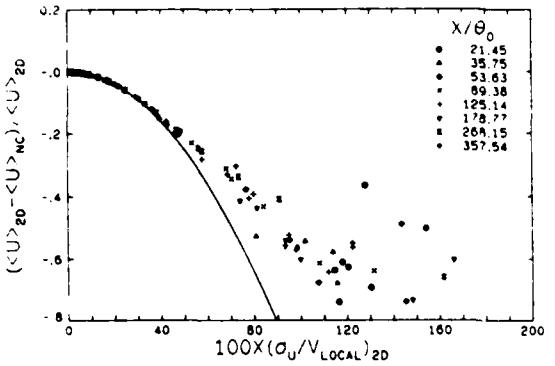

Fig. 9 Comparison of the corrected and biased mean U component velocity values versus the corrected local turbulence intensity.

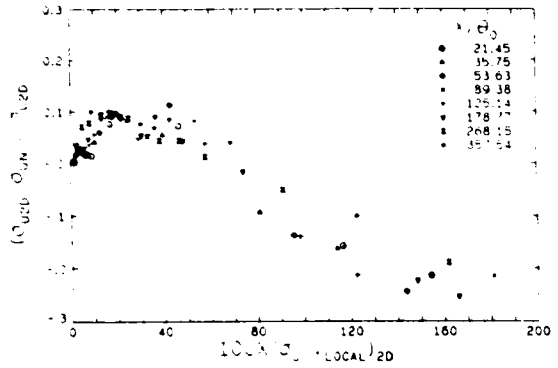

Fig. 10 Comparison of the corrected and biased U component turbulent intensities based on the freestream velocity.

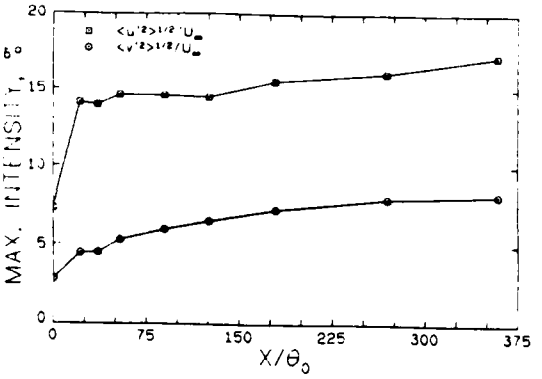

Fig. 13 Maximum turbulent intensity values for the ramp configuration.

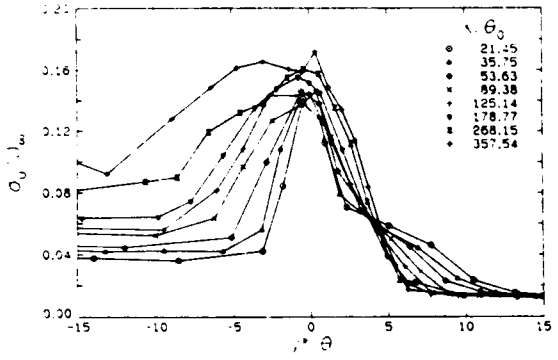

Fig. 11 U component turbulent intensities for the ramp configuration.

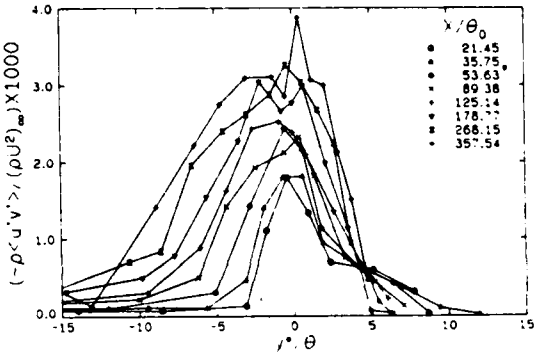

Fig. 14 Turbulent shear stress values for the ramp configuration.

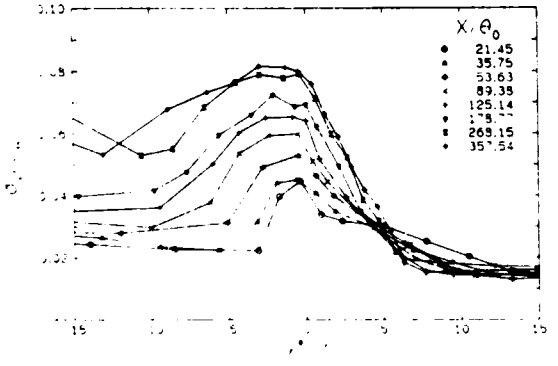

Fig. 12 V component turbulent intensities for the ramp configuration.

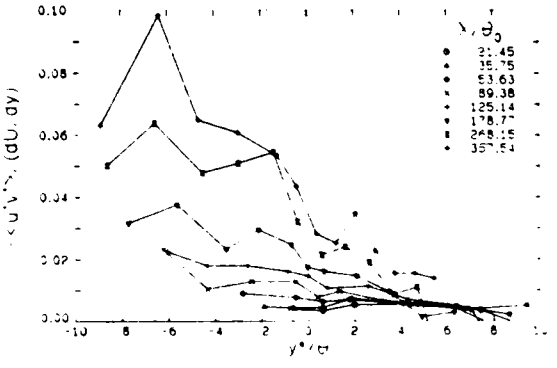

Fig. 15 Kinematic eddy viscosity values for the ramp configuration.

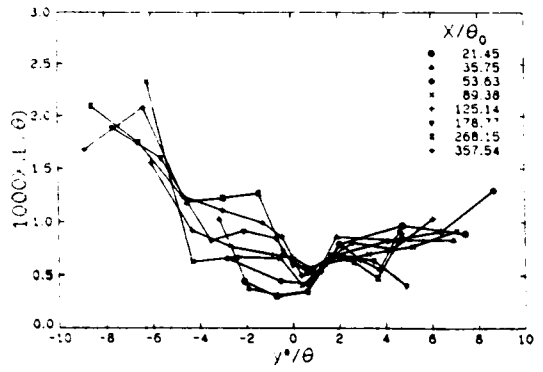

Fig. 16 Ramp configuration shear layer mixing lengths, $|u'v'|^{1/2}/(\partial U/\partial y)$.

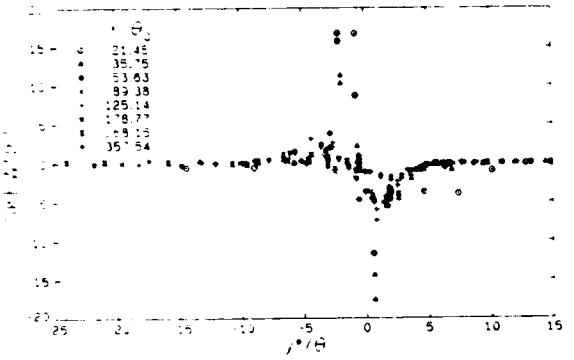

Fig. 17 The ramp configuration skewness factors for the U velocity component.

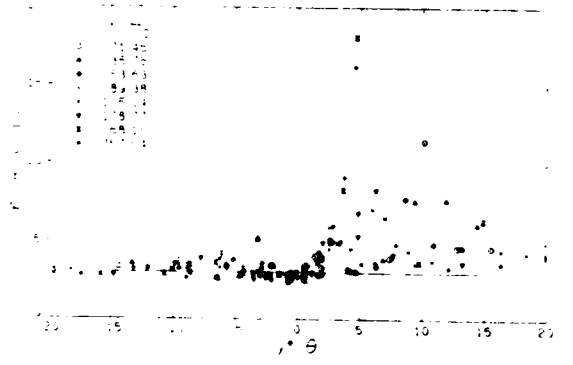

Fig. 18 The ramp configuration kurtosis values for the U velocity component.

SECTION B.2

AN EVALUATION OF LDV VELOCITY AND FRINGE BIAS EFFECTS IN SEPARATED HIGH SPEED TURBULENT FLOWS

Paper presented at the International Congress on
Instrumentation in Aerospace Simulation Facilities
(ICIASF '85 Record, IEEE Publication 85CH2210-3)

Stanford University

Stanford, California

August 26-28, 1985

Pages 297-308

by

H. L. Petrie, M. Samimy, and A. L. Addy

AN EVALUATION OF LDV VELOCITY AND FRINGE BIAS EFFECTS IN SEPARATED HIGH SPEED TURBULENT FLOWS

H. L. Petrie*
Pennsylvania State University
State College, PA 16804

M. Samimy**
Ohio State University
Columbus, OH 43210

A. L. Addy***
University of Illinois
at Urbana-Champaign
Urbana, IL 61801

Summary

The LDV velocity and fringe bias effects in highly turbulent separated flows are presented and discussed. The effects of velocity bias was found to be more substantial on the mean velocity and shear stresses than on the normal stresses. The addition of an estimated z velocity component term to the two-dimensional velocity inverse bias correction improves velocity bias correction when the measured 2-D velocity approaches zero. Also, the significance of fringe bias for two-component coincident LDV in separated flows are analyzed and procedures to eliminate the fringe bias are presented.

1. INTRODUCTION

This study is part of an ongoing program to investigate supersonic missile base region flows and the interaction between missile base and body flows. Features of these base flows includes separated regions of recirculating flow bounded by turbulent free shear layers and a recompression zone where the bounding shear layers merge and change direction. The experimental efforts of this investigation have been directed at the detailed study of simpler two-dimensional flows using laser Doppler velocimetry. These two-dimensional model experiments have important features in common with actual base flows and are better suited for study in small scale wind tunnels than complex axisymmetric flowfields [1]†.

The data presented below were taken in one such model experiment flowfield, shown in Fig. 1. A nominal Mach 2.5 flow with a fully developed turbulent approach boundary layer separates at a backward facing step and reattaches onto an inclined ramp downstream of the step. The ramp angle is adjusted to achieve a constant pressure separation at the backstep. This entire flowfield was surveyed from upstream of the backstep to downstream of reattachment with a two color, two-channel coincident frequency shifted laser Doppler velocimeter. References [2-5] provide further details. This paper will be directed toward coincident two channel LDV systems.

These model experiment flowfields contain regions of high turbulence intensity and in some cases these high intensities occur where the flow is supersonic. Thus, an extreme dynamic range of velocities is possible and at the outset it was expected that LDV velocity bias could have a substantial statistical effect on the results. Also, the combined effects of the two channel coincidence requirement and the wide dynamic range of velocities could result in a noticeable bias [6-10], even with a 40 MHz frequency shift.

An evaluation of the effect of these biases and the effectiveness and/or need for any corrective actions was felt to be essential to these LDV studies. Without such an effort, potentially large uncertainties and important unanswered questions would exist regarding the quality and accuracy of the results. The purpose of this paper is to present the results of this evaluation the techniques used in the process. This information should be of value to those doing counter base LDV in highly turbulent flows.

2. VELOCITY BIAS

McLaughlin and Tiederman [11] argued that the individual realization sampling process is biased towards higher velocities in turbulent flows because the volume of fluid and therefore the number of particles swept through the LDV measurement volume is proportional to the quantity being sampled, namely, the velocity. That is:

$$\Delta n = C\ A\ V_T\ \Delta t \tag{1}$$

where Δn is the number of particles sampled in time interval Δt, C is the number density of the particles, A is the cross sectional area of the measurement volume in the plane normal to the velocity vector, and V_T is the total velocity magnitude. If C and A are constant, then the data rate and probability of obtaining a sample is

---

* Research Associate, Applied Research Laboratory.
** Assistant Professor, Department of Mechanical Engineering.
*** Professor and Associate Head, Department of Mechanical and Industrial Engineering.
† Numbers in brackets refer to entries in REFERENCES.

CH2210-3/85/0000-0297 $1.00 © 1985 IEEE

directly proportional to the velocity; this is assumed in the following discussion.

TRANSIT TIME WEIGHTING

The particle transit time across the LDV measurement volume can be used as a weighting function to correct for velocity bias [10,12,13]. The transit time is, on average, inversely proportional to the velocity. This method of velocity bias correction has the advantage of not producing infinite weights and works just as well for one and two component LDV systems. However, LDV digital frequently counters often produce inferior results when operated in a total burst mode which determines the velocity using the transit time. This was the case in the current study. Also, the particle transit time through the LDV measurement volume is dependent on both the particle size and location of the particle pathline through the measurement volume [14]. This results in a scatter of the transit time weights for a given velocity vector. The particle size and its path through the measurement volume should not correlate with the velocity so the effect of this scatter should average out for sufficiently large samples. However, an increase in the size of the uncertainty interval of the velocity statistics for a given confidence level results.

The Doppler bursts were processed in the N-cycle mode in the present study. That is, a fixed number of cycles N_F, were required and used to determine the frequency of each burst. Transit time information was not available in this mode with the Doppler signal processors used. The N-cycle mode was used because it was less susceptible to noise and produced results superior to the total burst mode.

VELOCITY INVERSE WEIGHTING

A two-dimensional velocity inverse weighting function was used in the present study to correct for velocity bias. This is just a natural extension of the one-dimensional velocity inverse weight proposed by McLaughlin and Tiederman [11] that is possible with a coincident two channel LDV system. The velocity in the (x,y) plane was measured by the LDV with the measurement channels oriented at $\pm$ 45° to the horizontal streamwise direction. The z direction velocity component, W, was not measured but was expected to have a mean value of nearly zero in all cases.

A deficiency of this velocity inverse weight is the possibility of an infinite weight when the (x,y) plane velocities are simultaneously zero. This was rarely encountered in the present work but it did occur. Also, as the (x,y) plane velocities approach zero, the magnitude of the unmeasured z component becomes an increasingly significant part of the three-dimensional velocity magnitude. Even though this z velocity component had a zero mean value, its mean magnitude was not zero. As a result, the velocity magnitude in Equation (1) is on average underestimated when the (x,y) plane velocity is small. Thus, small velocity realizations will tend to be overweighted by the two-dimensional velocity inverse correction.

A simple approximate corrective action can be taken to account for the contribution of the z component to the velocity inverse weight. An estimate of the unmeasured z component turbulent intensity based on the measured (x,y) plane values combined with a geometric factor to account for the effective measurement volume cross sectional area can be used to determine an estimated averaged z component velocity magnitude. Such a procedure effectively limits the maximum allowed weight when both U and V are small in a reasonable way. Nakayama [15] added an estimated z component term to the velocity inverse weight, w_i, so that:

$$(2) \qquad w_i = \left[U_i^2 + V_i^2 + (a/b)^2 \sigma_w^2\right]^{-1/2}$$

where a/b is the ratio of the measurement volume diameter to its length; the long axis of the measurement volume ellipsoid is parallel to the z axis. This is also the ratio of its cross sectional area of the measurement volume in the (x,y) plane to that in the (y,z) plane with the origin at the measurement center. σ_w is the z component root mean square intensity level, its standard deviation, and U_i and V_i are the x and y component velocities of the ith realization. The z term, σ_z, is estimated as the average of the x and y component intensities. Since a/b is typically smaller than 1/20, the z component term will only be significant when U_i and V_i are small.

Off axis light collection can alter the effective measurement volume geometry and act to increase the effective area ratio, $(a/b)_e$, when the photodetector aperture is not large. In the present study, the effective length of the measurement volume, L_m, was calculated by procedures outlined in Reference 16. The effective (y,z) plane cross sectional area of the measurement volume was calculated by assuming a rectangular cross section of dimensions L_m by d_m, where d_m is the measurement volume diameter. With this approach, the effective area ratio for the LDV data discussed below was $(a/b)_e = 0.056$, which is approximately one-third larger than a/b.

The estimate of the added z term requires values of the intensities of the two measured components. One pass must be made through the data to determine these intensities and then a second pass must be made to calculate and include the estimated z term. In order to prevent an infinite weight from occurring on the first pass, a maximum allowable weight was set. The first pass maximum weight was that for a realization with a burst time one clock count less than would occur for a zero velocity in both channels. This is the smallest resolvable velocity increment in either channel at the zero velocity.

VELOCITY BIAS RESULTS AND DISCUSSION

With the above details and difficulties in mind, an examination of the effect of the velocity

bias and the bias correction was made. The results with the simple two-dimensional bias correction are given the most attention with comparison to the results with the added estimated z term on a limited basis.

Figure 2 shows probability density functions, PDF, of the x component velocity, U, taken across the mixing layer for the ramp flowfield in Fig. 1 at x = 75 mm downstream of the 25.4 mm backstep. The base of the ramp in Fig. 1 was at x = 101 mm. The freestream velocity was approximately 570 m/s. y^* is the distance from the $U/U_\infty = 0.5$ location and θ is the local mixing layer momentum thickness. The horizontal lines at the base of each PDF locate the ordinate and the short vertical lines indicate the mean of the PDF on the abscissa. The biased PDFs were formulated by adding a weighting factor of 1 to the histogram bin accumulator if a velocity realization fell within the range of the bin. The PDFs were normalized by dividing by the sum of these weights, which in this case is the total number of realizations in the sample. Constant bin widths were used so that normalization does not require division by the bin width for this comparison. The velocity bias corrected PDFs were obtained by the same procedure but the simple two-dimensional velocity inverse weighting factor was used. This visualization of the effect of the correction is informative and simple. It can be applied to examine directly the effect of any weighting function of the PDF.

The biased distributions in Fig. 2 exhibit a large decrease in the probability density about the U = 0 location in all cases where the probability density is sufficiently large near U = 0 to discern such details. This is true of all LDV data taken in this study. The decrease in the U velocity PDF is due to velocity bias and occurs because the U component is dominant in this flowfield such that the magnitude of the U velocity component correlates well with the total three-dimensional velocity magnitude. The V velocity PDFs, see Fig. 3, shows no such behavior at V = 0 because the event V = 0 correlates poorly with a zero three-dimensional velocity magnitude. However, the bias is still present and the V component statistics are affected by it.

The biased distributions of Fig. 2 are distinctly and unrealistically bimodal. That is not to say that a bimodal velocity PDF is unrealistic but that velocity bias acts to create or exaggerate the bimodal character. The velocity inverse correction eliminates or reduces this bimodal character; however, a tendency to overweight near the zero velocity occurs in a few cases in Fig. 2. The fact that the biased probabilities were not zero at U = 0 results from both the finite size of the histogram bins used to formulate the PDF and the fact that the y and z component velocity magnitudes were not on average zero when the U velocity was zero.

The biased, simple two-dimensional corrected, and estimated z term corrected U velocity component PDFs are compared in Fig. 4 at two of the measurement locations shown in Fig. 2. The estimated z term has a noticeable effect near U = 0 only and appears effective in eliminating the overweighting seen in the simple two-dimensional inverse corrected results.

The probability density contours of Figs. 5 and 6, which are the results for the data at y^*/θ = -6.56 and -10.65, respectively, in Fig. 2, provide a more detailed view of the effect of the bias. These two-dimensional PDFs were formulated and normalized following the procedures outlined for the one-dimensional PDFs above. The probability density increment between contour levels was constant and the same probability density levels were contoured at a given y^*/θ. The contours increase monotonically fromt the outermost curve, which is at the lowest probability density level, to the innermost curves at higher levels. The uncorrected biased contours in Fig. 5A follow the circles centered at the origin of the velocity plane closely indicating the expected dependence on the velocity magnitude and a nearly constant z component effect at small (x,y) plane velocities. The decrease in the probability density near the zero velocity is apparent in Fig. 6A also. The corrected results in Figs. 5B and 6B do not show such bias effects but these contours indicate overweighting near U = 0 as seen in the one-dimensional PDFs of Fig. 2 at these y^*/θ locations. The addition of the estimated z term to the weight reduces the gradient near the origin and no overweighting is apparent in Figs. 5C and 6C.

Another way of examining the bias that avoids the complications of contouring but uses all of the velocity magnitude information is to formulate PDFs of the measured two-dimensional velocity magnitude, V_{2D}. This is shown in Fig. 7 for the data at y^*/θ = -6.56 and -10.65. Each of the histogram bins used to formulate these PDFs had a constant width, ΔV_{2D} = 10 m/s. The histogram bin accumulators contain the sum of the weights for all of the data between concentric circles centered at the origin in the velocity plane with a difference in radii of ΔV_{2D} and an outer radius at the upper velocity limit of the histogram bin. PDF normalization requires division by the product of the sum of all the weights in the sample with the area of the current bin between the concentric circles in the velocity plane. The midpoints of each histogram bin in Fig. 7 are connected by straight line segments.

The biased data, the simple two-dimensional corrected result, and the estimated z term correction are compared in Fig. 7. The addition of the z term significantly reduces the maximum weight where the simple two-dimensional correction overweights appreciably, near the zero velocity magnitude. The expected form of the unbiased velocity magnitude PDF is not known but a smooth curve with a probability density near zero that is approximately equal to that found in equal distance on the opposite side of the maximum probability density location is expected. The exception to this would be the case where the most probable magnitude is zero. No appreciable

offsetting compensation for the velocity bias due to improvement of signal quality at lower velocity magnitudes, as discussed by Durao and Whitelaw [17], is indicated by the results shown in Fig. 7. If such an effect were significant, an increase in the biased PDFs with decreasing velocity magnitude comparable to that for the z term corrected results would be required.

The measured U and V velocity components appear to provide sufficient information to both observe the bias and correct for it reasonably well in the present study. However, this two-dimensional information may not be sufficient in a highly three-dimensional flow where no single velocity component dominates or in a situation where the dominant component is not measured or only partially measured. In such cases, an accurate z term estimate would be unlikely, the data will not show the bias as distinctly, if at all, and the correction will not work as desired. The bias is still entirely present in these situations but the data does not contain sufficiently complete velocity magnitude information to observe or correct for it. For an example of such a situation, consider a study of secondary flows in a corner, say the juncture of a wing with a fuselage, and the large chordwise velocity component is not measured.

Coincident two channel LDV systems are subject to a sampling bias due to time window constraints for coincidence. A validated signal must be received from both channels within an adjustable time window to be considered coincident. Differences in light scattering due to wavelength or polarization, differences in measurement volume size and fringe spacing between channels, or slight optical misalignment are a few of the possible factors that may lead to a spatial separation of where a Doppler burst is initiated in one channel with respect to the other channel. This corresponds to a temporal separation that is inversely proportional to the velocity. As a result, low velocity particles are less likely to satisfy the coincidence requirement than the high velocity ones. Time window biasing was noticeable for time windows less than 2.5 microseconds only and was not a factor in the present work [4].

Erdmann and Tropea [18,19] have statistically modeled the LDV sampling process for a normal distribution turbulent flow. The analysis predicts a shift from fully velocity biased to bias free results as the sampling process changes from free running processor to processor controlled. A free running processor is one that is able to process and transfer the data from every particle that generates a validated signal. In this case, the flow determines when particles are sampled. If the processor sampling rate is much less than the validated particle data rate, the processor samples at its constant maximum rate since a validated particle occurs almost immediately after the processor status is ready for more data. In this case, the results are predicted to be unbiased and the processor controls the sampling process.

The reduction of the bias between free running and processor controlled sampling has been observed experimentally [14,20,21] and it appears that if the sampling rate is 50 to 100 times less than the validated particle data rate, the data is unbiased. Conversely, the mean validated particle data rate must be significantly smaller than the processor sampling rate for the data to be completely biased. The processor sampiing rate exceeded the mean validated data rate by a factor of 30 or more in the current study and free running processor conditions were felt to have been closely approximated.

The analysis of Erdmann and Tropea [18,19] also predicts that in the limit as the turbulent intensity goes to zero the velocity bias of the mean is equal to the turbulence intensity squared, or:

$$\frac{\overline{U}_{BIASED} - \overline{U}_{TRUE}}{\overline{U}_{TRUE}} = \left(\frac{\sigma_u}{|V|}\right)^2 \qquad (3)$$

where σ_u is the U component standard deviation and $|V|$ is the local velocity magnitude. The negative of Equation (3) is shown in Fig. 8 with the U velocity mixing layer and recirculating flow data. The simple two-dimensional velocity inverse corrected results were taken as the true results for the comparison with theory. The statistical prediction and the corrected results are consistent. The low speed data of Johnson, et al., [14] is similar. The turbulence intensity based on the local mean velocity magnitude was 30% to 35% at $y^* = 0$, the middle of the mixing layer, so that the effect of the bias on the mean streamwise velocity was substantial for much of the flow. This local turbulent intensity increases from the high to the low velocity side of the mixing layer with the largest values occurring where the local mean velocity is near zero.

The effect of the bias on the standard deviations of the U and V velocity components is shown in Figs. 9 and 10. The trend is similar and non-monotonic in both cases. Generally, the effect of the velocity bias on these turbulence intensities is not large, less than 20% for most of the flow, and the effect on the V component was smaller than the U component by as much as a factor of two in parts of the flow. Figure 11 compares the corrected and biased Reynolds shear stress term, $\langle u'v' \rangle$. The effect of the bias on the shear term is approximately double that for the U velocity standard deviation and is not negligible in most of the flowfield.

Figure 2 provides some insight into the behavior of the bias observed in Figs. 9 and 10. At the freestream edge of the mixing layer, the U velocity PDF develops a long flat tail on the low speed side of the mean. These large negative fluctuations reduce the velocity magnitude and are therefore given larger velocity inverse weights than the rest of the data in the sample. This results in the initial increase in the U component standard deviation. The higher probability densities given these weighted large negative

fluctuations can be seen in Fig. 2. The V component follows this trend since it is the U velocity that determines the extent of the bias in most of the flow. The U and V fluctuations are not perfectly correlated so that the increase in the corrected V component intensity in Fig. 10 is smaller than that of the U component. The larger difference observed between the biased and corrected <u'v'> term indicates it is these largest fluctuations which contribute the most to the Reynolds shear stress. As the mean velocity magnitude decreases in a traverse across the mixing layer, the more heavily weighted near zero velocities occur with greater frequency and are closer to the decreasing mean. At the highest local turbulence intensities in Figs. 9 and 10, the mean velocity is near zero and the bias correction weights the data near the mean the most heavily. This leads to the decrease of the corrected standard deviations to values less than the biased result.

The combined effect of the bias correction of the mean velocity and standard deviation on the turbulence intensity based on the local mean velocity is shown in Fig. 12. The fractional difference between the corrected and biased intensities asymptotically approaches 30% and is larger than 10% in most of the flowfield.

3. FRINGE BIAS

Fringe biasing occurs because LDV signal processors require some minimum number of fringe crossings, N_F, for a validated Doppler burst. As a result, the effective cross sectional area of the measurement volume normal to the instantaneous velocity vector, A_e, is less than the total area, A, in Equation (1) and is a function of the vector direction and magnitude when frequency shifting is used. The following discussion is restricted to two-dimensional flow and neglects the z velocity component.

FRINGE BIAS ANALYSIS

The analysis of Buchave [8,9] for fringe bias is extended to consider frequency shifting under the assumptions of two-dimensional flow and small laser beam intersection angles. From Buchave [8,9] the effective to total measurement volume area ratio with no frequency shifting is:

$$(4) \qquad A_e/A = 1 - Q^2(1 + \tan^2\phi) = P$$

where Q is the ratio of the required number of fringe crossings to the maximum possible fringes, N_F/N_T, and ϕ is the angle between the velocity vector and the normal to the fringes in the direction defined as positive velocity. This area ratio is equal to the probability that a particle entering the measurement volume will cross N_F fringes.

This result must be modified to include frequency shifting to be of use in the present work. Consider a particle that crosses N unshifted fringes and has a velocity magnitude V_T. The Doppler burst time is:

$$(5) \qquad t_b = N\, d_f/V_T\, |\cos\phi|$$

where d_f is the fringe spacing. With frequency shifting, N_s fringes will sweep past any point in the measurement volume in time t_b such that:

$$(6) \qquad N_s = t_b|V_F|/d_f.$$

V_F is the velocity of the moving fringes and is positive or negative in accordance with the coordinate system defined for the velocities measured by the LDV and the direction of fringe motion. The fringe velocities for the coordinate system shown in Fig. 13 are both negative. ϕ is also indicated for both channels 0 and 1 for vector U in Fig. 13. Substituting for t_b from Equation (5) produces:

$$(7) \qquad N_s = N|V_F|/V_T|\cos\phi|.$$

The number of fringes crossed with frequency shifting is:

$$N_{fs} = N + N_s$$

Therefore, the ratio of the shifted to unshifted fringe crossings is:

$$(8) \qquad N_{fs}/N = 1/(1 - V_F/(V_T \cos\phi))$$

where the sign of V_T and $\cos\phi$ determine whether the number of fringes crossed is increased or decreased by frequency shifting.

The unshifted fringe crossing ratio, Q, in Equation (4) can be modified to account for the effects of frequency shifting. The requirement that N_F fringes can be met with frequency shifting when N_{fs} in Equation (8) is equal to N_F. The number of unshifted fringes, N, that would be crossed in this case is:

$$N = N_F/(1 - V_F/V_T \cos\phi)$$

and Equation (4) may be written as:

$$(9) \quad P = 1 - Q^2(1 + \tan^2\phi)/(1 - V_F/(V_T \cos\phi))^2.$$

This can be expressed as:

$$(10) \qquad P = 1 - Q^2/(\cos\phi - V_F/V_T)^2.$$

This result is equivalent to that by McDougall [22], when expressed in terms of the same area ratio, which is an extension of the analysis of fringe bias by Dimotakis [10] to the frequency shifted case. The approach taken by Buchave [8,9] differs from that of Dimotakis [10] but the results are equivalent.

The particles move with the fringe velocity when $\cos \phi = V_F/V_T$ and no fringes are crossed. The probability given by Equation (10) is zero or less when:

$$|\cos \phi - V_F/V_T| < Q. \tag{11}$$

Equation (11) defines a dead zone of conditions for which less than N_F fringes are crossed and the probability is taken as 0. These dead zones are shown for two orthoganal LDV channels in Fig. 14 for Q = 8/22 using the coordinate system in Fig. 13. In a coincident two channel LDV system, what is dead to one channel is dead to the system.

The probability that a particle will cross the required number of fringes in both coincident channels is:

$$P_{01} = \left[1 - \frac{Q_0^2}{(\cos \phi_0 - V_{F0}/V_T)^2}\right] \times \left[1 - \frac{Q_1^2}{(\cos \phi_1 - V_{F1}/V_T)^2}\right]. \tag{12}$$

Contours of this coincident probability are indicated in Fig. 14. Figure 15 shows P_{01} versus the instantaneous velocity angle with respect to the positive channel one direction, ϕ_1, for various ratios of the fringe velocity magnitude to the instantaneous velocity magnitude. The often cited rule of thumb that fringe bias is not significant for $|V_F|/V_T > 2$ is seen to be valid for the value of Q used in this figure, 8/22. However, the probability, P_{01}, changes by more than a factor of two with changing ϕ_1 for Q = 16/22 at this velocity ratio. The advantage of orienting the fringes such that ϕ_1 is 45° with respect to the mean velocity for the shift directions in Fig. 13 is apparent in Fig. 15.

FRINGE BIAS DISCUSSION

The use of Equations (10) and (12) is limited by a number of factors. First an accurate value of Q is required. The value Q = 8/22 used in Figs. 14 and 15 is the calculated result for an optical configuration used in the current study to the nominal e^{-2} intensity level. However, the effective value of Q will depend on particle size, gain levels, and thresholds and may vary for each burst with particle size if the particle size distribution is polydisperse. As a result it would be possible to get signals that are theoretically in the dead zone from particles larger than those for which the assumed value of Q is accurate. This did occur for badly fringe biased data in the present study. Also, the analysis is for the full ellipsoidal measurement volume but in many cases forward scatter collection optics view only a part of the measurement volume. These difficulties make the use of P_{01} as a corrective weighting factor, see Dimotakis [10], somewhat ambiguous. Nevertheless, this analysis can be used to avoid taking biased data or determining if data already taken is subject to significant fringe bias.

Methods of determining whether a significant fringe bias exists in the data require finding P_{01} for each data point. This only requires determining the angle of the velocity vector in addition to the velocity magnitude, which is needed for velocity bias correction, see Equation (12). Monitoring of the mean P_{01}, its standard deviation, and the minimum P_{01} of population samples would provide the experimentalist with information to judge whether or not data is fringe biased. Low minimum values of P_{01} indicate a likelihood that data are missed due to vectors occurring in the dead zone. A large variation of P_{01} within a sample population would indicate fringe bias is significant enough to change the measured velocity field statistics from the true values. As an example, fringe biased data taken in the mixing layer reattachment region had a mean $P_{01} = 0.87$, a standard deviation $\sigma_{01} = 0.18$, and a minimum $P_{01} = 0.0$. Data taken with a fringe velocity a factor of 2.35 larger had corresponding values of 0.98, 0.02, and 0.83 for the mean, standard deviation, and minimum P_{01}, respectively.

The probability inverse, $1/P_{01}$, can be used as a bias correcting weighting function to formulate fringe bias corrected statistics for comparison to uncorrected velocity field statistics [10]. Any substantial difference would indicate a significant fringe bias effect. The possibility of $P_{01} = 0$ requires setting a maximum allowable weight.

The above procedures were used in the missile base flow studies and as a result of this effort an optical configuration with a longer focal length lens and therefore a greater fringe spacing and fringe velocity was used in the reattachment region of the flowfield in Fig. 1 than used in the mixing layer. The use of optics that produce needlessly large fringe spacings and probe volume diameters to avoid fringe bias problems results in poorer spatial resolution and lower signal strength than necessary. Knowledge of the potential fringe bias through the above analysis can help select an optimal set of options for the problem under study.

4. CONCLUSIONS

Comparisons between velocity biased and biased corrected statistics were presented and discussed. The effect of velocity bias on the velocity probability density function can be substantial and velocity bias corrections worked reasonably well in compensating for the effects of the bias. The velocity bias changed the mean velocity and Reynolds shear stress appreciably in most cases but the effect on the root mean square velocity fluctuation level was not as substantial. The two-dimensional inverse correction for velocity bias was improved by the addition of an estimated z velocity component term. Fringe bias effects were analyzed for two channel frequency

shifted LDV systems and procedures for using this analysis and its limitations were discussed.

5. ACKNOWLEDGMENT

This research was supported by the U.S. Army Research Office under contracts DAAG 29-79-C-0184 and DAAG 29-83-K-0043. Dr. Robert E. Singleton served as the Contract Monitor.

6. REFERENCES

1. Addy, A. L., Amatucci, V. A., Kuntz, D. W., Petrie, H. L., and Samimy, M., "Base Flow and Related Model Experiments," Proceedings: Symposium on Rocket/Plume Fluid Dynamic Interactions, Vol. III, Bertin, J., Editor, University of Texas at Austin, Report 83-104, April 1983.

2. Petrie, H. L., Samimy, M., Addy, A. L., "A Study of Compressible Turbulent Free Shear Layers Using Laser Doppler Velocimetry," AIAA Paper No. 85-177, presented at AIAA 23rd Aerospace Sciences Meeting, Reno, Nevada, January 14-17, 1985.

3. Samimy, M., Petrie, H. L., and Addy, A. L., "An Experimental Study of Compressible Reattaching Free Shear Layers," AIAA Paper No. 85-1646, presented at AIAA 18th Fluid Dynamics, Plasma Dynamics, and Lasers Conference, Cincinnati, Ohio, July 15-17, 1985.

4. Petrie, H. L., "A Study of Compressible Turbulent Free Shear Layers Using Laser Doppler Velocimetry," Ph.D. Thesis, University of Illinois at Urbana-Champaign, Department of Mechanical and Industrial Engineering, April 1984.

5. Samimy, M., "An Experimental Study of Compressible Reattaching Turbulent Free Shear Layers," Ph.D. Thesis, University of Illinois at Urbana-Champaign, Department of Mechanical and Industrial Engineering, August 1984.

6. Whiffen, M. C., "Polar Response of an LV Measurement Volume," Proceedings of the Minnesota Symposium on Laser Velocimetry, University of Minnesota, 1975, pp. 589-590.

7. Whiffen, M. C., Lau, J. C., and Smith, M. D., "Design of LV Experiments for Turbulence Measurements," Rev. Sci. Instr., Vol. 48, No. 7, 1977, pp. 197-207.

8. Buchave, P., "Biasing Errors in Individual Particle Measurements with a LDA-Counter Signal Processor," The Accuracy of Flow Measurements by Laser Doppler Methods, Proceedings of the LDA Symposium, Copenhagen, Denmark, Hemisphere Publishing Co., New York, 1976, pp. 258-278.

9. Buchave, P., George, W. K., and Lumley, J. L., "The Measurement of Turbulence with the Laser-Doppler Anemometer," Annual Review of Fluid Mechanics, Vol. 11, Annual Reviews, Inc., Palo Alto, CA, 1979, pp. 443-503.

10. Dimotakis, P. E., "Single Scattering Particle Laser Doppler Measurements of Turbulence," AGARD CP-193, Applications of Non-Intrusive Instrumentation in Fluid Flow Measurements, 1976.

11. McLaughlin, D. K. and Tiedermann, W. G., Jr., "Biasing Correction for Individual Realization of Laser Anemometer Measurements in Turbulent Flow," The Physics of Fluids, Vol. 16, No. 12, 1973, pp. 2082-2088.

12. Buchave, P., "The Measurement of Turbulence with Burst Type Laser Doppler Anemometer-Errors and Correction Methods," Report TRL-196, State University of New York at Buffalo, 1979.

13. Hoesel, W. and Rodi, W., "New Biasing Elimination Method for Laser Doppler Velocimetry Counter Processing," Rev. Sci. Instr., Vol. 48, No. 7, pp. 910-919.

14. Johnson, D. A., Moddarress, D., and Owen, F., "An Experimental Verification of Laser Velocimeter Sampling Bias and Its Correction," Engineering Applications of Laser Velocimetry, ASME, New York, 1982, pp. 153-162.

15. Nakayama, A., "Measurements of Separating Boundary Layer and Wake of an Airfoil Using Laser Doppler Velocimetry," AIAA Paper No. 85-0181, presented at AIAA 23rd Aerospace Sciences Meeting, Reno, Nevada, January 14-17, 1985.

16. TSI, Inc., Laser Doppler Velocimeter Systems, Technical Data Section, 1980.

17. Durao, D. F. G. and Whitelaw, J. H., "Relationship Between Velocity and Signal Quality in Laser Doppler Anemometry," Journal of Physics, E: Scientific Instruments, Vol. 12, No. 1, 1979, pp. 47-50.

18. Erdmann, J. C. and Tropea, C., "Turbulence Induced Statistical Bias in Laser Anemometry," Proceedings of the Seventh Symposium on Turbulence, University of Missouri-Rolla, September 1981, pp. 129-138.

19. Erdmann, J. C. and Tropea, C., "Statistical Bias of the Velocity Distribution Function in Laser Anemometry," International Symposium on Application of Laser Anemometry to Fluid Mechanics, Lisbon, Portugal, July 1982, Paper 16.2.

20. Craig, R. R., Nejad, A. S., Hahn, E. Y., and Schwartzkopf, K. G., "A General Approach for Obtaining Unbiased LDV Data in Highly Turbulent Non-Reacting and Reacting Flows," AIAA Paper No. 84-0366, presented at AIAA 2nd Aerospace Science Meeting, Reno, Nevada, January 1984.

21. Stevenson, W. H., Thompson, H. D., and Roesler, T. C., "Direct Measurement of Laser Velocimeter Bias Errors in a Turbulent Flow," AIAA Journal, Vol. 20, No. 12, 1982, pp. 1720-1723.

7. FIGURES

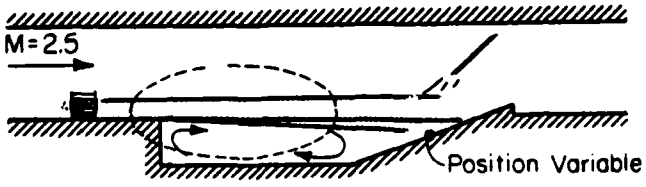

Fig. 1 Configuration of the model experiment.

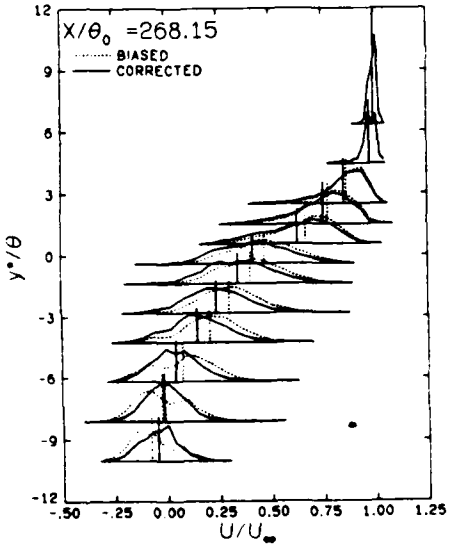

Fig. 2 Biased and corrected U velocity probability distributions across the mixing layer at x = 75 mm.

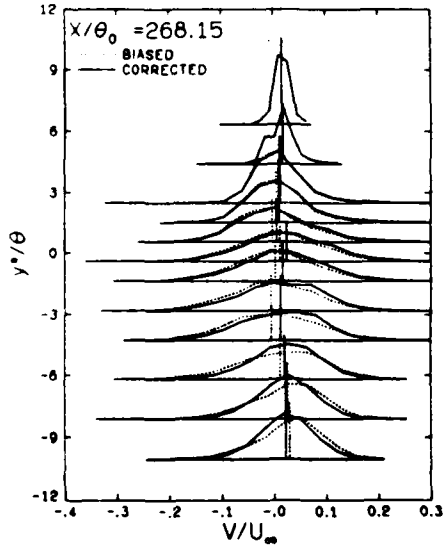

Fig. 3 V velocity probability distributions across the mixing layer at x = 75 mm.

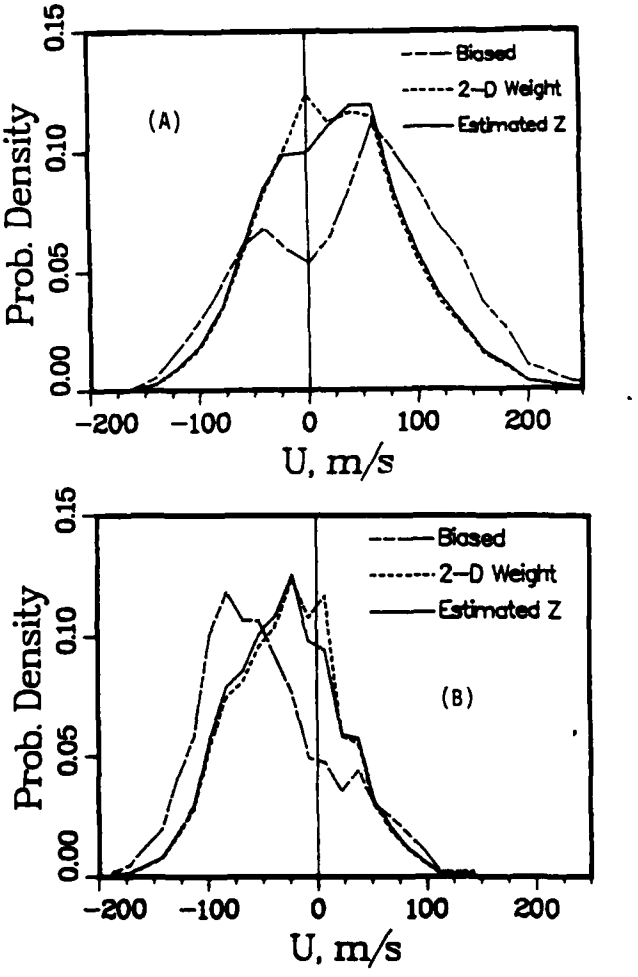

Fig. 4 Comparison of weighting function effects on 1-D PDFs at (A) y*/θ = -6.56 and (B) y*/θ = -10.65, x = 75 mm.

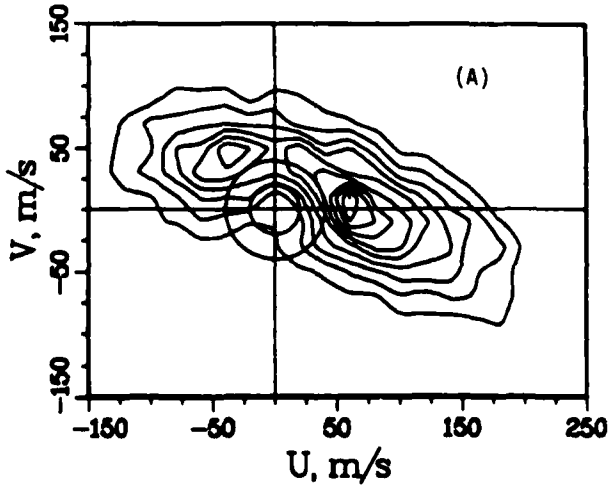

Fig. 5 continued

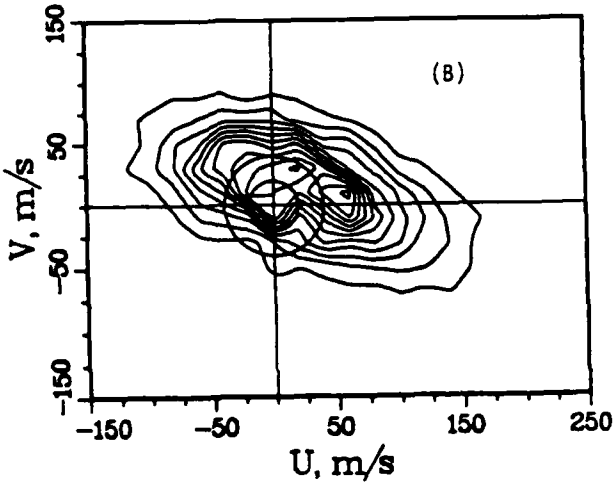

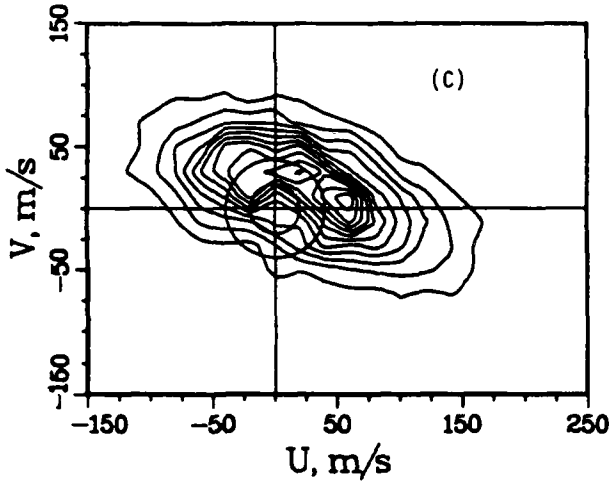

Fig. 5 Probability density contours with constant increments between contour levels; (A) biased, (B) 2-D corrected, (C) estimated z term, x = 75 mm, y*/θ = -6.56.

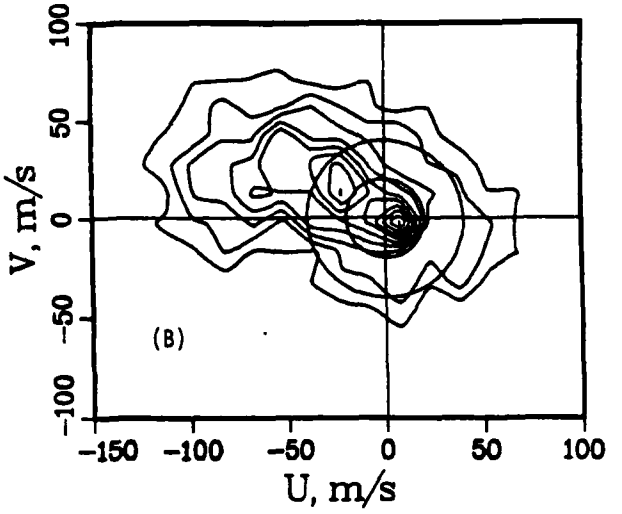

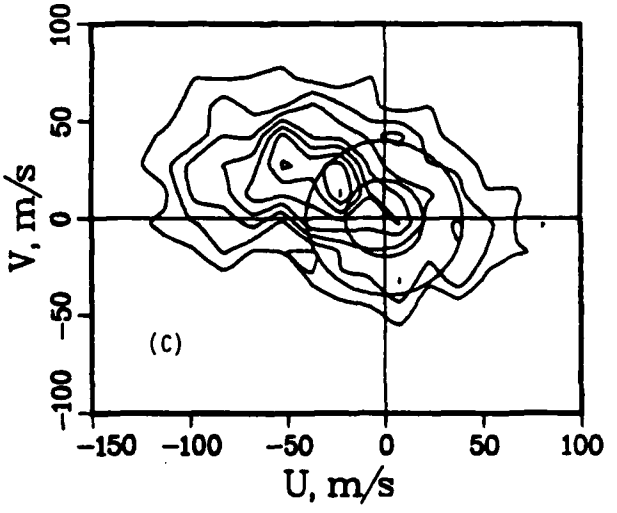

Fig. 6 Probability density contours with constant increments between contour levels; (A) Biased, (B) 2-D corrected, (C) estimated z term, x = 75 mm, y*/θ = -10.65.

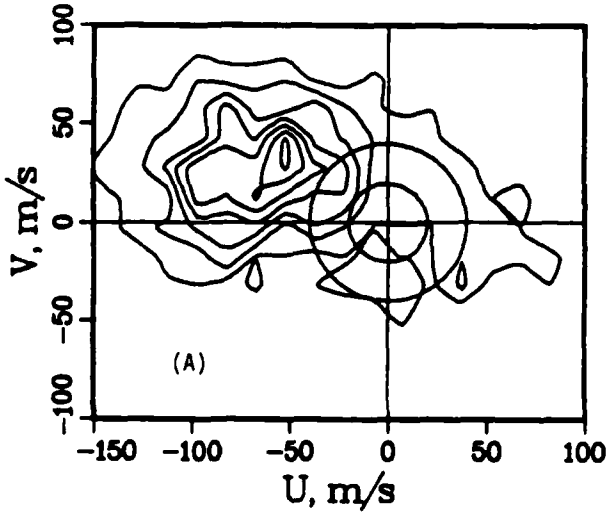

Fig. 6 continued

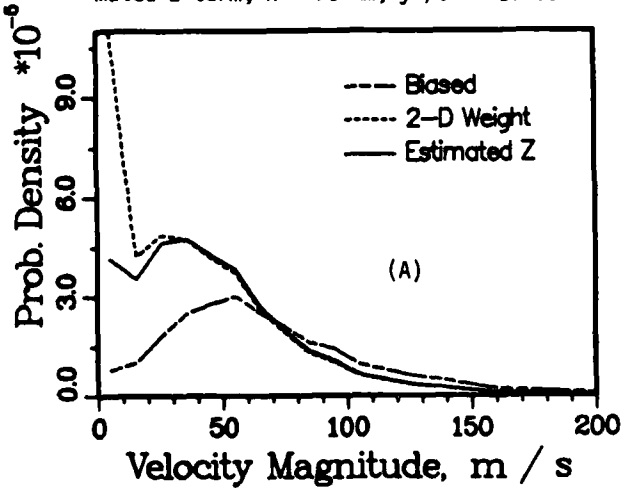

Fig. 7 continued

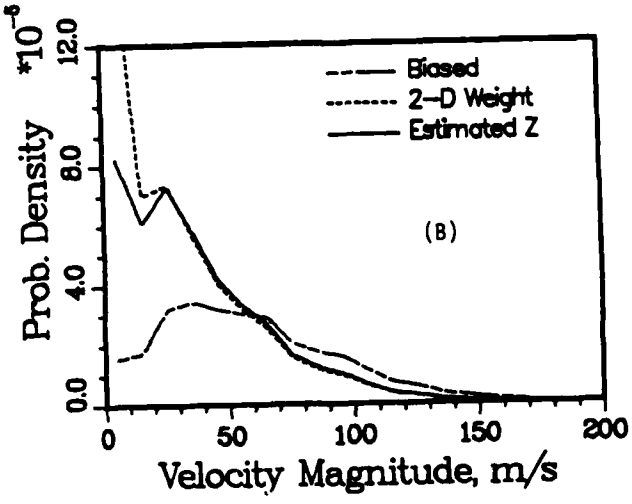

Fig. 7 2-D velocity magnitude probability density functions at x = 75 mm and (A) y*/θ = -6.56 and (B) y*/θ = -10.65.

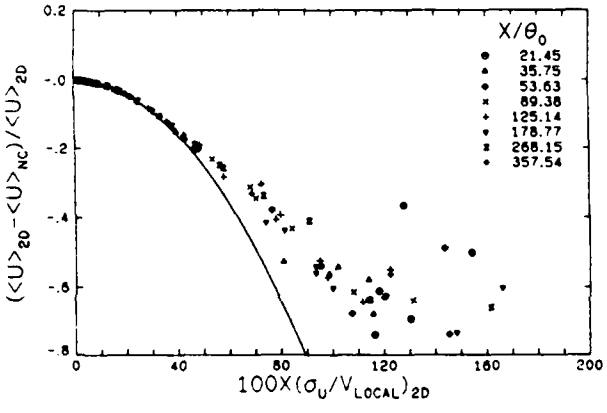

Fig. 8 Velocity bias in the mean U component versus the local turbulence intensity.

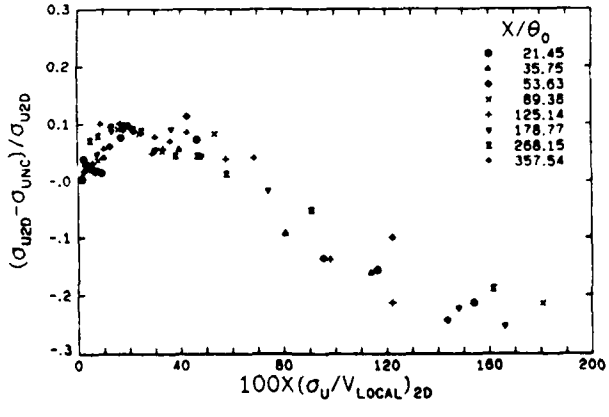

Fig. 9 Velocity bias of the standard deviation of the U component velocity fluctuations.

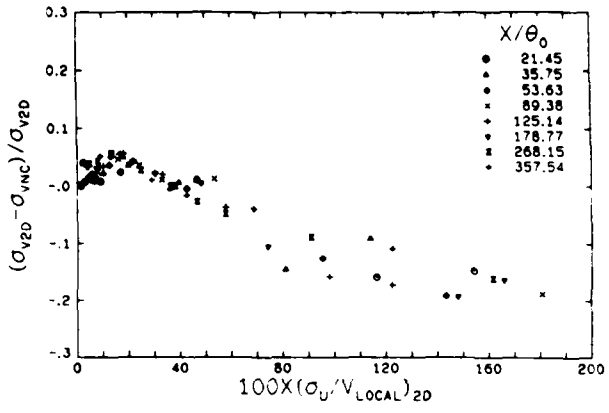

Fig. 10 Velocity bias of the standard deviation of the V component velocity fluctuations.

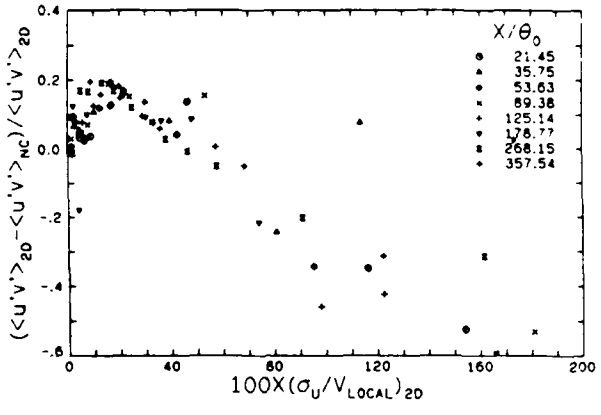

Fig. 11 Velocity bias of the Reynolds stress term.

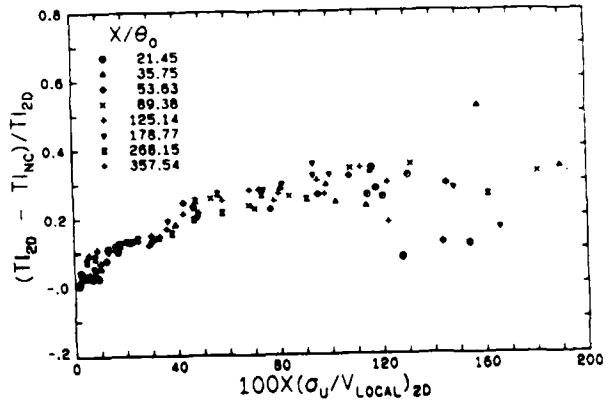

Fig. 12 Velocity bias of the local U component turbulence intensity.

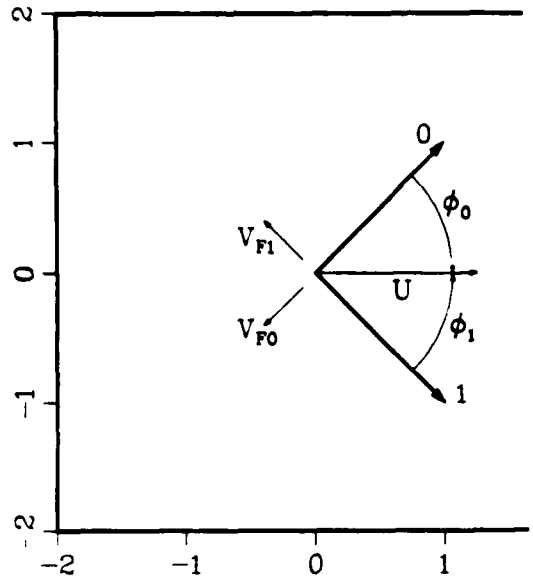

Fig. 13 Coordinate system used in fringe bias analyses.

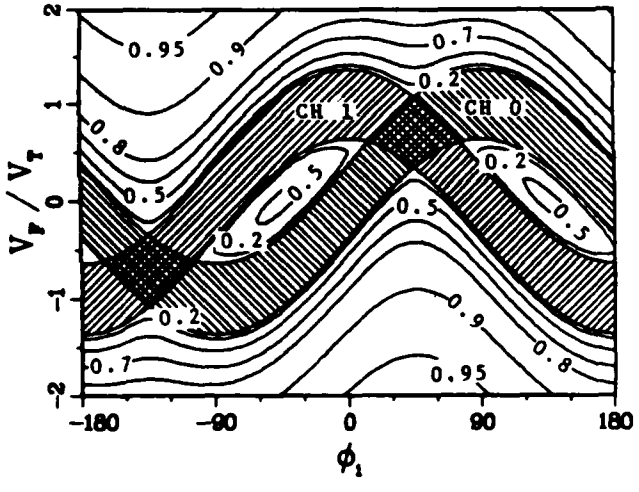

Fig. 14 Fringe biasing dead zones with contours of coincident probability, P_{01}, Q = 8/22.

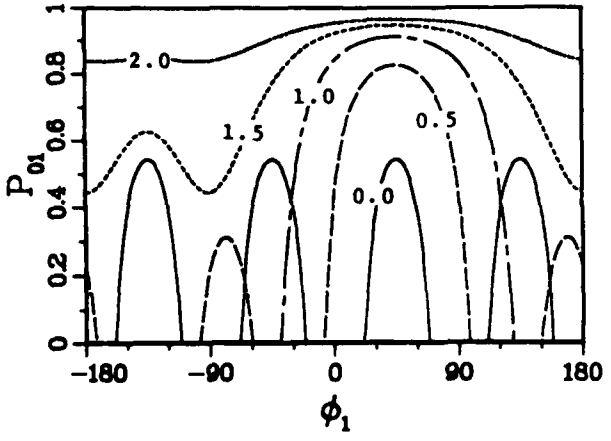

Fig. 15 Coincident probabilities for values of $|V_F|/V_T$ from 0 to 2, Q = 8/22.

SECTION B.3

EXPERIMENTAL STUDY OF SUPERSONIC FLOW OVER A BACKWARD-FACING STEP MODEL

Paper presented at the Symposium on Fluid Dynamics

University of Illinois at Urbana-Champaign

Urbana, Illinois

April 26-27, 1984

by

M. Samimy and A. L. Addy

EXPERIMENTAL STUDY OF SUPERSONIC FLOW OVER BACKWARD-FACING STEP MODEL

M. Samimy† and A. L. Addy††
Department of Mechanical and Industrial Engineering
University of Illinois at Urbana-Champaign
1206 West Green Street
Urbana, IL 61801

An experimental study was conducted in which a Mach 2.07 flow with a turbulent boundary layer thickness of 2.26 mm and a Reynolds number based on boundary layer momentum thickness of 12080 was separated at a 25.4 mm high step. The separated boundary layer formed a shear layer which was reattached to a wall parallel to the incoming flow direction. A detailed survey of the flowfield was made utilizing a two-component laser Doppler velocimeter, LDV, static pressure probes and a schlieren system. Turbulence properties of the flowfield were extracted from measured instantaneous velocities and compared to those of similar incompressible flows. In the free shear layer, the base region, and the recompression region, the turbulent kinetic energy, shear stress, and the turbulent third products showed good similarity between compressible and incompressible flows. The turbulence production level was much higher and the turbulent triple products were amplified much stronger in the reattachment region for compressible flow. In the redeveloping region where the changes in mean flow and turbulence properties are much faster in supersonic flows, there was not much similarity between supersonic and subsonic flows.

† Graduate Research Assistant.
†† Professor and Acting Head.

NOMENCLATURE

A_E = effective area of measuring volume

A_M = measuring volume area to e^{-2} intensity level

f = frequency

h = step height

k = turbulence kinetic energy, $(3/4)((u')^2 + (v')^2)$

L = mixing length scale

M = Mach number

N_F = number of fringes required to be crossed

N_T = total number of fringes in a measuring volume

p = pressure

P = probability of particle detection

Pr = start point of pressure rise and turbulence production

Q = N_F/N_T

r = reattachment

u = streamwise mean velocity

u_c = convection velocity of eddies

U = instantaneous velocity

u^* = Van Driest generalized velocity

u_τ = friction velocity

v = transverse mean velocity

V_T = total mean velocity

V_F = fringe velocity

w = $1 - \cos(\pi y/\delta)$, Coles wake function

x = distance from step along the model surface

y = height

δ = boundary layer thickness

ϕ = angle between instantaneous velocity and the normal vector to the fringes

λ = wavelength

ρ = density

σ = standard deviation

τ_B = transit time of particle

$\langle\ \rangle$ = ensemble average

Subscripts

0	channel 0 or value of the step
1	channel 1
∞	incoming freestream value
L	local
p	particle
pr	start point of pressure rise
r	reattachment
u	streamwise
v	transverse
w	wall

Superscripts

$(\bar{})$	mean value
$( )'$	fluctuation

INTRODUCTION

After years of intensive research, the mechanisms governing the highly turbulent separated flow region at the base of a blunt body are not yet well understood. Since the early 1950's, the analysis of supersonic base flows has been carried out along two paths, namely the Chapman-Korst component model [1-3] and the integral methods [4,5]. The objectives of these analyses were to develop an understanding of the physics of the flowfield at the base region of a blunt body and to formulate a flow model for predicting the base region pressure, temperature, and heat transfer characteristics.

The flow characteristics are very different in the expansion, mixing, recirculation, reattachment, and redevelopment regions and are changing drastically through each region; therefore, each region has to be modeled and analyzed separately. The reattachment and redevelopment components are almost always accompanied by a large adverse pressure gradient, streamline curvature, and flow direction change and are characterized by high turbulence intensities and production [6,7]. Yet, the reattachment and redevelopment processes have received the least attention, most likely due to the fact that it is difficult to obtain reliable data in this region. As a result, progress has been very slow in analytical and computational modeling.

The overall objectives of this study were to learn more about the physics of the reattachment and redevelopment processes and to obtain some reliable data for computational modeling purposes. Three sets of experiments were conducted: a Mach 2.46 flow was separated at a step with no change in flow direction and was attached downstream onto a 19.4° ramp, a Mach 2.07 flow was separated at a step and was impinged on another free shear layer, and a Mach 2.07 flow was separated at a step and was reattached to a plane parallel to the incoming flow direction. In the first experiment, the effect of expansion at the step was eliminated and the reattachment and redevelopment of a long constant pressure free shear layer with a well defined initial condition was studied. In the second experiment, the wall was removed by impinging one shear layer on another. An attempt was made to match the approach freestream Mach and Reynolds numbers to the reattachment in all three experiments. This paper concerns the results of the last experiment, considered to be the traditional backstep base flow problem. The results for the two other experiments are currently under analysis and will be presented in the literature upon completion.

EXPERIMENTAL APPARATUS

Experimental Configurations

The test section of the wind tunnel is shown in Fig. 1. The wind tunnel width was 50.8 mm and the step height was 25.4 mm. The approach Mach number, the stagnation pressure, and temperature were 2.07 ±1.1 percent, 528.1 kN/m^2 ±1.3 percent, and 293° K ±1 percent, respectively. The approach boundary layer and momentum thickness, and Reynolds number were 2.26 mm, 0.18 mm, and $6.67 \times 10^7/m$, respectively.

Velocity measurements were carried out at 15 axial locations. These locations are shown in Fig. 1 as stations 1 through 15. All the velocity

measurements were made in a vertical plane passing through the centerline of the model. Also, measurements were made in a vertical plane 8 mm off the centerline of the model at stations 9 and 10 to check the two-dimensionality of the flowfield near reattachment.

Pressure Surveys

The test model was instrumented with 0.5 mm diameter static pressure orifices on the centerline at the model floor spaced every 6.35 mm. Also, in three locations in the reattachment region, spanwise static pressure orifices were mounted and spaced every 9.5 mm to check the two-dimensionality of the flowfield.

LASER DOPPLER VELOCIMETRY CONSIDERATIONS

A two-color, two-component laser Doppler velocimeter, LDV, was utilized to make velocity measurements (see Fig. 2). A 600 mm focal length lens was used to focus two pairs of incoming beams with 22 mm beam spacings to form two sets of orthogonal fringes. Th fringe planes were ±45° to the wind tunnel axis. The measuring volume diameter and length were approximately 0.3 mm and 16.5 mm, respectively. The scattered light was collected 10° off-axis forward scatter which reduced the measuring volume length to approximately 4.4 mm. The fringe spacing was 13.56 μm for the blue beam (λ = 488 nm) and 14.30 μm for green beam (λ = 514.5 nm) which gave, respectively, 542.4 m/s and 572 m/s fringe velocities with 40 MHz frequency shifting. The time window for simultaneous measurements was varied from 1 μs in the freestream to 5 μs in regions where the velocity histogram included zero velocities.

Seed Particles

The LDV measures the velocity of light scattering particles embedded in the flow. This is not necessarily the velocity of flow. Thus, the ability of particles to respond to the fluctuations and mean flow gradients is of primary concern. Particle generation, insertion, size distribution, and response to flow fluctuations and gradients have received considerable attention [8-13].

In a moving particle frame of reference, the response of 1 micron particles for flow fluctuations is ranging from 20 to 40 kHz in different theoretical [11] and experimental [8,12] results. Turbulence is known in a fixed frame of reference and the relation between turbulence frequencies in a fixed frame of reference and moving particle frame of reference is a subject of controversy. Assuming that the turbulence frequency relative to moving particles is approximately the same as would be observed in a frame of reference moving at the local mean velocity, then the turbulence frequency in two cases is related by

$$f/f_p = | u_c/(u_c - u)| \qquad (1)$$

where f is turbulence frequency in a fixed frame, f_p is the frequency that seed particles are subject to, and u_c is the convective velocity of eddies.

In a compressible turbulent boundary layer [14], f/f_p is found to be 4 or greater. In a compressible turbulent shear layer, Ikawa [15] showed

that $u_c \approx u$, 0.8u, and 1.5u in the middle, upper, and lower part of the shear layer, respectively, therefore, $f/f_p > 3$.

For this investigation, particle generation was accomplished with an atomizer documented to produce particles with a mean diameter of approximately 0.8 μm if a light oil is atomized. A low viscosity silicon oil was atomized and the diameter of generated particles was estimated by measuring the relaxation of particle velocity downstream of an oblique shock wave [16,17]. The results indicated that the mean particle diameter was approximately 1 μm. Assuming that $f/f_p > 3$ holds in the recompression, reattachment, and redeveloping regions, then the response of these 1 μm particles should be adequate to follow the turbulent fluctuations in the range of energy containing eddies in most parts of the flowfield, except for the first part of the free shear layer with very high frequencies.

Velocity Bias

The individual velocity realization type data processor was used in these experiments. Since the probability of each measurement depends on the local flow velocity and its direction, assuming a uniform seeding, it is recognized that a simple averaging of the results will be biased [18,19]. The correction schemes for this bias include a weighting factor of $|1/V_T|$ or τ_B for each realization, where V_T is the total velocity and τ_B is the transit time of the particle. In these experiments $|1/V_T|$ was used as a weighting factor to correct velocity bias.

Fringe Bias

In a highly turbulent flowfield, fringe biasing occurs because the LDV signal processor requires a minimum number of fringes, N_F, to be crossed before a signal is accepted. Therefore, the effective measuring volume area normal to the velocity vector, A_E, is less than the total measuring volume area, A_M. The ratio of these areas for an ellipsoidal measuring volume is given by Buchhave [20] as

$$P = \frac{A_E}{A_M} = (1 - Q^2)(1 + \tan^2\phi) \qquad (2)$$

where ϕ is the angle between the instantaneous velocity vector and the normal vector to the fringe plane and $Q = N_F/N_T$ where N_T is the total number of fringes. In fact, this area ratio is the probability of particle detection with which each realization has to be weighted before the ensemble averaging process.

For the case of frequency shifting, Eq. (1) becomes [17]:

$$P = \frac{A_E}{A_M} = 1 - [Q^2/(1 - V_F/(|U|\cos\phi))^2]\,[1 + \tan^2\phi] \qquad (3)$$

where V_F is the fringe velocity and U is the magnitude of the instantaneous velocity. For a two-component simultaneous measurement, the overall probability is

$$P_{01} = P_0 \times P_1 \qquad (4)$$

where P_0 and P_1 are the probabilities of particle detection in channels 0 and 1.

All the experimental results are checked for fringe biasing. The difference between fringe bias corrected and uncorrected results was at worst 3 percent. Therefore, only the uncorrected results will be discussed here.

Spatial Resolution

The velocity determined from the LDV signal is assumed to correspond with the velocity at the center of the measuring volume. In fact, the velocity obtained is some type of average over the measuring volume. Also, the measured turbulent fluctuations consist of the actual fluctuations, the fluctuations due to the mean velocity gradients, and the fluctuations due to the gradients of the actual fluctuations.

In order to determine the effect of spatial resolution, some knowledge about the mean flowfield is required. Kried [21] and Karpuk and Tiederman [22] investigated spatial resolution and, using some simplifying assumptions, devised some schemes to determine errors. Assuming a linear mean velocity in the measuring volume which is not a bad assumption for the most part of the shear layer, the LDV measures the velocity at the center of the measuring volume [22]. With the assumption of linear mean velocity in the measuring volume, the added false turbulence intensity in the worst case for this experiment was only 1.9 percent of the actual turbulence intensity.

Counter Clock Resolution

The counters utilized two 250 MHz clocks with 90 degree out of phase with each other giving ± 1ns resolution. The maximum signal frequency was about 95 MHz which with 8 cycles counting the clock resolution was about 1.1 percent. Also, the clock resolution added about 1 percent false turbulence to freestream turbulence.

Statistical Uncertainty

The data rate for these experiments was about 400 samples per second in the freestream and decreased to about 20 samples per second in the base region. 1024 samples were collected in the base region and 2048 samples elsewhere. The local turbulence intensity in the base region was about 50 percent which with 95 percent confidence interval led to an uncertainty of ±3 percent in mean velocity and ±3.5 percent in turbulence intensities. Elsewhere in the flowfield the uncertainty was much lower.

Data Acquisition and Reduction

A schematic diagram of the data acquisition and reduction systems is shown in Fig. 3. A 600 mm lens was used to focus the four incoming beams to form the measuring volume with two sets of orthogonal fringes. The light scattered by the atomized silicon oil particles was collected by a 250 mm lens. The blue and green scattered lights were separated and were given to two photomultipliers. These signals were then given to the two counters. The validated measurements by the two counters were checked for coincidental requirement satisfaction and transferred into the memory of a PDP-11/03 mini-

computer by a direct access memory board. The mean velocities, turbulence intensities, and histograms obtained for both channels were plotted on the PDP-11/03 for immediate check of data. The raw data stored on floppy disk was later transferred to a PDP-11/34 mini-computer and stored on hard disks and magnetic tapes. Finally, the data were transferred from magnetic tape to the CYBER 175 for detailed analysis.

RESULTS AND DISCUSSION

Pressure Surveys

The wall pressure distribution is given in Fig. 4. At the step, static pressure decreased to the base pressure and then stayed constant for about 1.6 step heights. Reattachment occurred at about 2.76 step heights downstream of the step while complete pressure recovery was achieved in about 5 step heights.

Upstream Boundary Layer

An equilibrium flat-plate boundary layer with boundary layer and momentum thicknesses of 2.26 mm and 0.18 mm, respectively, and a Reynolds number of 6.69×10^7/m approached the step. A 250 mm lens with a measuring volume diameter of 0.13 mm and length of 1.82 mm was used for the velocity surveys.

Researchers agree that the logarithmic law of the wall and Coles wake law combined with the Van Driest compressibility transformation [7,23-26] is a successful scheme for correlating the similarity of compressible boundary layer profiles. Maise and McDonald [25], using this scheme, defined a single curve and could collapse experimental data from numerous equilibrium compressible boundary layer data with Mach numbers ranging from 1.47 to 4.93. The scatter in data was about 30 percent. Figure 5 shows the boundary layer data of the current investigation in comparison with the Maise and McDonald curve. The maximum difference between the present data and the curve is approximately 15 percent which indicated that the boundary layer was in equilibrium.

Figure 6 shows the present turbulence intensity data in the boundary layer which follows the general trend of LDV data of Petrie [17] and Johnson [10] and the hot-wire data of Dimotakis [27]. Also shown in Fig. 6 is the incompressible hot-wire data of Klebanoff [28]. The considerable scatter in the data could be the result of inappropriate scaling or due to experimental errors.

Figure 7 shows shear stress distributions in the boundary layer. The shear stress values on the wall are obtained from the mean velocity distribution. Petrie's [17] data agree in general trends and magnitudes with the present results. Johnson's [10] data falls off as it gets closer to the wall, which seems unrealistic. Johnson's results are questionable for three reasons. First, he did not measure the shear stress directly. Second, his sample size was only 100 which leads to an uncertainty of about 10 percent. Thirdly, he rejected all the samples beyond ±3 standard deviations which will result in a lower shear stress as it gets closer to the wall.

Two-Dimensionality of the Flowfield

Two-dimensionality of the flowfield at the reattachment region was checked using several methods. First, as shown in Fig. 4, there was no overshoot of the wall pressure in the redeveloping region which indicated that there was no three-dimensionality in the flowfield. Secondly, the spanwise pressure measurement in three locations, see Fig. 4, showed that in one-half of the span width pressure was within the accuracy of measurements, but close to the wall pressure increased approximately 6 percent. Thirdly, coating the floor in the reattachment region with a steam engine oil-zinc oxide mixture showed that there was about 1/8th of the span width side wall effect from each side and then a reattachment line at the middle. This line deteriorated towards the side walls. Fourthly, velocity measurements were made at Stations 9 and 10 at ±8 mm off the centerline. The results showed that the velocity field was uniform. Overall, the flowfield proved to be two-dimensional except very close to the side walls which showed some side wall effects.

Mean Velocity Surveys

The mean velocity vector field and streamwise mean velocity profiles are shown in Figs. 8 and 9. Three distinct regions were seen to exist. The first region was the large separation region with negative velocities reaching nearly 30 percent of the freestream values, similar in magnitudes to measurements made by Delery [29]. In this base region, the mean velocity gradients in the streamwise and transverse directions were very small. The second distinct region was the shear layer, which showed relatively constant velocity gradients similar to incompressible flows [30]. Lastly, the third distinct region was the redeveloping boundary layer in which there was a rapid "filling out" of the velocity profiles in a relatively short distance from reattachment.

The rapid "filling out" of the velocity profiles in the redeveloping region was also noticed by Settles, et al. [7]. In this region, Bradshaw and Wong [31] and Chandrsuda and Bradshaw [32] in incompressible flow and Settles, et al. [7] in supersonic flow showed that the data fell below the logarithmic wall-wake law. In fact, Bradshaw and Wong [31] found that this behavior was persistent up to about 50 step heights downstream of reattachment. They concluded that the turbulent length scale and mixing length in the redeveloping region must be abnormally large [7,31,2].

The mixing length is defined as

$$L = (- < u'v' >)^{1/2}/(\partial u/\partial y) \qquad (5)$$

and is shown in Fig. 10. The mixing length scale was very large in the redeveloping region. It was almost constant across the shear layer and in the streamwise direction until the reattachment region. It started increasing from the reattachment region and continued to grow in the redeveloping region up to the last station.

Turbulent Fluctuations Surveys

The streamwise turbulence intensity distribution is shown in Fig. 11. In a vertical station, turbulence intensity started increasing from the upper

edge of the shear layer and reached a maximum level around the middle of the shear layer which was coincident with the sonic line, see Fig. 1. Afterwards the turbulence intensity decreased toward the lower edge of the shear layer and stayed relatively constant in the base region. This trend continued up to the start of pressure rise, after which turbulence intensity was not constant in the base region anymore. Turbulence intensity increased drastically in the pressure rise region and stayed very high until reattachment and gradually decreased in the redeveloping region. At the last station, the turbulence intensity was still higher than that of the incoming boundary layer.

The flowfield revealed a strong anisotropy throughout the flowfield, see Fig. 12. The anisotropy was strongest in the reattachment region where the streamwise turbulence fluctuation was larger than the transverse turbulence fluctuation by a factor of 4.

The streamwise local turbulence intensity fluctuations are given in Fig. 13. At the lower edge of the shear layer where the local mean velocity was very small, the local turbulence intensity was the highest. In the recompression region around the sonic line, the turbulence intensity was about 50 percent. Also, in the base region the turbulence intensity was about 50 percent.

Figure 14 shows the distribution of the kinetic energy. The spanwise turbulence intensity was assumed to be between the streamwise and the transverse intensities. Figure 14 shows the same trends as the streamwise turbulence intensity. One important fact to notice was that the turbulence kinetic energy in the base region was quite high.

Figure 15 shows the shear stress distribution. It shows the same trends as the streamwise turbulence fluctuations with two differences. First, in the base region the shear stress was quite low while this was not the case in the turbulence fluctuations. Second, the shear stress values were significantly higher in the redeveloping region than those of the reattachment region. This definitely suggests the existence of the large eddies which have been pointed out by other research efforts [7,31,32].

Figure 16 shows the maximum values of the turbulence intensities and shear stress. The streamwise turbulence intensity increased mildly up to the beginning of the pressure rise. Then, it increased drastically and stayed constant up to reattachment and fell off gradually in the redeveloping region. The general pattern and values were comparable to incompressible flows [32,33],

The transverse turbulence intensity increased slowly up to reattachment, stayed constant through reattachment, and decreased gradually in the redeveloping region.

Two maximum shear stress terms are shown in Fig. 16. The $-\langle u'v' \rangle$ term increased gradually up to the core of recompression and started falling off before reattachment. The general pattern and values are very similar to those of incompressible flows [32,33]. The $-\bar{\rho}\langle u'v' \rangle$ term increased even through reattachment and fell off slowly afterwards. Also, the values are much lower than those of incompressible flows.

The decay of the shear stress in the reattachment region is a subject of current controversy. Bradshaw and Wong [31] believe that the pairing eddies in the free shear layer were torn in two in the reattachment region and caused the shear layer to decay. But Chandrusda and Bradshaw [32] and Kim, et al. [34] believe that some of the eddies proceed downstream while the others returned upstream and caused the shear stress to fall off. The existence of much larger stresses at the beginning of the redeveloping region makes one believe that neither of the two hypotheses would hold for compressible flows.

Turbulent Triple Products

In turbulence modeling using the turbulent kinetic energy or shear stress transport equation, one has to model turbulent triple products. All four components of the triple products $\langle(u')^3\rangle$, $\langle(u')^2v'\rangle$, $\langle(v')^3\rangle$, and $\langle u'(v')^2\rangle$ were obtained from experimental results. Since they showed similar trends and general features, only $\langle(u')^3\rangle$ will be discussed here.

Figure 17 shows the $\langle(u')^3\rangle$ component as a typical example. The triple products showed an almost axisymmetric feature about the center of the shear layer, peaking up on both sides and then approaching zero in both edges of the shear layer. Since the origin of the triple products are large eddies, they were essentially zero in the base region. The triple products were significantly amplified in the recompression region and were decreased through the redeveloping region with much faster decrease in the wall side. The incompressible flow results of Chardrsuda and Bradshaw [32] and Driver and Seegmiller [30] showed very similar features, except that there was not significant amplification of triple products in the recompression region.

Turbulence Production

The turbulence production plays an important role in streamwise evolution of the flow. The component of turbulence production which could be extracted from experimental data with reasonable accuracy was the production by shear stress. The turbulence production by shear stress is defined as

$$Pr = -\bar{\rho} \langle u'v' \rangle \times (\partial u/\partial y). \qquad (6)$$

In determining the average density from measured surface pressure, it was assumed that the pressure gradient in the transverse direction was negligible.

As shown in Fig. 18, the turbulence production was maximum around the sonic line and decreased toward the edges of the shear layer. There was no turbulence production in the base region. The range of the high turbulence production region across the shear layer and the maximum value of the turbulence production increased in the reattachment region. Gaviglio, et al. [6] observed the same kind of trend. The turbulence production in incompressible flow plotted at a few stations by Chandrsuda and Bradshaw [32] showed lower production level in incompressible flow.

Production level in the redeveloping region was quite high and decreased drastically in the streamwise direction. This behavior was also reported by Gaviglio, et al. [6].

CONCLUSIONS

The detailed experimental results of a flowfield were presented in which an equilibrium boundary layer with an edge Mach number of 2.07 and Reynolds number of 6.69×10^7/m was separated at a step and reattached on a surface parallel to the incoming flow direction. The recompression, reattachment, and redevelopment of the shear layer were investigated using a two-component LDV system, schlieren photographs, and static pressure probes. The following conclusions were drawn:

1. The turbulent field showed a strong anisotropy in the free shear layer, recompression, and reattachment regions. The maximum anisotropy was located around the sonic line with the ratio of the streamwise fluctuations to the transverse fluctuations in excess of 4.

2. The turbulent kinetic energy showed a pattern and magnitude similar to those of incompressible flow. It increased in the free shear layer, plateaued in the recompression region, and decreased gradually after reattachment. The turbulent kinetic energy was relatively high and constant in the base region.

3. The shear stress was extremely high in the redeveloping region which suggested the existence of very large eddies. The shear stress was also quite high in the recompression region. In the base region, the shear stress was very low.

4. The production of turbulence was high in the recompression region and higher in the redeveloping region.

5. The turbulence triple products showed a feature similar to that of the incompressible flow. The amplification of triple products was much higher than that of incompressible flow.

6. The mixing length scale was relatively small and constant in the free shear layer, but it was extremely high and increased in the streamwise direction in the redeveloping region.

7. In the redeveloping region, the changes in the mean flow and the turbulent properties were tremendous and there was not much comparison between supersonic and subsonic flows.

ACKNOWLEDGMENT

The research reported herein was supported by the U.S. Army Research Office under Contracts DAAG 29-79-C-0184 and DAAG 29-83-K-0043.

REFERENCES

1. Korst, H. H., R. H. Page, and M. E. Childs, "A Theory for Base Pressures in Transonic and Supersonic Flows," University of Illinois ME-TN-392-2, March 1955.

2. Korst, H. H., "A Theory for Base Pressures in Transonic and Supersonic Flow," J. of Applied Mech., December 1956, pp. 593-600.

3. Chapman, D. R., "An Analysis of Base Pressure at Supersonic Velocities and Comparison with Experiment," NACA TN 2137, 1950.

4. Lees, L., and B. L. Reeves, "Supersonic Separated and Reattaching Laminar Flows: I. General Theory and Application to Adiabatic Boundary Layer/Shock Wave Interactions," AIAA Journal, Vol. 2, No. 11, 1964, pp. 1907-1920.

5. Alber, I. E., and L. Lees, "Integral Theory for Supersonic, Turbulent Base Flows," AIAA Journal, Vol. 6, No. 7, 1968, pp. 1343-1351.

6. Gaviglio, J., J.-P. Dussauge, J.-F. Debieve, and A. Favre, "Behavior of a Turbulent Flow, Strongly Out of Equilibrium at Supersonic Speeds," Physics of Fluids, Vol. 20, No. 10, Part II, October 1977, pp. 5179-5192.

7. Settles, G. S., B. K. Baca, D. R. Williams, and S. M. Bogdonoff, "A Study of Reattachment of a Free Shear Layer in Compressible, Turbulent Flow," AIAA Paper 80-1408, 1980. Also, AIAA Journal, Vol. 20, No. 1, 1982, pp. 60-67.

8. Maxwell, B. R., and R. G. Seasholtz, "Velocity Lag of Solid Particles in Oscillating Gases and in Gases Passing Through Normal Shock Waves," NASA TN D-7490, March 1974.

9. Walsh, M. J., "Influence of Particle Drag Coefficient on Particle Motion in High-Speed Flow with Typical Laser Velocimeter Applications," NASA TN D-8120, February 1976.

10. Johnson, D. A., "Turbulence Measurements in a Mach 2.9 Boundary Layer Using Laser Velocimetry," AIAA Journal, Vol. 12, No. 5, 1974, pp. 711-714.

11. Hjelmfelt, A. T., Jr., and L. F. Mockros, "Motion of Discrete Particles in a Turbulent Fluid," Applied Science Research, Vol. 16, 1966, pp. 149-161.

12. Mazumder, M. K., B. D. Hoyle, and K. J. Kirsch, "Generation and Fluid Dynamics of Scattering Aerosols in Laser Doppler Velocimetry," Proc. of 2nd Int. Workshop on Laser Velocimetry, March 27-29, 1974, Vol. 2, pp. 234-269.

13. Melling, A., and J. H. Whitelaw, "Optical and Flow Aspects of Particles," Proc. of the LDA Symp., Copenhagen, Denmark, 1975, pp. 382-402.

14. Owen, F. K., and C. C. Horstman, "On the Structure of Hypersonic Boundary Layers," J. of Fluid Mech., Vol. 53, Pt. 4, 1972, pp. 611-636.

15. Ikawa, H., and T. Kubota, "Investigation of Supersonic Turbulent Mixing Layer with Zero Pressure Gradient," AIAA Journal, Vol. 13, No. 5, 1975, pp. 566-572.

16. Addy, A. L., V. A. Amatucci, D. W. Kuntz, H. L. Petrie, and M. Samimy, "Base Flow and Related Model Experiments," Proc. of the Symp. on Rocket/Plume Fluid Dynamics Interactions, Huntsville, AL, April 1983.

17. Petrie, H. L., "A Study of Compressible Turbulent Free Shear Layers," Ph.D. Thesis, Department of Mechanical and Industrial Engineering, University of Illinois at Urbana-Champaign, Urbana, IL, 1984.

18. McLaughlin, D. K., and W. G. Tiederman, "Biasing Correction for Individual Realization of Laser Anemometer Measurements in Turbulent Flows," Physics of Fluids, Vol. 16, No. 12, 1973, pp. 2082-2088.

19. Hoesel, W., and W. Rodi, "New Biasing Elimination Method for Laser-Doppler Velocimeter Counter Processing," Rev. Sci. Instrum., Vol. 48, No. 7, 1977, pp. 910-919.

20. Buchhave, P., "Biasing Errors in Individual Particle Measurements with the LDA-Counter Signal Processor," Proc. of LDV Symp., Copenhagen, Denmark, 1975, pp. 258-278.

21. Kried, D. K., "Laser-Doppler Velocimeter Measurements in Nonuniform Flow: Error Estimates," Applied Optics, Vol. 13, No. 8, 1974, pp. 1872-1881.

22. Karpuk, M. E., and W. G. Tiederman, Jr., "Effect of Finite-Size Probe Volume Upon Laser Doppler Anemometer Measurements," AIAA Journal, Vol. 14, No. 8, 1976, pp. 1099-1105.

23. Coles, D., "The Young Person's Guide to the Data," Proc. of 1968 AFOSR IFP Stanford Conf. on Computation of Turbulent Boundary Layers, Vol. 2, Stanford University, 1969, pp. 1-45.

24. Van Driest, E. R., "Turbulent Boundary Layer in Compressible Fluids," J. of the Aeronautical Sci., Vol. 18, March 1951, pp. 145-160.

25. Maise, G., and H. McDonald, "Mixing Length and Kinematic Eddy Viscosity in a Compressible Boundary Layer," AIAA Journal, Vol. 6, No. 1, 1968, pp. 73-80.

26. Baronti, P. O., and P. A. Libby, "Velocity Profiles in Turbulent Compressible Boundary Layers," AIAA Journal, Vol. 4, No. 2, 1966, pp. 193-202.

27. Dimotakis, P. E., D. J. Collins, and D. B. Lang, "Laser Doppler Velocimeter Measurements in Subsonic, Transonic, and Supersonic Turbulent Boundary Layer," Proc. of 3rd Int. Workshop on Laser Velocimetry, Purdue University, July 1978.

28. Klebanoff, D. S., "Characteristics of Turbulence in a Boundary Layer with Zero Pressure Gradient," Report 1247, 1955, NACA.

29. Delery, J. M., "ONERA Research on Afterbody Viscid/Inviscid Interaction with Special Emphasis on Base Flows," Proc. of the Symp. on Rocket/Plume Fluid Dynamics Interaction, Huntsville, AL, April 1983.

30. Driver, D. M., and H. L. Seegmiller, "Features of Reattaching Turbulent Shear Layer Subject to an Adverse Pressure Gradient," AIAA Paper 82-1029, 1982.

31. Bradshaw, P., and F. Y. F. Wong, "The Reattachment and Relaxation of Turbulent Shear Layer," J. of Fluid Mech., Vol. 52, Part 1, 1972, pp. 113-135.

32. Chandrsuda, C., and P. Bradshaw, "Turbulence Structure of a Reattaching Mixing Layer," J. of Fluid Mechanics, Vol. 110, 1981, pp. 171-194.

33. Eaton, J. K., and J. P. Johnston, "A Review of Research on Subsonic Turbulent Flow Reattachment," AIAA Journal, Vol. 19, No. 9, 1981, pp. 1093-1100.

34. Kim, J., S. J. Kline, and J. P. Johnston, "Investigation of Separation and Reattachment of a Turbulent Shear Layer: Flow over a Backward-Facing Step," Thermosciences Division, Department of Mechanical Engineering, Stanford University, Report MD-39, 1980.

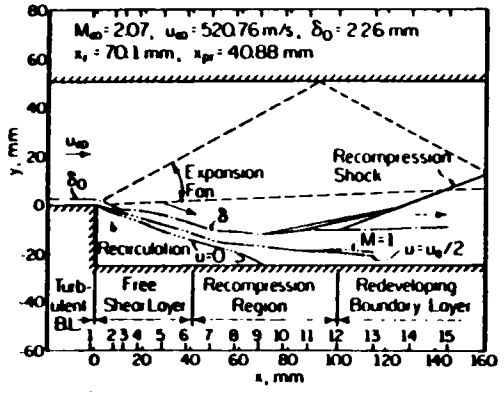

Figure 1 Test Model

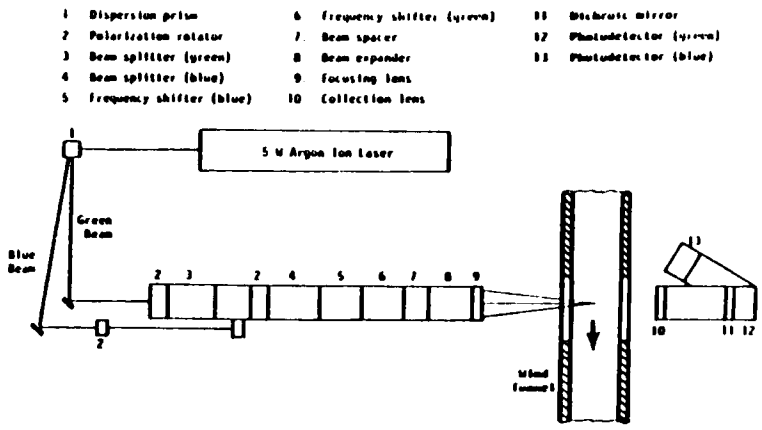

Figure 2 Schematic Diagram of LDV Components

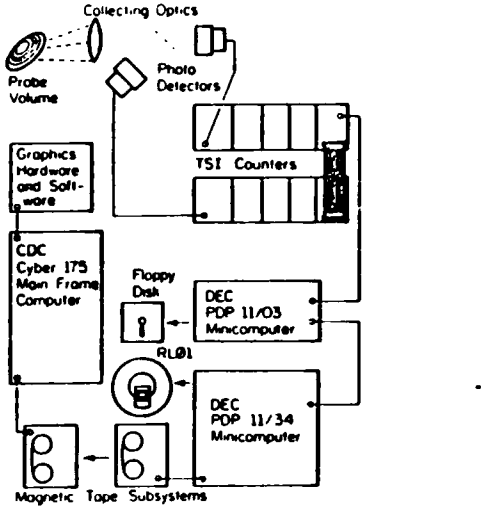

Figure 3 Schematic of Data Acquisition and Reduction Facilities

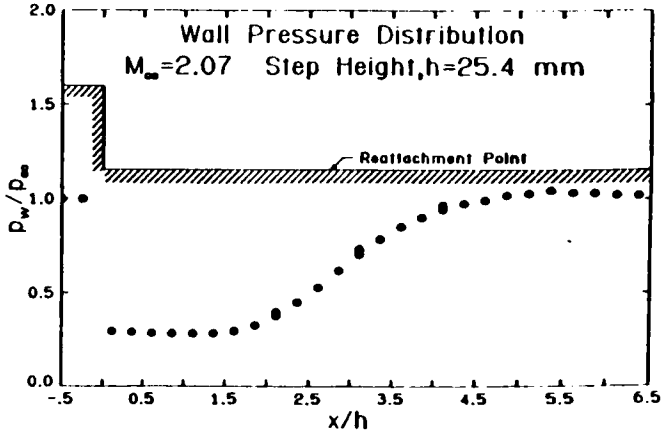

Figure 4 Wall Pressure Distribution

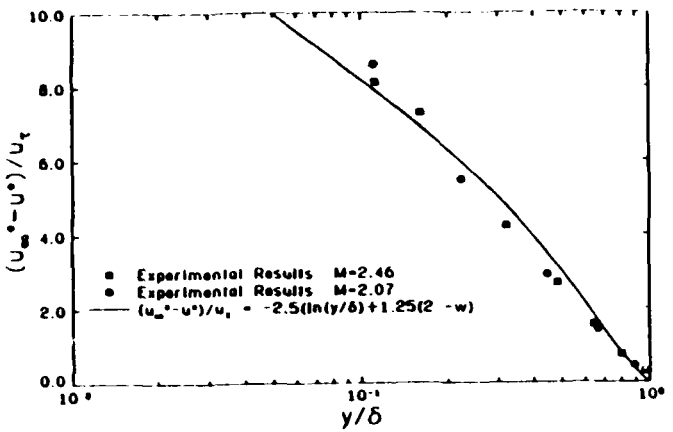

Figure 5 Boundary Layer Mean Velocity Profile

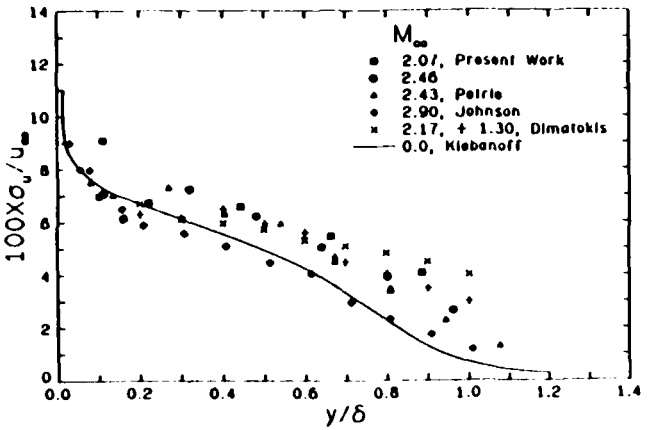

Figure 6 Distribution of Turbulent Intensity in Boundary Layer

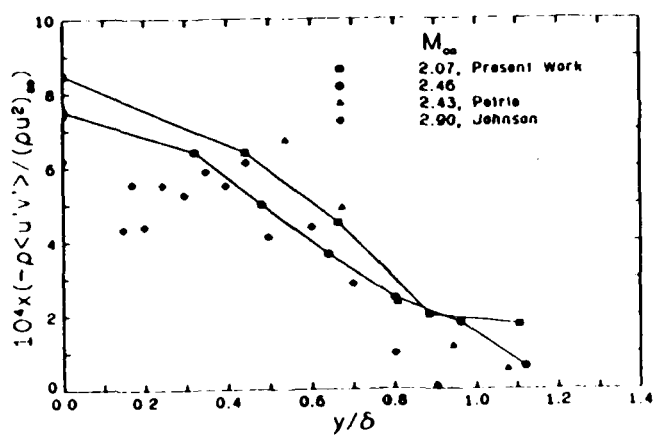

Figure 7 Distribution of Shear Stress in Boundary Layer

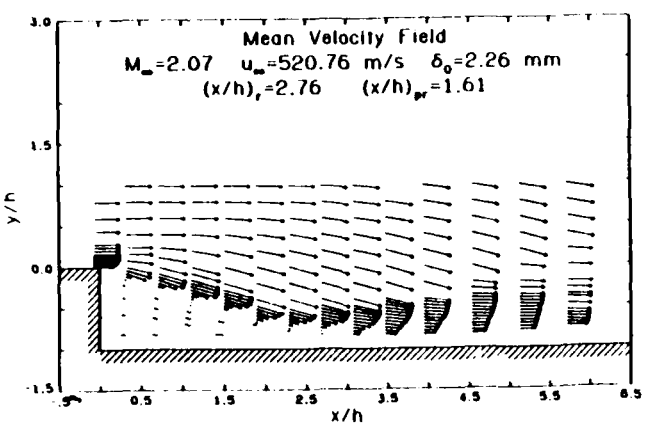

Figure 8 Mean Velocity Vector Field

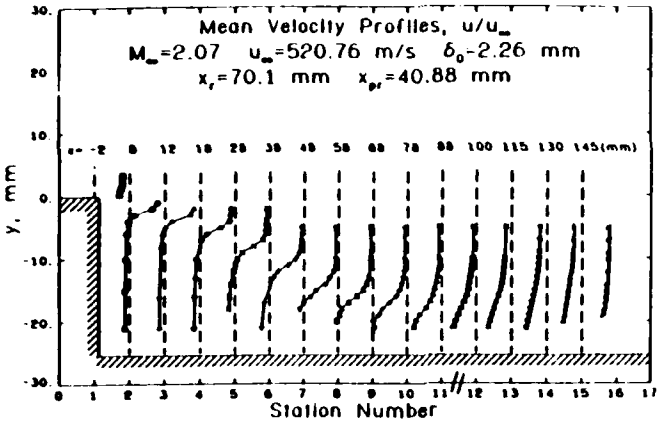

Figure 9 Streamwise Mean Velocity Profiles

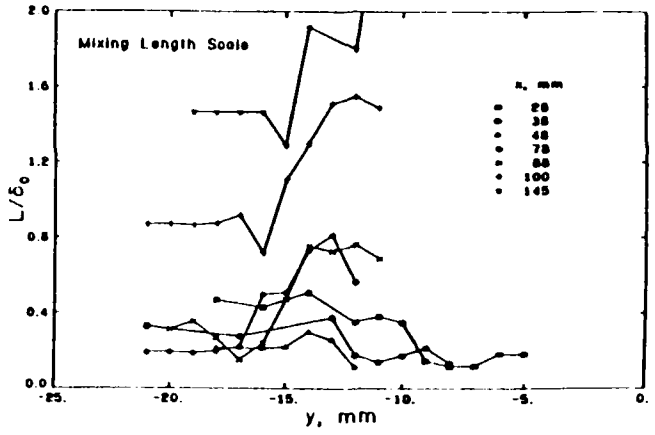

Figure 10 Distribution of Mixing Length Scale for Selected Stations

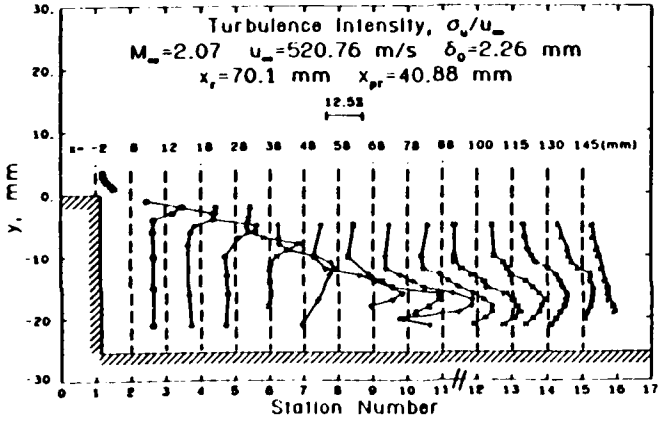

Figure 11 Streamwise Turbulence Intensity Distribution

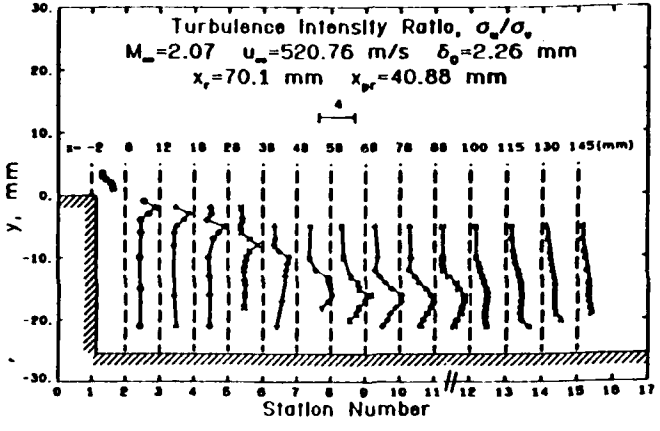

Figure 12 Turbulence Intensity Ratio

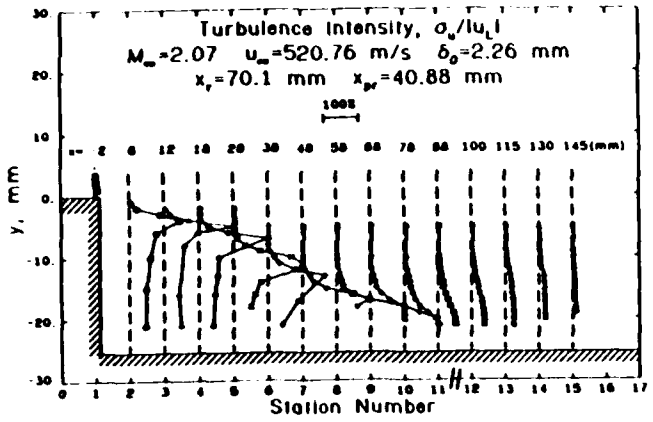

Figure 13 Streamwise Local Turbulence Intensity Distribution

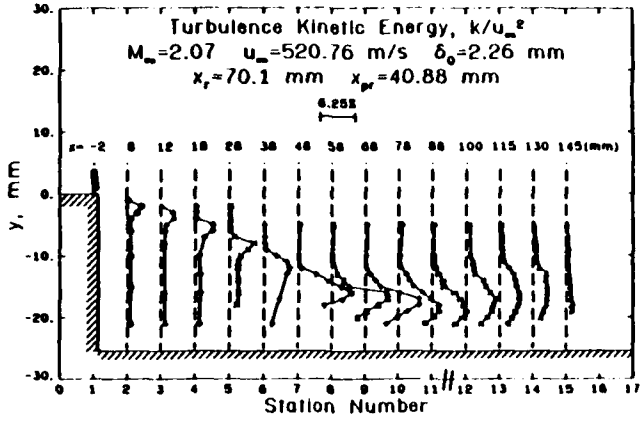

Figure 14 Turbulence Kinetic Energy Distribution

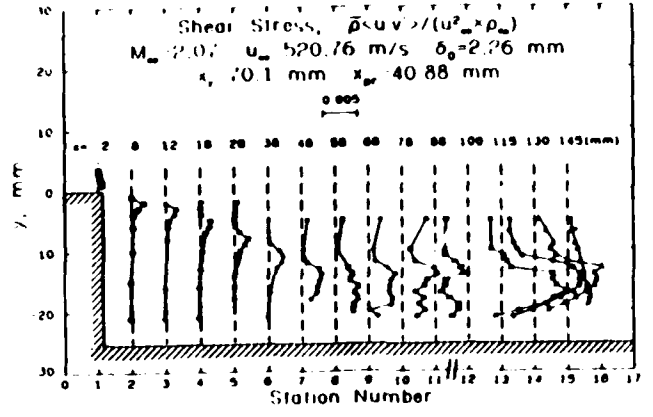

Figure 15 Shear Stress Distribution

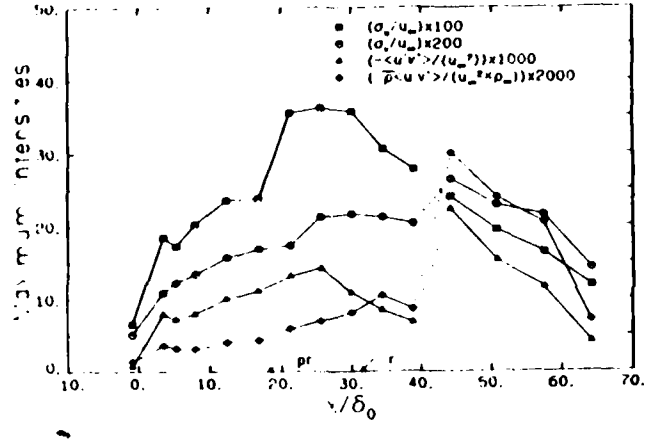

Figure 16 Maximum Values of Fluctuations (Pr: Start of Pressure Rise, r: Reattachment)

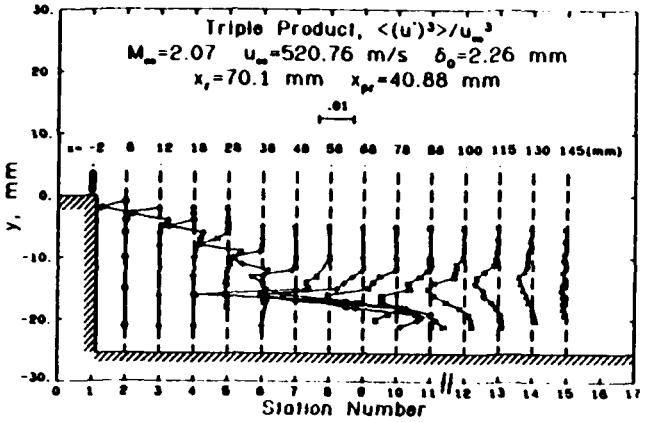

Figure 17 Turbulent Triple Product Distribution

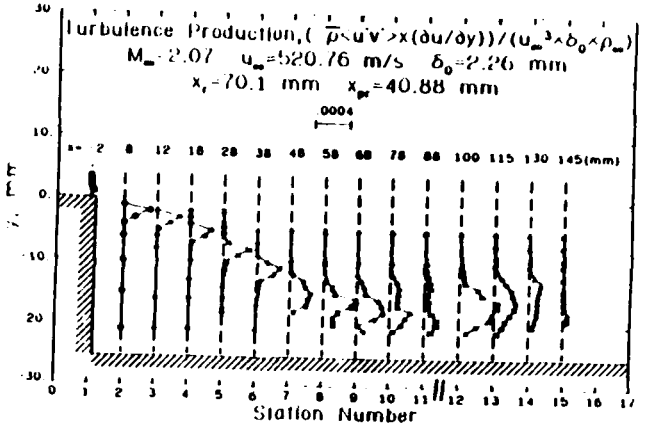

Figure 18 Turbulence Production

SYMPOSIUM ON FLUID DYNAMICS

April 26-27, 1984

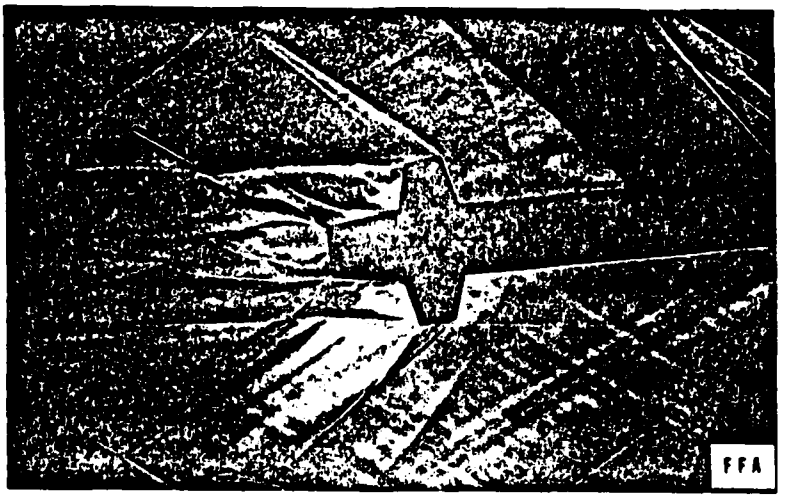

Department of Mechanical and Industrial Engineering
University of Illinois at Urbana-Champaign
1206 West Green Street
Urbana, IL 61801

SECTION B.4

EFFECTS OF EXPANSION AT THE STEP ON TURBULENCE CHARACTERISTICS OF COMPRESSIBLE FREE SHEAR LAYERS

Paper presented at the 63rd
Supersonic Tunnel Association Meeting

Dallas, Texas

April 14-16, 1985

by

M. Samimy and A. L. Addy

EFFECTS OF EXPANSION AT THE STEP ON TURBULENCE CHARACTERISTICS OF COMPRESSIBLE FREE SHEAR LAYERS

M. Samimy and A. L. Addy
Department of Mechanical and Industrial Engineering
University of Illinois at Urbana-Champaign

63rd Supersonic Tunnel Association Meeting
April 14-16, 1985
Dallas, Texas

EFFECTS OF EXPANSION AT THE STEP ON TURBULENCE CHARACTERISTICS OF COMPRESSIBLE FREE SHEAR LAYERS

M. Samimy* and A. L. Addy**
Department of Mechanical and Industrial Engineering
University of Illinois at Urbana-Champaign

The gross effects of expansion on turbulence characteristics of developing free shear layers was experimentally investigated by geometrical separation of a Mach 2.46 and a Mach 2.07 turbulent boundary layer flows from a backward-facing step. In the first set of experiments, the wind tunnel test section was designed to obtain flow separation at the step without any flow expansion or compression. In the second set of experiments, the static pressure dropped to approximately 30% of the incoming static pressure at the step of a classical backstep model. The severe distortion of the turbulence field by the expansion produced stronger anisotropy and significantly higher turbulence fluctuations and shear stresses in the developing shear layer of the simple backstep model which is in contrast to the previous reported results of decaying turbulence through the expansion. Also, significant distortion in the v component mean velocity in the backstep model was observed.

NOMENCLATURE

h	Step height
M	Mach number
p	Pressure
u	Mean velocity in the streamwise direction
v	Mean velocity in the transverse direction
x,y	Horizontal and vertical coordinates

---

* Visiting Research Assistant Professor.

** Professor and Associate Head.

$y_{.5}$	y coordinate distance where $u = 0.5u_e$
δ	Boundary layer or shear layer thickness, where $u = 0.99u_e$
ρ	Density
σ	Standard deviation with subscript u or v

Subscripts

$\overline{\quad}$	Mean value
'	Fluctuation from mean value

Superscripts

e	Adjacent freestream value
max	Maximum value
w	Wall value
∞	Freestream value before separation
0	Value of the boundary layer parameter before separation
0,.5,.99	Location where $u = 0$, $0.5u_e$, and $0.99u_e$

INTRODUCTION

The rapid expansion of compressible turbulent boundary layer at a separation corner and its effects on formation of free shear layer have been the subject of numerous investigations [1-15]. The state of the incoming boundary layer [10], the geometry of the separation corner [11], and the turbulence structure of the incoming boundary layer [12] have cited as significant influential parameters on the separation process of the boundary layer and formation process of the shear layer.

Flow visualization techniques have shown that the expansion of turbulent boundary layer causes the boundary layer turbulence to decay [13,14]. Hot-wire results of Lewis and Behrens [10] in the near wake of a wedge at Mach 4 showed existence of two-layer shear layer. The outer layer which was a remnant of the boundary layer was turbulent but the turbulence level decayed in

the streamwise direction and the inner shear layer was laminar. Also, the base region was observed to be laminar [10]. Narasimha and Viswanath [15] examined data from numerous investigations and concluded that for $\Delta p > 75\tau_0$, the relaminarization of turbulent boundary layer takes place and for $\Delta p < 60\tau_0$, no relaminarization occurs.

The objectives of this study were to investigate the near wake flowfield and to examine the effects of expansion on the turbulence field in the near wake. The detailed results of this investigation provides a good data base for computational modeling.

EXPERIMENTAL PROGRAM

A series of experiments were conducted in a small scale blowdown wind tunnel facility. The test models with corresponding wall pressure distributions are shown in Fig. 1. The wind tunnel width was 50.8 mm and the step height was 25.4 mm. The flow is left to right in both models.

The u mean velocity component and the corresponding turbulence fluctuations were chosen to correspond to the freestream flow direction; parallel to the x-coordinate at x = -2 mm in the simple backstep model and at x = -2 through x = 89.85 mm in the ramp model and rotated 15.39 degrees in the clockwise direction relative to the x-coordinate in the backstep configuration at x = 8 through x = 38 mm. The v mean velocity component and the corresponding turbulence moments were maintained orthogonal to the u component in both models.

The approach Mach numbers, Reynolds numbers, stagnation pressures and temperatures for the ramp and backstep configurations were (2.46 and 2.07), (5.01 x 10^7/m and 6.69 x 10^7/m), (528.1 and 528.1 kPa), and (297 and 293K), respectively. The approach boundary layer and momentum thicknesses for the ramp and the backstep configurations were (3.12 and 0.25 mm) and (2.26 and

0.18 mm), respectively. The freestream velocity and Mach number for the ramp and backstep configurations before separation were (571.8 m/s and 2.46) and (520.76 m/s and 2.07), respectively, and for the backstep configuration after separation were (594.59 m/s and 2.74).

The Laser Doppler System

A two-component laser Doppler velocimeter (LDV) system was used to make the velocity measurements. The frequency of one beam of each beam pair was shifted by 40 MHz in order to detect velocity direction. A 250 mm lens was used for the boundary layer survey in both configurations and the shear layer survey in the ramp model and a 350 mm lens was used for the shear layer survey in the backstep configuration. The measurement volume diameter and length for the 250 mm and 350 mm lenses were (0.131 and 1.83 mm) and (0.183 and 2.56 mm), respectively.

Seed particle generation was accomplished with a TSI Inc. six-jet atomizer. A 50 cP silicone oil was atomized and the effective mean diameter of the generated particles was estimated by measuring the relaxation of the velocity profiles downstream of an oblique shock wave [16]. The results indicated that the effective mean particle diameter was approximately 1 μm. The two-dimensional velocity inverse weighting factor was used to correct for possible velocity bias [17,18]. The measurement errors due to spatial resolution were estimated to be approximately 0.9% in the mean velocity and 1.9% in the turbulence intensity in the worst case. The statistical uncertainty due to limited sample size was estimated to be approximately ± 3% in the mean flow and ± 3.5% in the turbulence intensity in the worst case which occurred in the base region of both configurations.

Incoming Boundary Layers

The approach boundary layer and momentum thicknesses for the ramp and backstep models were (3.12 and 0.25 mm) and (2.26 and 0.18), respectively. The ratio of momentum thickness to boundary layer thickness was 0.0792 for the ramp and 0.0798 for the backstep, respectively. These values were approximately 10% and 5% higher than the theoretical values of Maise and McDonald [19]. The mean velocity profiles of the incoming boundary layers of the present study compared very well with the generalized profile of Maise and McDonald [19]. The maximum deviation of the present data with the curve of Maise and McDonald were approximately 5% for the ramp and 7.5% for the backstep results [17,18]. The boundary layer shear stress profiles showed a good agreement with the "best estimate" of Sandborn [17,20].

Static Pressure Results

The static wall pressure distribution non-dimensionalized by the static pressure before the step is shown in Fig. 1. The accuracy of the pressure measurements was approximately $\pm$ 0.6%. The pressure change in the streamwise direction in the ramp configuration was less than 4% from 12.5 mm before the separation to 96 mm after the separation. In the backstep configuration, the pressure at the separation point decreased to approximately 30% of the pressure before the step and then there was a gradual decrease of 1.8% up to x = 25 mm. Downstream of this point, the pressure increased gradually up to x = 46 mm where the sharp increase in pressure due to reattachment started. In both configurations, there was 1 to 2% pressure decrease from the freestream to the floor of the models.

Mean Flow Results

The streamwise mean velocity profiles are shown in a non-dimensionalized y coordinate in Fig. 2. The variable δ is the shear or boundary layer thickness, $\delta = y_{.99} - y_0$, where y_0, $y_{.5}$, and $y_{.99}$ are the locations of $u = 0$, $0.5u_e$, and $0.99u_e$. The sonic line and $u = 0.5u_e$ locations were nearly coincident all the way from the step to the redeveloping region in both configurations [17,18]. As can be seen in Fig. 2, the shear layer in the ramp configuration is in local equilibrium for $x > 20$ mm and in the backstep configuration for all of the survey stations. Thus, the expansion does not appear to affect the mean flow in the streamwise direction. There is some scatter in data in the lower part of the shear layer in both configurations which is the direct influence of the recirculating flow.

The growth rate of the free shear layer was 0.093 for the ramp configuration and 0.076 for the backstep configuration. These values were much higher than 0.062 reported by Ikawa and Kubota [21] for a constant pressure shear layer without any recirculation. The higher growth rates appear to be caused by the recirculating flow. In both configurations, there was a single clockwise recirculating bubble with the bubble in the ramp configuration being approximately twice as large as the bubble in the backstep configuration. The larger bubble in the ramp configuration caused more entrainment of flow by the shear layer in the ramp configuration and thus a larger growth rate of the shear layer. The maximum negative velocities in the base region were $0.20u_e$ for the ramp and $0.26u_e$ for the backstep configuration.

Figure 3 shows the transverse component mean velocity distributions for both configurations. In the ramp configuration, the transverse velocity within the shear layer shows positive values for $x \leq 40$ mm which is consistent with the other compressible free shear layer results [22]. On the other hand,

the backstep configuration results show negative velocities above the sonic line and positive velocities below the sonic line within the shear layer. The difference between two shear layer results appears to be a structural difference and the cause is the expansion of the boundary layer at the step in the backstep configuration. Even though the u and v component velocities show the velocities in the streamwise and the transverse direction, the actual survey of the shear layer in the backstep configuration was carried out in the y direction which was 15.39 degrees off from the normal to the free shear layer direction. Thus, the reported v component values should be treated with caution.

The streamwise component turbulence intensity distributions in both configurations showed a very pronounced peak which developed just downstream of separation and gradually spread as the shear layer grew [18]. The first survey stations in the ramp and backstep configurations were 10 and 8 mm from the step, respectively. The maximum turbulence intensities in these stations were 12.7 and 16%, respectively, which were approximately 1.8 and 2.4 times higher than the maximum turbulence intensities of the incoming boundary layers, respectively. Thus, it appears that the expansion of the boundary layer in the backstep model not only did not decay the turbulence, but enhanced the turbulence. This is in sharp contrast with Schlieren photographs [13,14] and some hot-wire measurements [10] which showed relaminarization of turbulence boundary layer after expansion. In the backstep experiments, the pressure drop through the expansion fan, Δp, was approximately 140 times the incoming boundary layer wall shear stress, τ_0. Based on examination of some experimental data, Narasimha and Viswanath [15] concluded that for $\Delta p > 75\tau_0$, the relaminarization takes place which does not agree with the present results. Since the first survey station is $3.54\delta_0$ downstream of the step, one

might think that the relaminarization and subsequent transition have already taken place within this distance which does not seem to be likely.

The maximum turbulence intensities and shear stresses are shown in Fig. 4 for both configurations. As can be seen in Fig. 4, just downstream of the separation, the turbulence intensity and shear stress values are higher in the backstep configuration and these high level fluctuations continue all the way downstream. The maximum turbulence intensities in the streamwise and transverse directions reached approximately (15% and 7.5%) for the ramp and (22% and 7.5%) in the backstep configurations, respectively. The shear stress values show similar trends and similar differences. The ratio of the maximum u intensity to the maximum v intensity in the shear layer region was approximately 1/2 for the ramp configuration which did not change from that of the incoming boundary layer, but this ratio was 1/3 for the backstep configuration. Petrie, et. al. [22] reported a value of 1/2 for this anisotropy ratio in a compressible shear layer without expansion and Champagne, et. al. [23] reported 2/3 for subsonic shear layer. This high anisotropy level, as well as the high turbulence fluctuations level in the free shear layer of the backstep configurations, are believed to be the direct result of the distortion of the turbulence field passing through the expansion waves at the step.

The maximum streamwise turbulence intensities in the recirculating flow of the ramp and backstep configurations were approximately 4% and 7%, respectively, in the first vertical station and 13% and 15%, respectively, in the last vertical station in the constant pressure free shear layer region. Again, the high turbulence level in the base region of the backstep configuration is in contrast to the results of Lewis and Behrens [10] which showed a laminar base region with incoming turbulent boundary layer. The shear stresses in the recirculating region in both configurations of the present

study were much smaller in comparison with the normal stresses which could be an indication of flapping motion of the shear layers.

CONCLUSIONS

A detailed experimental results of free shear layers formed by the geometrical separation of turbulent boundary layers from a backward-facing step with and without expansion at the step were presented. These results contradicted some of the earlier findings about the effects of expansion on turbulence characteristics of compressible turbulent boundary layer. The expansion at the step did not decay the boundary layer turbulence level as expected but increased it by a factor of 2.4. The recirculating flow appeared to be turbulent in both configurations. Also, the expansion caused a significant distortion in the v component mean velocity. More experimental data especially close to the step are needed to investigate probable relaminarization of the turbulent boundary layer through the expansion and subsequent transition location, if there are any.

ACKNOWLEDGMENT

This research was supported by the U.S. Army Research Office under contracts DAAG 29-79-C-0184 and DAAG 29-83-K-0043. Dr. Robert E. Singleton served as the Contract Monitor.

REFERENCES

1. Weinbaum, S., "Rapid Expansion of a Supersonic Boundary Layer and Its Application to the Near Wake," AIAA Journal, Vol. 4, No. 2, February 1966, pp. 217-226. Also Avco-Everett Research Report RR204, 1965.

2. Small, R. D. and Page, R. H., "Turbulent Boundary Layer Shape After a Corner Expansion," Aeronautical Journal, March 1973, pp. 146-147.

3. Pirri, A., "Decay of Boundary-Layer Turbulence in Near Wake of a Slender Body," AIAA Journal, Vol. 10, No. 5, 1972, pp. 657-663.

4. Bradshaw, P., "The Effect of Initial Condition on the Development of a Free Shear Layer," Journal of Fluid Mechanics, Vol. 26, 1966, pp. 225-236.

5. White, R. A., "Effect of Sudden Expansions or Compressions on the Turbulent Boundary Layer," AIAA Journal, Vol. 4, 1966, pp. 2232-2234.

6. Nash, J. F., "An Analysis of Two-Dimensional Turbulent Base Flow, Including the Effect of the Approaching Boundary Layer," Aeronautical Research Council R&M No. 3344, 1963.

7. Hama, F. R., "Experimental Studies on the Lip Shock," AIAA Journal, Vol. 6, No. 2, 1968, pp. 212-219.

8. Hama, F. R., "Estimation of the Strength of the Lip Shock," AIAA Journal, Vol. 4, No. 1, 1966, pp. 166-167.

9. Gerhart, P. M., "A Study of the Reattachment of a Turbulent Supersonic Shear Layer with Closure Condition Provided by a Control Volume Analysis," Ph.D. Thesis, University of Illinois at Urbana-Champaign, Department of Mechanical and Industrial Engineering, 1971.

10. Lewis, J. E. and Behrens, W., "Fluctuation Measurements in the Wake with and without Base Injection," AIAA Journal, Vol. 7, No. 4, 1969, pp. 664-670.

11. Roshko, A. and Thomke, G. J., "Effect of Shoulder Modification on Turbulent Supersonic Base Flow," AIAA Journal, Vol. 5, No. 4, pp. 827-829, 1967.

12. Bradshaw, P., "The Effect of Mean Compression of Dilation on the Turbulence Structure of Supersonic Boundary Layers," Journal of Fluid Mechanics, Vol. 63, 1974, pp. 449-464.

13. Small, R. D. and Page, R. H., "Turbulent Supersonic Boundary Layer Flow in the Neighborhood of a 90° Corner," Astronautica Acta, Vol. 18, No. 2, 1973, pp. 99-107.

14. Page, R. H. and Sernas, V., "Apparent Reverse Transition in an Expansion Fan," AIAA Journal, Vol. 8, No. 1, 1970, pp. 189-190.

15. Narashima, R. and Viswanath, P. R., "Reverse Transition at an Expansion Corner in Supersonic Flow," AIAA Journal, Vol. 13, No. 5, pp. 693-695, 1975.

16. Petrie, H. L., "A Study of Compressible Turbulent Free Shear Layers Using Laser Doppler Velocimetry," Ph.D. Thesis, University of Illinois at Urbana-Champaign, Department of Mechanical and Industrial Engineering, 1984.

17. Samimy, M., Petrie, H. L., and Addy, A. L., "A Study of Compressible Turbulent Reattaching Free Shear Layers," AIAA Paper 85-1646, 1985.

18. Samimy, M., "An Experimental Study of Compressible Turbulent Reattaching Free Shear Layers," Ph.D. Thesis, University of Illinois at Urbana-Champaign, Department of Mechanical and Industrial Engineering, 1984.

19. Maise, G. and McDonald, H., "Mixing Length and Kinematic Eddy Viscosity in a Compressible Boundary Layer," AIAA Journal, Vol. 6, No. 1, 1968, pp. 73-80.

20. Sandaborn, V. A., "A Review of Turbulence Measurements in Compressible Flow," NASA TM x-62, 337, March 1974.

21. Ikawa, H. and Kubota, T., "Investigation of Supersonic Turbulent Mixing Layer with Zero Pressure Gradient," AIAA Journal, Vol. 13, No. 5, 1975, pp. 566-572.

22. Petrie, H. L., Samimy, M., and Addy, A. L., "A Study of Compressible Turbulent Free Shear Layers Using Laser Doppler Velocimetry," AIAA Paper 85-0177, 1985.

23. Champagne, F. H., Pao, Y. H., and Wygnanski, I. J., "On the Two-Dimensional Mixing Region," Journal of Fluid Mechanics, Vol. 74, Part 2, 1976, pp. 209-250.

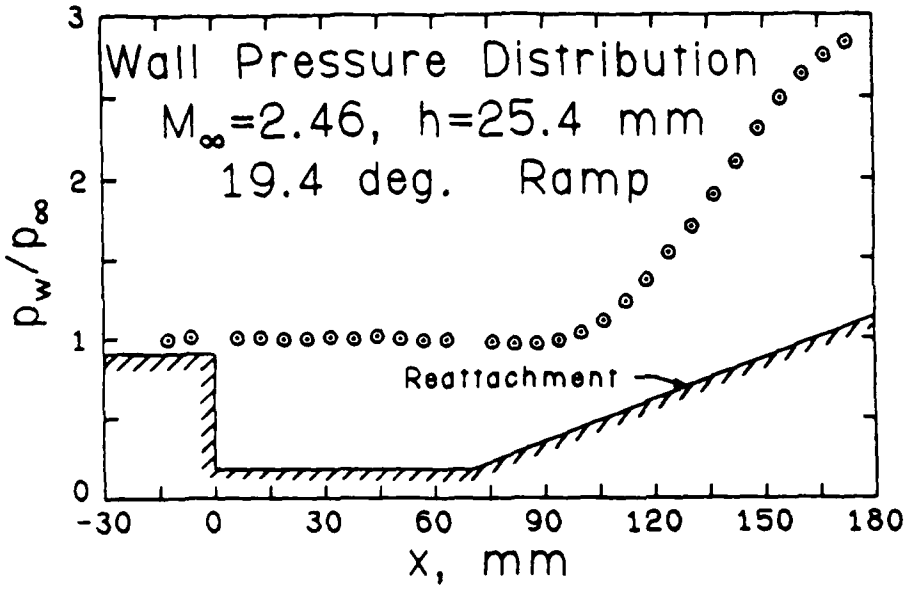

(a) Ramp configuration results.

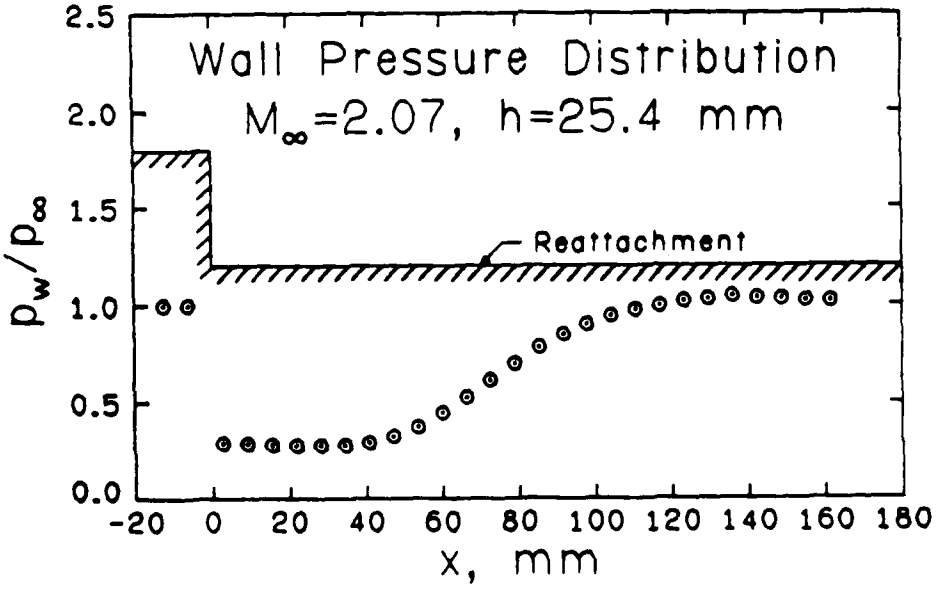

(b) Backstep configuration results.

Figure 1 Wall static pressure distributions measured on the models centerline.

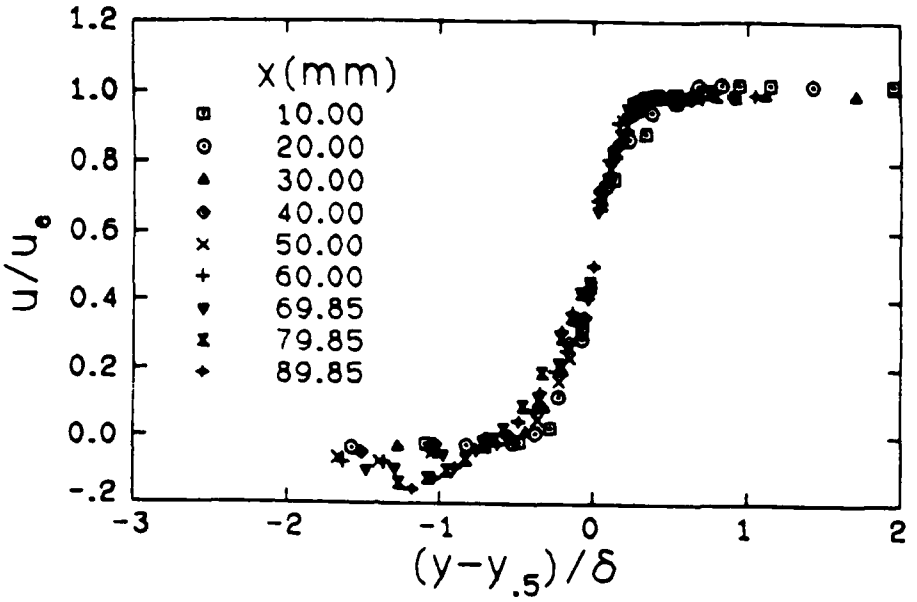

(a) Ramp configuration results.

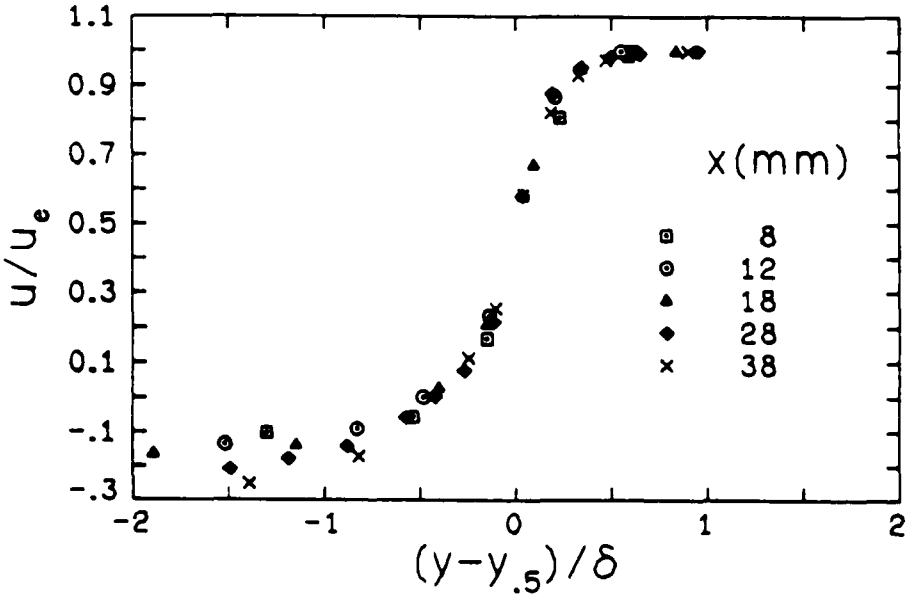

(b) Backstep configuration results.

Figure 2 Correlated streamwise mean velocity profiles.

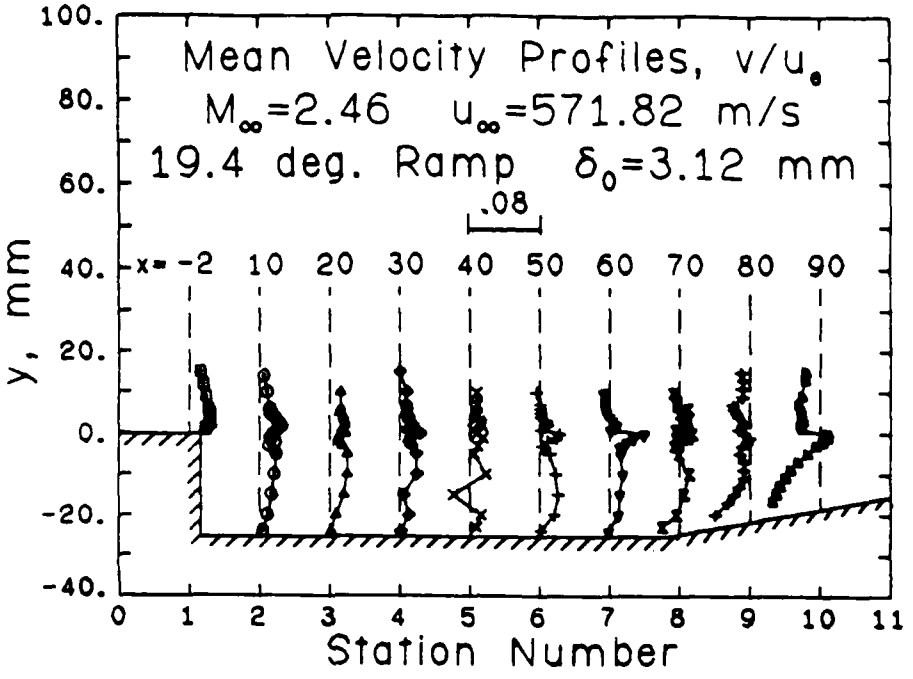

(a) Ramp configuration results.

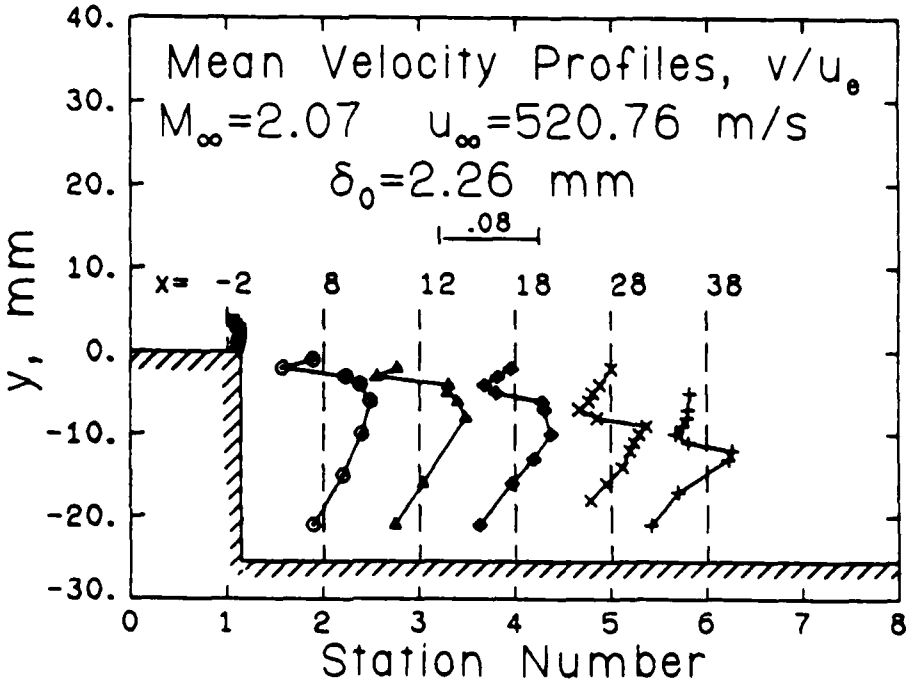

(b) Backstep configuration results.

Figure 3 Transverse component mean velocity profiles.

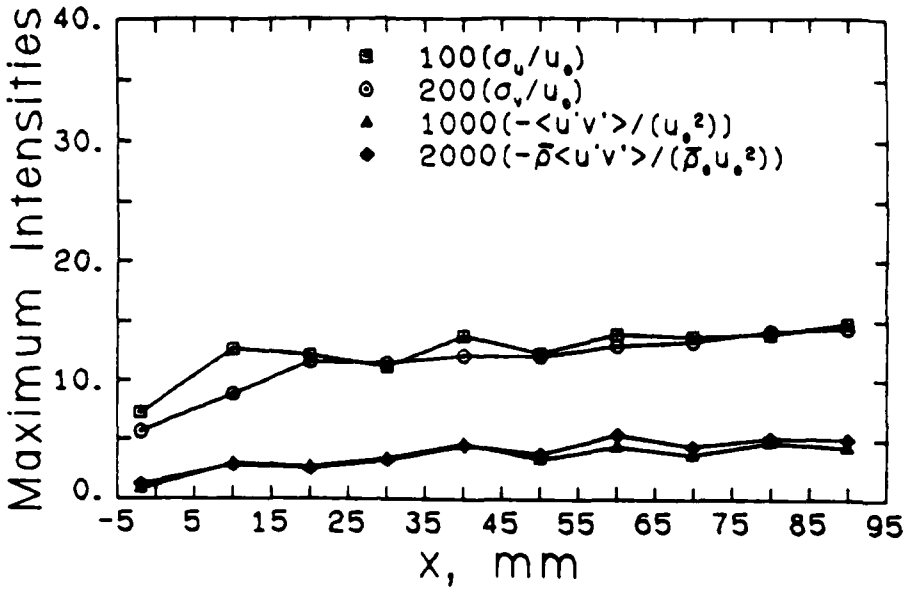

(a) Ramp configuration results.

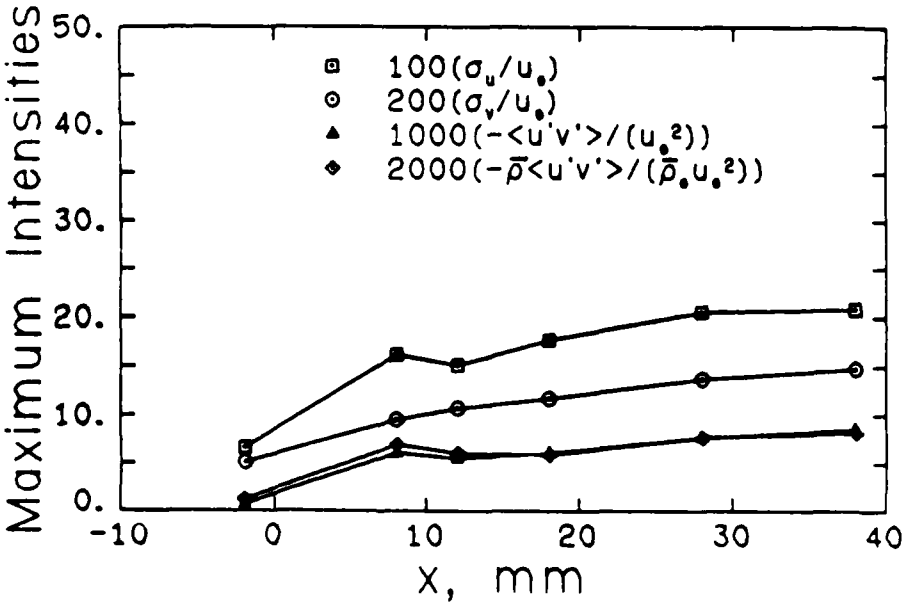

(b) Backstep configuration results.

Figure 4 Maximum turbulence fluctuations and shear stresses.

SECTION B.5

A STUDY OF COMPRESSIBLE TURBULENT REATTACHING FREE SHEAR LAYERS

Paper No. AIAA-85-1646

Presented at the AIAA 18th Fluid Dynamics and Plasmadynamics and Lasers Conference

Cincinnati, Ohio

July 16-18, 1985

by

M. Samimy, H. L. Petrie, and A. L. Addy

AIAA'85

AIAA-85-1646

A Study of Compressible Turbulent Reattaching Free Shear Layers

M. Samimy and A. L. Addy, Univ. of Illinois at Urbana-Champaign;
and H. L. Petrie, U.S. Army Missile Lab., Redstone Arsenal, AL

AIAA 18th Fluid Dynamics and Plasmadynamics and Lasers Conference

July 16-18, 1985 / Cincinatti Ohio

A STUDY OF COMPRESSIBLE TURBULENT REATTACHING FREE SHEAR LAYERS

M. Samimy*
University of Illinois
at Urbana-Champaign

H. L. Petrie**
U.S. Army Missile Laboratory
Redstone Arsenal, Alabama

A. L. Addy†
University of Illinois
at Urbana-Champaign

Abstract

An experimental investigation was conducted to study the two-dimensional, compressible, turbulent reattaching free shear layer formed by the geometrical separation of a Mach 2.46 flow with a turbulent boundary layer and a Reynolds number of 5.01×10^7/m from a 25.4 mm high backward facing step. The wind tunnel test section was specifically designed to obtain a constant pressure separation at the step. A detailed survey of the flowfield was made utilizing a Schlieren system, static pressure taps, and a two-component coincident laser Doppler velocimeter. In contrast to incompressible reattaching free shear layers, significant increases in the turbulence level, shear stress, and turbulent triple products were observed within the reattachment region. Large turbulence structure and enhanced mixing were observed in the redeveloping region.

Nomenclature

M	Mach number
p	Pressure
pr	Start of pressure rise
Pr	Turbulence production
r	Location of reattachment
u	Mean velocity in the streamwise direction
u*	Van Driest generalized velocity
u_τ	Friction velocity
x,y	Horizontal and vertical coordinates
$y_{.5}$	y component distance where $u = 0.5u_\infty$
δ	Boundary layer or shear layer thickness, where $u = 0.99u_\infty$
θ	Momentum thickness
ρ	Density
σ	Standard deviation with subscripts u or v
τ	Shear stress
$\langle\ \rangle$	Ensemble average

Superscripts

$\overline{\quad}$	Mean value
'	Fluctuation from mean value

Subscripts

max	Maximum value
pr	Start of pressure rise
r	Location of reattachment
u	Streamwise
v	Transverse
w	Wall value
z	Spanwise
∞	Freestream value
0	Value of the boundary layer parameter at the backstep and centerline value
0, .5,.99	Location where $\frac{u}{u_\infty} = 0, 0.5, 0.99$

Introduction

After many years of investigation, the problem of flow separation and subsequent flow recompression and redevelopment in the base region of a blunt based missile-type body still offers a great challenge to experimentalists and analytical and computational modelers. Since the early 1950's, analysis of separated flows for both laminar and turbulent supersonic base flows have been carried out along two paths, namely the Chapman-Korst component model[1,2]‡ and integral methods[3,4]. Even though these methods are good engineering tools for analyzing base flow problems, they lack generality and leave unanswered many questions regarding the fundamental fluid dynamic nature of the flow mechanisms and interactions within the separated base flow

* Visiting Research Assistant Professor, Department of Mechanical and Industrial Engineering, Member AIAA.
** National Research Council Associate, Member AIAA.
† Professor and Associate Head, Department of Mechanical and Industrial Engineering, Associate Fellow AIAA.

‡ Numbers in brackets refer to entries in References.

region. This lack of knowledge is most apparent when an attempt is made to extend the models to more complex systems, geometries, and/or flight conditions.

The lack of understanding of the physics of the separated flows and the lack of reliable experimental data have slowed progress in the numerical modelings of this problem. Recent papers by Marvin[5], Horstman, et. al.[6], and Weinberg, et. al.[7] have shown good computational prediction of the separated flowfields with a small separated region but only a qualitative prediction with a large separated region, especially in the highly turbulent reattachment and redevelopment region. The overall objectives of this study were to learn more about the fundamental nature of the recompression, reattachment, and redevelopment processes and to obtain some detailed data useful for analytical and computational modeling purposes.

Experimental Program

A series of dry, cold air experiments were conducted in a small scale blowdown wind tunnel facility[8]. The test section of the wind tunnel is shown in Fig. 1. The wind tunnel width was 50.8 mm and the step height was 25.4 mm. This configuration was specifically designed to eliminate the expansion effects at the separation point and provide a long constant pressure free shear layer with a well defined initial condition to the compression and reattachment processes. The ramp angle was 19.4° and the ramp leading apex distance from the step was 69.85 mm. Settles, et. al.[9], Hayakawa, et. al.[10], and Petrie, et. al.[11], have all used configurations similar to that of the present study. Settles and Hayakawa used a hot-wire anemometer to survey the entire flowfield in a wind tunnel facility with a Mach 2.92 incoming flow with a turbulent boundary layer. Petrie used the LDV to study only the constant pressure region of the shear layer in a Mach 2.44 incoming flow with a turbulent boundary layer. Ikawa and Kubota[12] and Petrie, et. al.[11] also generated constant pressure shear layers over a backward-facing step by using mass bleed from the floor of the wind tunnel. Ikawa and Kubota used a hot-wire anemometer and Petrie, et. al. used an LDV in their investigation of the constant pressure region of the free shear layer.

Information obtained from Schlieren photographs, static pressure data, and LDV results were used to construct Fig. 1 and the regions of the flowfield with distinct features are identified for later discussion. The curves of $u = 0$, $0.5u_\infty$, $0.99u_\infty$, and the sonic line, $M = 1$, are shown. As can be seen, the $M = 1$ and $u = 0.5u_\infty$ locations were almost coincident. The station numbers where the vertical surveys of the flowfield were carried out are shown above the x-axis in this figure.

The approach Mach number, Reynolds number, stagnation pressure, and stagnation temperature were 2.46, 5.01×10^7/m, 528.1 kPa, and 297 K, respectively. The approach boundary layer and momentum thicknesses were 3.12 and 0.25 mm, respectively.

Laser Doppler Velocimetry Considerations

A two-color, two-component laser Doppler velocimeter (LDV) system was utilized to make the velocity measurements. The frequency of one beam of each beam pair was shifted by 40 MHz in order to detect velocity direction and to eliminate fringe bias[13-15]. A 250 mm focal length lens was used for the velocity measurements within the boundary layer and the initial part of the shear layer and a 600 mm focal length lens was used for the velocity measurements in reattachment and redevelopment region. The measurement volume diameter and length for the 250 mm and 600 mm lens were (0.131 and 1.83 mm) and (0.314 and 4.39 mm), respectively. The 600 mm lens produced a large fringe spacing and a large fringe velocity in the measurement volume. These were desirable LDV system characteristics because of the high turbuence intensities expected in the reattachment and redevelopment region[9] and possible fringe bias problems that may have resulted from the two-component coincident LDV[8].

Seed particle generation was accomplished with a commercial six-jet atomizer. A 50 cP silicone oil was atomized and the effective mean diameter of the generated particles was estimated by measuring the relaxation of the velocity of particles downstream of an oblique shock wave[16]. The results indicated that the effective mean particle diameter was approximately 1 μm.

The individual velocity realization type data processor used in these experiments had the capability of measuring and storing 83.3 k coincident samples per second. The maximum data rate was approximately 2,000 samples per second with the 250 mm lens and 400 samples per second with the 600 mm lens. Therefore, the sampling process was totally controlled by the flow. According to Erdmann and Tropea[17,18] this "free running" processor condition is comletely velocity biased. The two-dimensional velocity inverse weighting factor, $|1/V_T|$, was used to correct for velocity bias where V_T is the total velocity.

The digital frequency counters used in these experiments had a ± 1 ns resolution. The maximum Doppler signal frequency was approximately 95 MHz and the uncertainty due to counter clock resolution in a five to eight frequency comparison could reach 3.1% at this frequency. Thus, the comparison level was set at 4% to avoid discarding data because of clock resolution.

In the separation region just downstream of the step, the velocity gradient across the shear layer was very large; therefore, errors in the velocity statistics due to spatial resolution were the largest. In this region, measurement errors due to spatial resolution were estimated to be 0.9% in mean velocity and 1.9% in turbulence intensity[19,20].

The data rate was approximately 2,000 samples per second in the freestream and dropped to 20 samples per second in the recirculating region. The following number of samples were collected: 1,024 in the freestream, 2,048 in the recirculating region, and 4,096 elsewhere. Therefore, the

statistical uncertainty due to the limited sample size was estimated to be approximately ± 3% in the mean velocity and ± 3.5% in the turbulence intensity in the recirculating region. Elsewhere in the flowfield the statistical uncertainty was much lower.

Fringe bias occurs because the LDV frequency counters require a minimum number of fringes to be crossed before a signal is accepted[13-15]. Due to the highly turbulent nature of the flow in the present experiments, it was thought, at the outset, that fringe bias would be the major problem in designing these experiments. The fringe bias analysis of Buchhave[13] was modified to incorporate frequency shifting and was then used to correct for possible fringe bias[8]. The largest difference between the results which were corrected and uncorrected for fringe bias was 3%. Consequently, only the uncorrected results are presented herein.

Experimental Results

In this section, the experimental results are presented and compared to the results of previous studies. The nature of the incoming boundary layer, the pressure field, and the two-dimensionality of the flowfield are first discussed and then the results for the mean flow and the turbulent flow are presented.

Incoming Boundary Layer

Two-component and one-component velocity measurements were made to within 1 and 0.25 mm of the wall, respectively. The approach boundary layer and momentum thicknesses were determined to be 3.12 and 0.25 mm, respectively. The ratio of momentum thickness to boundary layer thickness was 0.0792 which was approximately 10% higher than the value reported by Maise and McDonald[21].

Maise and McDonald[21] defined a single curve which was based on the wall-wake law coupled with the Van Driest compressibility transformation and showed that they could collapse experimental data from numerous equilibrium compressible boundary layer flows. The maximum scatter of the data relative to their curve was approximately 30%. Figure 2 shows the boundary layer data of the current study in comparison with the Maise and McDonald curve. The maximum difference between the present data and their curve is less than 5%; this is a good indication that the boundary layer of the present study was in the equilibrium stage. Since the skin friction coefficient, C_f, was not measured directly, it was determined from the wall-wake law. The value of C_f determined by this method was 0.00138 which is in a good agreement with the values of Settles, et. al.[9] and Petrie, et. al.[11].

The boundary layer shear stress profile is shown in Fig. 3. Also included in Fig. 3 are: the incompressible results of Klebanoff[22], the "best estimate" for the supersonic boundary layer shear stress distribution given by Sandborn[23], and the hot-wire and LDV data of Johnson and Rose[24] for a Mach 2.9 boundary layer flow. The present data agree well with the LDV data of Johnson and Rose and with the "best estimate" of Sandborn up to $y/\delta = 0.8$, but in the upper edge of the boundary layer, the present data show somehow higher values.

Static Pressure Results

The wall pressure distribution non-dimensionalized by static pressure before the step is shown in Fig. 4. The accuracy of the pressure measurements was approximately ± 0.6%. The pressure change was less than 4% from 12.5 mm before separation to 96 mm after separation. The reattachment location, which was determined by coating the ramp surface with a steam engine oil-zinc oxide mixture, was located 128.02 mm downstream of the step and 4.91 mm vertically below a straight horizontal line extended from the step, see Fig. 4. At the last station, x = 172.72 mm, the pressure ratio was 2.83 which was significantly less than the final expected recovery pressure ratio of approximately 3.25. The experimental results of Roshko and Thomke[25], Sirieix, et. al.[26], and Settles, et. al.[9] have shown that the reattachment process is to a significant degree independent of the wall geometry or disturbances downstream of the reattachment location. Therefore, the relatively short length of the present ramp downstream of the reattachment location would be expected not to disturb the reattachment process during the current investigation.

Spanwise wall pressure distributions in three streamwise locations are shown in Fig. 5. As can be seen, the variations in the spanwise pressure distributions do not show any significant trends and are all within ± 0.8% of the centerline pressure. Since the accuracy of the pressure measurements was determined to be ± 0.6%, the flow was found to be two-dimensional within ± 19 mm of the wind tunnel centerline.

Two-Dimensionality of the Flowfield

Spanwise cellular structure has been noticed in the reattachment region using surface flow visualization[16,25,27]. This structure was also observed in the present experiments by coating the ramp surface with a steam engine oil-zinc oxide mixture. This structure was absent in the recent experimental study of Settles, et. al.[9]. Thus, the existence of such spanwise motions are still a point of discussion and concern. Some detailed pressure measurements by Roshko and Thomke[25] have indicated that these secondary motions have very small effects on the static pressure distribution. The spanwise surface pressure distributions in two streamwise locations in the reattachment and redevelopment regions of the present study, which were discussed earlier and are shown in Fig. 5, are in agreement with the findings of Roshko and Thomke[25].

Uniformity of the mean velocity and turbulence field across the tunnel in the reattachment and redevelopment regions was confirmed by LDV measurements which were made ± 8.0 mm on either side of the centerline of the wind tunnel at x = 130 and 140 mm. The variation in data for the worst cases was ± 2.1% in the mean velocity, ± 2.8% in the streamwise turbulence intensity, and ± 2.7% in the shear stress. Since the turbulence

intensities and shear stress reached maximum values near x = 140 mm, these variations were within the statistical uncertainty of the finite sample sizes. LDV measurements further off-center were not possible due to reflections of laser light from the windows.

Based on the spanwise pressure measurements and off-center LDV measurements, it is concluded that the mean flowfield was uniform within a region ± 19 mm of the centerline. From LDV measurements, the turbulence field was shown to be uniform within ± 8.0 mm of the wind tunnel centerline.

Mean Flow Results

The mean velocity profiles for all stations are shown in Fig. 6. The abscissa shows the vertical station numbers, the dashed vertical lines show the locations of zero velocities for each station, and the number above the dashed lines show the x locations of the stations. The mean velocities were normalized by the approach freestream velocity, u_∞ = 571.82 m/s. The variation in freestream velocity above the shear layer was ± 1.4%. The mean flow has a wake profile until reattachment; after reattachment, the wake flow feature starts to diminish. The decay of the wake feature is so slow that even at the last station, the velocity profiles show some remnant of the wake profile.

The mean velocity vector field in the recirculation region is shown in Fig. 7. There was a single clockwise recirculating bubble which was centered above the leading apex of the ramp; in a similar ramp configuration experiment, Petrie, et. al.[11], found a similar recirculating bubble. Weinberg, et. al.[7] applied a Navier-Stokes code with an algebraic mixing length turbulence model to a similar ramp configuration with an approach Mach 2.92 flow and a ramp angle of 20 degrees and found two clockwise and one counterclockwise recirculating bubbles. It can be seen from Fig. 7 that the recirculating flow was directed toward the separation point. This was also noticed by Petrie, et. al.[11], but the Navier-Stokes' code of Weinberg, et. al.[7] did not capture this feature of the recirculating bubbles. This feature needs to be studied carefully since it could contribute to the onset of plume induced flow separation on afterbodies with a centered propulsive jet.

The maximum negative velocity measured in the base region was $0.2u_\infty$ which occurred where the minimum wall pressure was measured. Petrie, et. al.[11], in a similar experiment, Delery[28] with a transonic freestream and a supersonic propulsive jet, and Etheridge and Kemp[29] in a subsonic flow over a step measured maximum negative velocities of $0.19u_\infty$, $0.30u_\infty$, and $0.18u_\infty$, respectively.

The streamwise mean velocity profiles are shown in a non-dimensionalized y coordinate in Fig. 8. The variable δ is the shear or boundary layer thickness with the classical definition of $\delta = y_{.99} - y_0$ where y_0, $y_{.5}$, and $y_{.99}$ are the locations of $u = 0$, $0.5u_\infty$, and $0.99u_\infty$. As can be seen from this figure, the collapse of these data is good from two stations after separation up to one station after reattachment. The collapse of these data showed that in spite of a very large adverse pressure gradient, the mean flow in the recompression, reattachment, and initial part of the redeveloping region is in local equilibrium. It was surprising to see local equilibrium in the reattaching and redeveloping regions under such a large adverse pressure gradient. There are ample experimental results to support the existence of local equilibrium in boundary layer flows under moderate pressure gradients[30-32]. The similarity parameter, which is used to correlate some overall boundary layer shape parameter in supersonic flows, is the Clauser pressure gradient coefficient which is defined as $(\delta_k^*/\tau_w)(\partial p/\partial x)$ where δ_k^* is the boundary layer kinematic thickness and τ_w is the wall shear stress. In contrast to the above cited studies, no pressure term was used in the similarity parameter of the present results.

Self-similarity of the mean flow is achieved when the shear layer growth rate becomes linear. A detailed examination of the velocity data and constant velocity lines showed that the mean velocity self-similarity was achieved approximately $16\delta_0$ or $200\theta_0$ downstream of the step. Self-similarity in similar experiments by Petrie, et. al.[11], Settles, et. al.[9], and Ikawa and Kubota[12] were attained at $18.8\delta_0$, $18\delta_0$, and $22\delta_0$ downstream of the step, respectively. The growth rate of the free shear layer was 0.093 which was higher than the values of .078 and .062 obtained by Petrie, et. al.[11] and Ikawa and Kubota[12], respectively, and which was 1.74 times smaller than the incompressible shear layer growth rate of Liepmann and Laufer[33].

Turbulent Field Results

The streamwise component turbulence intensities are shown in Fig. 9. The x location of each station is given above the profiles. The vertical dashed line at each station shows the local zero. As can be seen, a very pronounced peak turbulence intensity developed just downstream of separation and gradually spread as the shear layer grew. This behavior was also observed by Petrie, et. al.[11] in supersonic, Delery[28] in transonic, and Driver and Seegmiller[34] in subsonic flows. The peak values increased through recompression and reached a maximum in the reattachment region and decayed afterwards. In the recirculating region, the turbulence intensity was very high; it was nearly constant at each vertical station and increased in the downstream direction.

The streamwise turbulence intensities nondimensionalized with u_∞ did not collapse onto a single curve as the mean velocity data did in Fig. 8. In Fig. 10 the maximum turbulence intensity at each station was used to non-dimensionalize the turbulence intensity data. The turbulence field for x > 30 mm is locally similar above the sonic line. This was also observed by Petrie, et. al.[11] in the free shear layer; however, it was surprising to see such local similarity existing in the turbulence field for the reattachment and redevelopment regions under such a large adverse pressure gradient. The maximum turbulence intensities occurred near $y = y_{.5}$ which was approximately coincident with the sonic line, see Fig. 1.

Hayakawa, et. al.[10] used a hot-wire anemometer for turbulence measurement in a similar geometry with an incoming Mach 2.92 flow with a turbulent boundary layer. Their results showed that the maximum mass flow fluctuations occurred in the supersonic region of the shear layer. The differences between the present results and Hayakawa's results could be due to the difference between turbulence fluctuation and mass flow fluctuation and/or due to difficulties involved in hot-wire calibration for local Mach numbers of 1.2 or less[10,35] where the maximum intensities occurred during the present study.

The non-dimensionalized transverse component turbulence intensities are shown in Fig. 11. In contrast to subsonic shear layers[36,37], the location of the v component maximum turbulence intensities shifted toward the lower velocity side of the mixing layer. The cause of this turbulence behavior change is perhaps the combined effects of compressibility and mean density change across the shear and redeveloping boundary layer. The v component turbulence intensity, non-dimensionalized with the maximum turbulence intensity at each station, collapsed above the sonic line as did the streamwise turbulence data.

Evolutionary profiles of the turbulent shear stress are shown in Fig. 12. In the calculation of the mean density, $\bar{\rho}$, some interpolations were involved, therefore, at Stations 12-17 the mean density is believed to be accurate within $\pm$ 6.0%. Similar to the u component turbulence intensity, a sharp peak in the shear stress profile developed soon after separation and spread as the shear layer grew. The shear stress increased through recompression, reattachment, and redevelopment of the boundary layer. The maximum shear stress values at each station occurred near the sonic line. The shear stress non-dimensionalized with the maximum shear stress at each station collapsed onto a single curve above the sonic line as did the turbulence intensities.

The shear stress fluctuations in the recirculating flow were negligibly small in comparison to the normal stress values, see Fig. 9. The large values of the turbulence intensities and the very low values of the shear stress in the recirculating flow could be indicative of a low frequency flapping motion of the reattaching shear layer. Subsonic flow results[34,38,39] showed relatively high shear stress in the recirculating flow.

The maximum turbulence intensities and shear stresses are shown in Fig. 13. The onset of pressure rise and the reattachment location are shown with pr and r in Fig. 13. The maximum u and v intensity components reached 15% and 7.5%, respectively, in the constant pressure shear layer. The ratio of the maximum u intensity to the maximum v intensity in the shear layer region was approximately 1/2 which was similar to that of Petrie, et. al.[11] but lower than the 2/3 reported for subsonic flows[37]. The maximum u and v component intensities were approximately 22% and 9%, respectively, and both occurred one station after reattachment. The maximum shear stress with the density term increased through recompression and reattachment and reached approximately 0.7% in the redeveloping boundary layer while the maximum shear stress without the density term leveled off at approximately 0.5% in the reattachment region.

All the experimental results for the subsonic shear layer reattachment in the backward facing step configuration reported in a review paper by Eaton and Johnson[40] showed the peak values of the maximum u component intensity and maximum shear stress occurred approximately one step height before reattachment followed with a rapid decay. The causes of the rapid decay of turbulence intensity and shear stress for subsonic flows in the reattachment region are not known. The candidate causes are: the stabilizing streamline curvature, the adverse pressure gradient, and the strong interaction with the wall[39,40]. Whatever the mechanism(s) is/are for subsonic flow, it seems that compressibility effects are more dominant in the supersonic flow reattachment and there is no turbulence fluctuation decay before or at reattachment.

In turbulence modeling using the turbulent kinetic energy or the shear stress transport equation, one needs to model the turbulent triple products. The evolutionary profiles of one component of the triple products are shown in Fig. 14. Similar to subsonic plane mixing layers and reattaching shear layers[34,39], the triple products were observed to be roughly antisymmetrical about the mixing layer center for all four components[8]. The $\langle(u')^3\rangle$ and $\langle u'(v')^2\rangle$ components reached the negative minimum in the upper portion and positive maximum in the lower portion of the shear layer which was similar to subsonic shear layers[34,36,39]. The $\langle(u')^2v'\rangle$ and $\langle(v')^3\rangle$ components reached positive maximum in the upper portion and negative minimum in the lower portion of the shear layer which were just the opposite of the subsonic reattaching free shear layers. Therefore, this appears to be another fundamental difference between compressible and incompressible shear layers which shows the different characteristics of the diffusion of turbulent kinetic energy in the transverse direction in compressible and incompressible shear layers.

Similar to incompressible reattaching shear layers[34,39], all four components of the triple products were negligibly small in the recirculating flow. Since the major contributions of triple products come from large scale turbulence and there is no large scale motion in the recirculating flow, this was expected. The local values of all four components of the triple products increased dramatically through recompression, reattachment, and redevelopment which meant large scale motion and increased length scale in these regions. This behavior was not observed in subsonic flows, rather the triple products on the wall side started decreasing before the reattachment region. Chandrsuda and Bradshaw[39] attributed this behavior to imposition of the v = 0 condition by the wall and limitation of the large eddies which are the major contributors of the triple products. Existence of large shear stresses, see Fig. 12, and large triple products could mean large scale motion and large turbulence length scales in the redeveloping boundary layer.

The turbulence production plays an important role in the streamwise evolution of separated

flowfields. The component of turbulence production which could be obtained experimentally with reasonable accuracy was the production by shear stresses, $Pr = -\rho\langle u'v'\rangle \partial u/\partial y$. The turbulence production profiles developed a peak soon after separation and spread as the shear layer grew, see Fig. 15. The peak value at each station was located around the sonic line and reached a maximum near the reattachment region and started decaying afterwards.

Conclusions

A detailed experimental study of reattaching compressible, turbulent, free shear layers using LDV technique was carried out. Local similarity of the mean flow was observed through the shear layer, the reattachment, and the initial part of the redeveloping boundary layer. The mean flow and the turbulence field above the sonic line correlated with the local shear or the local boundary layer thickness. The growth rate of the shear layer was 1.74 times less than that of incompressible shear layer. In contrast to incompressible reattaching shear layers, the turbulence intensities, shear stress, and turbulent triple products were significantly increased through reattachment. Existence of large turbulent triple products and large shear stress in the recompression, reattachment, and redevelopment regions indicated the presence of a large scale turbulence field in these regions. Evolution of the turbulence field in reattaching compressible shear layers seems to be very complex and offers a great challenge to turbulence modelers. Probably models based on the shear stress transport equation with relatively sophisticated models for the turbulent triple products are required.

Acknowledgment

This research was supported by the U.S. Army Research Office under contracts DAAG 29-79-C-0184 and DAAG 29-83-K-0043. Dr. Robert E. Singleton served as the Contract Monitor.

References

[1] Chapman, D. R., An Analysis of Base Pressure at Supersonic Velocities and Comparison with Experiment," NACA TN 2137, 1950.

[2] Korst, H. H., "A Theory for Base Pressures in Transonic and Supersonic Flow," Journal of Applied Mechanics, December 1956, pp. 593-600.

[3] Lees, L. and Reeves, B. L., "Supersonic Separated and Reattaching Laminar Flows: I. General Theory and Application to Adiabatic Boundary Layer/Shock Wave Interactions," AIAA Journal, Vol. 2, No. 11, 1964, pp. 1907-1920.

[4] Alber, I. E. and Lees, L., "Integral Theory for Supersonic Turbulent Base Flows," AIAA Journal, Vol. 6, No. 7, 1968, pp. 1343-1351.

[5] Marvin, J. G., "Turbulence Modeling for Computation/Aerodynamics (Invited)," AIAA Paper 82-0164, 1982.

[6] Horstmann, C. C., Settles, G. S., Bogdonoff, S. M., and Williams, D. R., "A Reattaching Free Shear Layer in Compressible Turbulent Flow - A Comparison of Numerical and Experimental Results," AIAA Journal, Vol. 20, No. 1, 1982, pp. 79-85.

[7] Weinberg, B. C., McDonald, H., and Shamroth, S. J., "Navier-Stokes Compuputations of Aft End Flow Fields," Final Report, U.S. Army Research Office Contract DAAG 29-79-C-0003, Scientific Research Associates, Inc., Glastonbury, Connecticut, May 1982.

[8] Samimy, M., "An Experimental Study of Compressible Turbulent Reattaching Free Shear Layers," Ph.D. Thesis, Department of Mechanical and Industrial Engineering, University of Illinois at Urbana-Champaign, 1984.

[9] Settles, G. S., Baca, B. K., Williams, D. R., and Bogdonoff, S. M., "A Study of Reattachment of a Free Shear Layer in Compressible, Turbulent Flow," AIAA Paper 80-1408, 1980. Also, AIAA Journal, Vol. 20, No. 1, 1982, pp. 60-67.

[10] Hayakawa, K., Smits, A. J., and Bogdonoff, S. M., "Turbulence Measurements in a Compressible Reattaching Shear Layer," AIAA Paper 83-0299, 1983. Also, AIAA Journal, Vol. 22, No. 7, 1984, pp. 889-895.

[11] Petrie, H. L., Samimy, M., and Addy, A. L., "A Study of Compressible Turbulent Free Shear Layers Using Laser Doppler Velocimetry," AIAA Paper 85-0177, 1985.

[12] Ikawa, H. and Kubota, T., "Investigation of Supersonic Turbulent Mixing Layer with Zero Pressure Gradient," AIAA Journal, Vol. 13, No. 5, 1975, pp. 566-572.

[13] Buchhave, P., "Biasing Errors in Individual Particle Measurements with the LDA-Counter Signal Processor," Proc. of LDV Symposium, Copenhagen, Denmark, 1975, pp. 258-278.

[14] Dimotakis, P. E., "Single Scattering Particle Laser Doppler Measurements of Turbulence," AGARD-CP-193, 1976, pp. 10-1 to 10-14.

[15] Whiffen, M. C., "Polar Response of an LV Measurement Volume," Proceedings of the Minnesota Symposium on Laser Velocimetry, University of Minnesota, 1975, pp. 589-590.

[16] Petrie, H. L., "A Study of Compressible Turbulent Free Shear Layers Using Laser Doppler Velocimetry," Ph.D. Thesis, Department of Mechanical and Industrial Engineering, University of Illinois at Urbana-Champaign, 1984.

[17] Erdmann, J. C. and Tropea, C., "Turbulence Induced Statistical Bias in Laser Anemometry," Proceedings of the Seventh Symposium on Turbulence, University of Missouri-Rolla, September 1981, pp. 129-138.

[18] Erdmann, J. C. and Tropea, C., "Statistical Bias of the Velocity Distribution Function in Laser Anemometry," International Symposium on Applications of Laser Doppler Anemometry to Fluid Mechanics, Lisbon, Portugal, July 1982, Paper 16.2.

[19] Kried, D. K., "Laser-Doppler Velocimeter Measurements in Nonuniform Flow: Error Estimates," Applied Optics, Vol. 13, No. 8, 1974, pp. 1872-1881.

[20] Karpuk, M. E. and Tiederman, W. G., "Effect of Finite-Size Probe Volume Upon Laser Doppler Anemometer Measurements," AIAA Journal, Vol. 14, No 8, 1976, pp. 1099-1105.

[21] Maise, G. and McDonald, H., "Mixing Length and Kinematic Eddy Viscosity in a Compressible Boundary Layer," AIAA Journal, Vol. 6, No. 1, 1968, pp. 73-80.

[22] Klebanoff, D. S., "Characteristics of Turbulence in a Boundary Layer with Zero Pressure Gradient," NACA Report No. 1247, 1955.

[23] Sandborn, V. A., "A Review of Turbulence Measurements in Compressible Flow," NASA TM X-62, 337, March 1974.

[24] Johnson, D. A. and Rose, W. C., "Laser Velocimeter and Hot-Wire Anemometer Comparison in a Supersonic Boundary Layer," AIAA Journal, Vol. 13, No. 4, 1975, pp. 512-515.

[25] Roshko, A. and Thomke, G. J., "Observations of Turbulent Reattachment Behind an Axisymmetric, Downstream-Facing Step in Supersonic Flow," AIAA Journal, Vol. 4, No. 6, 1966, pp. 975-980.

[26] Sirieix, M., Mirande, J., and Delery, J., "Experiences Fundamentales sur le Recollement Turbulent d un Jet Supersonique," NATO AGARD CP NO. 4, Part I, 1966, pp. 353-391.

[27] Inger, G. R., "Three-Dimensional Heat- and Mass-Transfer Effects across High-Speed Reattaching Flows," AIAA Journal, Vol. 15, No. 3, 1977, pp. 383-389.

[28] Delery, J. M., "ONERA Research on Afterbody Viscid/Inviscid Interaction with Special Emphasis on Base Flows," Proc. of the Symposium on Rocket/Plume Fluid Dynamic Interactions, Huntsville, Alabama, April 1983.

[29] Etheridge, D. W. and Kemp. P. H., "Measurements of Turbulent Flow Downstream of a Rearward-Facing Step," Journal of Fluid Mechanics, Vol. 86, Part 3, 1978, pp. 545-566.

[30] Laderman, A. J., "Adverse Pressure Gradient Effect on Supersonic Boundary Layer Turbulence," AIAA Journal, Vol. 18, No. 10, 1980, pp. 1186-1195.

[31] Lewis, J. E., Gran, R. L., and Kubota, T., "An Experiment on the Adiabatic Compressible Turbulent Boundary Layer in Adverse and Favorable Pressure Gradients," Journal of Fluid Mechanics, Vol. 51, Part 4, 1972, pp. 657-672.

[32] Coles, D., "Remarks on Equilibrium Turbulent Boundary Layers," Journal of the Aeronautical Sciences, Vol. 24, 1957, pp. 495-506.

[33] Liepmann, H. W. and Laufer, J., "Investigation of Free Turbulent Mixing," NACA TN 1257, 1947.

[34] Driver, D. M. and Seegmiller, H. L., "Features of Reattaching Turbulent Shear Layer Subject to an Adverse Pressure Gradient," AIAA Paper 82-1029, 1982.

[35] Kovasznay, L. S. G., "The Hot-Wire Anemometer in Supersonic Flow," Journal of Aeronautical Sciences, Vol. 71, Part 4, 1950, pp. 565-573.

[36] Wygnanski, I. and Fiedler, H. E., "The Two-Dimensional Mixing Region," Journal of Fluid Mechanics, Vol. 41, 1970, pp. 327-361.

[37] Champagne, F. H., Pao, Y. H., and Wygnanski, I. J., "On the Two-Dimensional Mixing Region," Journal of Fluid Mechanics, Vol. 74, Part 2, 1976, pp. 209-250.

[38] Bradshaw, P. and Wong, F. Y. F., "The Reattachment and Relaxation of Turbulent Shear Layer," Journal of FLuid Mechanics, Vol. 52, Part I, 1972, pp. 113-135.

[39] Chandrsuda, C. and Bradshaw, P., "Turbulence Structure of a Reattaching Mixing Layer," Journal of Fluid Mechanics, Vol. 110, 1981, pp. 171-194.

[40] Eaton, J. K. and Johnston, J. P., "A Review of Research on Subsonic Turbulent Flow Reattachment," AIAA Journal, Vol. 19, No. 9, 1981, pp. 1093-1100.

Figures

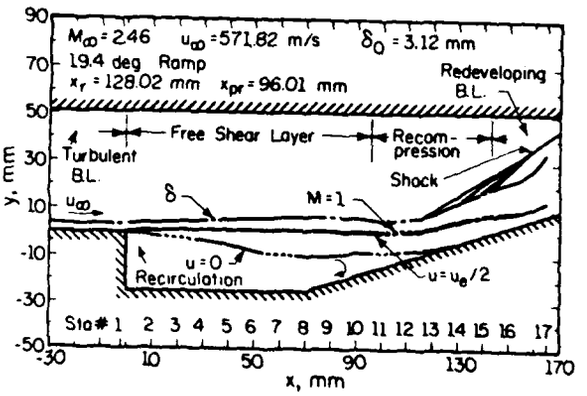

Fig. 1 Scaled map of the flowfield.

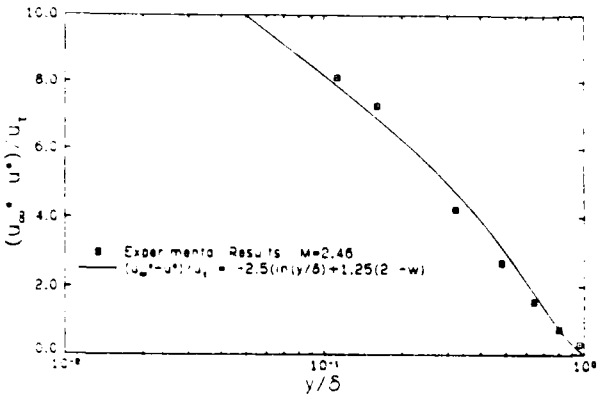

Fig. 2 Boundary layer mean velocity profile and generalized curve of Maise and McDonald[21].

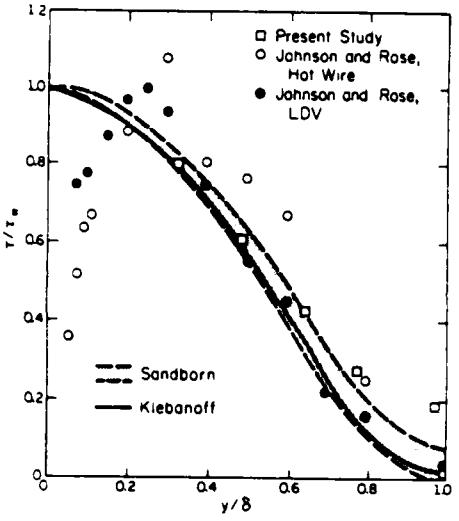

Fig. 3 Boundary layer shear stress profile.

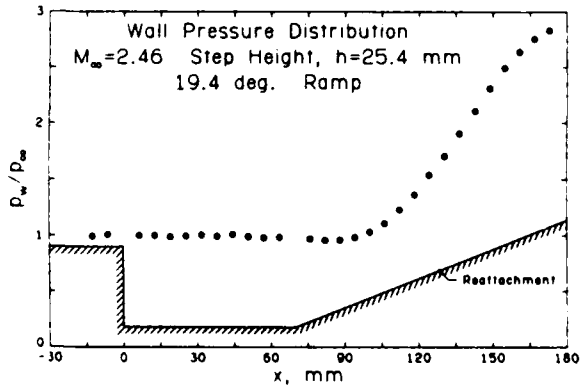

Fig. 4 Streamwise wall static pressure distribution measured on the model centerline.

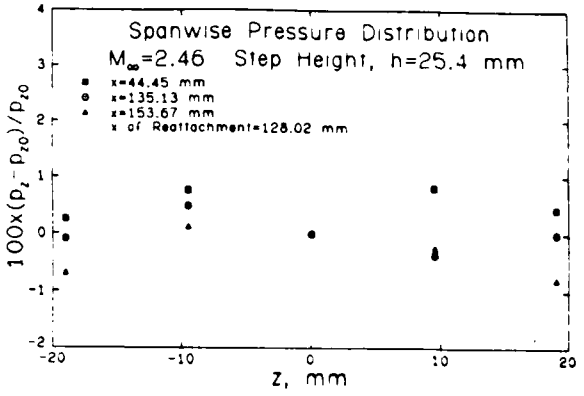

Fig. 5 Spanwise wall pressure distributions.

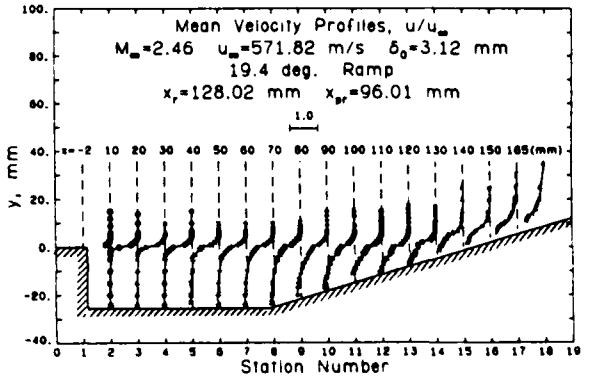

Fig. 6 Streamwise mean velocity profiles.

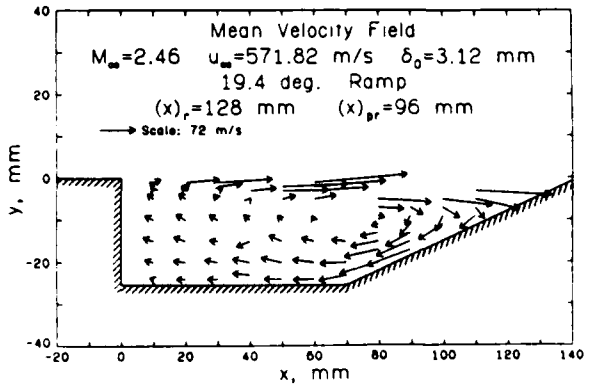

Fig. 7 The recirculating flow mean velocity vector field.

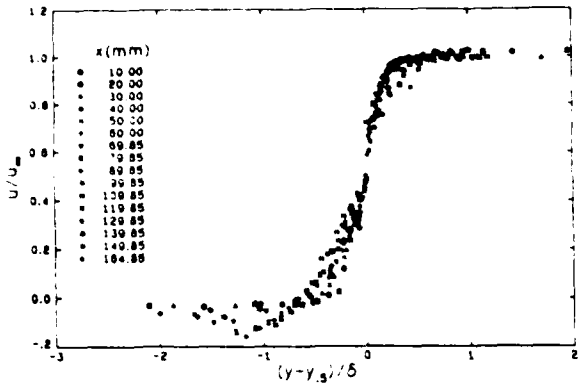

Fig. 8 Correlated streamwise mean velocity profiles.

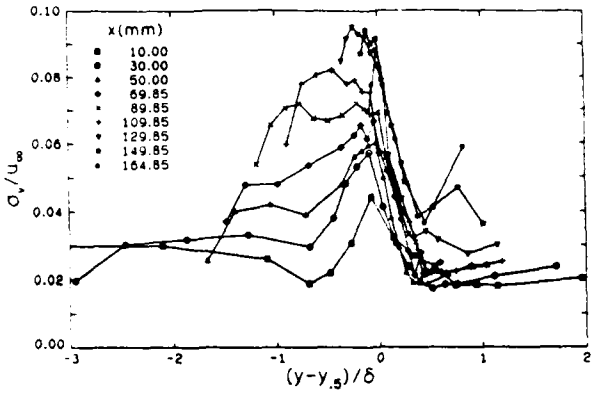

Fig. 11 Correlated transverse component turbulence intensity distributions.

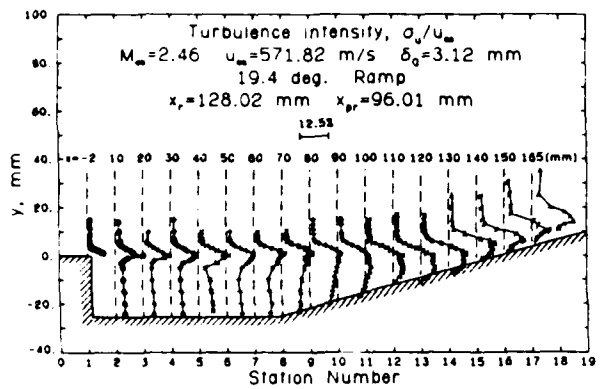

Fig. 9 Streamwise component of the turbulence intensity.

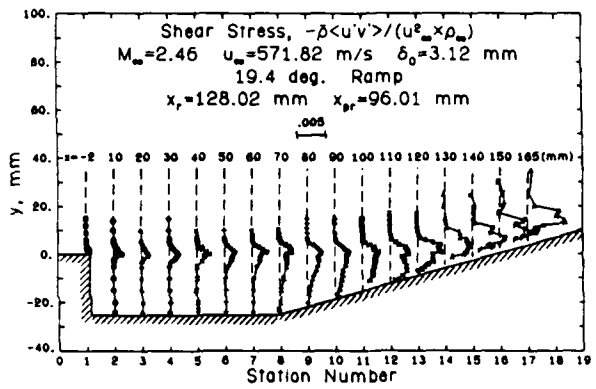

Fig. 12 Turbulent shear stress profiles.

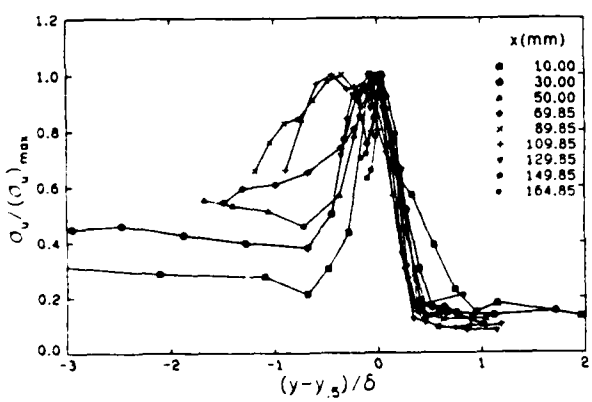

Fig. 10 Correlated streamwise turbulence intensity distributions.

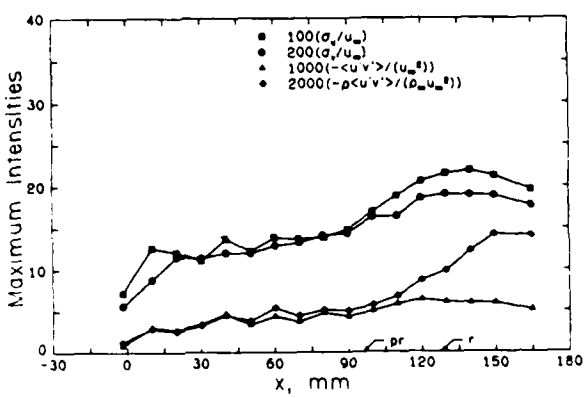

Fig. 13 Maximum turbulence fluctuations and shear stresses.

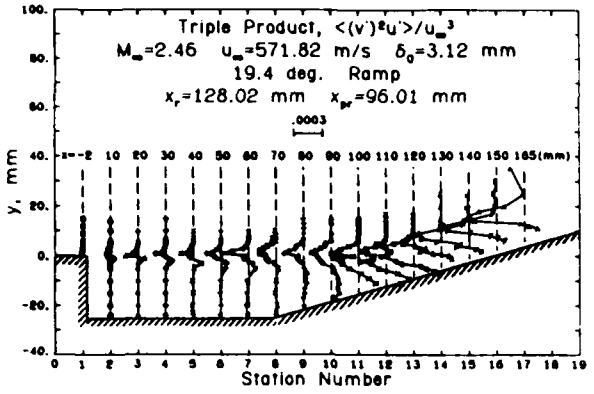

Fig. 14 Turbulent triple product.

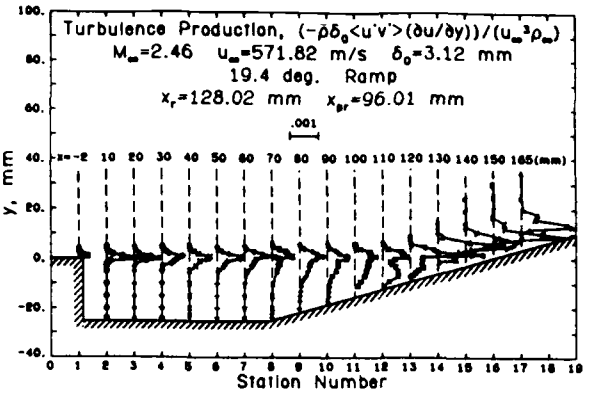

Fig. 15 Turbulence production.

SECTION B.6

REATTACHMENT AND REDEVELOPMENT OF COMPRESSIBLE TURBULENT FREE SHEAR LAYERS

Paper presented at the Winter Annual Meeting of ASME as part of the International Symposium on Laser Anemometry

Miami Beach, Florida

November 17-22, 1985

(Published as International Symposium on Laser Anemometry, FED-Vol. 33, New York, 1985, pp. 159-166)

by

M. Samimy, H. L. Petrie, and A. L. Addy

REATTACHMENT AND REDEVELOPMENT OF COMPRESSIBLE TURBULENT FREE SHEAR LAYERS

M. Samimy, Assistant Professor
Department of Mechanical Engineering
The Ohio State University
Columbus, Ohio

H. L. Petrie, Research Associate
Applied Research Laboratory
Pennsylvania State University
State College, Pennsylvania

A. L. Addy, Professor and Associate Head
Department of Mechanical and Industrial Engineering
University of Illinois at Urbana-Champaign
Urbana, Illinois

ABSTRACT

A series of experiments were conducted to investigate the recompression, reattachment, and redevelopment of a two-dimensional, compressible, turbulent free shear layer formed by the geometrical separation of a Mach 2.07 high Reynolds number flow with a turbulent boundary layer from a 25.4 mm high backward facing step. A detailed survey of the flowfield was made utilizing Schlieren technique, static pressure measurements, and a two-component laser Doppler velocimeter. The distortion of the turbulence field resulting from the boundary layer expansion at the step was found to produce a strong anisotropy which continued throughout the shear layer and was enhanced in the reattachment region. In comparison with similar shear layers which were produced without expansion at the step, higher level turbulence intensities and shear stresses were observed. The mean flow and turbulence field data and the Schlieren photographs indicated the existence of large scale turbulence in the reattachment and redevelopment regions and enhanced mixing by the large scale turbulence in the redevelopment region.

NOMENCLATURE

h	Step height
M	Mach number
p	Pressure
r	Location of reattachment
u	Mean velocity in the streamwise direction
u^*	Van Driest generalized velocity
u_τ	Friction velocity
x,y	Horizontal and vertical coordinates
$y_{.5}$	y component distant where $u = 0.5u_e$
δ	Boundary layer or shear layer thickness, where $u = 0.99u_e$
Π	Wave strength parameter
ρ	Density
σ	Standard deviation with subscript u or v
τ	Shear stress
$\langle\ \rangle$	Ensemble average

Superscripts

$\overline{\quad}$	Mean value
$'$	Fluctuation from mean value

Subscripts

e	Adjacent freestream value
pr	Start of pressure rise
r	Location of reattachment
w	Wall value and Coles wake function
∞	Freestream value before separation
0	Value of the boundary layer parameter just before separation
$0\ .5\ .99$	Location where $u = 0$, $0.5u_e$, and $0.99u_e$

INTRODUCTION

The reattachment and redevelopment of turbulent free shear layers occur in many practical engineering problems and have been the subject of numerous

[1] Associate Member ASME.
[2] Associate Member ASME.
[3] Fellow ASME.

investigations over the past three decades. Due to the complexity of the flowfield, the research efforts have been focused on simple geometries. Flow over a backward-facing step geometry, which has a fixed separation point and which contains all the features of the reattaching flows, has been widely used in experimental studies of subsonic (1-4)[4] and supersonic reattaching flows (5-8) in an effort to understand the reattachment and redevelopment processes and to identify flow mechanisms involved in these processes.

A data base has been developed for reattaching subsonic free shear layers and a basic understanding of such flows has been achieved (2). However, more experimental data are needed to clarify some of the speculations about the existence and role of the large eddies in the reattachment region. Numerous difficulties exist in obtaining accurate turbulence data in compressible reattaching free shear layers (6-8); therefore, much more work needs to be done for this type of flow. The overall objectives of this study were to investigate the compressible reattaching free shear layers, the effects of the boundary layer expansion at the step on the reattachment process, and to provide detailed data for analytical and computational modelers.

EXPERIMENTAL PROGRAM

A series of dry, cold air experiments were conducted in a small scale blowdown wind tunnel facility. The test section of the wind tunnel is shown in Fig. 1. The wind tunnel width was 50.8 mm and the step height was 25.4 mm. Information obtained from Schlieren photographs, static pressure measurements, and LDV results were used to construct Fig. 1, and the regions of the flowfield with distinct features are identified for later discussion. The curves of u = 0, $0.5u_e$, $0.99u_e$, where u_e is the adjacent freestream mean velocity, and the sonic line, M = 1, are shown in this figure. As can be seen, the M = 1 and u = $0.5u_e$ locations were nearly coincident all the way from the step to the redeveloping region. The station numbers, 1-15, refer to locations where the vertical surveys were made in the flowfield and are shown above the x-axis in Fig. 1.

The u velocity component direction was defined to correspond to the freestream flow direction; parallel to the x-coordinate at stations 1 and 12 through 15 and rotated 15.39 degrees in a clockwise direction relative to the x-coordinate at stations 2 through 11. The v velocity component was orthogonal to the corresponding u component.

The approach Mach number, Reynolds number, stagnation pressure, and stagnation temperature were 2.07, 6.69×10^7/m, 528.1 kPa, and 293K, respectively. The approach boundary layer and momentum thicknesses were 2.26 and 0.18 mm, respectively. The freestream velocity and Mach number after the expansion and after the recompression shock wave were (594.59 m/s and 2.74) and (512.37 m/s and 2.01), respectively.

Laser Doppler Velocimetry Considerations

A two-component coincident laser Doppler velocimeter (LDV) system was used to make the velocity measurements. The frequency of one beam of each beam pair was shifted by 40 MHz in order to detect velocity direction and to eliminate fringe bias (9-11). Lenses with focal lengths of 250 mm, 350 mm, and 600 mm were used for the velocity measurements within the incoming boundary layer, the initial part of the shear layer, and reattachment and redevelopment region, respectively. The measurement volume diameter and length for the 250 mm, 350 mm, and 600 mm focal length lenses were (0.131 and 1.83 mm), (0.183, 2.56 mm), and (0.314, 4.39 mm), respectively. The 600 mm lens produced a large fringe spacing and a large fringe velocity in the measurement volume. These were desirable LDV system characteristics because of the high turbulence intensities expected in the reattachment and redevelopment region and possible fringe bias problems that may have resulted from the two-component coincident requirement.

Seed particle generation was accomplished with a TSI Inc. six-jet atomizer. A 50 cP silicone oil was atomized and the effective mean diameter of the generated particles was estimated by measuring the relaxation of the velocity of particles downstream of an oblique shock wave (12). The results indicated that the effective mean particle diameter was approximately 1 μm. The seed particles of the present investigations should follow the mean flow in the major portion of the flowfield except in the immediate vicinity of the expansion and the shock waves. Also, the response of 1 μm particles to turbulence fluctuations is believed to be adequate in the range of energy containing eddies perhaps up to 100 kHz; for further discussion of LDV particle dynamics, see Reference 13.

The individual velocity realization type data processor used in these experiments had the capability of measuring and storing 83.3k coincident samples per second. The maximum data rate was approximately 2000 samples per second with the 250 and 350 mm lenses and 400 samples per second with the 600 mm lens. Therefore, the sampling process was totally controlled by the flow. Erdmann and Tropea (14,15) showed that this "free running" processor condition is completely velocity biased. The two-dimensional velocity inverse weighting factor was used to correct for velocity bias.

In the developing shear layer just downstream of the step, the velocity gradient across the shear layer was very large; therefore, errors in the velocity statistics due to spatial resolution were the largest. In this region, measurement errors due to spatial resolution were estimated to be approximately 0.9% in mean velocity and 1.9% in turbulence intensity (16). The statistical uncertainty due to the limited sample size was estimated to be approximately ± 3% in the mean velocity and ± 3.5 in the turbulence intensity in the recirculating region where the data rate was very low and only 1024 samples were collected. Elsewhere in the flowfield the statistical uncertainty was much lower.

The fringe bias analysis of Buchhave (9) was modified to incorporate frequency shifting and was then used to correct for possible fringe bias (16). The largest difference between the mean velocity results which were corrected and uncorrected for fringe bias was 3%. Consequently, only the uncorrected results are presented herein.

[4] Numbers in parentheses refer to entries in REFERENCES.

EXPERIMENTAL RESULTS

In this section, the experimental results are presented and compared to the results of previous studies. The nature of the incoming boundary layer, the pressure field, and the two-dimensionality of the flowfield are first discussed and then the results for the mean flow and the turbulent flow are presented.

Incoming Boundary Layer

Two-component and one-component velocity measurements were made to within 1 and 0.25 mm of the wall, respectively. The approach boundary layer and momentum thicknesses were determined to be 2.26 and 0.18 mm, respectively. The ratio of momentum thickness to boundary layer thickness was 0.0798 which was approximately 5% higher than the value predicted by the method of Maise and McDonald (17) for a similar Mach number.

Maise and McDonald (17) defined a single curve which was based on the wall-wake law coupled with the Van Driest compressibility transformation and showed that they could collapse experimental data from numerous equilibrium compressible boundary layer flows. The maximum scatter of the data relative to their curve was approximately 30%. Figure 2 shows the boundary layer mean velocity data of the current study in comparison with the Maise and McDonald curve. The maximum difference between the present data and their curve is approximately 7.5%. Figure 2 also shows the data from a recent Mach 2.46 boundary layer measurement conducted by the present authors (8). The skin friction coefficient, C_f, used in Fig. 2 was determined from the wall-wake law. The value of C_f determined by this method was 0.00176 which is in a good agreement with the values reported in the literature for similar Mach numbers (18).

Two-Dimensionality of the Flowfield

The wall static pressure distribution non-dimensionalized by the static pressure before the step is shown in Fig. 3. The accuracy of the pressure measurements was approximately ± 0.6%. As shown in Fig. 3, the pressure at the separation point decreased to approximately 30% of the pressure before the step and then there was a gradual decrease of 1.8% up to x = 25 mm. Downstream of this point, the pressure increased gradually up to x = 46 mm where the sharp increase in pressure started. Figure 3 shows an overshoot of the final recovery pressure of approximately 4.2% in the redeveloping region; this could be an indication of some three-dimensionality of the flowfield in the reattachment region.

Spanwise wall pressure measurements in the reattachment and redevelopment region indicated a pressure rise toward the side walls with a maximum pressure difference of 6.0% from the tunnel centerline pressure. This was another indication of three-dimensionality in the flowfield. In a recent investigation in the same wind tunnel, the present authors did not find any spanwise pressure rise in reattachment and redevelopment region with a fully developed free shear layer approaching the reattachment region (8). In the present study, the shear layer approaching the reattachment region was still in the developing stage. Therefore, it appears that the state of the shear layer approaching the reattachment region influences the two-dimensionality of the flowfield in the reattachment and redevelopment region.

Uniformity of the mean velocity and turbulence field across the tunnel in the reattachment and redevelopment region was evaluated by LDV measurements which were made at ± 8.0 mm on either side of the centerline of the wind tunnel at x = 68 and 78 mm. The variation in data for the worst cases was ± 2.3% in the mean velocity, ± 3.1% in the streamwise turbulence intensity, and ± 2.9% in the shear stress. Since the turbulence intensities and shear stresses were very high in these two stations, these variations were within the statistical uncertainty of the finite sample sizes. LDV measurements further off-center were not possible due to reflections of the laser light from the windows. Although the two-dimensionality of the flowfield deteriorated toward the side walls, it was concluded from the LDV measurement that the flowfield was two-dimensional within ± 8.0 mm of the wind tunnel centerline.

Mean Flow Results

The mean velocity profiles for all vertical measurement stations are shown in Fig. 4. The abscissa shows the vertical station numbers, each dashed vertical line indicates the location of zero velocity for that station, and the numbers above the dashed lines provide the x locations of the stations. The mean velocities were normalized by the approach boundary layer freestream velocity, u_∞ = 520.76 m/s. The mean flow in the shear layer region has a wake profile until reattachment; after the reattachment, the wake flow feature starts to diminish. Only the last two stations show boundary layer-type profiles.

A single clockwise recirculating bubble was detected in the recirculating region with a maximum negative velocity of 153.79 m/s ($0.26u_e$). The maximum reverse flow velocity occurred where the minimum wall pressure was measured. In other investigations with supersonic flows (8,19) and with subsonic flow (20) over backward steps, the maximum reverse flow velocities on the order of $0.2u_e$ have been measured.

The streamwise mean velocity profiles are shown in a non-dimensionalized y coordinate in Fig. 5. The variable δ is the shear layer or boundary layer thickness with the classical definition of $\delta = y_{.99} - y_0$ where y_0, $y_{.5}$, and $y_{.99}$ are the locations of $u = 0$, $0.5u_e$, and $0.99u_e$ and u_e is the adjacent freestream velocity. As can be seen, the collapse of these data using this non-dimensional coordinate is good from separation up to x = 100 mm. The collapse of these data indicated that in spite of a very large adverse pressure gradient, the mean flow in the recompression, reattachment, and initial part of the redeveloping region is in local equilibrium. Local similarity was also observed in another set of experiments in the reattachment and redevelopment region by the present author (8). There are many experimental results to support the existence of local similarity in boundary layer flows under moderate pressure gradients (18,21,22). All of these studies have used a pressure gradient term in the similarity parameter; however, no pressure term was used in the similarity parameter of the present results.

Final pressure recovery was achieved after station 12 where it appears that the wake component has vanished. There is a noticeably fast filling out of the velocity profiles after station 12 in the

redeveloping region. Selected velocity profiles in the redeveloping region are replotted in Fig. 6. While the profile at x = 78 mm is a wake profile, at the last station, x = 145 mm, the velocity ratio reaches 0.9 at 0.48 away from the wall. Settles, et. al. (6) continued their measurements further downstream and noticed even faster filling out of the profiles. This behavior suggests enhanced mixing by large scale turbulence motion. As will be discussed later, the existence of large scale turbulence was also indicated by the presence of large shear stresses and turbulent triple products in the reattachment and redevelopment region.

The redeveloping boundary layer wake-strength parameter, Π, is shown in Fig. 7. The Π values varied from 13.6 at x = 100 mm, which is just before complete recovery, to 1.4 at the last station, x = 145 mm. Settles, et. al. (6) continued their survey much further downstream of the reattachment location than in the present experiments and they observed that the wake-strength parameter continued to decrease and finally dropped below the equilibrium value at their last station. In a subsonic reattaching shear layer flow, Bradshaw and Wong (1) continued their survey much further downstream of reattachment and concluded that the wall-wake law was not applicable until approximately 30 incoming shear layer thickness downstream of the reattachment location. Also, the friction coefficient, C_f, which was determined from the all-wake profiles in the present study, varied from 0.00014 at x = 115 mm to 0.00107 at the last station; the expected equilibrium value of C_f was approximately 0.00150.

Turbulent Field Results

The streamwise turbulence intensities in a non-dimensionalized y coordinate is shown in Fig. 8. As can be seen, the turbulence data did not collapse onto a single curve as the mean velocity data did in Fig. 5. Also, the streamwise turbulence intensity profiles did not collapse when non-dimensionalized by the maximum intensity at each station. In recent experiments by the present authors, a Mach 2.46 turbulent boundary layer flow was separated at a constant pressure at a backward-facing step to form a long constant pressure shear layer which reattached onto a ramp (8). In these experiments, non-dimensionalizing the streamwise turbulence intensities and shear stresses by the maximum values at each station collapsed the profiles above the sonic line in the free shear layer, the reattachment region, and the initial part of the redeveloping boundary layer. In the present experiments, the free shear layer approaching the reattachment region was still in the developing stage. Thus, the observed difference could be caused by the state of the shear layer approaching the reattachment and/or by the expansion of the boundary layer at the step in the present experiment which appears to distort the turbulence field and cause higher turbulence intensities and shear stresses in the developing shear layer.

As can be seen in Fig. 1, the maximum turbulence intensities in the free shear layer and in the reattachment region occurred near $y = y_{.5}$ which was nearly coincident with the sonic line. This behavior was also observed in other supersonic (8,19) and subsonic (23,24) free shear layer experiments.

Evolutionary profiles of the turbulent shear stress are shown in Fig. 9. The x location of each station is given above the profiles. The vertical dashed line at each station shows the local zero location. In the calculation of the mean density, $\bar{\rho}$, some interpolations were involved; at stations 7-15, the mean density is believed to be accurate within $\pm$ 6.0%. As can be seen in Fig. 9, a very pronounced peak in the shear stress profile developed just downstream of separation and gradually spread as the shear layer grew. This behavior was also observed in streamwise turbulence intensity profiles. Similar trends were observed by the present authors in other supersonic shear flows (8,19), by Delery (25) in transonic shear flows, and by Driver and Seegmiller (4) in subsonic shear flows. The maximum shear stress values occurred near the sonic line. In the redeveloping region, the shear stress values were extremely high and decayed rapidly in the streamwise direction. These large shear stress values in the redeveloping boundary layer are another sign of the existence of large eddies in this region of the flowfield.

The ratios of shear stress fluctuations in the recirculating flow to the maximum shear stress at each station was noticeably smaller than the corresponding normal stress ratios. This was also observed in other compressible free shear layers (8,19,25). The large values of the turbulence intensities and the very low values of the shear stress in the recirculating flow could be an indication of a low frequency flapping motion of the reattaching free shear layer. In contrast, subsonic shear flow results (1-4) showed relatively high shear stresses in the recirculating flow.

The maximum turbulence intensities and shear stresses are shown in Fig. 10. The onset of the pressure rise and the reattachment location are identified in Fig. 10 by pr and r, respectively. The dotted lines in Fig. 10 indicate the change of the velocity coordinate system, as was discussed in the experimental program section. The maximum u and v fluctuation components reached approximately 25% and 8%, respectively, in the constant pressure shear layer. The ratio of the maximum u intensity to the maximum v intensity in the shear layer region was approximately 1/3 which was lower than the 1/2 reported for free shear layers without expansion at the step (8,19) and much lower than the 2/3 reported for subsonic flows (24). This high anisotropy level, as well as, the higher normal and shear stresses in the free shear layer of the present experiments appear to be the result of the distortion of the turbulence field passing through the expansion waves at the step.

The maximum u and v component turbulence intensities were 36% and 22%, respectively, and occurred in the reattachment region. The anisotropy ratio, σ_u/σ_v, reached approximately 1/3.5 in this region. The maximum shear stress values also occurred in the reattachment region. The experimental results for subsonic reattaching shear layers (2) showed that the peak values of the maximum u component intensity and maximum shear stress occur about one step height upstream of reattachment and are followed by a rapid decay. The v = 0 constraint at the wall at the reattachment location is cited as the probable cause for this behavior in subsonic flows (2,3). Whatever the cause(s) is/are for subsonic flow, it seems that compressibility effects are more dominant in supersonic flow reattachment and there is no turbulence fluctuation decay before reattachment.

The evolutionary profiles of one component of the turbulent triple products are shown in Fig. 11.

Similar to subsonic plane mixing layers and reattaching free shear layers (3,4), all four components of the triple products were observed to be roughly antisymmetrical about the mixing layer center. Similar to subsonic flows, the $\langle(u')^3\rangle$ and $\langle u'(v')^2\rangle$ components of the triple products reached minimum values in the upper part of the shear layer and maximum values in the lower part of the shear layer. In contrast to subsonic flows, the $\langle(u')^2v'\rangle$ and $\langle(v')^3\rangle$ components of the triple products reached maximum values in the upper and minimum values in the lower part of the shear layer. This seems to be another fundamental difference between compressible and incompressible shear layers which is related to the different characteristics of the diffusion of turbulent kinetic energy in the transverse direction.

All four components of the triple products significantly increased through recompression, reattachment and the initial part of the redeveloping boundary layer; this indicated that large scale motion and increased length scales existed in these regions. These results also support the similar conclusions drawn from Figs. 4, 6, and 9. In subsonic flows (3,4), the triple products on the wall side started decreasing before the reattachment region. This behavior was attributed (3) to imposition of the $v = 0$ condition by the wall at the reattachment location and the limitation of the large eddies which are the major contributors to the triple products.

CONCLUSIONS

Detailed experimental results of the reattachment and redevelopment of compressible turbulent free shear layers using LDV were documented. Expansion of the flow at the step appeared to produce a significant distortion in the turbulence field, stronger anisotropy, and larger turbulence intensities and shear stresses just downstream of the separation location which were enhanced through recompression and reattachment. The mean streamwise velocity profiles but not the turbulence field profiles correlated well with the local shear layer thickness or the local redeveloping boundary layer thickness. In contrast to incompressible reattaching shear flows, the existence of large shear stresses and amplified turbulence triple products in the reattachment region indicated the existence of large scale turbulence in this region. The very rapid "filling out" of the mean velocity profile and the rapid decay of the shear stresses and triple products in the redeveloping region were attributed to enhanced mixing in the redeveloping boundary layer due to these large structures.

ACKNOWLEDGMENT

This research was supported by the U.S. Army Research Office under contracts DAAG 29-79-C-0184 and DAAG 29-83-K-0043. Dr. Robert E. Singleton served as the Contract Monitor.

REFERENCES

1. Bradshaw, P. and Wong, F. Y. F., "The Reattachment and Relaxation of Turbulent Shear Layer," Journal of Fluid Mechanics, Vol. 52, Part I, 1972, pp. 113-135.

2. Eaton, J. K. and Johnston, J. P., "A Review of Research on Subsonic Turbulent Flow Reattachment," AIAA Journal, Vol. 19, No. 9, 1981, pp. 1093-1100.

3. Chandrsuda, C. and Bradshaw, P., "Turbulence Structure of a Reattaching Mixing Layer," Journal of Fluid Mechanics, Vol. 110, 1981, pp. 171-194.

4. Driver, D. M. and Seegmiller, H. L., "Features of Reattaching Turbulent Shear Layer Subject to an Adverse Pressure Gradient," AIAA Paper 82-1029, 1982.

5. Roshko, A. and Thomke, G. J., "Observations of Turbulent Reattachment Behind an Axisymmetric, Downstream-Facing Step in Supersonic Flow," AIAA Journal, Vol. 4, No. 6, 1966, pp. 975-980.

6. Settles, G. S., Baca, B. K., Williams, D. R., and Bogdonoff, S. M., "A Study of Reattachment of a Free Shear Layer in Compressible, Turbulent Flow," AIAA Paper 80-1408, 1980. Also, AIAA Journal, Vol. 20, No. 1, 1982, pp. 60-67.

7. Hayakawa, K., Smits, A. J., and Bogdonoff, S. M., "Turbulence Measurements in a Compressible Reattaching Shear Layer," AIAA Paper 83-0299, 1983. Also, AIAA Journal, Vol. 22, No. 7, 1984, pp. 889-895.

8. Samimy, M., Petrie, H. L., and Addy, A. L., "A Study of Compressible Turbulent Reattaching Free Shear Layers," AIAA Paper 85-1646, 1985; also will be published in the February issue of the AIAA Journal.

9. Buchhave, P., "Biasing Errors in Individual Particle Measurements with the LDA-Counter Signal Processor," Proc. of LDV Symposium, Copenhagen, Denmark, 1975, pp. 258-278.

10. Dimotakis, P. E., "Single Scattering Particle Laser Doppler Measurements of Turbulence," AGARD-CP-193, 1976, pp. 10-1 to 10-14.

11. Whiffen, M. C., "Polar Response of an LV Measurement Volume," Proceedings of the Minnesota Sumposium on Laser Velocimetry, University of Minnesota, 1975, pp. 589-590.

12. Petrie, H. L., "A Study of Compressible Turbulent Free Shear Layers Using Laser Doppler Velocimetry," Ph.D. Thesis, Department of Mechanical and Industrial Engineering, University of Illinois at Urbana-Champaign, 1984.

13. Samimy, M., "An Experimental Study of Compressible Turbulent Reattaching Free Shear Layers," Ph.D. Thesis, Department of Mechanical and Industrial Engineering, University of Illinois at Urbana-Champaign, 1984.

14. Erdmann, J. C. and Tropea, C., "Turbulence Induced Statistical Bias in Laser Anemometry," Proceedings of the Seventh Symposium on Turbulence, University of Missouri-Rolla, September 1981, pp. 129-138.

15. Erdmann, J. C. and Tropea, C., "Statistical Bias of the Velocity Distribution Function in Laser Anemometry," International Symposium on Applications of Laser Doppler Anemometry to Fluid Mechanics, Lisbon, Portugal, July 1982, Paper 16.2.

16. Kried, D. K., "Laser-Doppler Velocimeter Measurements in Nonuniform Flow: Error Estimates," Applied Optics, Vol. 13, No. 8, 1974, pp. 1872-1881.

17. Maise, G. and McDonald, H., "Mixing Length and Kinematic Eddy Viscosity in a Compressible Boundary Layer," AIAA Journal, Vol. 6, No. 1, 1968, pp. 73-80.

18. Laderman, A. J., "Adverse Pressure Gradient Effect on Supersonic Boundary Layer Turbulence," AIAA Journal, Vol. 18, No. 10, 1980, pp. 1186-1195.

19. Petrie, H. L., Samimy, M. and Addy, A. L., "A Study of Compressible Turbulent Free Shear Layers Using Laser Doppler Velocimetry," AIAA Paper 85-0177, 1985.

20. Etheridge, D. W. and Kemp, P. H., "Measurements of Turbulent Flow Down-stream of a Rearward-Facing Step," Journal of Fluid Mechanics, Vol. 86, Part 3, 1978, pp. 545-566.

21. Lewis, J. E., Gran, R. L., and Kubota, T., "An Experiment on the Adiabatic Compressible Turbulent Boundary Layer in Adverse and Favorable Pressure Gradients," Journal of Fluid Mechanics, Vol. 51, Part 4, 1972, pp. 657-672.

22. Coles, D., "Remarks on Equilibrium Turbulent Boundary Layers," Journal of the Aeronautical Sciences, Vol. 24, 1957, pp. 495-506.

23. Wygnanski, I. and Fiedler, H. E., "The Two-Dimensional Mixing Region," Journal of Fluid Mechanics, Vol. 41, 1970, pp. 327-361.

24. Champagne, F. H., Pao, Y. H., and Wygnanski, I. J., "On the Two-Dimensional Mixing Region," Journal of Fluid Mechanics, Vol. 74, Part 2, 1976, pp. 209-250.

25. Delery, J. M., "ONERA Research on Afterbody Viscid/Inviscid Interaction with Special Emphasis on Base Flows," Proc. of the Symposium on Rocket/Plume Fluid Dynamic Interactions, Huntsville, Alabama, April 1983.

FIGURES

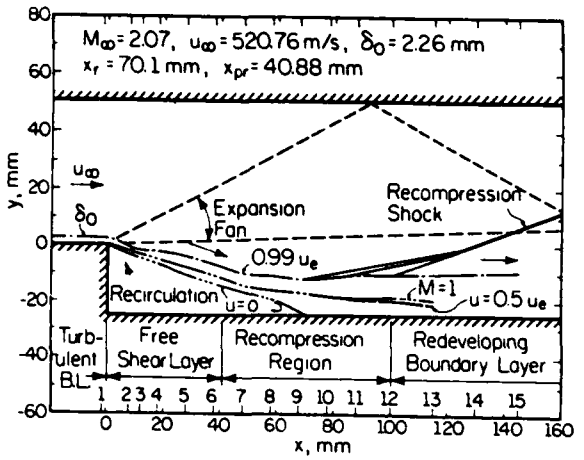

Fig. 1 Scaled map of the flowfield.

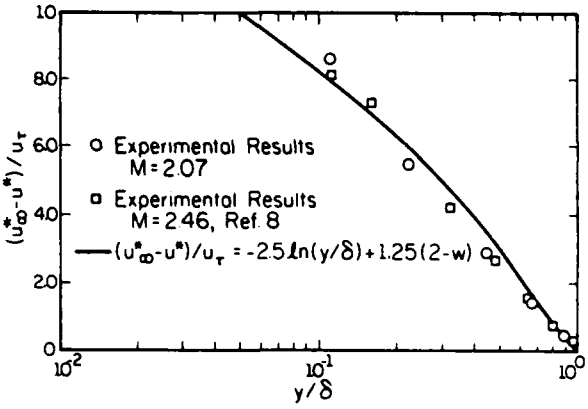

Fig. 2 Boundary layer mean velocity profile and generalized curve of Maise and McDonald [17].

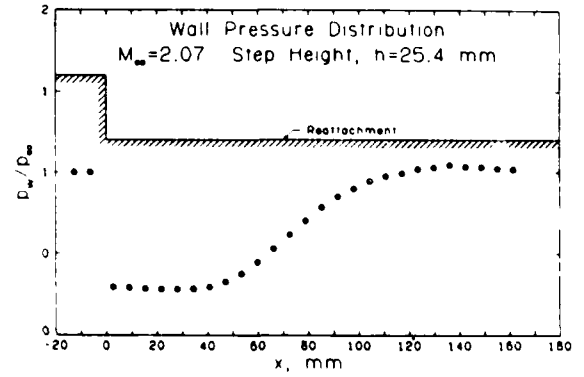

Fig. 3 Streamwise wall static pressure distribution measured on the model centerline.

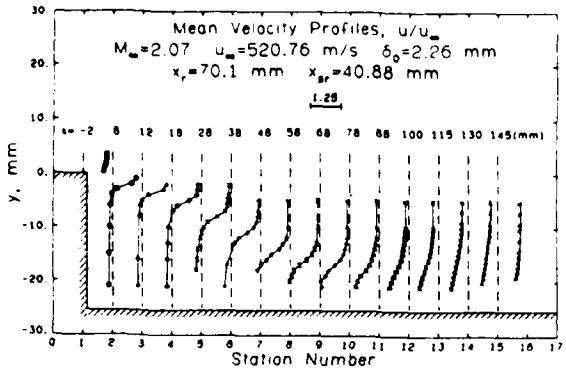

Fig. 4 Streamwise mean velocity profiles.

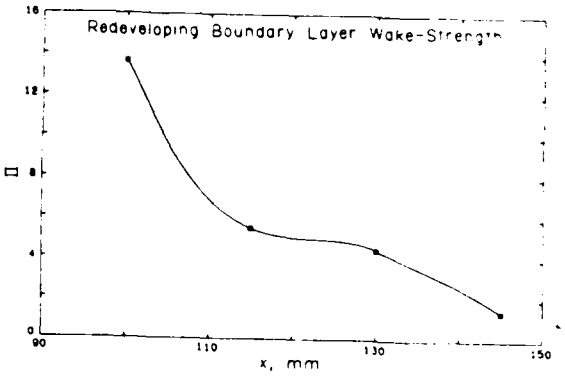

Fig. 7 The redeveloping boundary layer wake-strength parameter.

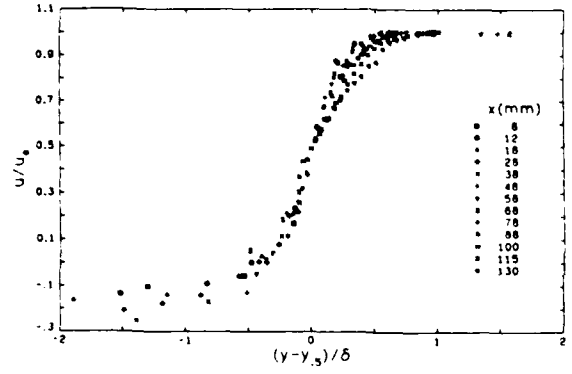

Fig. 5 Correlated streamwise mean velocity profiles.

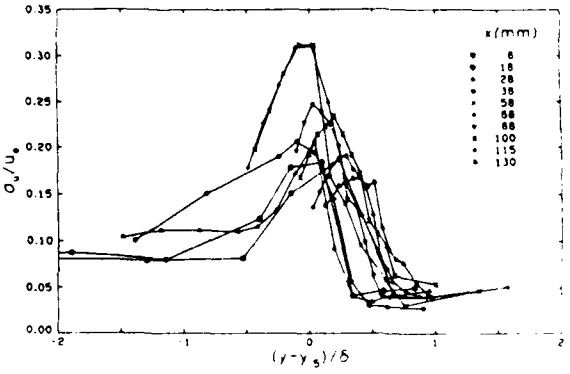

Fig. 8 Streamwise turbulent intensity distributions.

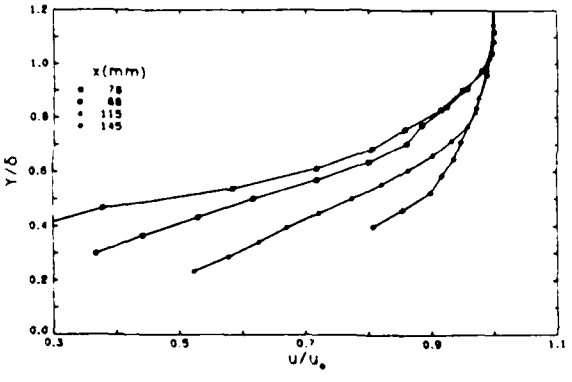

Fig. 6 Streamwise mean velocity profiles in the redeveloping region; Y is the vertical distance from the wall.

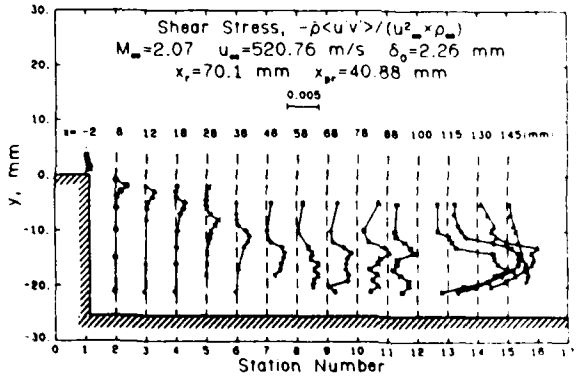

Fig. 9 Turbulent shear stress profiles.

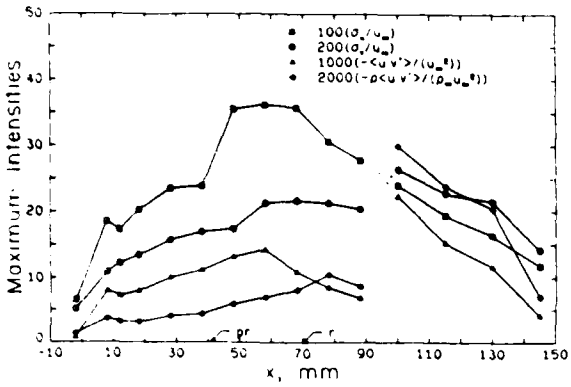

Fig. 10 Maximum turbulence fluctuations and shear stress.

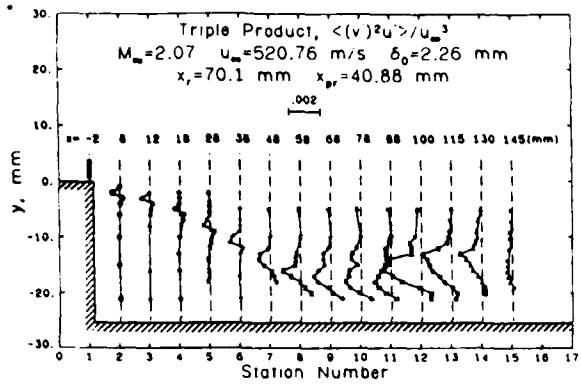

Fig. 11 Turbulent triple product distributions.

SECTION B.7

INTERACTION BETWEEN TWO COMPRESSIBLE TURBULENT FREE SHEAR LAYERS

Paper No. AIAA-86-0443

Presented at the AIAA 24th Aerospace Sciences Meeting

Reno, Nevada

January 6-9, 1986

by

M. Samimy and A. L. Addy

AIAA'86

AIAA-86-0443

Interaction Between Two Compressible Turbulent Free Shear Layers

M. Samimy, The Ohio State Univ., Columbus, OH; and A. L. Addy, Univ. of Illinois, Urbana, IL

AIAA 24th Aerospace Sciences Meeting

January 6-9, 1986/Reno, Nevada

INTERACTION BETWEEN TWO COMPRESSIBLE TURBULENT FREE SHEAR LAYERS

M. Samimy*
Mechanical Engineering Department
The Ohio State University
Columbus, OH 43210

A.L. Addy**
Mechanical and Industrial
Engineering Department
University of Illinois
Urbana, IL 61801

Abstract

Experimental results of interaction between two compressible, two-dimensional, turbulent free shear layers is presented. The shear layers were formed by geometrical separation of two high Reynolds number turbulent boundary layer flows with Mach numbers 2.07 and 1.50 from a 25.4 mm high backward-facing step. A two-component coincident laser Doppler velocimeter was utilized for a detailed flowfield survey. Both shear flows show general features similar to those of compressible free shear layers reattaching onto a solid surface; large scale turbulence in the recompression and reattachment regions and very enhanced mixing in the redeveloping region. The free shear layer with lower freestream Mach number shows high turbulence intensities and higher rate of increase of turbulence intensities in streamwise direction which appear to be caused by higher entrainment of reversed flow recirculating from highly turbulent reattachment region.

Introduction

This study is part of an extensive research program to investigate recompression and reattachment of compressible turbulent free shear layers and subsequent redeveloping boundary layers. The experimental efforts of this research have been focused on simple two-dimensional backward-facing step geometries. These types of simple models which have fixed separation point, and contain all the features of the separated flows, have been widely used for many years in subsonic and supersonic flows[1-9].

Three different configurations have been investigated in this research program in order to gain some basic knowledge about high velocity separated flows. In the first configuration[6], a Mach 2.46 flow with turbulent boundary layer separated at a 25.4 mm step and formed a free shear layer which attached onto a ramp. The position and angle of the ramp was adjusted so that the incoming boundary layer separated at the step without any pressure change. The detailed turbulence results showed a gradual increase of turbulence intensities and shear stress through the constant pressure shear layer, strong increase through the recompression and reattachment zone, and a gradual decrease after the reattachment. This was in sharp contrast to incompressible shear flow results which show sharp decay of turbulence intensity and shear stress upstream of the reattachment location. The maximum local turbulence intensities and shear stresses occurred around sonic line in each vertical survey which was in disagreement with earlier hot-wire results[5] which showed these parameters peaked in supersonic region of the shear layer. Large scale turbulence in the lower edge of the shear layer at the reattachment region and very enhanced mixing in redeveloping boundary layer were detected which confirmed the earlier observations[4].

In the second configuration[7], a Mach 2.07 flow with a turbulent boundary layer separated at the step and subsequently formed free shear layer attached onto a flat plate which was parallel to the incoming boundary layer flow direction. The general trends of turbulence intensities and shear stress were similar to those obtained in first configuration with the exception of much higher fluctuations levels and higher anisotropy ratio. Since the Mach and Reynolds numbers of free shear layers in two configurations were comparable, therefore, the differences seem to be caused by distortion of turbulence field through the expansion at the step of the second configuration. Also, the streamwise turbulence intensity increase through the separation at the step for the backstep experiment was approximately 1.3 higher than the ramp results. These results were in sharp contrast to the earlier observations by Schlieren technique[10,11] and measurements made by hot-wire technique[12] which all showed decay of turbulence level through expansion at the step. Some systematic experiments needed to clarify this discrepancy.

In the third configuration which is the subject of this paper, the interaction between two shear flows was investigated; see Fig. 1. The objective was further exploration of the compressible shear flows especifically effects of interaction of shear flow with solid wall at the reattachment on turbulence scale and structure.

Experimental Program

A series of dry, cold air experiments were conducted in a small scale blowdown wind tunnel facility. The wind tunnel width and height were 50.8 and 101.6 mm, respectively, and the step height was 25.4 mm; see Fig. 1. The approach Mach number, Reynolds number, stagnation pressure, and stagnation temperature were 2.07, 5.85×10^7/m, 457.3 kPa, and 295 K, respectively, for the upper boundary layer and 1.50, 3.37×10^7/m, 233.8 kPa,

* Assistant Professor, Member AIAA
** Professor and Associate Head, Associate Fellow AIAA

and 205 K, respectively, for the lower boundary layer. The freestream Mach and Reynolds number after expansion at the step were 2.56 and 3.98 x 10^7/m, respectively, for the upper shear flow and 2.23 and 2.32 x 10^7/m, respectively, for the lower shear flow. The Mach and Reynolds numbers of the upper free shear flow and two earlier configurations[6,7] were designed to be comparable for comparison of data.

For the ease of presentation of the results, the dashed line in Fig. 1 is used to separate the upper flow from the lower flow. The u velocity component direction was defined to correspond to the freestream flow direction; parallel to the x-coordinate for the incoming boundary layer flows, rotated 12.4 degrees relative to the x-coordinate in a clockwise direction for the upper shear flow, and rotated 18.5 degrees in counter-clockwise direction for the lower shear flow. The v velocity component was orthogonal to the corresponding u component.

A two-component coincident laser Doppler velocimeter (LDV) system was used to make the velocity measurements. The detailed LDV consideration and errors involved have been reported earlier[5,6], and will not be repeated here. The LDV results reported here are corrected for velocity bias. The fringe bias correction was found unnecessary by using large focal length lens in highly turbulence region of the flowfield. Silicone oil particles with mean diameter of 1 μm were used for seeding the flow. The spatial resolution was better than 1% for the mean flow and 1.8% for the second order fluctuations measurements. The statistical uncertainty due to limited number of samples was better than ±2.8% for the mean flow and ±3.2% for the turbulence intensity measurements.

Experimental Results

The Approach Boundary Layer

Two-component and one-component velocity measurements were made to within 1 and 0.25 mm of the wall, respectively. The approach boundary layer and momentum thicknesses for the upper and lower boundary layers were measured to be (2.26 and 0.18 mm) and (1.50 and 0.14 mm), respectively. The ratio of momentum thickness to boundary layer thickness for the upper and lower flows were approximately 5% and 1%, respectively, higher than the values predicted by the method of Maise and McDonald[13]. Based on these and earlier results[6,7], it appears that Maise and McDonald's prediction of compressible turbulent boundary layer momentum to boundary layer thicknesses ratio is in better agreement with experimental results in low Mach numbers.

Figure 2 shows the boundarylayers mean velocity data of the present study in comparison with the Maise and McDonald curve[13]. The Mach 1.50 boundary layer results show much better agreement with the curve than the Mach 2.07 results do. The skin friction coefficients, C_f, used in Fig. 2 were determined from the wall-wake law which were 0.00176 and 0.00247 for the upper and lower flows, respectively. These friction factors are in the range of values reported by Laderman[14] for comparable Mach and Reynolds numbers.

The boundary layer streamwise turbulence intensity results for both flows show consistently higher values than those for incompressible flow of Klebanoff[15], but in relatively good agreement with the data of Dimotakis, et. al.[16] with comparable Mach numbers. The boundary layer shear stress profiles follow closely Sandborn's[17] "best estimate" for equilibrium compressible boundary layer. The streamwise component of skewness and flatness factors peak sharply at the outer edge of the boundary layers for both flows, then decline rapidly for the upper boundary layer and gradually for the lower boundary layer flow. Mach 2.85 turbulent boundary layers of Hayakawa et. al.[18] and Mach 2.43 results of Petrie et. al.[8] showed skewness profiles similar to that of Mach 2.07 flow of present study.

Two-Dimensionality of the Flowfield

All the LDV data presented in this paper correspond to the centerline location of the wind tunnel. The uniformity of the mean flow and turbulence field across the tunnel was checked by additional LDV measurements at ±10 mm on either side of the centerline of the wind tunnel at x = 28, 38, and 46 mm. The deviation of data from centerline data were the largest around the sonic lie at x = 28 and 38 mm where turbulence fluctuations were very high and so was the statistical uncertainty[6-8]. The maximum spanwise variation of data in mean velocity, streamwise turbulence intensity, and shear stress were ±1.9%, 2.8%, and 2.5%, respectively. These variations were within the statistical uncertainty of the limited number of sample size in the present experiments[6-8]. Since further off-center LDV measurements were not possible due to the reflection of the laser light from the glass windows of the wind tunnel, therefore, we can conclude that the flow was two-dimensional within ±10 mm of the centerline.

The Mean Flow Results

The mean velocity profiles for all vertical measurement stations, including boundary layer profiles, are shown in Fig. 3. The abscissa shows the vertical station numbers, vertical dashed lines indicate the location of zero velocity for each station, the numbers above the dashed lines give the x-locations of the stations, and the horizontal dashed line chosen to separate the upper and lower flows for the ease of presentation of the experimental results. The u velocity component direction was defined to correspond to the freestream flow direction; parallel to the x-coordinate, see Fig. 1, at station 1 for the incoming boundary layer flows, rotated 12.4 degrees in clockwise direction for the upper shear flow, and 18.5 degrees in counter-clockwise direction for the lower shear flow. The v velocity component was orthogonal to the corresponding u component. The upper and lower flow mean velocities were non-dimensionalized by u_{∞_1} and u_{∞_2}, respectively, where u_{∞_1} and u_{∞_2} are the upper and the lower boundary layers freestream velocities, respectively.

The mean velocity results for both flows show similar trends up to the last three stations where both flows start showing fast "filling out" of the profiles. In last three stations, the rate of profiles "filling out" seems to be faster for the lower flow. This rapid development in mean velocity profiles have been also observed in the redeveloping boundary layers[4,7]. The Schlieren photographs of the present flowfield and earlier[7] experiments have shown existence of large eddies stretched in streamwise direction which seem to

cause very enhanced mixing in redeveloping regions. This matter will be further discussed in presentation of turbulence field results.

The Turbulence Field

The streamwise turbulence intensities for all the stations are shown in Fig. 4. The maximum turbulence intensity in each station occurs around the sonic line for both shear flows which is consistent with earlier LDV results[6-8] and disagrees with hot-wire results[5] which located the maximum in the supersonic region. In stations 3-7, the absolute maximum turbulence intensity in each station for lower flow is higher than the upper flow and shows faster streamwise growth which could be a Mach number effect which means larger entrainment of recirculating flow coming from highly turbulent reattachment region or could be the effect of stronger distortion of the turbulence field through expansion at the step. In stations 8-10, the maximum turbulence intensity in each station for both flows spreads across the shear layer and also decays in streamwise direction. An almost uniform turbulence intensity across both shear layers in the last station confirms existence of enhanced mixing in redeveloping region which was also observed by fast "filling out" of the mean velocity profiles in Fig. 3.

The transverse turbulence intensity profiles are shown in Fig. 5. In two stations after expansion at the step, maximum turbulence intensity occur around the sonic line which is similar to streamwise turbulence intensity. Around the reattachment and afterwards, the peak turbulence intensity occurs at the interface region of two flows which shows high turbulence momentum exchange between two flows. The anisotropy ratio, δ_u/δ_v, peaks around sonic line for both flows and decays rapidly toward interface of two flows. As shown in Figs. 4-6, at the interface of two shear flows after reattachment, Reynold shear stress is small and anisotropy ratio is nearly one. This type of turbulence is called isotropic turbulence in crude sense[18].

The evolutionary kinematic shear stress profiles are shown in Fig. 6. The general trend to some extent is similar to the streamwise turbulence intensity evolution; maximum stress occurring around the sonic line, very high shear stress in recompression and reattachment regions, and absolute shear stress level in lower flow higher than the upper one. The shear stress in the interface of two shear flows is very small which is similar to subsonic flows behind airfoils[20] and blunt bodies[21]. Growth of maximum shear stress in both free shear layers in streamwise direction and existence of very large shear stress around reattachment region of this study are consistent with earlier results where free shear layers attached onto solid surfaces[6,7]. This seems to indicate that imposition of $v = 0$ by solid wall at the reattachment region doesn't affect turbulence intensity or scale in compressible reattaching shear flows while in incompressible reattaching shear flows[1,22], the $v = 0$ restriction is believed to be the cause of significant turbulent intensity and scale decay in the reattachment region.

The maximum turbulence intensities and kinematic shear stresses are shown in Fig. 7. The general trends are the same for both shear flows and similar to earlier results[6,7]. The plateau in maximum turbulence intensities in compressible flows occur around reattachment region while same type of plateau have been observed in incompressible flow about one step height before reattachment. The approximate reattachment location was determined from oil streaks on glass windows to be at x = 35 mm. The rate of increase of turbulence intensities and shear stress are higher for lower shear flow with lower Mach number. The freestream Mach numbers for the upper and lower shear flows are 2.56 and 2.23, respectively. The growth rate of compressible shear layers are approximately a factor of 2 or more less than the average incompressible results[6-8]. For compressible shear flows, the growth rate is inversely proportional to Mach number[23,24]. Therefore, the lower shear layer growth and entrainment rate are higher. The entrained recirculating flow coming from highly turbulent reattachment region could be charging up turbulence field of the lower shear flow and causing higher turbulence intensity and shear stress. Another possible cause could be the larger distortion of the turbulence field passing though 18.5 degrees expansion at the step for the lower flow in comparison to upper flow with only 12.4 degrees expansion.

The ratio of the kinematic shear stress to the estimated turbulent kinetic energy is shown in Fig. 8 where k is estimated to be $(3/4)(\delta_u^2 + \delta_v^2)$. Harsha and Lee[25] examined this parameter for boundary layer, two-dimensional and circular jet, and wake data in incompressible flows. They concluded that a value of 0.3 for this parameter is a reasonable value for computational purposes. Bradshaw and Ferriss'[26] and Bradshaw[27] assumed a value of 0.15 for the parameter in their compressible boundary layer calculations. This parameter which is called turbulence "structure parameter" in general doesn't vary significantly, but as is seen in Fig. 8, the variation in this flowfield is significant. Another turbulence "structure parameter", shear stress correlation coefficient defined as $u'v'/\delta_u\delta_v$, showed similar trend confirming significant turbulence structural change in the flowfield.

Figures 9 and 10 show two components of turbulence triple products. The results show significant increase in triple products, which most probably means increase in turbulence scale in the recompression and interaction regions. This is similar to results obtained in free shear layers reattaching onto a solid wall and may be interpreted that solid boundaries at the reattachment region don't have significant impact on the turbulence scale and also based on Fig. 7 on turbulence intensities. This is in contrast to speculation of significant effects of solid wall at the reattachment on turbulence characteristics in subsonic flows[1,22].

Two components of triple products namely $\langle (v')^2u' \rangle$, Fig. 9, and $\langle (u')^3 \rangle$ show behaviors in transverse direction similar to those of incompressible shear flows[1,22] which means similar streamwise turbulence diffusion characteristic in incompressible and compressible shear layers. The significant difference between incompressible and compressible shear flows occur in $\langle (u')^2v' \rangle$ and $\langle (v')^3 \rangle$ components of triple products which is related to the diffusion of turbulence in transverse direction. In compressible shear flows, see Fig. 10, in the lower edge of both shear flows and also in the interaction region, turbulence diffusion is inward (toward centerline) and in upper edges of the shear flows it is outward (away

from centerline). This is opposite to incompressible shear flow cases and seems to be a significant structural difference.

Figure 11 shows kinematic turbulence production which excludes significant density change through recompression and reattachment. Turbulence production is very high in developing shear flows which is similar to subsonic reattaching shear flows[28] and other compressible reattaching shear flows[7,8], but the high level of production in recompression and reattachment region have not been observed in incompressible flows. The dramatic decay of turbulence production in the redeveloping region is obviously caused by fast "filling out" of mean velocity profiles in this region which confirms enhanced mixing and is consistent with earlier results[28].

Conclusions

Detailed experimental results of interaction between two free shear layers utilizing two-component coincident LDV were documented. The general trends for both shear layers are the same and similar to those of compressible shear layers reattaching onto solid surfaces. Therefore, in contrast to incompressible reattaching shear layers where imposition of v = 0 restriction by the solid surface at the reattachment location believed to significantly decrease turbulence scale and intensities, this doesn't appear to be the case in compressible shear flows. Also, the results confirmed earlier findings of essential structural difference between compressible and incompressible shear flows especially in terms of diffusion of turbulence energy in transverse direction. The turbulence intensity levels and rate of increase in streamwise direction in shear layer with lower Mach number were higher which could be caused by either higher entrainment rate of highly turbulent recirculating flow and/or by higher distortion of turbulence field at the separation location.

Acknowledgement

This research was supported by the U.S. Army Research Office with Dr. Robert E. Singleton as the Contract Monitor.

References

1. Eaton, J.K. and Johnston, J.P., "A Review of Research on Subsonic Turbulent Flow Reattachment," AIAA Journal, Vol. 19, No. 9, 1981, pp. 1093-1100.

2. Chapman, D.R., "An Analysis of Base Pressure at Supersonic Velocities and Comparison with Experiment," NACA TN 2137, 1950.

3. Roshko, A. and Thomke, G.J., "Observations of Turbulent Reattachment Behind an Axisymmetric Downstream-Facing Step in Supersonic Flow," AIAA Journal, Vol. 4, No. 6, 1966, pp. 975-980.

4. Settles, G.S., Baca, B.K., Williams, D.R., and Bogdonoff, S.M., "A Study of Reattachment of a Free Shear Layer in Compressible, Turbulent Flow," AIAA Journal, Vol. 20, No. 1, 1982, pp. 60-67.

5. Hayakawa, K., Smits, A.J., and Bodgonoff, S.M., "Turbulence Measurements in a Compressible Reattaching Shear Layer," AIAA Journal, Vol. 22, No. 7, 1984, pp. 889-895.

6. Samimy, M., Petrie, H.L. and Addy, A.L., "A Study of Compressible Turbulent Reattaching Free Shear Layers," AIAA paper 85-1646, presented at the AIAA 18th Fluid Dynamics, Plasma Dynamics, and Lasers Conference, Cincinnati, OH, July 1985, also will be published in the February 1986 issue of the AIAA Journal.

7. Samimy, M., Petrie, H.L., and Addy, A.L., "Reattachment and Redevelopment of Turbulent Free Shear Layers," to be presented at the ASME Winter Annual Meeting, Miami Beach, Florida, November 1985.

8. Petrie, H.L., Samimy, M., and Addy, A.L., "A Study of Compressible Turbulent Free Shear Layers Using Laser Doppler Velocimetry," AIAA paper 85-0177, 1985.

9. Ikawa, H., and Kubota, T., "Investigation of Supersonic Turbulent Mixing Layer with Zero Pressure Gradient," AIAA Journal, Vol. 13, No. 5, 1975, pp. 566-572.

10. Page, R.H. and Serans, V., "Apparent Reverse Transition in an Expansion Fan," AIAA Journal, Vol. 8, No. 1, 1970, pp. 189-190.

11. Small, R.D. and Page, R.H., "Turbulent Supersonic Boundary Layer Flow in the Neighborhood of a 90° Corner," Astronautica Acta, Vol. 18, No. 2, 1973, pp. 99-107.

12. Lewis, J.E. and Behrens, W., "Fluctuation Measurements in the Wake With and Without Base Injection," AIAA Journal, Vol. 7, No. 4, 1969, pp. 664-670.

13. Maise, G. and McDonald, H., "Mixing Length and Kinematic Eddy Viscosity in a Compressible Boundary Layer," AIAA Journal, Vol. 6, No. 1, 1968, pp. 73-80.

14. Laderman, A.J., "Adverse Pressure Gradient on Supersonic Boundary Layer Turbulence," AIAA Journal, Vol. 18, No. 10, 1980, pp. 1186-1195.

15. Klebanoff, D.S., "Characteristics of Turbulence in a Boundary Layer with Zero Pressure Gradient," NACA Report No. 1247, 1955.

16. Dimotakis, P.E., Collins, D.J., and Lang, D.B., "Laser Doppler Measurements in Subsonic, Transonic, and Supersonic Turbulent Layers," Laser Velocimetry and Particle Sizing, Thompson, H.D. and Stevenson, W.H., Editors, Hemisphere Publishing Company, New York, 1979, pp. 208-219.

17. Sandborn, V.A., "A Review of Turbulence Measurements in Compressible Flow," NASA TM X-62-337, March 1974.

18. Havakawa, K., Smits, A.J., and Bogdonoff, S.M., "Hot-Wire Investigation of an Unseparated Shock-Wave/Turbulent Boundary Layer Interaction," AIAA Journal, Vol. 22, No. 5, 1984, pp. 579-585.

19. Townsend, A.A., The Structure of Turbulent Shear Flow, Cambridge University Press, New York. Second Edition, 1976.

20. Andreopoulos, J. and Bradshaw, P., "Measurements of Interacting Turbulent Shear Layers in the Near Wake of a Flat Plate," J. Fluid Mech., Vol. 100, Pt. 3, 1980, pp. 639-668.

21. Palmer, M.D. and Keffer, J.F., "An Experimental Investigation of an Asymmetrical Turbulent Wake," J. Fluid Mech., Vol. 53, Pt. 4, 1972, pp. 593-610.

22. Chandrsuda, C. and Bradshaw, P., "Turbulence Structure of a Reattaching Mixing Layer," J. Fluid Mech., Vol. 110, 1981, pp. 171-194.

23. Channapragader, R.S., "Compressible Jet Spread Parameter for Mixing Zone Analysis," AIAA Journal, Vol. 1, No. 9, 1963, pp. 2188-2190.

24. Birch, S.F. and Eggers, J.M., "A Critical Review of the Experimental Data for Developed Free Turbulent Shear Layers," NASA SP-321, Free Turbulent Shear Flows, Vol. 1, Conference Proceedings, Langley Research Center, 1972.

25. Harsha, P.T. and Lee, S.C., "Correlation Between Turbulent Shear Stress and Turbulent Kinetic Energy," AIAA Journal, Vol. 8, No. 8, 1970, pp. 1508-1510.

26. Bradshaw, P. and Ferriss, D.H., "Calculation of Boundary Layer Development Using the Turbulent Energy Equation: Compressible Flow on Adiabatic Walls," J. Fluid Mech., Vol. 46, Pt. 1, 1971, pp. 83-110.

27. Bradshaw, P., "Mean Compression Effects in Turbulent Boundary Layers," J. Fluid Mech., Vol. 63, Pt. 3, 1974, pp. 449-464.

28. Gaviglio, J., Dussauge, J.P., Debieve, J.F., and Farre, A., "Behavior of a Turbulent Flow Strongly out of Equilibrium at Supersonic Speeds," Physics of Fluids, Vol. 20, No. 10, Pt. 2, 1977, pp. 5179-5192.

FIGURES

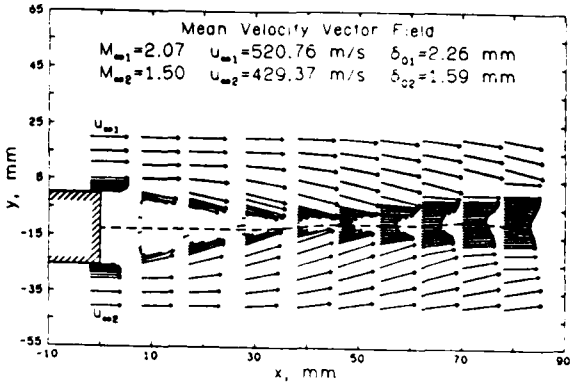

Figure 1. Mean velocity vector field

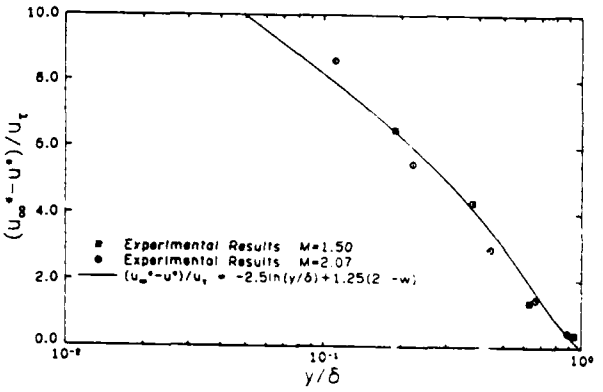

Figure 2. Boundary layer mean velocity profiles and generalized curve of Maise and McDonald[13]

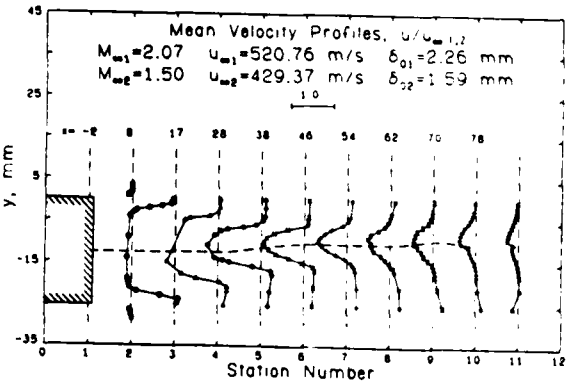

Figure 3. Streamwise mean velocity profiles ($u_{\infty 1,2}$ means $u_{\infty 1}$ for the upper flow and $u_{\infty 2}$ for the lower flow)

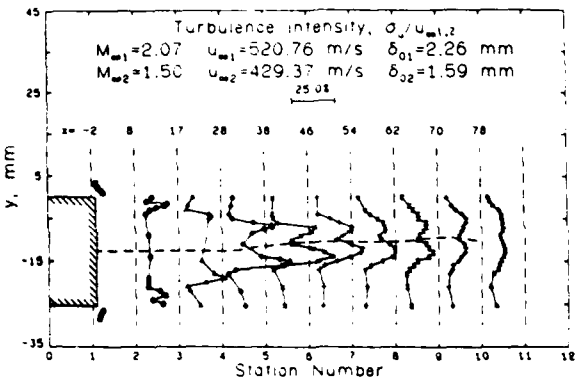

Figure 4. Streamwise turbulence intensity profiles

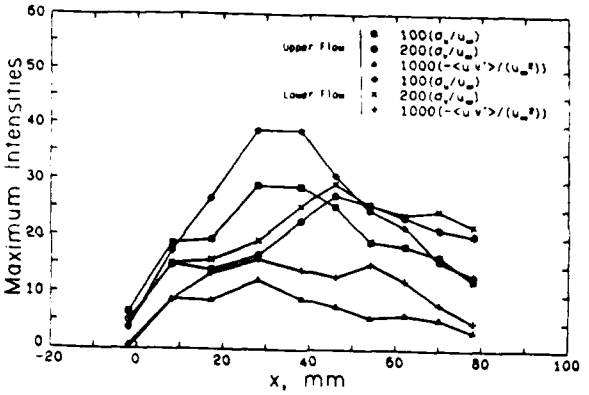

Figure 7. Maximum turbulence fluctuations and shear stresses

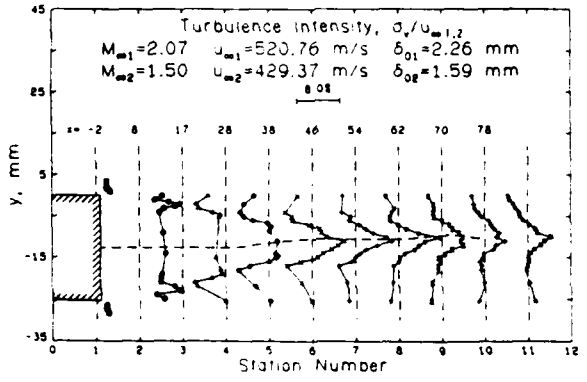

Figure 5. Transverse turbulence intensity profiles

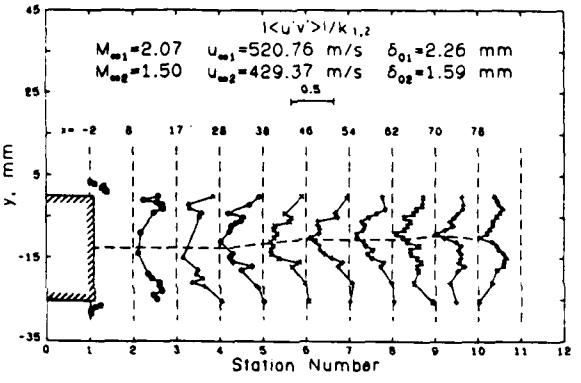

Figure 8. Turbulence "structure parameter" profiles

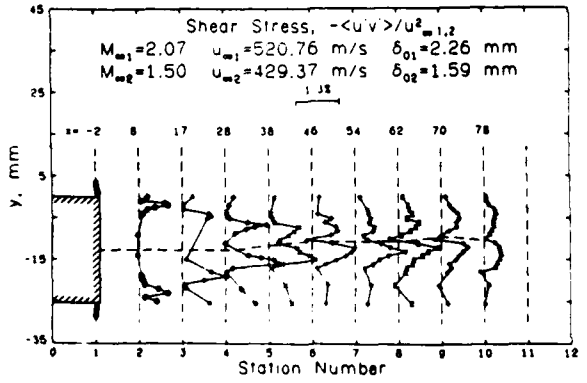

Figure 6. Evolutionary shear stress profiles

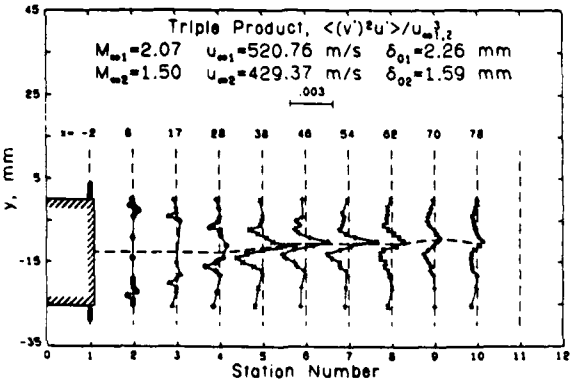

Figure 9. Turbulent triple product

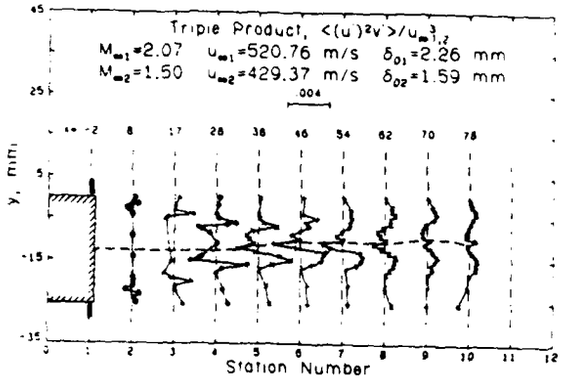

Figure 10. Turbulent triple product

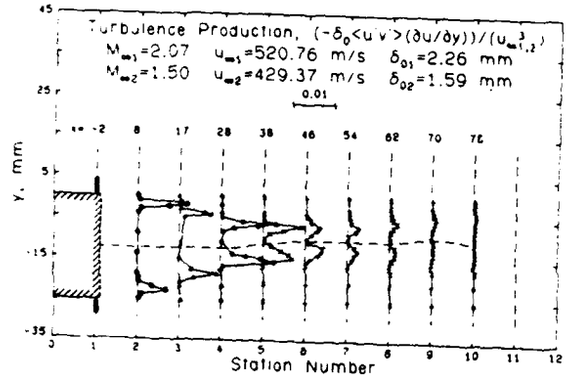

Figure 11. Turbulence production

SECTION B.9

AN EXPERIMENTAL STUDY OF THE SHOCK WAVE-TURBULENT BOUNDARY LAYER INTERACTION

Paper presented at the Winter Annual Meeting of ASME as part of the International Symposium on Laser Anemometry

Miami Beach, Florida

November 17-22, 1985

(Published as International Symposium on Laser Anemometry, FED-Vol. 33, New York, 1985, pp. 173-178)

by

D. W. Kuntz, V. A. Amatucci, and A. L. Addy

AN EXPERIMENTAL STUDY OF THE SHOCK WAVE-TURBULENT BOUNDARY LAYER INTERACTION

D. W. Kuntz
Aerothermodynamics Division
Sandia National Laboratories
Albuquerque, New Mexico

V. A. Amatucci, Graduate Research Assistant and A. L. Addy, Professor and Associate Head
Department of Mechanical and Industrial Engineering
University of Illinois at Urbana-Champaign
Urbana, Illinois

ABSTRACT

An experimental investigation was conducted to study the interaction between a shock wave and a turbulent boundary layer. The boundary layer was formed on the floor of a wind tunnel operating with a freestream Mach number of 2.94 and a Reynolds number based on boundary layer thickness of 3.1×10^5. A 20 degree compression corner model was used to generate the interaction flowfield. Measurement techniques used in this investigation included Schlieren photography, surface static pressure measurement, surface streak pattern measurement, and laser Doppler velocimetry (LDV). The LDV was used to make two-color, two-component coincident velocity measurements within the redeveloping boundary layer downstream of the interaction. The results of the LDV measurements indicated that both the mean and turbulent flow properties of the boundary layer were significantly altered by the interaction, with large increases in the longitudinal turbulence intensity and Reynolds stress observed in the redeveloping boundary layer.

NOMENCLATURE

Re_δ	Reynolds number based on boundary layer thickness
u	Mean velocity component parallel to the wind tunnel floor or ramp surface
v	Mean velocity component perpendicular to the wind tunnel floor or ramp surface
X	Longitudinal coordinate
Y	Vertical coordinate
Y^*	Displaced vertical coordinate
α	Ramp angle
δ	Boundary layer thickness
δ^*	Boundary layer displacement thickness
δ_0	Undisturbed boundary layer thickness at X = 0
θ	Boundary layer momentum thickness
π	Wake strength parameter
$\langle\ \rangle$	Root-mean-square quantity

Subscripts

e	Boundary layer edge condition
∞	Freestream condition, upstream of the shock wave

Superscripts

$\overline{\quad}$	Ensemble average
'	Fluctuation from the mean value

INTRODUCTION

The interaction between a shock wave and a turbulent boundary layer occurs frequently in high speed flight. A thorough understanding of the effects of the interaction on the downstream boundary layer is essential if flows of this nature are to be predicted accurately. The purpose of this investigation was to make accurate, reliable, and well-documented measurements within the redeveloping boundary layer downstream of a shock wave-turbulent boundary layer interaction, and thus aid in the understanding of the fundamental nature of these highly complex flowfields.

The shock wave-boundary layer interaction in this investigation was generated by a compression corner

or ramp, mounted directly on the floor of a small-scale supersonic wind tunnel. Flowfields of this type can contain a separated region near the corner location, depending upon ramp angle and the other flow properties. The principal features of the separated compression corner flowfield are shown in Fig. 1. The incoming boundary layer separates upstream of the corner. The separation shock wave originates deep within the boundary layer near the separation point and extends up into the freestream. The upstream boundary layer becomes a free shear layer as a result of the separation process and subsequently reattaches on the ramp surface. The shock structure caused by the reattachment process coalesces to form a single reattachment shock which in turn coalesces with the separation shock to form the single oblique shock wave associated with a sudden change in flow direction in supersonic flow. Downstream of reattachment, the boundary layer redevelops into an equilibrium turbulent boundary layer.

The objective of this study was to make detailed turbulence measurements within the redeveloping boundary layer downstream of a shock wave-turbulent boundary layer interaction and compare the properties of the redeveloping boundary layer with the properties of the undisturbed boundary layer. A compression corner angle of 20 degrees was used to generate a flowfield with a relatively large separated flow region. Surface static pressure measurements, Schlieren photographs, and surface flow visualization techniques were used to determine some of the mean flowfield characteristics. A two-color, two-component laser Doppler velocimeter was used to make mean and turbulent velocity measurements within this highly complex flowfield.

EXPERIMENTAL FACILITIES

The wind tunnel used in this investigation was part of the blow down wind tunnel facility located in the Mechanical Engineering Laboratory of the University of Illinois. Compressed air at approximately 965 kPa (140 psia) was supplied to the wind tunnel stagnation chamber through a piping network. The pressure in the stagnation chamber was regulated by means of a pneumatically operated control valve which was capable of maintaining the selected stagnation pressure with an accuracy of ± 1.5 percent during data acquisition.

The test section within the wind tunnel had a square cross section 10.2 cm on a side. A solid aluminum nozzle block produced a Mach number of 2.94 with a maximum deviation of less than 1 percent in the test section. Transparent windows in the wind tunnel side walls provided the optical access necessary for Schlieren photography and laser Doppler velocimetry. Additional details of the wind tunnel facility can be found in Reference 1.

A stagnation pressure of approximately 483 kPa (70 psia) was used during the course of this investigation. This stagnation pressure was high enough to ensure that the flow within the freestream of the wind tunnel was completely supersonic, yet was low enough to allow run times of approximately 90 seconds. The flowfield stagnation temperature was close to the ambient temperature within the laboratory, thus yielding nearly adiabatic conditions within the wind tunnel boundary layers.

Detailed surveys were made of the boundary layer which had formed on the lower wall of the wind tunnel using the two-component laser Doppler velocimeter. The results of these surveys indicated that the boundary layer was nearly fully developed, but some changes in the velocity profile were still taking place with X. The boundary layer in the center of the test section had a thickness of 8.27 mm ($u_e = 0.99u_\infty$). A curve fit of the boundary layer data with the transformed wall-wake law of Maise and MacDonald (2)[4] yielded a wake strength parameter, π, of 0.98, which is somewhat high but not without precedence (1). Integration of the definitions of displacement and momentum thickness yielded values of $\delta^* = 3.11$ mm and $\theta = 0.57$ mm. The Reynolds number within the test section based on boundary layer thickness, Re_δ, was 3.1×10^5.

The model used in this investigation is shown in Fig. 2, along with the coordinate system used in the presentation of the experimental results. The 20 degree compression corner model consisted of a ramp mounted on a ramp support, with the forward part of the ramp support forming the lower wind tunnel wall upstream of the corner. The section of the model downstream of the ramp sloped gradually back down to the floor level to reduce the disturbances within the wind tunnel test section caused by the model during the experiment.

The ramp and ramp support were made of aluminum and anodized flat black to reduce laser light reflections during the LDV measurements. The model support was sealed along the side walls and upstream of the corner where the support mated with the wind tunnel floor with linear o-ring material. The corner was sealed with a gasket sealing compound. Static pressure taps 0.57 mm in diameter were located every 2.54 mm longitudinally on the surface of the ramp and on the model support upstream of the corner.

The model used in this study spanned the full 10.2 cm width of the test section. It may have proved beneficial to have used a narrower ramp model with splitter plates located along the sides to eliminate the effects of the side wall boundary layers on the shock wave-boundary layer interaction, similar to those used in other studies (3,4). However, the side wall splitter plates would have denied optical access to the interaction region, and thus would have made LDV measurements impossible. As a result of this, it was decided to use a full span model and to experimentally determine the extent of the side wall boundary layer interference with surface flow pattern measurements.

MEASUREMENT TECHNIQUES

The primary measurement technique employed in this investigation was laser Doppler velocimetry. The LDV system was used to make detailed flowfield measurements within the upstream and redeveloping turbulent boundary layers, and the majority of information presented here is a result of this measurement technique. To complete the study of this flowfield, Schlieren photographs, surface static pressure measurements and surface streak pattern measurements

[4]Numbers in parentheses refer to entries in REFERENCES.

were used to determine the quality of the wind tunnel flowfield, and to determine other properties of interest in the regions near the compression corner.

The laser Doppler velocimeter used in this study was a two-color, two-component system utilizing optical and electronic components manufactured by Thermal Systems Incorporated (TSI). A Spectra-Physics 5-watt argon-ion laser operating in the multi-line mode was used to provide the necessary laser light. The beam from this laser was split into its various components with a dispersion prism, and the two most powerful beams, the green beam with wavelength of 514.5 nm and the blue beam with wavelength of 488.0 nm, were used in these experiments. Each of these beams was split into two equal intensity parallel beams, and one of each of the pairs of beams was then passed through a Bragg cell which shifted the frequency by 40 MHz. A 350 mm focal length lens was used to redirect the four parallel beams, causing them to cross at a single point within the wind tunnel to generate the measurement volume. A measurement volume diameter of 0.18 mm and a measurement volume length of 6.1 mm were obtained with this optical arrangement. The collection optics were located on the opposite side of the wind tunnel in the forward scatter position and were rotated 10 degrees off the optical axis to simplify alignment and to reduce the effective length of the measurement volume to less than 2 mm. The transmitting and receiving optics were mounted on a traversing table which allowed manual positioning of the measurement volume within the wind tunnel with an accuracy of ± 0.1 mm.

A 250 mm focal length lens was used to collect the scattered light, and a filter arrangement was used to separate the green and blue signals. Two photomultipliers converted the scattered light of each color into voltage signals for analysis.

The photomultipliers were connected to TSI frequency counters which filtered the signals and performed validation checks to eliminate erroneous signals. The output from the counters was stored directly in the memory of a Digital PDP 11-03 minicomputer, which converted the counter output into velocities and stored the data on a floppy disk. The data was then transferred to a Hewlett-Packard 9000 series computer for thorough analysis.

The seed particles for the LDV measurements in this investigation were generated by atomizing silicone oil. The oil droplets were introduced in the stagnation chamber upstream of the wind tunnel. A series of experiments was conducted to determine the size of these particles in which two-component velocity measurements were made downstream of an oblique shock wave generated by an 8 degree compression corner in the Mach 2.94 flowfield. The particle response was compared to the predicted response of particles of various sizes. The results of this study indicated that the silicone oil droplets had an effective mean diameter of 1.5 to 2 μm. Particles of this size have been shown to have a sufficient frequency response to track large scale velocity fluctuations found downstream of shock wave-turbulent boundary layer interactions (1). Some particle lag was measured in the regions immediately downstream of the shock wave due to the large velocity gradient generated by the shock wave. The measurements reported in this study were confined to regions far enough from the shock wave such that the effects of particle lag were not significant.

The statistical uncertainty involved in determining mean velocities from individual velocity measurements in turbulent flowfields is a function of the sample size and the local turbulence intensity. The sample size in this investigation was increased as local turbulence intensity increased, with 1024 samples taken when the local turbulence intensity was less than 10 percent, 2048 samples taken when the local turbulence intensity was between 15 and 25 percent, 3072 samples taken when the local turbulence intensity was between 25 and 30 percent, and 4096 samples taken when the local turbulence intensity exceeded 30 percent. From a statistical analysis, the uncertainty in mean velocity was found to be less than 2 percent and the uncertainty in turbulence intensity was found to be less than 3.6 percent for the measurements of the redeveloping boundary layer downstream of the 20 degree compression corner.

Mean and turbulent flow properties computed from LDV data have been shown in the literature to be affected by certain biasing errors, most notably velocity biasing (5) and fringe biasing (6). Velocity biasing results from the fact that in a turbulent flow with uniformly distributed particles, a larger volume of fluid passes through the measurement volume during periods when the velocity is higher than the mean, than when the velocity is lower than the mean. Thus, a simple average of the individual velocity measurements is biased towards higher velocities. Fringe biasing results from the fact that a particle must cross a pre-selected number of fringes within the measurement volume for its velocity to be measured. Thus, particles traveling in a direction parallel to the fringe plane are not "seen" by the LDV and this results in a bias in favor of particles traveling perpendicular to the fringe plane. The effects of velocity biasing were essentially eliminated from the results of this investigation by weighting the velocity measurements with the two-dimensional velocity bias correction factor, $1/(u^2 + v^2)^{1/2}$ (1). The effects of fringe biasing were significantly reduced by frequency shifting such that the fringes moved in a direction opposite to that of the mean flow, and by orienting the fringe planes at ± 45 degrees relative to the wind tunnel floor for the upstream boundary layer surveys, and at ± 45 degrees relative to the ramp surface for the downstream boundary layer surveys. A comparison between the two-dimensional velocity bias corrected data and data corrected with both the two-dimensional velocity bias correction and a fringe bias correction based on the study of Buchhave (6) showed that the effects of fringe bias were not significant in comparison to the effects of velocity bias, and thus the results presented here were corrected with the velocity bias correction only.

EXPERIMENTAL RESULTS

The Schlieren system was used to view the 20 degree compression corner flowfield during the initial phases of this investigation. The freestream flow was observed to be completely supersonic and some unsteadiness was observed in the separation shock structure similar to that reported by Dolling and Murphy (7) in a 24 degree compression corner flowfield. Surface streak patterns were used to determine the separation and reattachment locations, and to determine the extent of the influence of the side wall boundary layers on the flowfield. Separation was found to take place a distance of 1.63 δ_0 upstream of the corner. The separation line was relatively straight

and spanned the center 5 cm of the wind tunnel. Reattachment occurred a distance of 0.52 δ_0 from the corner on the ramp face, with the reattachment line spanning the center 7 cm of the wind tunnel. Some three-dimensional effects were seen in the streak lines within the separated region near the wind tunnel side walls, but it is felt that these effects did not disturb the centerline flow downstream of reattachment.

The mean surface static pressure distribution is shown in Fig. 3. The solid line to the right of the experimental data represents the theoretical downstream pressure determined from oblique shock wave theory. It can be seen in this figure that the pressure rise began well upstream of the corner (X = 0.0) due to the presence of the separated region. The pressure distribution exhibits the "kink," or triple inflection point characteristic which is typical of separated compression corner flowfields (3). The static pressure on the ramp face rose gradually and reached a plateau level within 5.5 percent of the theoretical value.

The mean streamwise velocity profiles upstream and downstream of the shock wave-boundary layer interaction are shown in Fig. 4. The profiles downstream of the interaction exhibit wake-like properties, similar to those observed by other investigators downstream of separated compression corners (3), and downstream of reattaching free shear layers (8). These wake-like profiles resulted from the shear layer velocity profile which formed the initial condition for the redeveloping boundary layer. The shear layer formed from the upstream boundary layer separation and developed its wake-like characteristics from interaction with the separated region in the compression corner. The velocity profiles downstream of reattachment experienced a rapid "filling out," which can be seen in this figure. This rapid change in the boundary layer profiles was most likely caused by enhanced turbulent mixing due to the formation of large scale eddies, and further adds to the wake-like appearance of the boundary layer profiles. The decrease in the measured streamwise velocity with X, which can be seen in the outer regions of the boundary layers downstream of the corner, was caused by a combination of two effects. The surface static pressure distribution, shown in Fig. 3, indicates that the pressure was still rising at the longitudinal locations where the velocity profiles shown in Fig. 4 were measured. Thus, the flow in this region was still turning and decelerating in the final stages of the compression process. Also, it is possible that the effects of particle lag may have contributed to the decrease of u with X, and the extent to which particle lag is affecting the results is uncertain.

The vertical velocity component profiles for the compression corner flowfield are presented in Fig. 5. The negative vertical velocities in the outer regions of the boundary layers are further indications that the change in flow direction during the recompression process takes place gradually. The small positive vertical velocities seen in the lower regions of the last two stations in Fig. 5 accompany the rapid "filling out" of the streamwise profiles seen in Fig. 4, and are a result of the severe changes which are taking place within the boundary layer as the wake-like characteristics diminish.

The longitudinal turbulence intensity, nondimensionalized with the freestream velocity upstream of the shock wave, is shown in Fig. 6. It can be seen in this figure that the turbulence intensity was significantly increased by the interaction between the shock wave and the boundary layer. The turbulence intensity profiles reach a maximum value within the central regions of the boundary layer, and decrease as both the freestream and the wall are approached. The turbulence can be seen spreading vertically with the intensity profiles becoming flatter in the downstream stations. A gradual decrease in the peak turbulence intensity accompanies this diffusion process as the boundary layer recovers from the effects of the interaction process. It can be seen, however, that the turbulence intensity profile at the last measurement station was still substantially different from the upstream profile, and that the ramp was of insufficient length for the boundary layer to return to equilibrium conditions.

The vertical turbulence intensities, $\langle v' \rangle$, nondimensionalized by u_∞, are presented in Fig. 7. The vertical turbulence intensity, like the streamwise turbulence intensity, was significantly amplified by the interaction. However, unlike the streamwise turbulence intensity, the vertical turbulence intensity shows very little dependence on Y, and is nearly constant throughout the redeveloping boundary layer and within the freestream downstream of the shock wave. There is a slight tendency for $\langle v' \rangle$ to reach a maximum near the edge of the boundary layer, but this characteristic is not found in all the profiles.

The kinematic Reynolds stress, $\overline{u'v'}$, nondimensionalized with the square of the undisturbed freestream velocity, u_∞^2, is presented in Fig. 8. It can be seen in this figure that, like the streamwise turbulence intensity, the Reynolds stress was significantly increased by the interaction. The large magnitude of the Reynolds stress is further indication of the existence of large scale turbulent structures within the redeveloping boundary layer. The Reynolds stress profiles reach maximum values in the central regions of the boundary layers, with the maximum value in each profile decreasing as the flow proceeds downstream. The Reynolds stress, like the turbulence intensity, diffuses outward through the boundary layer as the effects of the interaction begin to diminish.

The trends in the Reynolds stress of this investigation agree quite well with those found by Muck and Smits (4) in their investigation of a 20 degree compression corner flowfield with similar flow conditions. The tendency for the Reynolds stress to reach a maximum in the central regions of the boundary layer, the gradual decay in Reynolds stress with X downstream of the interaction, and the vertical diffusion of the Reynolds stress in the boundary layer can all be seen in their hot wire results. However, the magnitudes of $-\overline{(u'v')}/u_\infty^2$ reported by Muck and Smits are significantly lower than the results of the current investigation, with the maximum values differing by factors greater than 2. This large discrepancy is most likely caused by calibration problems associated with the slanted hot wire technique used by these authors. Muck and Smits state that the hot wire calibration is only valid in regions in which the Mach number component normal to the wire exceeds 1.2. Taking into account the 30 degree yaw angle of the slanted hot wires, this yields a lower Mach number limit of 1.39. The local Mach numbers at the regions of maximum Reynolds stress in the current

investigation were all below 1.39. In addition to these low mean Mach numbers, the high turbulence intensities in these regions indicate that the local Mach number frequently drops far below the calibration limits, and these periods of low Mach number contribute significantly to the magnitude of $\overline{u'v'}$. Considering these factors, it is not surprising that a discrepancy exists between Reynolds stresses measured with slanted hot wires, and those measured with two-component LDV systems in highly turbulent flowfields.

CONCLUSIONS

The interaction between the shock wave and the turbulent boundary layer, and the resultant separated region, caused significant changes in both the mean and turbulent properties of the boundary layer. The mean velocity profiles appear very wake-like as a result of the separation and reattachment processes, and experience a very rapid "filling out" as the flow proceeds downstream. The longitudinal turbulence intensity and Reynolds stress are significantly amplified by the interaction, and reach maximum values within the central regions of the boundary layer. The Reynolds stress values obtained in this investigation are significantly higher than values which have been measured in similar flowfields with slanted hot wires, and this discrepancy is believed to be due to the calibration problems associated with hot wire systems in highly turbulent supersonic flows. The rapid acceleration of the fluid near the wall and the large Reynolds stress values within the redeveloping boundary layer indicate the presence of large scale turbulent structures in the flow downstream of the shock wave-turbulent boundary layer interaction.

ACKNOWLEDGMENT

Support for this research was provided by the U.S. Army Research Office through contract monitor Dr. Robert E. Singleton under Research Grant DAAG 29-79-C-0184 and Research Grant DAAG 29-83-K-0043; and the Department of Mechanical and Industrial Engineering at the University of Illinois at Urbana-Champaign.

REFERENCES

1. Kuntz, D. W., "An Experimental Investigation of the Shock Wave-Turbulent Boundary Layer Interaction," Ph.D. Thesis, Department of Mechanical and Industrial Engineering, University of Illinois at Urbana-Champaign, 1985.

2. Maise, G. and McDonald, H., "Mixing Length and Kinematic Eddy Viscosity in a Compressible Boundary Layer," AIAA Journal, Vol. 6, No. 1, January 1968, pp. 73-80.

3. Settles, G. S., Fitzpatrick, T. J., and Bogdonoff, S. M., "Detailed Study of Attached and Separated Compression Corner Flowfields in High Reynolds Number Supersonic Flow," AIAA Journal, Vol. 17, No. 6, June 1979, pp. 579-585.

4. Muck, K. C. and Smits, A. J., "Behavior of a Turbulent Boundary Layer Subjected to a Shock-Induced Separation," AIAA Paper 84-0097, 1984.

5. McLaughlin, D. K. and Tiederman, W. G., "Biasing Correction for Individual Realization of Laser Anemometer Measurements in Turbulent Flows," The Physics of Fluids, Vol. 16, No. 12, 1973, pp. 2082-2088.

6. Buchhave, P., "Biasing Errors in Individual Particle Measurements with the LDA-Counter Signal Processor," Proceedings of the LDA-Symposium, Copenhagen, Denmark, 1975.

7. Dolling, D. S. and Murphy, M., "Wall Pressure Fluctuations in a Supersonic Separated Compression Ramp Flowfield," AIAA Paper 82-0986, 1982.

8. Samimy, M., "An Experimental Study of Compressible Turbulent Reattaching Free Shear Layers," Ph.D. Thesis, Department of Mechanical and Industrial Engineering, University of Illinois at Urbana-Champaign, 1984.

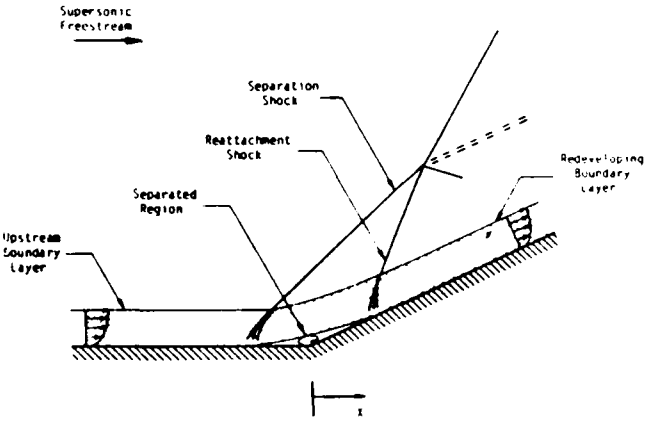

Fig. 1 Separated compression corner flowfield

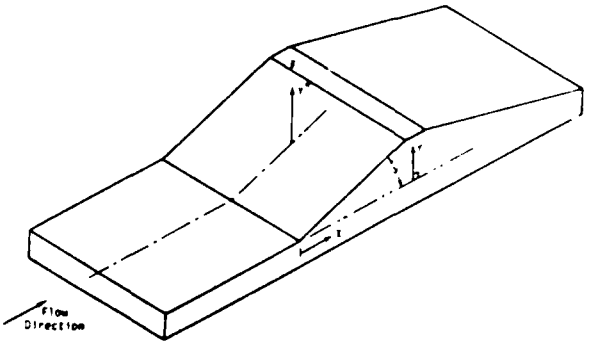

Fig. 2 Compression corner model and coordinate system

AD-A172 814 FLUID DYNAMIC MECHANISMS AND INTERACTIONS WITHIN SEPARATED FLOWS (U) ILLINOIS UNIV AT URBANA DEPT OF MECHANICAL AND INDUSTRIAL ENG A L ADDY ET AL JUL 86 3/3

UNCLASSIFIED UILU-ENG-86-4006 ARO-19823 19-EG F/G 20/4 NL

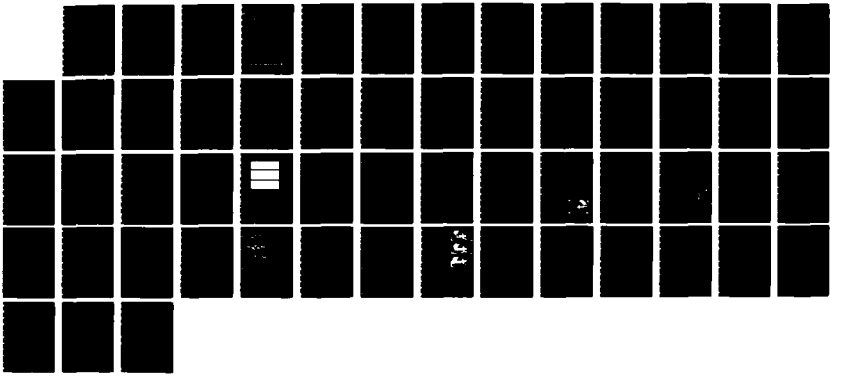

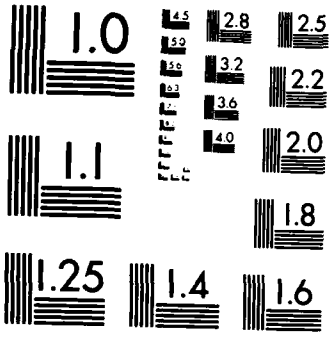

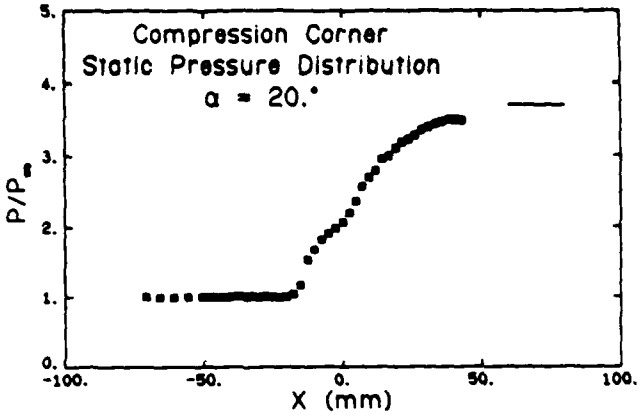

Fig. 3 Mean surface static pressure distribution

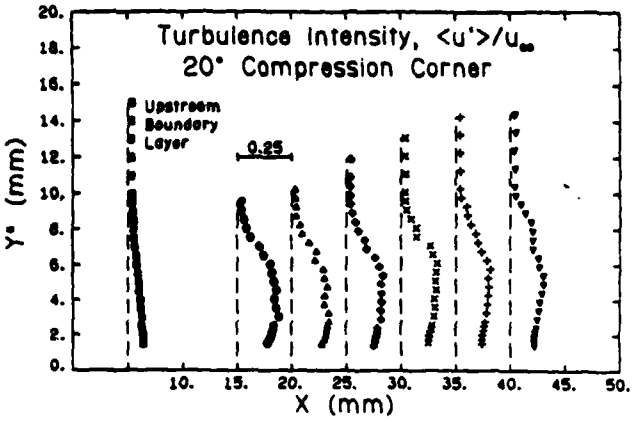

Fig. 6 Longitudinal turbulence intensity profiles

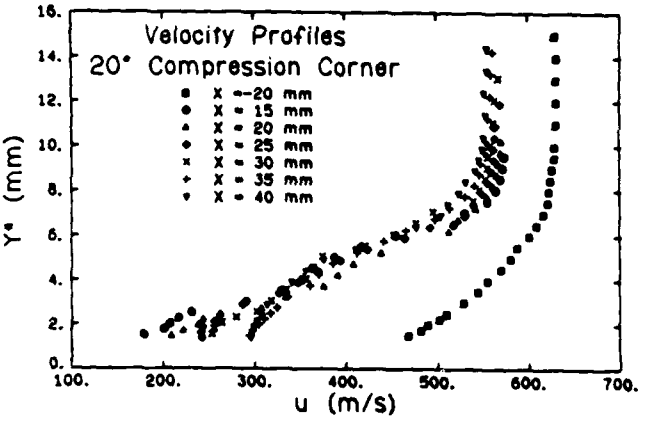

Fig. 4 Mean streamwise velocity profiles

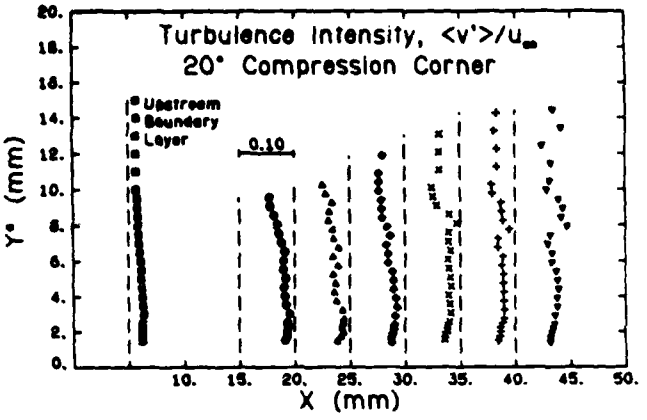

Fig. 7 Vertical turbulence intensity profiles

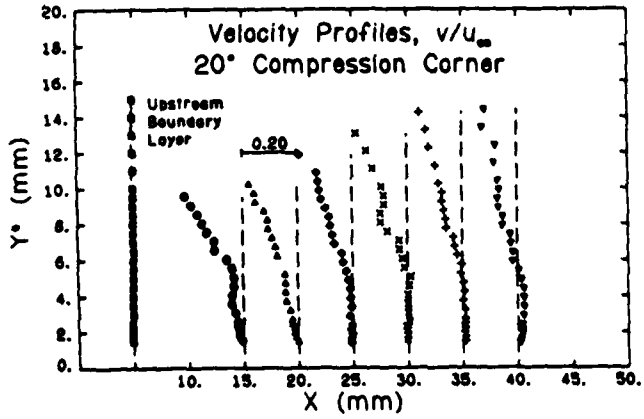

Fig. 5 Mean vertical velocity profiles

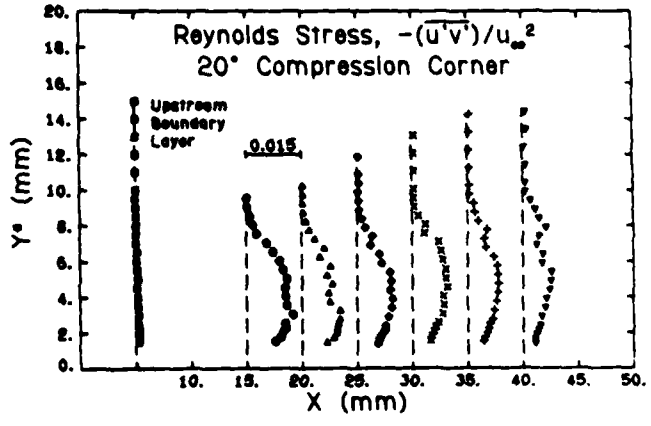

Fig. 8 Reynolds stress profiles

SECTION B.10

THE TURBULENT BOUNDARY LAYER PROPERTIES DOWNSTREAM OF THE SHOCK WAVE-BOUNDARY LAYER INTERACTION

Paper No. AIAA-86-0348

Presented at the AIAA 24th Aerospace Sciences Meeting

Reno, Nevada

January 14-17, 1986

by

D. W. Kuntz, V. A. Amatucci, and A. L. Addy

AIAA'86

AIAA-86-0348

The Turbulent Boundary Layer Properties Downstream of the Shock Wave-Boundary Layer Interaction

D. W. Kuntz, Sandia National Lab., Albuquerque, NM; and V. A. Amatucci and A. L. Addy, Univ. of Illinois at Urbana-Champaign, Urbana, IL

AIAA 24th Aerospace Sciences Meeting

January 6-9, 1986/Reno, Nevada

THE TURBULENT BOUNDARY LAYER PROPERTIES DOWNSTREAM OF THE SHOCK WAVE-BOUNDARY LAYER INTERACTION

D. W. Kuntz*
Aerothermodynamics Division
Sandia National Laboratories
Albuquerque, New Mexico

V. A. Amatucci** and A. L. Addy†
Department of Mechanical and Industrial Engineering
University of Illinois at Urbana-Champaign
Urbana, Illinois

Abstract

An experimental investigation was conducted to study the interaction between a shock wave and a turbulent boundary layer. Compression corner models mounted on a wind tunnel floor were used to generate the oblique shock wave in the Mach 2.94 flowfield. Ramp angles of 8, 12, 16, 20, and 24 degrees were used to produce the full range of possible flowfields, including flow with no separation, flow with incipient separation, and flow with a significant amount of separation. The principal measurement technique used was laser Doppler velocimetry (LDV), which was used to make two component coincident velocity measurements within the redeveloping boundary layer downstream of the interaction. The results of the LDV measurements indicated that the boundary layer was significantly altered by the interaction. The mean streamwise velocity profiles downstream of the separated compression corners were very wake-like in nature, and the boundary layer profiles downstream of all the interactions showed an acceleration of the flow nearest the wall as the boundary layers began to return to equilibrium conditions. Significant increases in turbulence intensities and Reynolds stresses were caused by the interactions, and indications of the presence of large scale turbulent structures were obtained in the redeveloping boundary layers.

Nomenclature

M	Mach number
P	pressure
Re_δ	Reynolds number based on boundary layer thickness
u	mean velocity component parallel to the wind tunnel floor or ramp surface
v	mean velocity component perpendicular to the wind tunnel floor or ramp surface
X	longitudinal coordinate
X^+	longitudinal coordinate parallel to the ramp plane
Y	vertical coordinate
Y^*	displaced vertical coordinate
α	ramp angle
δ	boundary layer thickness
δ^*	boundary layer displacement thickness
δ_0	undisturbed boundary layer thickness at X = 0
θ	boundary layer momentum thickness
Π	wake strength parameter
$< >$	root-mean-square quantity

Subscripts

e	boundary layer edge
MAX	maximum
R	reattachment
S	separation
∞	freestream condition, upstream of the shock wave

Superscripts

$\overline{\ }$	ensemble average
	fluctuation from the mean value

*Member of Technical Staff, Member AIAA.

**Graduate Research Assistant, Student Member AIAA.

†Professor and Associate Head, Associate Fellow AIAA.

Introduction

The interaction between a shock wave and a turbulent boundary layer has been a topic of interest to researchers for many years. Flowfields of this type occur frequently in high speed flight, and a thorough knowledge of the effects of the shock wave on the boundary layer properties is necessary for accurate flowfield prediction. The investigation described in this report was conducted in order to provide detailed mean and turbulent flowfield properties within boundary layers downstream of shock wave-turbulent boundary layer interactions of various strengths.

A review of the literature published in this area indicates that there is an need for additional measurements within shock wave-boundary layer interaction flowfields [1]. A great deal of effort has been dedicated to determining mean properties within these flowfields [2-5], and some investigations have measured turbulent flowfield properties [6-12]. Unfortunately, the few investigations which have used hot wire or laser Doppler velocimeter (LDV) systems to study these flowfields have been limited to single component measurements, and thus have presented a rather limited amount of information. The numerical simulations of these flowfields have achieved some degree of success, but no turbulence model has yet been developed which can be used to predict all aspects of the problem accurately. Advances in turbulence modeling await a better understanding of the nature of turbulence itself. The current investigation was conducted with a two component LDV system, and thus has produced new information concerning the nature of the turbulence downstream of the shock wave-turbulent boundary layer interaction.

Compression corner models, or ramps mounted on the wind tunnel floor, were used to generate the oblique shock waves for this study. Ramp angles of 8, 12, 16, 20, and 24 degrees were used to produce the full range of possible flowfields, including flow with no separation, flow with incipient separation, and flow with a significant amount of separation. In this manner, the effects of increasing shock strength on the turbulent properties of the boundary layer were studied systematically.

Measurement techniques used in this investigation included Schlieren photography, surface static pressure measurement, surface streak pattern measurement, and laser Doppler velocimetry. The LDV system was used to make two component coincident velocity measurements within the upstream boundary layer and within the redeveloping boundary layers downstream of the interactions. The two component nature of the LDV system allowed direct measurement of the two instantaneous velocity components. This data then enabled calculation of the two mean velocity components, as well as various turbulence properties such as turbulence intensities, Reynolds stress, turbulence structure parameters, skewness and flatness coefficients, and turbulence triple products. Space limitations prevent the presentation of all the data obtained, but a complete presentation of this data can be found in Reference 1. The purpose of this paper is to present a overview of the data obtained in this investigation, with emphasis on the effects of increasing shock strength on the various flowfield parameters.

Experimental Facilities

The experiments described in this paper were conducted in the Mechanical Engineering Laboratory of the University of Illinois at Urbana-Champaign. The wind tunnel used operated in the blow down mode and had a 10.2 by 10.2 cm square test section. A solid aluminum nozzle produced a Mach number of 2.94 within the test section. Transparent windows within the wind tunnel side walls provided the optical access necessary for Schlieren photography and laser Doppler velocimetry. Additional details of the wind tunnel facility can be found in Reference 1.

The data of this investigation was obtained with a wind tunnel stagnation pressure of approximately 483 kPa (70 psia). This pressure level was high enough to ensure proper supersonic operation of the wind tunnel, yet was low enough to permit relatively long run times of approximately 90 seconds. The stagnation temperature was near the ambient temperature in the laboratory facility, and thus the wind tunnel operated with nearly adiabatic conditions within the wall boundary layers.

Detailed boundary layer surveys were made with the two component LDV in the turbulent boundary layer which formed on the floor of the wind tunnel in the absence of the compression corner model. This boundary layer was found to be nearly fully developed, with only very small differences in the dimensionless profiles existing between measurement stations within the test section. The boundary layer in the center of the test section had a thickness of 8.27 mm ($u_\epsilon = 0.99\ u_\infty$). A curve fit of the boundary layer data with the transformed wall-wake law of Maise and McDonald[13] yielded a wake strength parameter, Π, of 0.98, which is somewhat high but not without precedence[1]. Integration of the definitions of displacement and momentum thickness yielded values of $\delta^* = 3.11$ mm and $\theta = 0.57$ mm. The Reynolds number within the test section based on boundary layer thickness, Re_δ, was 3.1×10^5.

A diagram of a typical compression corner model is shown in Fig. 1 with the coordinate system used in the presentation of the experimental data. A complete compression corner model consisted of a ramp mounted on a ramp support. The forward part of the ramp support formed the lower wind tunnel wall upstream of the corner. The section of the model downstream of the end of the ramp sloped gradually down to the floor level of the wind tunnel to reduce the disturbances caused by the models during the wind tunnel startup process.

The five ramp models and the ramp support were made of aluminum and anodized flat black to reduce laser light reflections during the LDV measurements. The model support was sealed along the side walls and upstream of the corner where the support mated with the

wind tunnel floor with linear o-ring material. The junction between the ramp and the ramp support which formed the compression corner was sealed with gasket sealing compound. Static pressure taps 0.57 mm in diameter were located every 2.54 mm longitudinally on the surface of the ramps and on the model support upstream of the corner.

The models used in this study spanned the full 10.2 cm width of the test section. It may have proven beneficial to have used narrower ramp models with splitter plates located along the sides to eliminate the effects of the side wall boundary layers on the shock wave-boundary layer interaction, similar to those used in other studies [2-9]. However, the side wall splitter plates would have denied optical access to the interaction region, and thus would have made LDV measurements impossible. As a result, it was decided to use full span models and to experimentally determine the extent of the side wall boundary layer interference with surface flow pattern measurements.

Measurement Techniques

The primary measurement tool used in this investigation was a two color laser Doppler velocimeter system. This system was used to obtain two component mean velocity and turbulence property measurements in both the upstream and redeveloping downstream boundary layers within the five compression corner flowfields. In addition to the LDV measurements, surface static pressure measurements, surface streak pattern measurements, and high speed Schlieren photographs were also taken. The pressure measurements were used to determine the location of the beginning of the interaction, and to ensure that the ramp models were long enough to achieve a complete pressure rise. The surface streak patterns were used to check for flowfield three-dimensionality, and to determine the existence of separation, and the separation and reattachment locations. The Schlieren photographs were used to map the flowfield, and to look for any gross flowfield unsteadyness.

The LDV system used in this investigation was a two color, two component system utilizing optical and electronic components manufactured by Thermal Systems Incorporated (TSI). A Spectra-Physics five Watt argon-ion laser operating in the multi-line mode produced the necessary laser light. The beam from the laser was split into its principal components with a dispersion prism, and the green beam, with a wavelength of 514.5 nm, and the blue beam, with a wavelength of 488 nm, were used by the system. Each of these two beams was reflected down the optical axis with plane surface mirrors, and split into two equal intensity parallel beams with beamsplitting optics. One beam of each of the two sets of parallel beams was then passed through a Bragg cell in order to shift the frequency by 40 MHz. The four parallel beams were then passed through a 350 mm focal length lens, which caused the four beams to cross at a single point. This produced the measurement volume containing the two orthogonal fringe patterns necessary for two component velocity measurements.

The beam spacing and 350 mm lens used in this investigation produced a measurement volume diameter of approximately 0.18 mm and a measurement volume length of approximately 6 mm. The fringe spacing was approximately 8.5 μm, and the fringe velocity due to the frequency shifting was approximately 340 m/sec. The laser and transmitting optics were mounted on a traversing table which could be moved manually in three directions by means of threaded rod arrangements with an accuracy of approximately 0.1 mm. In this manner the measurement volume could be positioned at any location within the wind tunnel test section.

The collection optics were located on the opposite side of the wind tunnel test section, and consisted of a 250 mm focal length lens to collect the scattered light and a dichroic mirror and filter arrangement to separate the two color signals. These optical components were oriented 10 degrees off the optical axis in order to simplify alignment procedures, and to reduce the effective measurement volume length to less than 2 mm. Photomultipliers converted the scattered light signals to analog voltage signals, and TSI frequency counters were used to determine the frequencies of the signals, and to perform validation checks to remove erroneous data. The output from the counters was stored directly in the memory of a Digital Equipment Corporation PDP 11-03 minicomputer, which converted the output into velocities and stored the data on floppy disks. The data was then transferred to a Hewlett-Packard 9000 series computer for thorough analysis.

The seed particles used in this investigation consisted of silicone oil droplets which were introduced into the wind tunnel stagnation chamber. A series of experiments was conducted with the LDV system to determine the mean particle size, in which two component velocity measurements were made immediately downstream of the oblique shock wave generated by the 8 degree compression corner in the Mach 2.94 flowfield. The mean velocity measurements were then compared to predicted velocities of particles of various sizes in the same flowfield conditions. The results of this series of experiments indicated that the silicone oil droplets had a mean effective diameter of between 1.5 and 2 μm. Particles of this size have been shown to have a sufficient frequency response to track the large scale velocity fluctuations that exist downstream of shock wave-turbulent boundary layer interactions [1]. The effects of particle lag were seen to some extent in the mean velocity measurements in the regions immediately downstream of the oblique shock waves due to the large velocity gradients in these regions. The influence that particle lag had on the data obtained in this investigation will be discussed during the presentation of the experimental results.

The statistical uncertainties involved in determining mean velocities from individual velocity measurements is a function of the sample size and the local turbulence intensity. The sample size in this investigation was

increased as local turbulence intensity increased, with 1024 samples taken when the local turbulence intensity was less than 15 percent, 2048 samples taken when the local turbulence intensity was between 15 and 25 percent, 3072 samples taken when the turbulence intensity was between 25 and 30 percent, and 4096 samples taken when the local turbulence intensity exceeded 30 percent. From a statistical analysis, the uncertainty in mean velocity was found to be less than 2 percent for all velocity profiles with the exception of the two profiles nearest the compression corner in the 24 degree flowfield, in which local turbulence intensities reached values greater than 100 percent and the statistical uncertainty in mean velocity is of the order of 3 percent. The statistical uncertainty in turbulence intensity can be shown to be a function of sample size only, and for the current investigation was everywhere less than 3.6 percent.

Mean and turbulent flow properties computed from LDV data obtained with counter type signal processors have been shown in the literature to be affected by biasing errors, most significantly velocity biasing [14] and fringe biasing [15]. Velocity biasing results from the fact that in a turbulent flow with uniformly distributed particles, a larger volume of fluid passes through the measurement volume during periods when the velocity is higher than the mean, than when the velocity is lower than the mean. Thus, a simple average of the individual velocity measurements is biased towards higher velocities. Fringe biasing results from the fact that a particle must pass through a given number of fringes within the measurement volume for its velocity to be measured. Thus, particles traveling in a direction parallel to the fringe plane are not "seen" by the LDV, and this results in a bias in favor of particles traveling perpendicular to the fringe plane. The measurements of this investigation were corrected for the effects of velocity biasing by weighting each measurement with the two-dimensional velocity bias correction factor $1/(u^2 + v^2)^{1/2}$. The effects of fringe biasing were significantly reduced by the frequency shifting, which caused the fringes to move in the upstream direction, and by orienting the fringes at ±45 degrees relative to the wind tunnel floor for the upstream boundary layer measurements, and at ±45 degrees relative to the ramp surface for the 12, 16, 20, and 24 degree compression corner redeveloping boundary layer measurements. It was not necessary to rotate the fringes at ±45 degrees relative to the 8 degree ramp surface due to the small flow angle and low turbulence intensities in this flowfield. A comparison between the two-dimensional velocity bias corrected data and data corrected with both the velocity bias correction and a fringe bias correction based on the analysis of Buchhave[15] showed that the effects of fringe bias were not significant in comparison to the effects of velocity bias, and thus the results presented here were corrected with the velocity bias correction only.

Experimental Results

The Schlieren system was used to view the five compression corner flowfields during the initial phase of this investigation. The freestream flow was observed to be completely supersonic, and some unsteadyness was observed in the shock structures, particularly in the large ramp angle configurations, similar to the unsteadyness reported by Dolling and Murphy[16] in a 24 degree compression corner flowfield. The presence of separation near the corner was clearly visible in the Schlieren photographs of the 16, 20, and 24 degree flowfields.

Surface streak patterns were obtained with two techniques, one using an extremely viscous oil, and a second using a kerosene-zinc oxide mixture. These techniques indicated the presence of separation in the 16, 20, and 24 degree compression corner flowfields, as well as the presence of an extremely small amount of separation in the 12 degree compression corner flowfield. This result is consistent with the results of Settles[2], who found a very small separated region in a Mach 3, 10 degree compression corner flowfield using a similar surface flow pattern technique. From the results of these surface streak patterns, the dimensionless separation locations, X_S/δ_0, were found to be -0.12, -0.71, -1.63, and -2.95, for the 12, 16, 20, and 24 degree flowfields, respectively. The dimensionless reattachment locations, X_R^+/δ_0, were found to be 0.09, 0.15, 0.52, and 1.11, for the 12, 16, 20, and 24 degree flowfields, respectively. The surface streak patterns indicated some three dimensionality in the 16, 20, and 24 degree compression corner flowfields due to the presence of the side wall boundary layers. As mentioned previously, this could have been significantly reduced with the use of side wall fences to reduce the effects of the wind tunnel walls. However, the optical access necessary for the LDV measurements made the use of fences impossible. In all configurations, the reattachment line was found to be very straight and free of three-dimensional effects for at least the center 7 cm of the 10.2 cm test section width. The LDV measurements were limited to the regions upstream of separation and downstream of reattachment, and thus it is believed that the three-dimensional effects within the separated regions had a negligible effect on the LDV measurements.

The surface static pressure distributions for the five compression corners are presented in Fig. 2. The solid lines on the right side of the figure are the theoretical downstream static pressures calculated with two-dimensional oblique shock wave theory. The pressure distributions on the surface of the ramps indicate that, with the possible exception of the 24 degree configuration, the ramps were long enough to achieve full pressure recovery within the boundary layer. The 24 degree ramp was approximately 14 percent shorter than the critical ramp length according to the theory of Hunter and Reeves[17]. However, the reattachment point was over four boundary layer thicknesses upstream of the end of the ramp, and the pressure near the end of the ramp was only 3 percent less than the theoretical value. Thus it appears that the

24 degree model was very close to the length required for full pressure recovery, and any effects of the less than optimum length were essentially negligible.

The boundary layer velocity profiles for the 12 and 24 degree compression corners are shown in Figs. 3 and 4. The profiles for these two corners were chosen for presentation because they best illustrate the effects of large separation regions on the mean velocity profiles. The horizontal axis in these figures is the velocity component parallel to the wind tunnel floor for the upstream boundary layer data, and parallel to the ramp surface for the downstream data. The vertical axis is the distance from the wind tunnel floor, or ramp surface, measured perpendicular to the upstream flow direction.

The effects of particle lag can be seen in the velocity profiles of the 12 degree configuration, in which the velocity just outside the boundary layer is relaxing toward the correct downstream value. Within the boundary layer the effects of particle lag diminish, as the distance from the measurement position to the shock wave increases. The velocity in the region nearest the wall downstream of the 12 degree corner can be seen increasing with X. This results from the steeper shock wave in the lower Mach number regions of the boundary layer, which causes a larger fractional decrease in the velocity than the shock wave in the outer regions of the boundary layer. Thus downstream of the interaction, the flow nearest the wall must accelerate as the boundary layer begins to return to an equilibrium state. This behavior was also seen in the 8 and 16 degree corner redeveloping boundary layers, due to the similarity of the flows with only small amounts of separation.

The velocity profiles downstream of the 24 degree compression corner exhibit wake-like properties, similar to those observed by other investigators downstream of separated compression corners [3-5]. These wake-like profiles are the result of the redeveloping downstream boundary layer having a shear layer velocity profile as its initial condition at reattachment. The shear layer velocity profiles develop over the length of the separated region starting at the separation point of the upstream boundary layer. The velocity profiles downstream of reattachment experience a rapid "filling out," as can be seen in Fig. 4. This rapid change in the boundary layer profiles is most likely caused by enhanced turbulent mixing, due to the formation of large scale eddies. The decrease in the measured streamwise velocity with X, which can be seen in the outer regions of the boundary layer downstream of the 24 degree compression corner is caused by a combination of two effects. The surface static pressure distributions, shown in Fig. 2, indicate that the pressure was still rising at the longitudinal locations where the velocity profiles shown in Fig. 4 were measured. Thus, the flow in these regions was still turning and decelerating in the final stages of the recompression process. Also, the effects of particle lag may be contributing to the decrease in u with X. The rather complicated two stage compression process caused by the presence of the separation and reattachment shock structures makes it infeasible to predict the particle lag in these regions. Thus the extent to which particle lag is contributing to this effect is uncertain.

The streamwise turbulence intensity, $\langle u' \rangle$, nondimensionalized by the freestream velocity upstream of the interaction, u_∞, is plotted for the 16 degree compression corner flowfield in Fig. 5. The turbulence intensity in the upstream boundary layer is also included for comparison. This data was chosen for presentation because it illustrates the trends of the turbulence intensity profiles seen in the data of all five flowfield configurations. In each of the redeveloping boundary layers, the level of the turbulence intensity was significantly increased by the interactions, with the amount of increase directly related to ramp angle, and thus shock strength. The turbulence intensity was found to reach a peak within the central regions of the boundary layers, and then decrease as the wall was approached. This can be seen in the data of Fig. 5. The turbulence intensity in each configuration could be seen spreading vertically with the intensity profiles becoming flatter at the downstream stations. This vertical diffusion can also be seen in the data of Ardonceau[12] downstream of a Mach 2.25 compression corner. A gradual decrease in the peak turbulence intensity accompanied this diffusion process as the boundary layer recovered from the effects of the interaction.

The maximum streamwise turbulence intensities for each measurement station are presented in Fig. 6. The maximum values plotted in this figure clearly show the increase in maximum turbulence intensity with ramp angle, and the gradual decrease of this quantity with X. Further analysis of the data from this investigation indicated that the location of the maximum turbulence intensity in each profile was also directly related to ramp angle, with the maximum values of turbulence intensity occurring further from the ramp surface for the larger shock strength interactions. A comparison of this data with the mean velocity profiles indicated that the maximum values of turbulence intensity occurred in the regions of maximum $\partial u/\partial Y^*$, due to the higher values of turbulence production in these regions of the boundary layers. It was also found that, in spite of the vertical diffusion of the turbulence within the boundary layers, the location of the maximum values remained essentially constant as the flow proceeded downstream.

Vertical turbulence intensity profiles, $\langle v' \rangle / u_\infty$, are shown in Fig. 7 for the 12 degree compression corner flowfield. The data obtained in this configuration is considered representative of the data obtained for all five configurations in this investigation. It can be seen in this figure that the effect of the shock wave was to increase the vertical turbulence intensity through the interaction. A comparison of the $\langle v' \rangle$ profiles from the five configurations indicates that, similar to the $\langle u' \rangle$ data, the amount of increase in this quantity was directly related to ramp angle, and thus shock strength. However, unlike the $\langle u' \rangle$ data, the $\langle v' \rangle$ profiles show little or no dependence on the distance from the ramp surface, Y^*. It can also be seen in Fig. 7 that the vertical turbulence intensity was significantly increased in the regions outside the

boundary layer. This data, in conjunction with other turbulence statistics obtained in this investigation, such as turbulent triple products and skewness and flatness factors, indicated that there was a significant alteration of the freestream turbulence structure caused by the presence of the oblique shock wave. Further studies are necessary to determine the exact nature of the effects of the oblique shock waves on the turbulence structure within the freestream flowfield.

The effects of particle lag on the mean velocity measurements can be seen in Fig. 3 in the outer regions of the boundary layer immediately downstream of the 12 degree shock wave. Some influence of this particle lag was expected in the measured turbulence intensities. In regions of significant particle lag, a false turbulence was expected due to different size particles decelerating at different rates, and thus producing a broad velocity histogram. However, no indications of the effects of particle lag were observed in any of the turbulence intensity profiles. The streamwise and vertical turbulence intensities in the freestream regions with significant particle lag were very similar to the values measured in the freestream regions with no significant lag. This is indicative of a relatively uniform particle size distribution, such that the false turbulence generated by the lag was insignificant in comparison to the magnitude of the turbulence within the boundary layers.

The Reynolds stress profiles for the 16 degree compression corner flowfield, nondimensionalized with u_∞^2, are presented in Fig. 8. It can be seen in this figure that the magnitude of the Reynolds stress was significantly increased by the shock wave. In all configurations the Reynolds stress reached a peak within the boundary layer and then decreased as the wall was approached. The tendency for the Reynolds stress to reach a maximum within the central regions of the boundary layer has been reported by other investigators in compression corner flowfields [7-9], as well as in reattaching free shear layers [18].

The maximum Reynolds stresses for each boundary layer profile are shown in Fig. 9. Like the turbulence intensity, the maximum Reynolds stress is a strong function of ramp angle, with very large values associated with the 20 and 24 degree compression corner flowfields. These large Reynolds stresses imply the existence of large scale eddies, which were also indicated by the rapid "filling out" of the wake-like boundary layers downstream of the 20 and 24 degree shock waves. A steady decrease in Reynolds stress with X can be seen in this figure, as the turbulence began to dissipate and diffuse through the boundary layers. The dissipation of the turbulence, however, was an extremely gradual process, and even in the weakest interaction, the ramp was of insufficient length to allow the turbulence to completely return to equilibrium conditions.

The trends in the Reynolds stresses of this investigation agree quite well with those found by various researchers working with similar flowfields [7-9]. The dependency of the increase in Reynolds stress on α, the gradual decay in Reynolds stress with X downstream of the interaction, and the vertical diffusion of the Reynolds stress in the boundary layer can all be seen in the data of Jayaram and Smits[7] for an 8 degree corner, and the data of Muck and Smits[8,9] for 16 and 20 degree compression corners. However, the magnitudes of $-\overline{u'v'}/u_\infty^2$ reported by these authors are significantly lower than the results of the current investigation, with the maximum values differing by factors of 2 to 4 depending on ramp angle. This large discrepancy is most likely caused by calibration problems associated with the slanted hot wire technique used in these investigations. These authors state that the hot wire calibration is only valid in regions in which the Mach number component normal to the wire exceeds 1.2. Taking into account the 30 degree yaw angle of the slanted hot wires, this yields a lower Mach number limit of 1.39. The local mean Mach numbers at the regions of maximum Reynolds stress in the current investigation are all below 1.39 for the 16, 20, and 24 degree configurations, and are close to this value for much of the data of the 8 and 12 degree configurations. In addition to these low mean Mach numbers, the high turbulence intensities in these regions indicate that the instantaneous local Mach number frequently drops far below the calibration limits, and these periods of low Mach number contribute significantly to the magnitude of $-\overline{u'v'}$. Considering these factors, it is not surprising that a large discrepancy exists between Reynolds stresses measured with slanted hot wires and those measured with two component LDV systems in highly turbulent flowfields.

Conclusions

The interaction between an oblique shock wave and a turbulent boundary layer results in significant changes in both the mean and turbulent structure of the boundary layer flowfield. The mean velocity profiles measured in this investigation indicated that the inner regions of the boundary layer were decelerated to a greater degree than the outer regions by the interaction. The profiles downstream of interactions with large amounts of separation were very wake-like in nature, with the inner regions accelerating rapidly as the boundary layers began to return to equilibrium states. Turbulence intensities and Reynolds stress values were significantly increased by the interaction, with the amount of increase directly related to ramp angle, and thus shock strength. The measured profiles of longitudinal turbulence intensity and Reynolds stress reached peak values within the central regions of the boundary layers, with the distance from the peak values to the ramp surface also directly related to shock strength. The Reynolds stress values obtained in this investigation were significantly higher than values which have been measured in similar flowfields with slanted hot wires, and this discrepancy is believed to be due to the calibration problems associated with hot wire systems in highly turbulent supersonic flows. The turbulent structure within the redeveloping boundary layer relaxed very

gradually towards equilibrium values, such that the size limitations imposed by the wind tunnel used in this investigation prohibited the use of ramps of sufficient length to allow a complete return of the turbulent properties to upstream equilibrium values. The rapid "filling out" of the mean velocity profiles, and the large values of the measured Reynolds stresses indicated the presence of large scale turbulent structures in the flow downstream of the shock wave-turbulent boundary layer interactions.

Acknowledgment

Support for this research was provided by the U.S. Army Research Office through contract monitor Dr. Robert E. Singleton under Research Grant DAAG 29-79-C-0184 and Research Grant DAAG 29-83-K-0043; and the Department of Mechanical and Industrial Engineering at the University of Illinois at Urbana-Champaign.

References

[1]Kuntz, D. W., "An Experimental Investigation of the Shock Wave-Turbulent Boundary Layer Interaction," Ph.D. thesis, Department of Mechanical and Industrial Engineering, University of Illinois at Urbana-Champaign, Urbana, Illinois, 1985.

[2]Settles, G. S., "An Experimental Study of Compressible Turbulent Boundary Layer Separation at High Reynolds Numbers," Ph.D. thesis, Princeton University, Princeton, New Jersey, 1975.

[3]Settles, G. S., Bogdonoff, S. M., and Vas, I. E., "Incipient Separation of a Supersonic Turbulent Boundary Layer at High Reynolds Numbers," *AIAA Journal*, Vol. 14, No. 1, January 1976, pp. 50-56.

[4]Settles, G. S., Vas, I. E., and Bogdonoff, S. M., "Details of a Shock-Separated Turbulent Boundary Layer at a Compression Corner," *AIAA Journal*, Vol. 14, No. 12, December 1976, pp. 1709-1715.

[5]Settles, G. S., Fitzpatrick, T. J., and Bogdonoff, S. M., "Detailed Study of Attached and Separated Compression Corner Flowfields in High Reynolds Number Supersonic Flow," *AIAA Journal*, Vol. 17, No. 6, June 1979, pp. 579-585.

[6]Hayakawa, K., Smits, A. J., and Bogdonoff, S. M., "Hot-Wire Investigation of an Unseparated Shock-Wave/Turbulent Boundary Layer Interaction," AIAA Paper 82-0985, 1982.

[7]Jayaram, M. and Smits, A. J., "The Distortion of a Supersonic Turbulent Boundary Layer by Bulk Compression and Surface Curvature," AIAA Paper 85-0299, 1985.

[8]Muck, K. C. and Smits, A. J., "The Behavior of a Compressible Turbulent Boundary Layer Under Incipient Separation Conditions," Presented at the 4th Symposium on Turbulent Shear Flows, Karlsruhe, West Germany, September 1983.

[9]Muck, K. C. and Smits, A. J., "Behavior of a Turbulent Boundary Layer Subjected to a Shock-Induced Separation," AIAA Paper 84-0097, 1984.

[10]Rose, W. C. and Johnson, D. A., "Turbulence in a Shock-Wave Boundary-Layer Interaction," *AIAA Journal*, Vol. 13, No. 7, July 1975, pp. 884-889.

[11]Modarress, D. and Johnson, D. A., "Investigation of Turbulent Boundary-Layer Separation Using Laser Velocimetry," *AIAA Journal*, Vol. 17, No. 7, July 1979, pp. 747-752.

[12]Ardonceau, P. L., "The Structure of Turbulence in a Supersonic Shock-Wave/Boundary-Layer Interaction," *AIAA Journal*, Vol. 22, No. 9, September 1984, pp. 1254-1262.

[13]Maise, G. and McDonald, H., "Mixing Length and Kinematic Eddy Viscosity in a Compressible Boundary Layer," *AIAA Journal*, Vol. 6, No. 1, January 1968, pp. 73-80.

[14]McLaughlin, D. K. and Tiederman, W. G., "Biasing Correction for Individual Realization of Laser Anemometer Measurements in Turbulent Flows," *The Physics of Fluids*, Vol. 16, No. 12, 1973, pp. 2082-2088.

[15]Buchhave, P., "Biasing Errors in Individual Particle Measurements with the LDA-Counter Signal Processor," Proceedings of the LDA-Symposium, Copenhagen, Denmark, 1975.

[16]Dolling, D. S. and Murphy, M., "Wall Pressure Fluctuations in a Supersonic Separated Compression Ramp Flowfield," AIAA Paper 82-0986, 1982.

[17]Hunter, Jr., L. G. and Reeves, B. L., "Results of a Strong Interaction, Wake-Like Model of Supersonic Separated and Reattaching Turbulent Flows," *AIAA Journal*, Vol. 9, No. 4, April 1971, pp. 703-712.

[18]Samimy, M. "An Experimental Study of Compressible Turbulent Reattaching Free Shear Layers," Ph.D. thesis, Department of Mechanical and Industrial Engineering, University of Illinois at Urbana-Champaign, Urbana, Illinois, 1984.

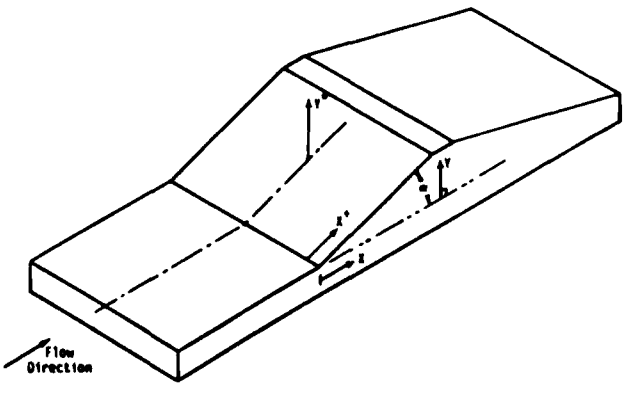

Fig. 1 Compression Corner Coordinate System.

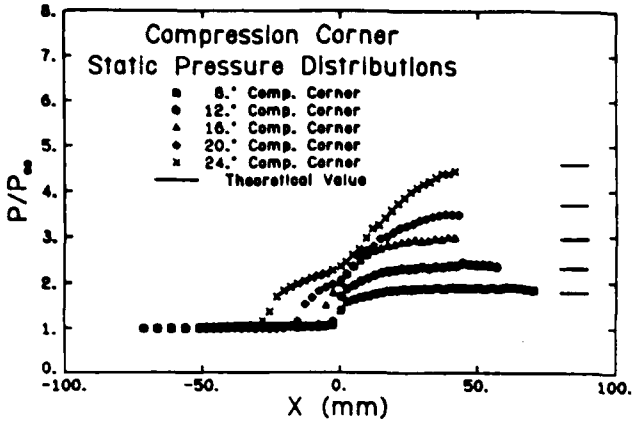

Fig. 2 Surface Static Pressure Distributions.

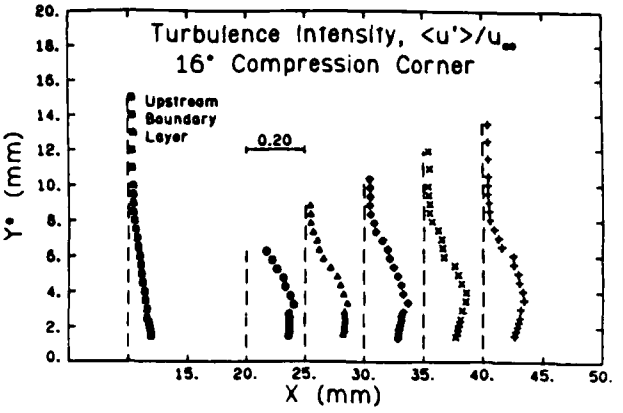

Fig. 5 Streamwise Turbulence Intensity Profiles for the 16 Degree Compression Corner Flowfield.

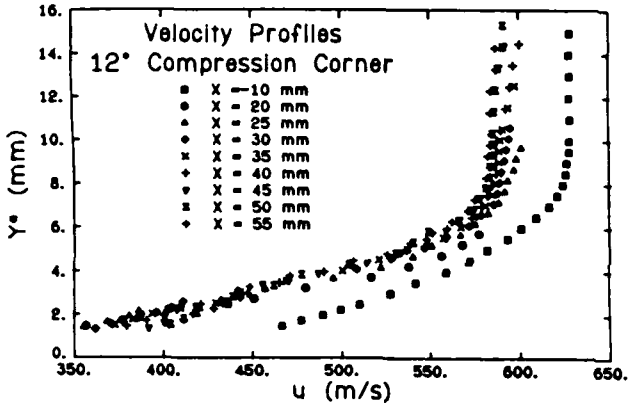

Fig. 3 Streamwise Velocity Profiles for the 12 Degree Compression Corner Flowfield.

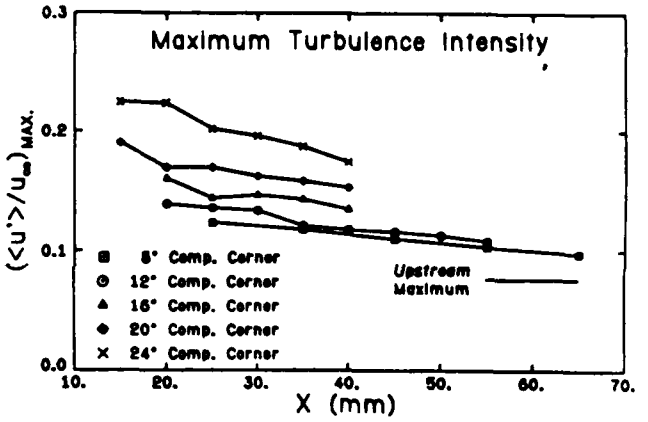

Fig. 6 Maximum Streamwise Turbulence Intensities for the Five Compression Corner Flowfields.

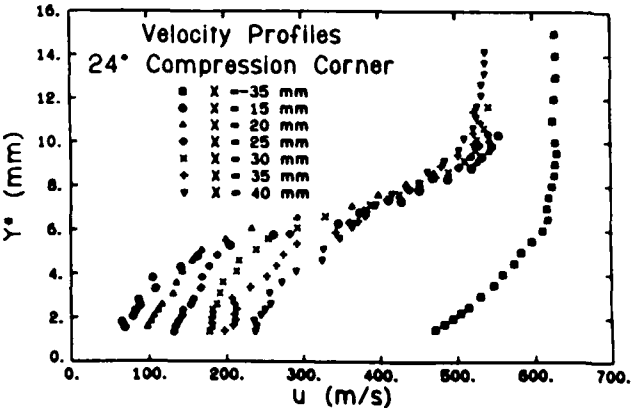

Fig. 4 Streamwise Velocity Profiles for the 24 Degree Compression Corner Flowfield.

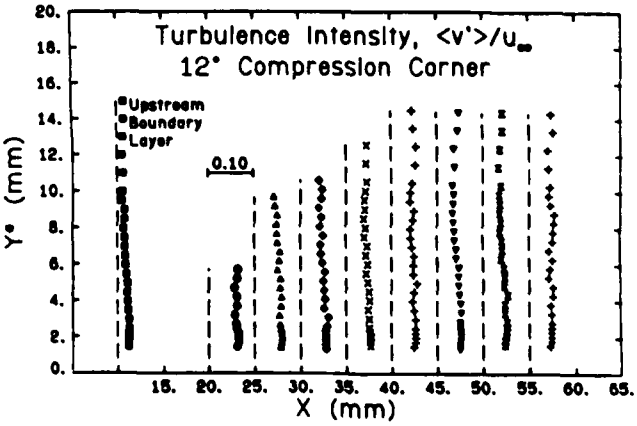

Fig. 7 Vertical Turbulence Intensity Profiles for the 12 Degree Compression Corner Flowfield.

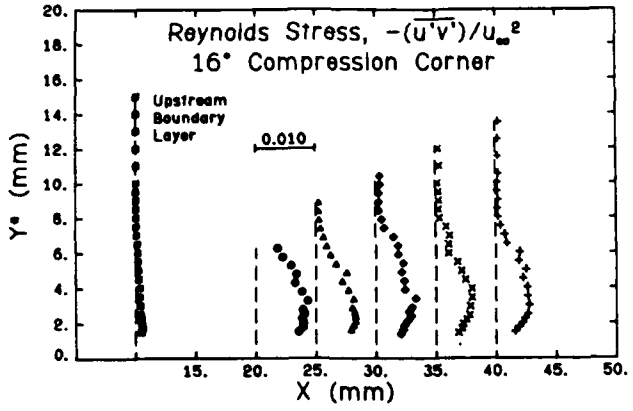

Fig. 8 Reynolds Stress Profiles for the 16 Degree Compression Corner Flowfield.

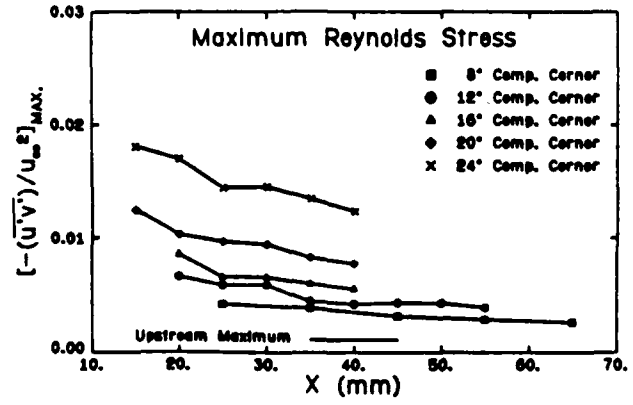

Fig. 9 Maximum Reynolds Stresses for the Five Compression Corner Flowfields.

APPENDIX C

COMPUTATIONAL ANALYSIS OF POWER-ON BASE FLOW

SAMPLE OF IMPROVED NUMERICAL COMPUTATION WITH THE THIN-LAYER NAVIER-STOKES EQUATIONS OF THE TURBULENT BASE PRESSURE FOR POWER-ON TRANSONIC FLIGHT

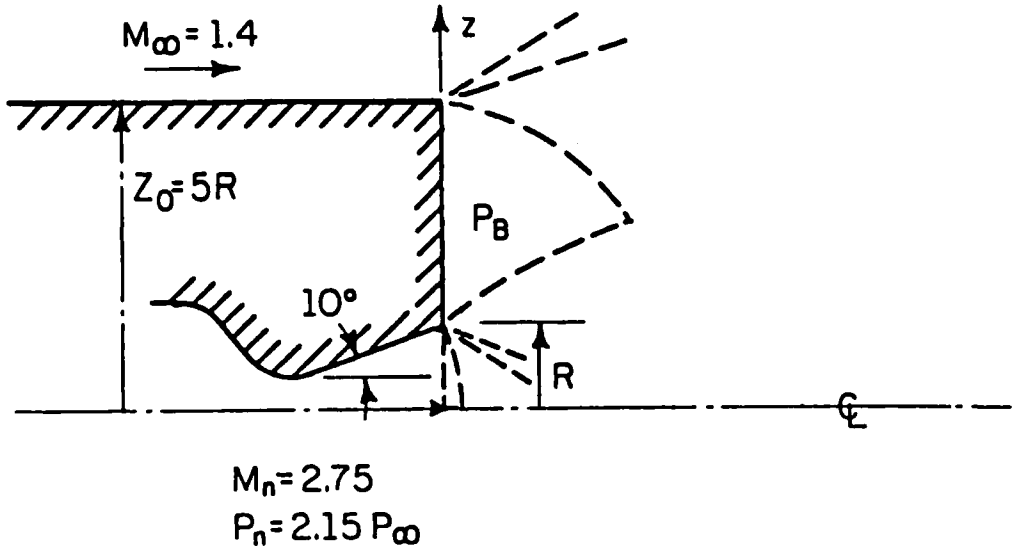

- Base flow configuration for the experiments and for the computational and component-model prediction methods.

SAMPLE OF IMPROVED NUMERICAL COMPUTATION WITH THE THIN-LAYER NAVIER-STOKES EQUATIONS OF THE TURBULENT BASE PRESSURE FOR POWER-ON TRANSONIC FLIGHT

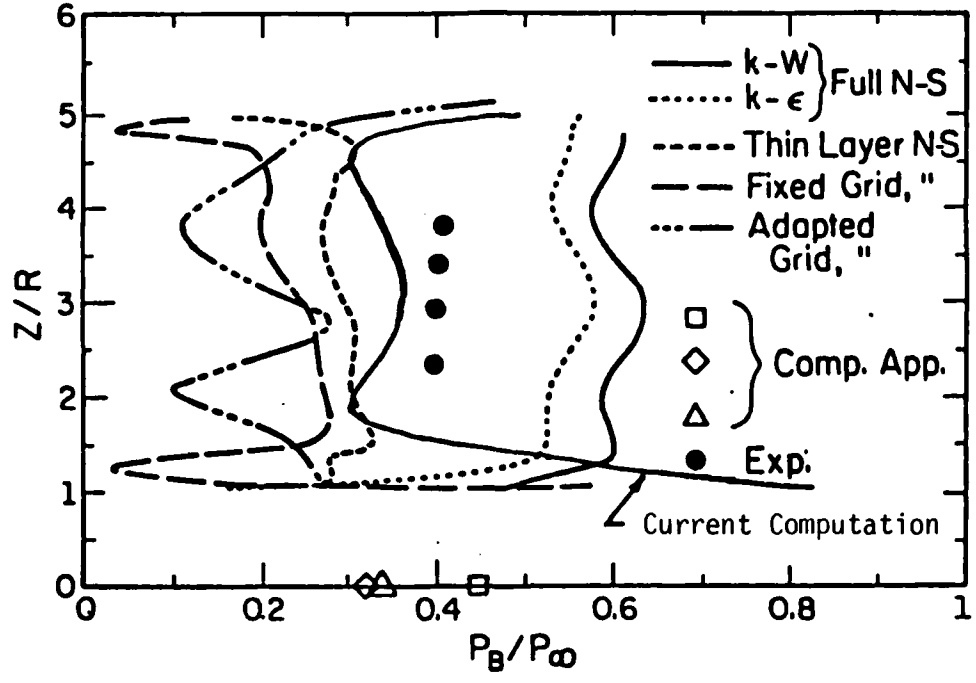

- Comparison of base pressure and its variation across the base as determined from experiments and as predicted from the current computational method and other methods.

(The base flow configuration and the base pressure results from experiments and prediction methods, except the current computation, are taken from AIAA Paper No. 85-1618 entitled, "Comparison of Experiment and Computation for a Missile Base Region Flowfield with a Centered Propulsive Jet" by H. L. Petrie and B. J. Walker.)

APPENDIX D

MODELING OF PROPULSIVE JET PLUMES AND THE EFFECTS ON AFTERBODY AND BASE FLOWS

SECTON D.1

WIND TUNNEL INVESTIGATIONS OF THE PLUME-MODELING METHODOLOGY SUGGESTED BY KORST

Paper presented at the Symposium on Fluid Dynamics

University of Illinois at Urbana-Champaign

Urbana, Illinois

April 26-27, 1984

by

J. Agrell, S.-E. Nyberg, and R. A. White

WIND TUNNEL INVESTIGATIONS OF THE PLUME-MODELING METHODOLOGY SUGGESTED BY KORST

J. Agrell, S.-E. Nyberg
The Aeronautical Research Institute of Sweden (FFA)
Box 11021, S-161 11 Bromma, Sweden

R.A. White
University of Illinois at Urbana-Champaign,
Urbana, IL 61801, U.S.A.

ABSTRACT

A description of wind tunnel investigations made to verify the plume-modeling methodology suggested by Korst is given. The lay-outs of the specifically made hot gas facility and the model as well as the geometry of the different kind of nozzles used are presented. Base pressure and separation distance results for a propulsive conical afterbody in the Mach number range 1.1 to 3.0 at zero angle of attack are shown. Some results demonstrating the influence of the more complicated flowfields which arose at angles of attack up to 20° and of flowfields generated by deflected fins at angles of attack up to 6° are also presented.

The validity of the plume modeling methodology has been confirmed by comparison of results for two propellants with different specific heat ratios, Freon-22 (γ=1.16) and air (γ=1.4). The modeling scheme is satisfactory even at high angles of attack $\alpha<20^{\circ}$ and effects of controls are acceptably simulated.

INTRODUCTION

Basis for the Korst modeling methodology [1,2] is the assumption that a prototype plume is properly simulated by a model plume if the two plumes have the same contour in the flowfield adjacent to the afterbody. The concept presumes that the initial plume deflection angle and the plume shape (radius of curvature) of the prototype plume is duplicated by the model plume, and that proper consideration of plume pliability is taken. The merits and potential of this modeling scheme have been evaluated in a series of wind tunnel tests carried out by FFA in close cooperation with the Gas Dynamics Laboratory at the University of Illinois at Urbana-Champaign. It is the purpose of this paper to review the technique used and to present some results and the conclusions.

EXPERIMENTAL TECHNIQUE

Propellants selected for the plume simulation tests were compressed dry air (γ=1.40) and compressed heated Freon-22 (γ=1.16). A hot gas facility has been built specifically to deliver heated Freon [3,4,5], Figs 1 and 2. The model used is built up of a 14 degrees half-angle nose cone, a cylindrical centerbody and an 8-degree conical boattail of one diameter length, Fig.3. The overall length is 9.5 diameters. The model is supported by a strut, which provides the propellant. The rear part of the centerbody, the boattail and the base region are all instrumented with pressure taps, Fig.4. A set of four deflectable fins can be attached to the afterbody, Fig.5.

MODELING FROM AIR TO FREON AT M_E = 2.0 AND 3.0

The first series of tests [5,6] were carried out at the free stream Mach number M_E = 2.0 and at zero angle of attack with nozzles modeling from air (prototype) to Freon (model), Fig.6. A typical base pressure result is, shown in Fig.7. The agreement between prototype and model base pressures is satisfactory not only for the design pressure but also for a rather wide range of off-design conditions. Also shown are a few results for the Freon nozzle tested with air to illustrate the shortcomings of retaining nozzle similarity. Slope modeling of these results gives reasonable correspondence to the prototype data but at effectively much lower pressure ratios. At these conditions, with essentially no separation, the radius of curvature is less important. In contrast to the methodology suggested by Korst, which is based on distorted nozzle geometries, very high stagnation pressures would be required for modeling with gases of higher than prototype specific heat ratios. For the separation location, as shown in Fig.8, the nozzle designed according to "weak shock modeling" provides the best correlation, particularly near the design pressure ratio.

Some tests at off-design free stream Mach number conditions were undertaken to gain insight into the range of applicability of the plume deflection angle-radius of curvature (shape) model method. Thus while the nozzles were designed for M_E = 2.0 free stream condition tests were also run at M_E = 3.0. Fig.9 shows the base pressure, which can be seen to be satisfactory particularly in the lower base pressure regime. The more sensitive separation distance, however, shows poorer correlation, Fig.10. This may be explained by the increasing importance of plume curvature for large separated regions.

MODELING FROM FREON TO AIR. M_E = 2.0

Zero Angle of Attack

In later tests [6] nozzles modeling from Freon (prototype) to air (model) have been used. As the specific heat ratio for Freon-22 is γ=1.16, which is appropriate for simulation of combustion type products, this modeling is relevant for typical plume simulation in wind tunnels. The geometry of the prototype was chosen to be as realistic as possible, i.e. to have a shape similar to a typical rocket nozzle, see Fig.11.

Base pressure results are shown in Fig.12 and separation distances in Fig.13. The two air (model) nozzle results agree very well with each other, and the correlation with the Freon (prototype) nozzle results is quite good. Also shown for comparison are the results of using cold air in the prototype nozzle (no modeling). The poor agreement with the Freon results is obvious.

It is believed that the small discrepancy between the prototype and the model results is significant despite being fairly small. Possible explanations for the discrepancy lie in the fact that the calculation of the air (model) nozzles was based on the assumption that the approach conditions at the Freon (prototype) nozzle exit are produced by conical source flow [10] and neglecting viscid effects during the impingement process. Refined calculations of the flow in the prototype nozzle have shown that the deviations from conical source flow are such that the plume shape is affected to such an extent that it may be of importance. A new air (model) nozzle taking the deviations from source flow into consideration was therefore calculated (M_L=1.6, see Fig.14) and wind tunnel tested. The results shown in Fig.14 agree, however, very well with the earlier air nozzle results. This indicates that the discrepancy between Freon and air results is probably not due to the deviations from conical source flow at the Freon nozzle exit.

Effects of Angle of Attack

Although the modeled nozzles have been calculated for axisymmetric flow, tests have been made at low angles of attack ($-6^\circ<\alpha<6$) [6] and at high angles of attack ($-20^\circ<\alpha<+20^\circ$) [7,8,9] to examine the limits of the modeling procedure. To facilitate the evaluation of the simulation of the angle of attack effects on the base pressure the pressure difference $\Delta(P_B/P_E)_\alpha = (P_B/P_E)_\alpha - (P_B/P_E)_{\alpha=0}$ has been calculated and is shown for the circumferential angle ϕ=0 as a function of angle of attack in Fig.15 for the three nozzles. It can be seen that the angle of attack effect of the Freon (prototype) nozzle is quite well simulated.

The separation location S/D at the circumferential angle ϕ=0 is in Fig.16 shown versus the angle of attack for the design jet stagnation pressure. The simulation is quite good, except at low positive angles of attack, which means when the vortex flow starts to build up.

The results confirm that the basic validity of the Korst modeling methodology is satisfactory also within the angle of attack range investigated ($-20^{o}<\alpha<+20^{o}$).

Effects of Control Fins

Wind tunnel tests have been carried out [7,8,9] to investigate the limitations of the Korst modeling methodology when the afterbody is exposed to the complex external flowfield generated by aft-mounted controls in combination with angle of attack. The angle of attack range was $-6^{o}<\alpha<+6^{o}$ and the controls were set at $\delta=0^{o}$ and $\pm 10^{o}$.

To isolate the effects of controls on base pressure ratio more clearly the difference between the results with and without controls have been calculated and the results for all three nozzles have for comparison been plotted together versus angle of attack. The results at the design jet stagnation pressure for the circumferential angles ϕ investigated is shown as a sample in Fig.17.

After analyzis of all test results it is concluded that the effects of the fins on base pressure obtained with the Freon (prototype) nozzle is in general satisfactorily simulated by the air (model) nozzles. A few local exceptions seem to occur in areas, where interaction between control wakes and the separated base region might be very sensitive to one parameter, e.g. the jet stagnation pressure. Apart from this few points the modeling seems to be valid even for severe combinations of control angles, angle of attack and off-design jet stagnation pressure. It is noted, however, that the effect of controls on base pressure ratio obtained with the air (model) nozzles is often somewhat larger than the effect with the Freon (prototype) nozzle.

MODELING FROM FREON TO AIR M_E = 0.8-1.1

The final series of wind tunnel tests in the current program are carried out at transonic free stream Mach numbers. Exploratory tests have been made with the M_L=1.6 air nozzle at Mach numbers M_E=0.8, 1.0 and 1.1 in the angle of attack range, $\alpha=\pm 6^{o}$, Fig.18. The tests with the Freon nozzle have just started. Some preliminary base pressure results are shown in Fig.19 at M_E = 1.1 as a function of jet stagnation pressure in the prototype plane. As can be seen a small discrepancy exist between the prototype and model results. The discrepancy seems to have the same character and magnitude as at M_E = 2.0.

CONCLUSIONS

An analysis of the results obtained at Mach number M_E=2.0 allows the following conclusions for the model configurations tested:

1. The Korst modeling methodology concept of congruent plumes as determined by radius of curvature and initial slope with proper consideration of plume pliability at the design condition for prototype and modeled nozzles successfully correlates both base pressure and flow separation in the vicinity of the base.

2. There are in the test results indications of a minor systematic discrepancy between the Freon and the air results.

3. The modeling concept is good even if the jet stagnation pressure deviates ±25° percent from the design pressure.

4. The modeling scheme is satisfactory even at high angles of attack $\alpha<\pm 20^{\circ}$.

5. The effects of aft-mounted control fins are simulated satisfactorily. This includes cases where the controls are deflected ($\delta=\pm 10^{\circ}$) in combination with angle of attack ($-6^{\circ}<\alpha<6^{\circ}$).

6. Preliminary test results at M_E= 1.1 indicate that the modeling concept is good also at transonic speeds.

ACKNOWLEDGEMENT

This research program is supported jointly by the European Research Office, U.S. Army, Contract No. DAJA37-81-C-1213, and The Aeronautical Research Institute of Sweden (FFA). The authors also want to thank H.H. Korst for his continued interest, encouragement, and support during the investigation.

NOMENCLATURE

D	Forebody diameter
M	Mach number
	Circumferential location index
N	Axial location index
P	Pressure
R	Radius
S	Separation distance
X	Axial coordinate
α	Angle of attack
γ	Specific heat ratio
δ	Control deflection angle
θ	Conical angle
ϕ	Circumferential angle

Subscripts:

B	Base condition
E	External flow (free stream)
I	Internal flow
L	Nozzle lip condition
M	Model
O	Stagnation condition
P	Prototype
ϕ	Condition at circumferential angle ϕ

REFERENCES

1. Korst, H.H.: Approximate determination of jet contours near the exit of axially symmetrical nozzles as a basis for plume modeling.
TR-RD-72-14, Aug.1972, US Army Missile Command, Redstone Arsenal, Ala., U.S.A.

2. Korst, H.H. and Deep, R.A.: Modeling of plume induced interference problems in missile aerodynamics.
AIAA Paper No. 79-0362, 17th Aerospace Sciences Meeting, New Orleans, LA., 15-17 Jan. 1979.

3. Nyberg, S.-E., Agrell, J. and Hevreng, T.:
Investigation of modeling concepts for plume-afterbody flow interactions.
Grant DA-ERO-78-G-028, 1st Annual Technical Report, Febr. 1979.

4. Nyberg, S.-E., Agrell, J. and Hevreng, T.:
Investigation of modeling concepts for plume-afterbody flow interactions.
Grant DA-ERO-78-G-028, 2nd Annual Technical Report, Febr.1980.

5. Korst, H.H., White, R.A., Nyberg, S.-E. and Agrell, J.: The simulation and modeling of jet plumes in wind tunnel facilities.
Paper 80-0430, presented at the AIAA 11th Aerodynamic Testing Conference, Coloroado Springs, Colorado, U.S.A., 18-20 March 1980. Also published in J. of Spacecraft and Rockets, Vol.18 No.5, Sept-Oct. 1981, pp. 427-434.

6. Nyberg, S.-E. and Agrell, J.: Investigation of modeling concepts for plume-afterbody flow interactions.
Grant DA-ERO-78-G-028, Final Technical Report, Nov. 1981.

7. Nyberg, S.-E. and Agrell, J.: Effects of control fins and angle of attack on plume-afterbody flow simulation.
Contract No. DAJA 37-81-C-1213, Annual Technical Report, Febr. 1983.

8. Nyberg, S.-E. and Agrell, J.: Wind tunnel simulations of plume-induced interference effects.
Proc. Symp. on "Rocket/Plume Fluid Dynamics Interactions", Huntsville, Alabama, 5-7 April 1983.

9. White, R.A., Agrell, J. and Nyberg, S.-E.: The wind tunnel simulation of propulsion jets and their modeling by congruent plumes including limits of applicability.
Paper 84-0232 presented at the AIAA 22nd Aerospace Sciences Meeting, Reno, Nevada, January 9-12, 1984.

10. White, R.A.: Advanced research/analysis of plume induced interference flow.
Proc. Symp. on "Rocket/Plume Fluid Dynamics Interactions", Huntsville, Alabama, 5-7 April 1983.

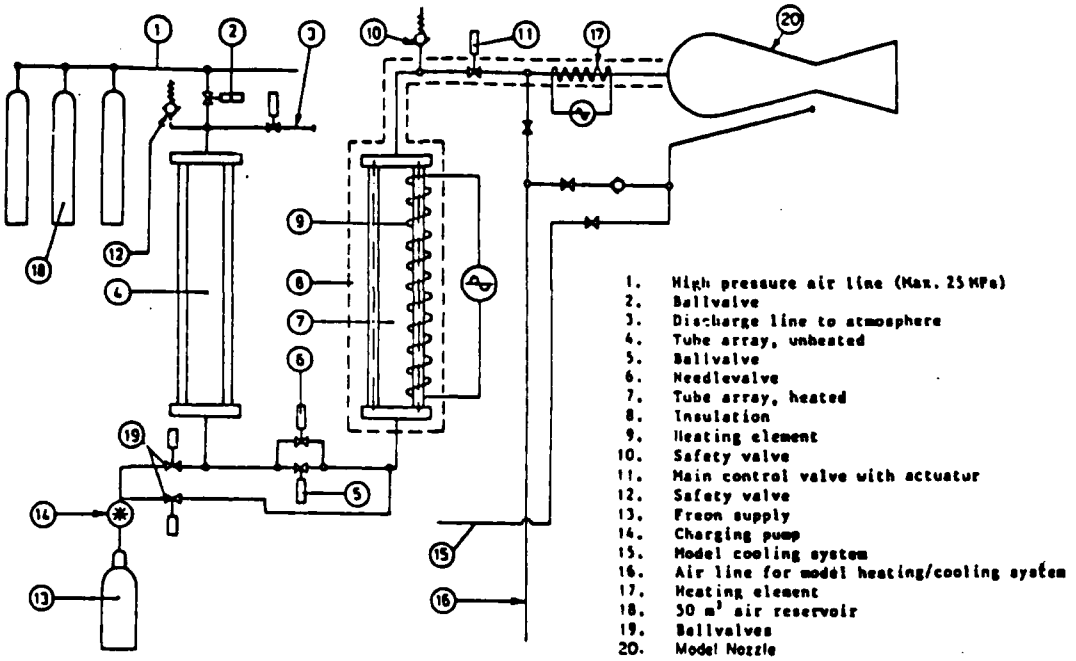

Fig. 1. Annotated Schematic of Air Driver System, Freon Heater and Nozzle

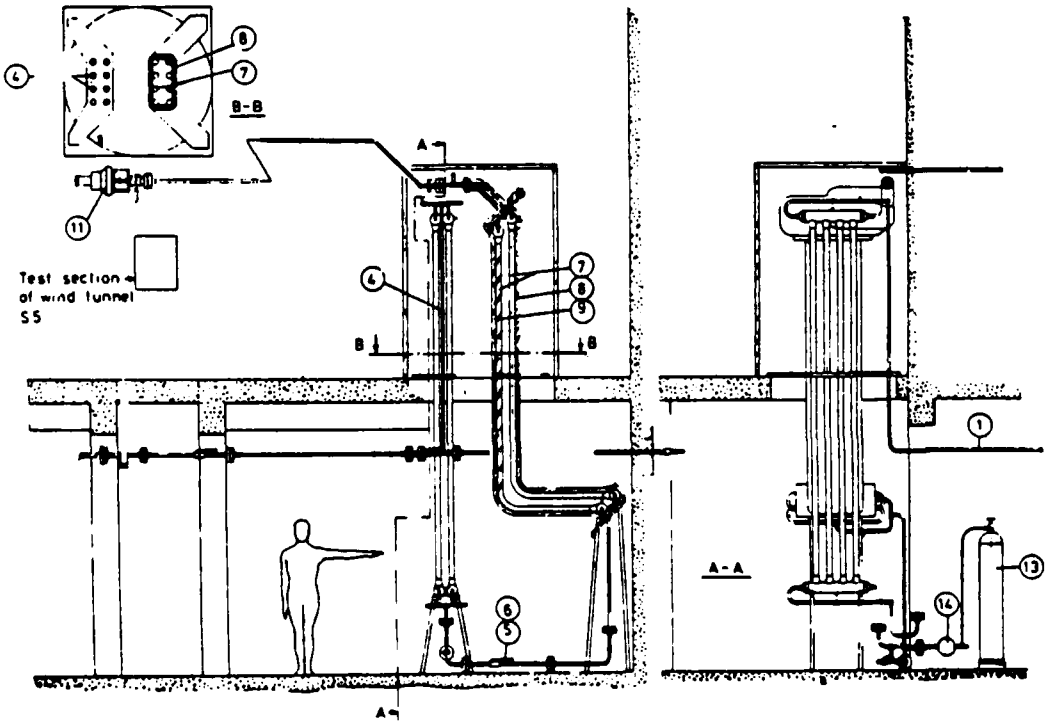

Figure 2. Freon supply facility. Numbers in circles refer to item list in Figure 1

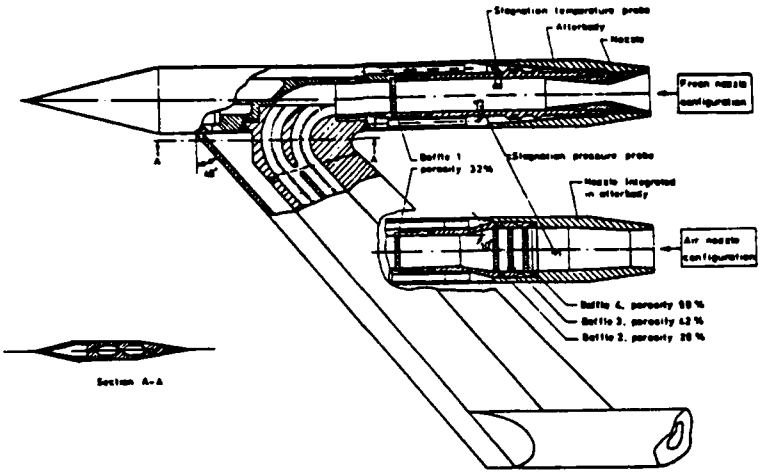

Fig. 3. Modified Model II of Current Modeling Tests

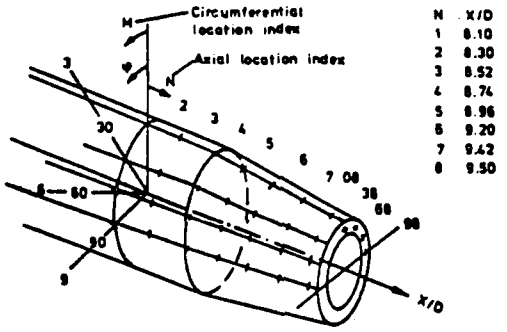

Fig. 4. Location of pressure taps on boattail.

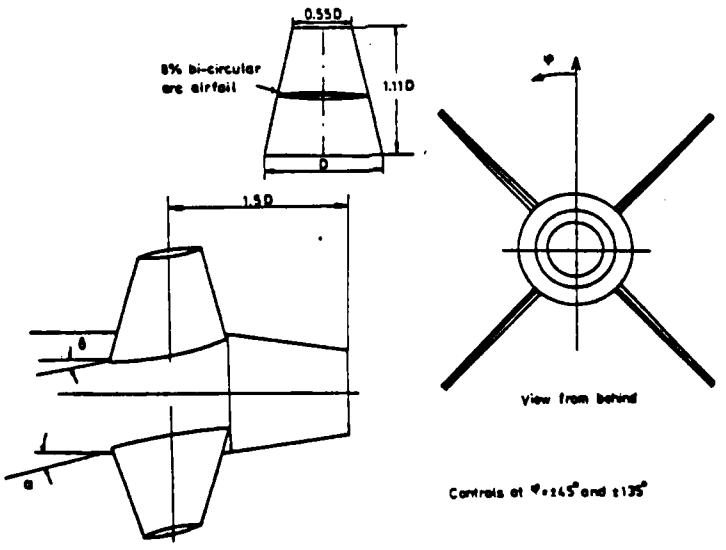

Fig. 5 Control dimensions and definition of control deflection angles.

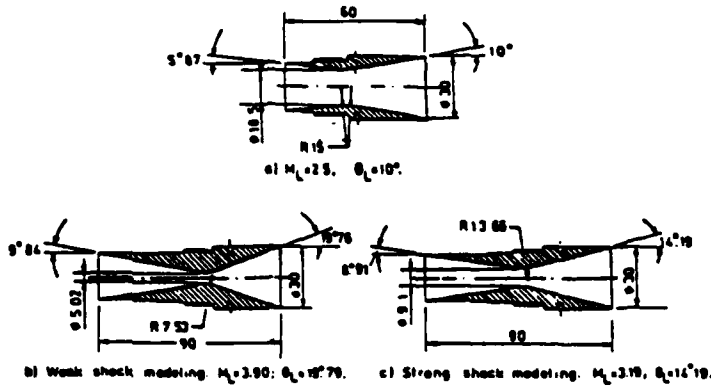

Fig. 6. Nozzles modeling from air to Freon (a) Prototype nozzle (Air, $\gamma_P = 1.4$). (b,c) Model nozzles (Freon 22, $\gamma_M = 1.16$) (Dimensions are in millimeters)

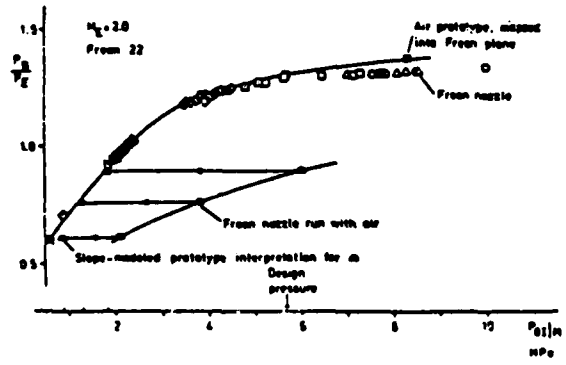

Fig. 7. Base pressure P_B/P_E versus jet stagnation pressure P_{OI} for Freon nozzle (Strong shock modeling).

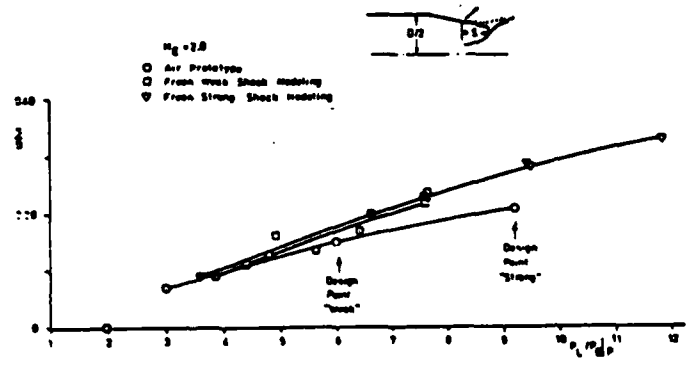

Fig. 8. Separation location vs lip pressure for air (prototype) and Freon (model) nozzles.

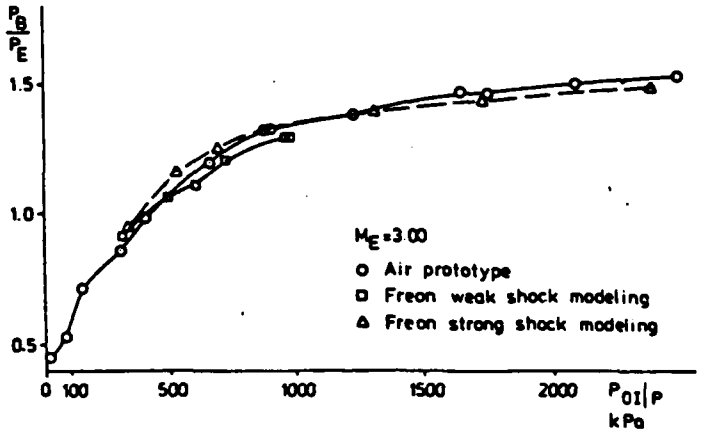

Figure 9. Base pressure versus jet stagnation pressure.

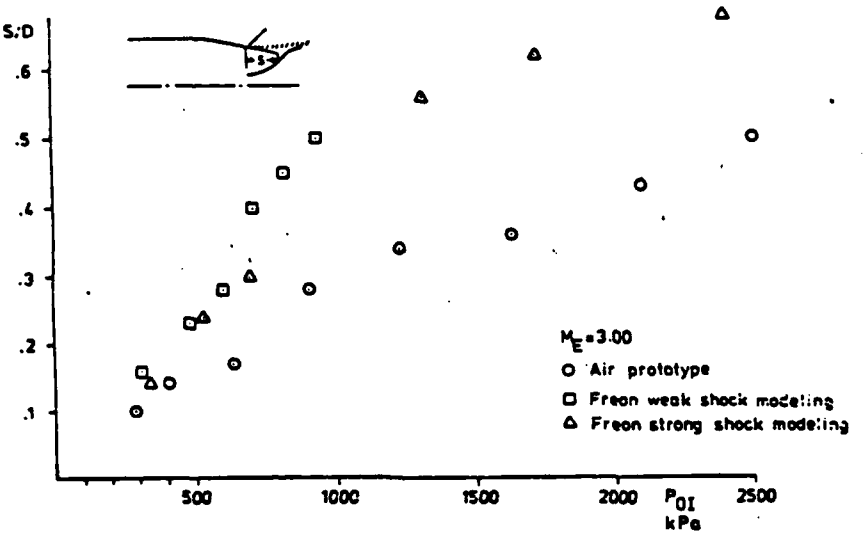

Figure 10. Separation location versus jet stagnation pressure.

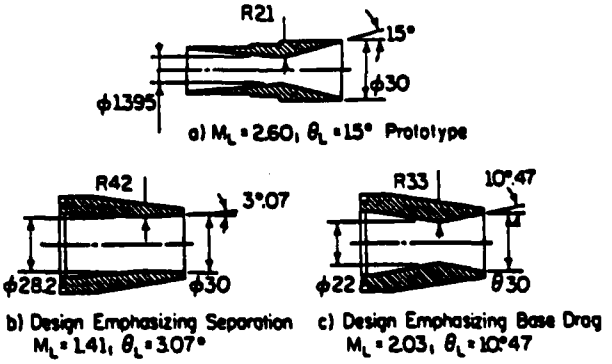

Fig. 11. Prototype Nozzle with γ = 1.16 and Two Model Nozzles (Air, γ = 1.40) Emphasizing Different Operating Conditions

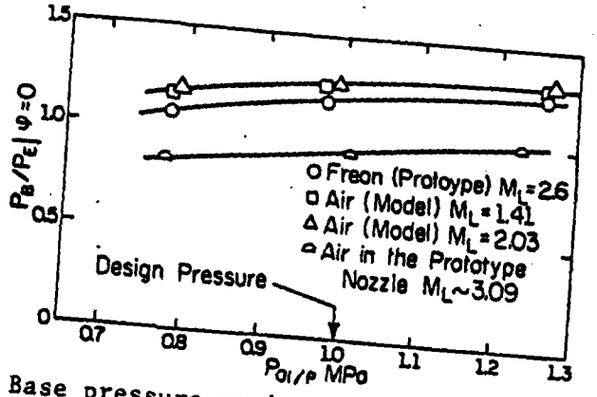

Fig. 12. Base pressure ratio for Freon (prototype) and air (model) versus nozzle stagnation pressure in prototype plane.

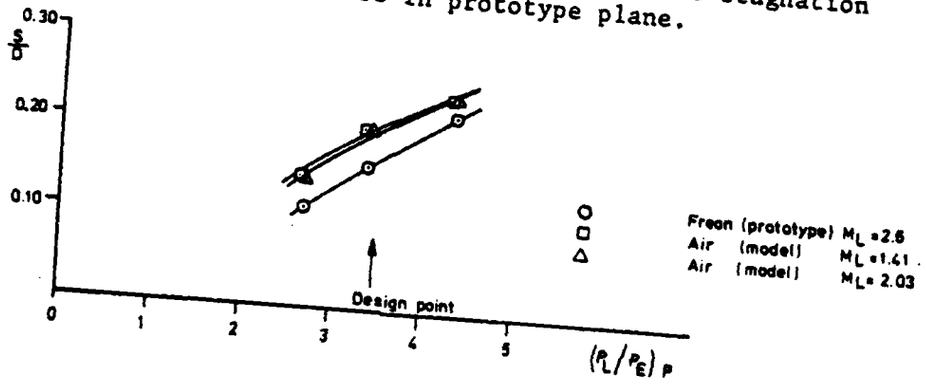

Fig. 13. Separation Location versus Lip Pressure for Freon (Prototype) and Air (Model) Nozzles

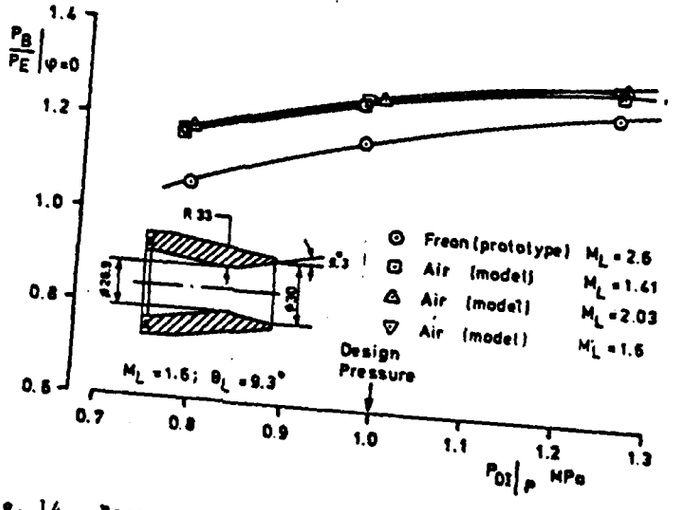

Fig. 14 Base pressure ratio for Freon (prototype) and air (model) versus nozzle stagnation pressure in prototype plane.

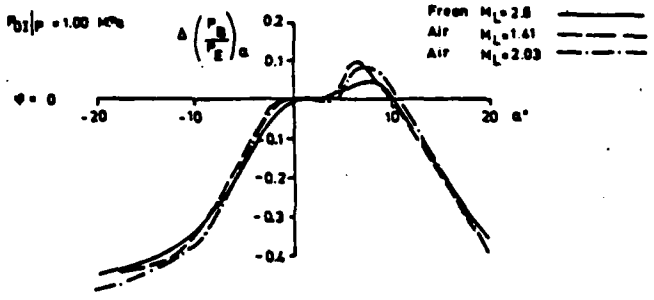

Fig. 15. Effect on base pressure ratio of angle of attack $\Delta(P_B/P_E)_\alpha = (P_B/P_E)_\alpha - (P_B/P_E)_{\alpha=0}$ versus angle of attack α at stagnation pressure $P_{OI}|_P$ = 1.00 MPa = design pressure.

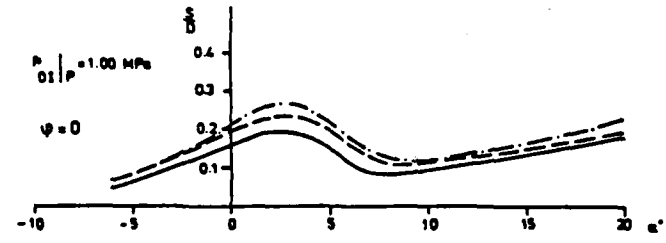

Fig. 16. Separation location S/D at $\varphi = 0$ versus angle of attack α for Freon (prototype) and air (model) nozzles at stagnation pressures $P_{OI}|_P$ = 1.00 MPa = design pressure.

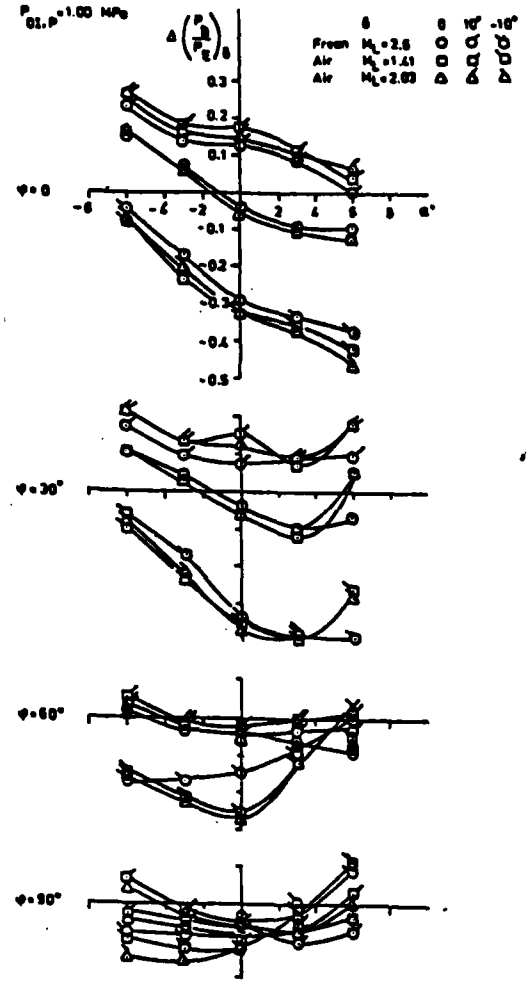

Fig. 17. Effect on Base Pressure Ratio of Controls $\Delta(P_B/P_E)_\delta = (P_B/P_E)_{\text{with controls}}$ minus $(P_B/P_E)_{\text{without controls}}$ versus Angle of Attack α at Stagnation Pressure $P_{OI,P}$ = 1.00 MPa

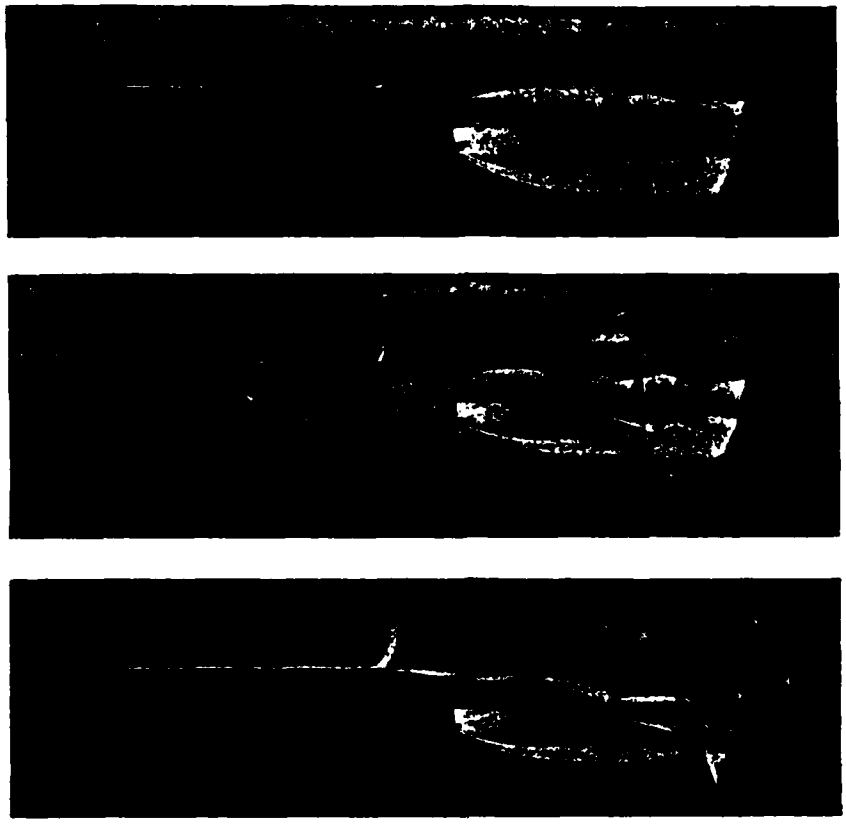

$M_E = 0.8$
$P_{0I} = 1.5$ MPa

$M_E = 1.0$
$P_{0I} = 1.0$ MPa

$M_E = 1.1$
$P_{0I} = 1.0$ MPa

Fig. 18. Schlieren pictures
Air model nozzle $M_L = 1.6$.

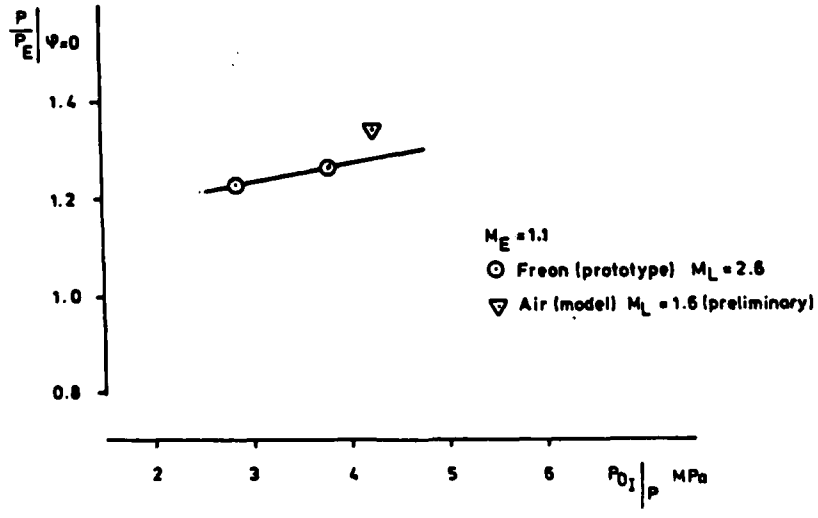

Fig. 19. Base pressure ratio for Freon (prototype) and air (model) versus nozzle stagnation pressure in prototype plane.

SYMPOSIUM ON FLUID DYNAMICS

Department of Mechanical and Industrial Engineering

University of Illinois at Urbana-Champaign

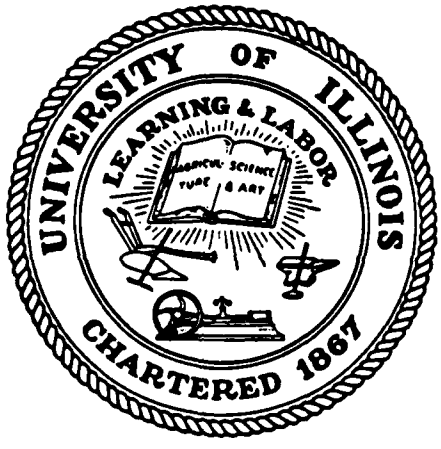

APRIL 26-27, 1984

SECTION D.2

THE WIND TUNNEL SIMULATION OF PROPULSIVE JETS AND THEIR MODELING BY CONGRUENT PLUMES INCLUDING LIMITS OF APPLICABILITY

Paper No. AIAA-84-0232

Presented at the AIAA 22nd Aerospace Sciences Meeting

Reno, Nevada

January 9-12, 1984

by

R. A. White, J. Agrell, and S.-E. Nyberg

AIAA-84-0232

The Wind Tunnel Simulation of Propulsive Jets and Their Modeling by Congruent Plumes Including Limits of Applicability

R.A. White, Univ. of Illinois, Urbana, Il; and
J. Agrell and S.-E. Nyberg, Aeronautical Research Institute of Sweden, Bromma, Sweden

AIAA 22nd Aerospace Sciences Meeting

January 9-12, 1984/Reno, Nevada

THE WIND TUNNEL SIMULATION OF PROPULSION JETS AND THEIR MODELING BY CONGRUENT PLUMES INCLUDING LIMITS OF APPLICABILITY

R. A. White*, J. Agrell**, S.-E. Nyberg**

ABSTRACT

In a previous paper, the authors described a new high pressure hot gas facility for the study of aerodynamic interference effects caused by plume induced separation from propulsion afterbodies and results of an experimental study using Freon (prototype) and air (model) to evaluate the merits and potential of a new methodology for plume simulation by congruent plumes with gases of dissimilar specific heat ratios. The previous results confirmed the theory for a limited range of test conditions. This paper describes improvements in the modeling methodology to allow for congruent plumes produced from non-ideal nozzle flows and extends the test conditions to complex afterbody and wake flows caused by angle of attack and afterbody mounted control fins at incidence. The current results show that the modeling methodology gives good agreement for the base pressure and separation location for stagnation pressure ratios of ±25° from the design condition, for angles of attack as high as ±20°, and with the effects of control fins deflected ±10° in conjunction with angle of attack of ±6°. A small but systematic difference between the Freon and air results is evident and possible explanations are offered that will be investigated in future tests.

NOMENCLATURE

Geometry

	Afterbody
D	Forebody diameter [m]
L	Boattail length [m]
M,N	Pressure tap location index, see Fig. 8
X	Axis of attack [m], see Fig. 8
α	Angle of attack [deg.], see Fig. 9
β	Boattail angle [deg.], see Fig. 9
ϕ	Circumferential angle [deg.], see Figs. 8 and 9
δ	Control deflection angle [deg.], see Fig. 9
	Nozzle
R_L	Exit or lip radius [m]
θ_L	Conical divergence angle [deg.]

Tunnel Flow

P_{OE}	Stagnation pressure [Pa]
P_E, P_e	Free stream static pressure [Pa]
M_E	Free stream Mach No. [-]
U	Axial velocity in the boundary layer
U_E	Free stream velocity

Nozzle Flow

M_L	Lip Mach No. [-]*
P_{OI}	Nozzle stagnation pressure [Pa]
P_L	Lip pressure [Pa]
T_{OI}	Nozzle stagnation temperature [°C]
γ	Specific heat ratio [-]
ω_L	Prandtl-Meyer angle corresponding to M_L [deg.]

Plume

M_F	Surface Mach No. [-]
θ_F	Initial surface slope [deg.]
R_C	Initial surface curvature [m]
ω_F	Prandtl-Meyer angle corresponding to M_F [deg.]

Wake Conditions

S	Separation distance measured from end of boattail [m]
P_b, P_B	Base pressure [Pa]

Coefficients

$\Delta(P_B/P_E)_\alpha$	Effect on base pressure of angle of attack $\Delta(P_B,P_E)_\alpha = (P_B/P_E)_\alpha - (P_B/P_E)_{\alpha=0}$
$\Delta(P_B/P_E)_\delta$	Effect on base pressure of controls $\Delta(P_B/P_E)_\delta = (P_B/P_E)_{\text{with controls}} - (P_B/P_E)_{\text{without controls}}$

Subscripts

M	Model
P	Prototype
A	Air
F	Freon

INTRODUCTION

The interaction of rocket or jet plumes with the external flowfield and surrounding launch equipment or adjacent surfaces is crucial to total system performance[1]. Such interactions determine the near wake base pressure and temperatures, the flow over portions of the vehicle surface in the case of upstream external flow separation, the wake flowfield at angle of attack, afterbody mounted control surface effectiveness, and launch equipment performance. Thus, the plume-slipstream interference flowfield affects aerodynamic performance by introducing drag penalities through lower than ambient base pressure or leads, as the ratio of jet stagnation-to-ambient pressure increases as for highly accelerated vehicles, to plume-induced separation[2]. In extreme conditions, such separation can lead to loss of stability and/or degradation of control effectiveness[3].

*University of Illinois at Urbana-Champaign, Urbana, IL 61801.
**Aeronautical Research Institute of Sweden (FFA), Bromma, Sweden.

*Conical source flow assumed, otherwise nozzle geometry and lip conditions have to be specified in greater detail, see Ref. [17].

The understanding of plume induced separation is therefore a vital factor in missile design. Consequently, wind tunnel testing is an important element during the early phases of model and prototype work. The inter-dependence of theory, design, and modeling to prototype development and eventually operational vehicles is clearly essential. Indeed, modeling, particularly with respect to wind tunnel testing, spans the entire development lifetime of a missile design. Thus, both the analytical and wind tunnel test programs must be viewed as crucial future contributors to improved theoretical models and the rapidly expanding field of computation fluid dynamics (CFD) which is still strongly dependent on experimental results for guidance[4] and verification.

The generation of rocket or jet plumes in wind tunnel investigations must, consequently, account for all or part of the factors affecting the induced flowfield, see Fig. 1, including plume shape, plume deflection, mass entrainment along the shear layers, wake closure (impingement), viscous and dynamic effects, temperature, influence of specific heat ratio and molecular weight, and possibly energy release through chemical reactions. The difficulty in attempting to simulate all of these parameters simultaneously is well known[5] and indeed a research program to determine and validate simulation techniques for special conditions such as those of the cryogenic National Transonic Facility (NTF) has been suggested[6]. Since all parameters cannot, in general, be simulated simultaneously in a wind tunnel, it becomes essential to determine the importance of the individual factors discussed above. This information has, in general, been lacking although recent simulation studies[7] have contributed strongly to this area of knowledge. On the other hand, strictly empirical correlations have been utilized for some specific applications such as the space shuttle.

These factors are particularly significant since the hope of accurately computing (CFD) the complex flow fields of the type shown in Fig. 2, or determining practical empirical correlating parameters for such flows, is at this time, at best, remote. Consequently, the design of rocket propelled missiles will rely on wind tunnel testing and proper plume simulation for the foreseeable future.

The availability of an analytical concept[8] for generating plumes of prescribed geometry and pliability using gases with different physical properties than typical propellants led to the planning and construction of a hot gas facility which has been constructed at the Aeronautical Research Institute of Sweden (FFA) for jet plume simulation with a variety of gases[9,10,11]. The facility has served to evaluate the merits and potential of the plume simulation methodology suggested by Korst[8,12]. Earlier theoretical modeling of propulsive jets[12] and experimental studies have confirmed the basic validity of the methodology under restricted conditions[11], i.e. single-centered jet and no-control surfaces, and small, $\alpha \leq 6°$, angles of attack. A follow-up research program, jointly sponsored by the European Research Office and by FFA, makes use of the special characteristics of the FFA hot Freon facility to examine the limits of modeling methodologies[13] for severe but realistic conditions which are beyond available computational methods yet are needed in performance prediction for full scale flight vehicles. The current two-year program includes extension of earlier work[11,13] for simple configurations in terms of the Mach number regime, angle of attack, and modifications for some complex models to examine interference effects of control surfaces.

It is the purpose of this paper to review briefly the technique used in the above mentioned investigations and to present some recent comprehensive results obtained during the first year of the research program[11] on the limits of congruent plume modeling[8].

METHODOLOGY

While in wind tunnel testing of rockets the need for some method of producing a plume, or its equivalent, has long been recognized, the success and understanding of the approaches utilized has had a rather non-uniform history. This is despite the fact that a basic understanding of the problem and even the establishment of relations accounting, in principle, for the influence of all pertinent variables was given in 1959 by Korst, et al.[14]. The importance of generating the correct jet plume geometry has been stressed in prior efforts to establish modeling laws between propellant gases having dissimilar specific heat ratios[8,11,15]. This was brought about by at least the partial recognition of the fact that modeling of plume interactions requires geometrically congruent jet boundaries, correct pressure-rise jet boundary deflection characteristics, and similar mass entrainment characteristics along the wake boundaries.

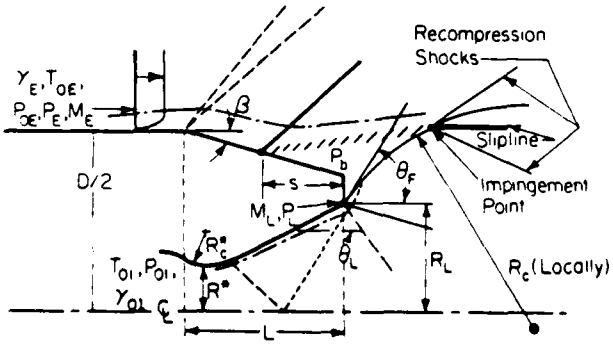

Fig. 1 Flow Configuration for Plume Induced Separation from a Conical Afterbody and Identification of Geometric and Operational Parameters

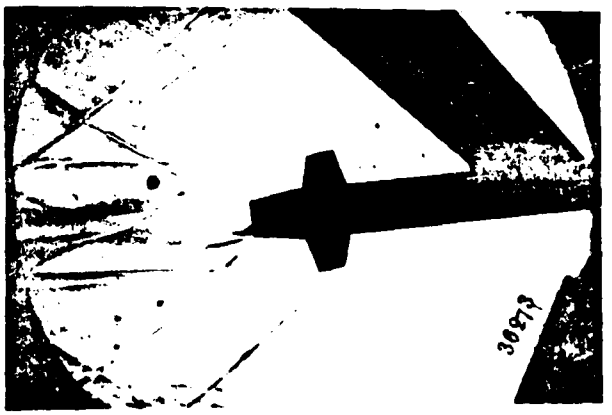

Fig. 2 Finned Missile Afterbody in Supersonic Flow, $M_\infty = 2$; Angle of Attack, $\alpha = -6°$; Control Surface Angle, +10°

The geometrical requirements, however, were at first only specified[15,16] in terms of the initial expansion angle of the jet, ε, in Fig. 1. This may be sufficient to deal with cases in which large scale plume-induced separation is not present and where there is little initial plume curvature but not for high engine to freestream pressure ratios typical of highly accelerating missiles, see Fig. 2. For cases with plume induced large scale separation effects as in Fig. 1, additional constraints, both geometric and dynamic, are obviously necessary.

In 1979, Korst and Deep[12] proposed a modeling technique which allows the matching of both the initial deflection angle and the plume shape through its local radius of curvature, R_c, and satisfying the local pressure rise at impingement of the plume and external flow. A second-order approximation for dealing with axisymmetric centered expansions was used for calculating the plume curvature[12]. This approach, in conjunction with conditions at the nozzle outlet, allows for sweeping simplifications in interpretation of the results if the nozzle flow can be assumed to be locally conical. The latter was initially assumed to be reasonable for typical prototype nozzles of relatively high Mach number, although it was recognized that this may not always be truly representative particularly for wind tunnel models. While such a generalization is not correct in many cases, the overall conclusions relative to the modeling procedures remain correct. An improved analysis which removes the conical flow restriction, albeit with additional computational complications, has also been developed[17]. The limits of applicability of modeling by such congruent plumes for different gases as outlined above have been investigated for centered jets under restricted test conditions[7]. One of the objectives of this study was to examine the applicability and limits for a broad range of wind tunnel test conditions.

EXPERIMENTAL EQUIPMENT

Simulation Test Facility

The wind tunnel used in this investigation of plume simulation by compressed air and Freon-22, is the FFA's tunnel S5[18]. It is of an intermittent suck down type and has two-dimensional solid nozzle blocks for supersonic speeds and a test section of 0.45 x 0.57 m. Tunnel stagnation pressure and temperature are approximately equal to atmospheric conditions.

Compressed dry air for plume simulation is available from the high pressure storage of the FFA's hypersonic facilities,[18] which allows the storage of 50 m^3 of air at a pressure of 25 MPa. The temperature can be selected in the range -20° to +300°C and the maximum flow rate is 2.7 kg/s.

A hot gas facility, primarily intended for various types of heated Freon, is available for plume simulation. Freon-22 has been chosen for all tests up to now. Cost and chemical stability, which allows it to be heated to sufficiently high temperatures without chemical breakdown, were major factors in its selection. The ratio of specific heats, γ, at the nozzle exit and for plume expansion conditions, is in the range of 1.16 to 1.18, which is appropriate for simulation of combustion-type jet products.

The basic system utilizes the above mentioned high pressure storage which is used, in the simulation system as an essentially constant pressure driver for the Freon. Figure 3 is an annotated schematic of the Freon system, the test model, and the high pressure driver. Details of component design, construction, and operating procedures are given in Ref. 9 along with a discussion of the temperature control requirements and the system developed for this purpose. The systems performance tests are presented in Ref. 10 and a condensed review of the facility can be found in Ref. 11.

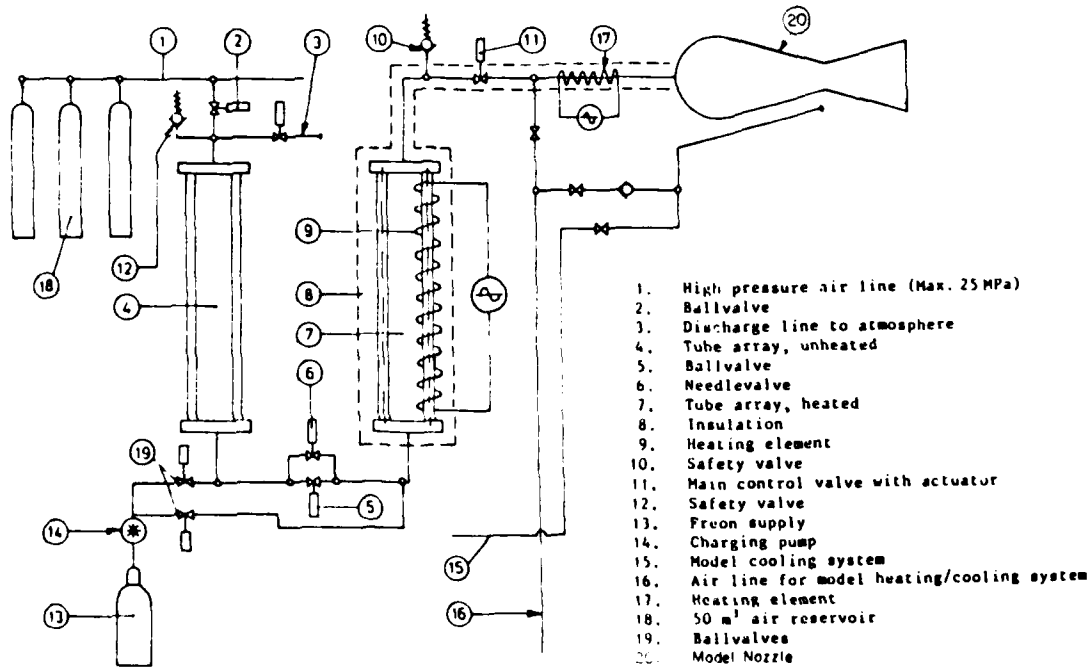

Fig. 3 Annotated Schematic of Air Driver System, Freon Heater and Nozzle

Selection of Design Condition and Model Geometries

The nozzles used for the plume modeling tests were identical with the nozzles utilized in earlier tests[10] modeling from Freon (prototype) to air (model). As the specific heat ratio for Freon-22 is $\gamma = 1.16$, which is appropriate for simulation of combustion-type jet products, this modeling is relevant for typical plume simulation in wind tunnels. The geometry of the prototype was chosen to be as realistic as possible, e.g. to have a shape similar to a typical rocket nozzle (see Fig. 4a, $M_{L,P} = 2.60$, $\theta_{L,P} = 15°$, and $P_L/P_E|_P = 3.48$). The calculated data of the model air nozzles are $M_{L,M} = 1.41$, $\theta_{L,M} = 3.07°$, and $P_L/P_E|_M = 6.03$ for separation flow modeling; and $M_{L,M} = 2.03$, $\theta_{L,M} = 10.47°$, and $P_L/P_E|_M = 5.07$ for base pressure modeling. Unfortunately, the calculated air nozzles could not be accommodated in the original afterbody due to the large throat areas. It was, therefore, necessary to construct two new afterbodies with integrated nozzles, see Figs. 4b and c, and Figs. 5 and 6. Each afterbody was provided with the pressure tubing needed for measurement of the surface pressure distribution at angle of attack.

Wind Tunnel Model

The basic model shown in Fig. 5 is built up of a 14 degree half-angle nose cone, a cylindrical centerbody of 50 mm diameter and a set of interchangeable afterbodies and propulsive nozzles. The overall length is 9.5 diameters in the plume-modeling tests. The model is supported just behind the conical nose by a strut with 40° sweep back which also provides the gas for the jet. A congruent model can also be mounted on a sting with or without the capability of simulating a gas jet. In this latter case, the jet plume effect can also be simulated by solid bodies. Figure 7 shows the model in the wind tunnel. The rear part of the centerbody, the boattail, and the base region are all instrumented with pressure taps (Fig. 8). A set of four stabilizing or control fins can be attached to the afterbody as shown in Fig. 9. In this test, the controls were positioned circumferentially at $\phi = \pm 45°$ and $\pm 135°$. The four controls, arranged as shown in Fig. 9, had a bi-circular arc airfoil of 8 percent thickness, a span of 1.11 diameter, a root chord of 1.0 diameter and a tip chord of 0.55 diameter. The control pivots were located at semi-chord and positioned on the model 1.5 diameter from the base. The controls could be set at deflection angles of $\delta = 0$ and $\pm 10°$.

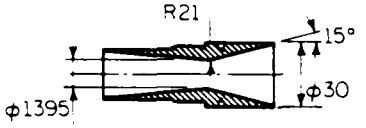

a) $M_L = 2.60$, $\theta_L = 15°$ Prototype

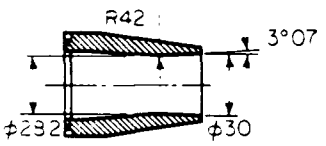

b) Design Emphasizing Separation
$M_L = 1.41$, $\theta_L = 3.07°$

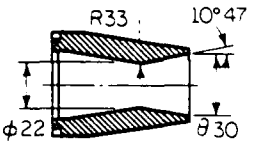

c) Design Emphasizing Base Drag
$M_L = 2.03$, $\theta_L = 10°47$

Fig. 4 Prototype Nozzle with $\gamma = 1.16$ and Two Model Nozzles (Air, $\gamma = 1.40$) Emphasizing Different Operating Conditions

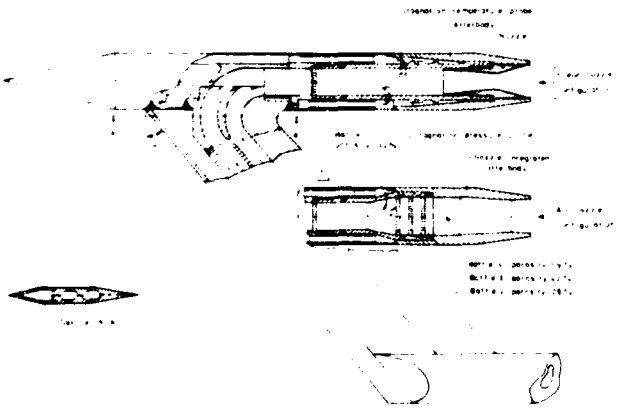

Fig. 5 Modified Model II of Current Modeling Tests

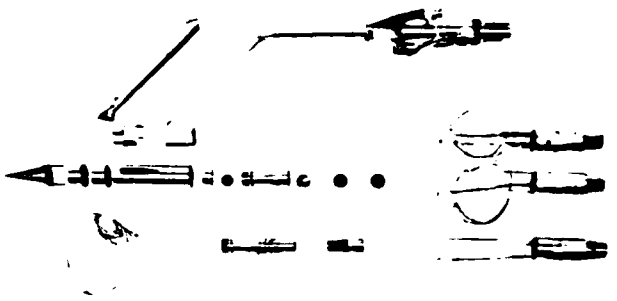

Fig. 6 Photograph of Model Parts

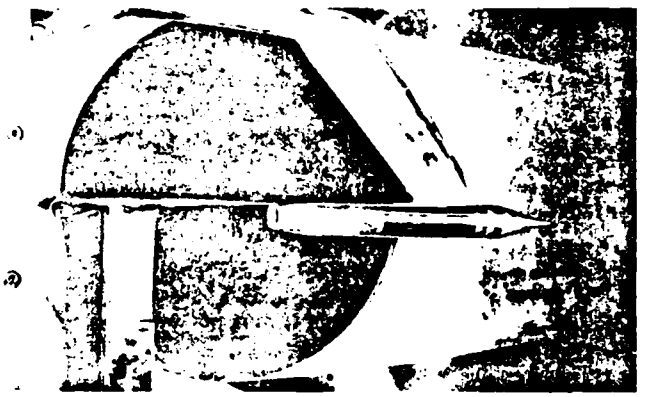

Fig. 7 Model in Wind Tunnel and Movable Probe for Nozzle Exit Mach Number Calibration

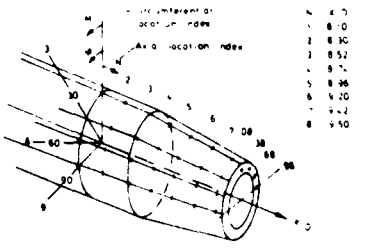

Fig. 8 Location of Pressure Taps on Boattail

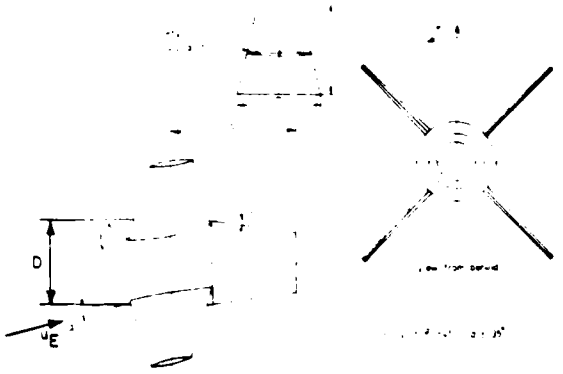

Fig. 9 Control Dimensions and Definition of Control Deflection Angles

The conical nose of the model was equipped with a 10 mm wide transition trip of carborundum grits of 0.5 to 0.8 mm size, 85 mm from the apex. A row of steel balls of 0.5 mm diameter welded to the control surfaces and located 4 mm downstream of the leading edge with 3 mm spacing constituted the transition trips on the controls.

Instrumentation

The pressures on the afterbody were recorded by fast response pressure transducers (National Semiconductor, 0 to 30 psia). The transducer outputs were fed into the ordinary data recording and reduction system of the wind tunnel. The system which is based on a General Automation SP 16/65 real time computer, can record and evaluate up to 48 channels with a maximum scanning rate of 40 kHz. The stagnation pressures in the wind tunnel and in the propulsive jet were recorded by 15 and 500 psia transducers, respectively, and the propellant stagnation temperature was recorded by a Cr-Al thermocouple in a ventilated radiation shield.

Schlieren photographs were taken for each run and oil-flow pictures for selected cases. The Schlieren system had two alternative light sources, one short duration spark lamp with an exposure time of approximately 2×10^{-6} second and one mercury vapor lamp with continuous light. In most cases, black and white and color Schlieren pictures were taken simultaneously.

PLUME MODELING EXPERIMENTS

Test Conditions

The tests were carried out in the FFA's S5 wind tunnel[18] at a freestream Mach number $M_E = 2.0$ and a corresponding Reynolds number 6×10^6 based on the model length. The nozzles were tested at the design stagnation pressure and at pressures 25 percent below and above this value. The nominal propulsive jet stagnation condition used are shown in Table 1. In an earlier investigation[19], the boundary layer approaching the afterbody, measured at an axial station X/D = 7.6 (corresponding to 0.4 diameter in front of the hinge axis of the controls) was found to be 5.79 mm for $U = 0.99\, U_E$. The displacement and the momentum thicknesses were 1.55 and 0.48 mm, respectively.

Zero Angle of Attack Results

Base pressure ratios, P_B/P_E, measured for the Freon (prototype) and the air (model) nozzles versus the jet stagnation pressure, P_{0I}, as measured in the settling chamber of the nozzle are shown in Fig. 10.

The same base pressure ratios with the air (model) nozzle results transformed into the Freon (prototype) plane are plotted versus the prototype stagnation pressure in Fig. 11. The two air (model) nozzle results agree very well with each other, and the correlation with the Freon (prototype) nozzle results is quite good. Also shown for comparison are the results of using cold air in the prototype nozzle (no modeling). The poor agreement with the Freon results is obvious. It is believed, however, that the small discrepancy between the prototype and the model results is significant despite being fairly small.

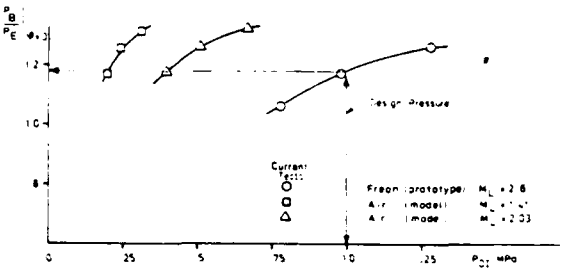

Fig. 10 Base Pressure Ratio for Freon (Prototype) and Air (Model) versus Nozzle Stagnation Pressure

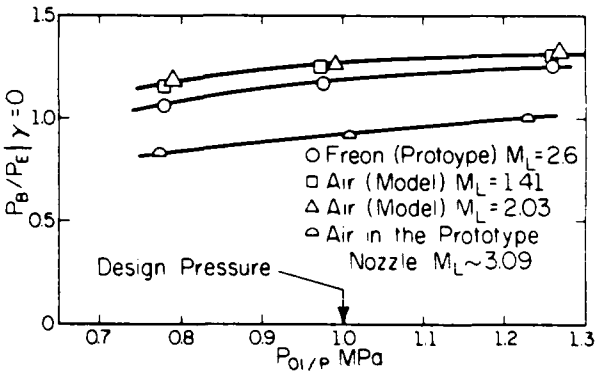

Fig. 11 Base Pressure Ratio for Freon (Prototype) and Air (Model) versus Nozzle Prototype Plane

Table 1 Propulsion Job Stagnation Conditions

Propellant	Nozzle, M_L	Stagnation pressure, MPa			Stagnation temperature, °C
Freon	2.6	0.76	1.0	1.25	104 - 150
Air	1.41	0.19	0.25	0.30	-20 - 20
Air	2.03	0.40	0.53	0.66	-20 - 20

Possible explanations for the discrepancy lie in the fact that the calculation of the air (model) nozzles was based on the assumption that the approach conditions at the Freon (prototype) nozzle exit are produced by conical source flow[17] and neglecting viscid effects during the impingement process. Refined calculations of the flow in the prototype nozzle have shown that the deviations from conical source flow are such that the plume shape is affected to such an extent that it may be of importance. A new air (model) nozzle taking these deviations from source flow into account has been calculated and will be investigated. Tests to determine the contribution of viscid effects during recompression are also planned.

The separation locations as determined from longitudinal pressure distributions and from Schlieren photographs are shown versus prototype lip pressure ratio in Fig. 12 for the Freon (prototype) and air (model) nozzles. Again the air results agree very well but a minor systematic discrepancy between Freon (prototype) and air (model) seems to be established.

Schlieren pictures of the flow for the three nozzles at the design stagnation pressure are presented in Fig. 13 together with a plot overlay of

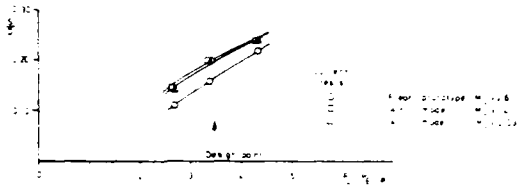

Fig. 12 Separation Location versus Lip Pressure for Freon (Prototype) and Air (Model) Nozzles

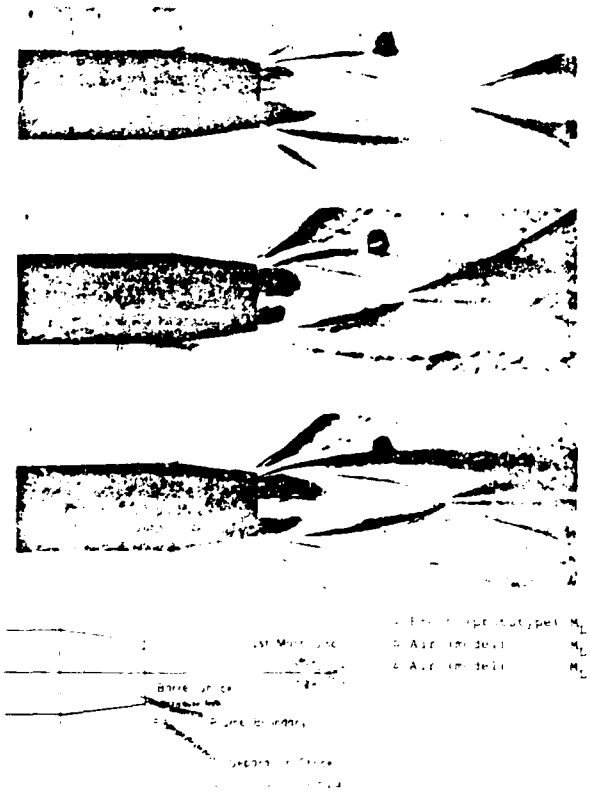

Fig. 13 Schlieren Photographs from Tests at Design Conditions (α = 0; P_{0I} = 1.0 MPa)

some of the significant features in the pictures. In this scale, no differences in plume shape have been observed, but minor differences in the location of the separation shock are detected and appreciable differences in the shape of the inner (barrel) shock are noticed. The latter is to be expected due to the difference in nozzle flow field Mach number.

Effects of Angle of Attack

The base pressure ratio, P_B/P_E, for the model without controls is plotted as a function of the angle of attack α for the Freon nozzle (prototype) in Fig. 14 and for the air (model) nozzles in Figs. 15 and 16. Results are presented for the jet stagnation pressures and circumferential angles investigated.

It is of interest to note that for the major part of the angle of attack range α = -20° to +6°, the pressures for the meridian angles ϕ = 0 - ±90° have been measured on the side of the model which is averted from the support; however, at α = +10° and +20°, the measurements had to be made on the support side. Judging from the curves at ϕ = 90°, the symmetry is as good for α = ±10 and ±20 as for lower angles of attack, which indicates that the differences in support interferences are of minor importance.

To facilitate the evaluation of the simulation of the angle of attack effects on the base pressure the difference, $\Delta(P_B/P_E)_\alpha = (P_B/P_E)_\alpha - (P_B/P_E)_{\alpha=0}$ is shown as a function of angle of attack in Figs. 17 through 19 for the three nozzles. It can be seen that the angle of attack effect of the Freon (prototype) nozzle is very well simulated at positive and at small negative angles of attack. At large negative angles of attack, i.e. on the wind side where there is no separation, the simulation shows systematic, although for practical purposes still tolerable, deviations. It is also observed that the agreement between the two air nozzle results is generally very good and that the discrepancy between the Freon and air results has the same character as at zero angle of attack, which means that there is in most cases a slightly stronger angle of attack effect on the base pressure with the air nozzles than there is with the Freon nozzle.

The separation location, S/D, at the circumferential angle ϕ = 0 is shown in Fig. 20 versus the angle of attack for different jet stagnation pressures. It can be seen that the simulation is quite good, except at low positive angles of attack, which means on the lee side when the vortex flow starts to build up. The deviations are largest at the highest jet stagnation pressure. The two air nozzle results agree very well and the discrepancy between the Freon and the air results are, as could be expected, of the same character as the base pressure results.

Shown in Fig. 21 is a sample of the circumferential variation of the separation location at α = 10° angle of attack and for different jet stagnation pressures as obtained from pressure measurements. Oil flow and Schlieren pictures for the same angle of attack and the design jet stagnation pressure are presented in Fig. 22. The separation lines shown in Fig. 21 have for the two higher stagnation pressures been drawn using the detailed information from oil flow pictures. For the lowest stagnation pressure, no oil-flow pictures were available, but it has been assumed that the separation is of the same kind. It is obvious from these figures that the circumferential variation of

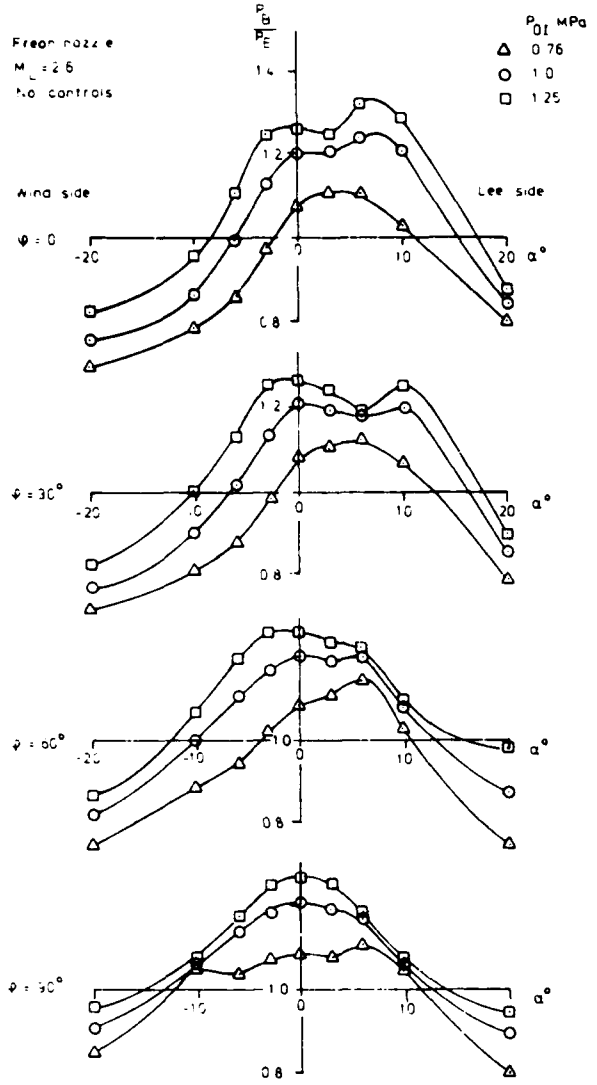

Fig. 14 Base Pressure Ratio for Freon (Prototype) M_L = 2.6 Nozzle versus Angle of Attack α for Jet Stagnation Pressures P_{0I} and Circumferential Angles ϕ Investigated (Model without Controls)

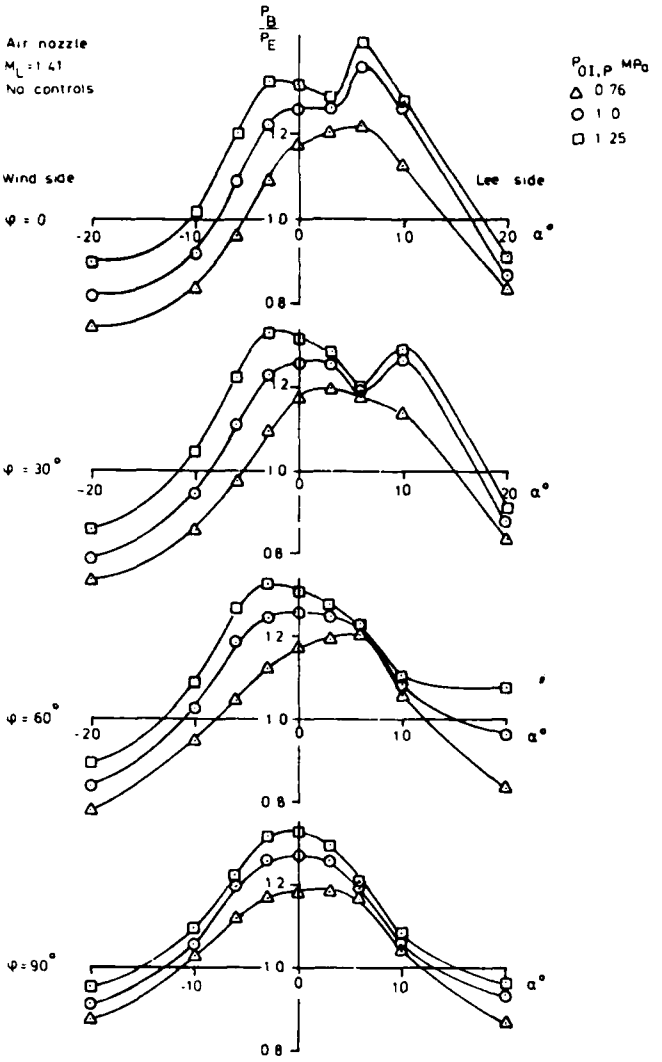

Fig. 15 Base Pressure Ratio for Air (Model) M_L = 1.41 Nozzle versus Angle of Attack α for Jet Stagnation Pressures P_{0I} and Circumferential Angles ϕ Investigated (Model without Controls)

the separation location is quite well simulated at this angle of attack but the correlation is better between the air results than it is between Freon and air.

Effect of Control Fins

The base pressure ratio, P_B/P_E, for the model with controls is plotted as a function of the angle of attack α for the Freon (prototype) nozzle in Fig. 23 and for the air (model) nozzles in Figs. 24 and 25. The results are presented for the jet stagnation pressures and circumferential angles investigated and corresponding results for the model without controls are also shown.

To isolate the effects of controls on base pressure ratio more clearly, the difference between the results with and without controls have been calculated for comparison and results for all three nozzles have been plotted together in Figs. 26 through 28 versus angle of attack. Results are depicted for the circumferential angles and jet stagnation pressures investigated. Selected Schlieren pictures are presented in Fig. 29.

It is observed that the effect of the fins on base pressure obtained with the Freon (prototype) nozzle is, in general, satisfactorily simulated by the air (model) nozzles. The few local exceptions seem to occur in areas where interaction between the control wake and the separated base region might be very sensitive to one parameter, e.g. the jet stagnation pressure. Apart from these few points, the modeling seems to be valid even for severe combinations of control angles, angle of attack, and off-design jet stagnation pressure. It is noted, however, that the effect of controls on base pressure ratio obtained with the air (model) nozzles is often somewhat larger than the effect with the Freon (prototype) nozzle.

CONCLUSIONS

A two-year program has been undertaken to examine the limits of the plume modeling methodology

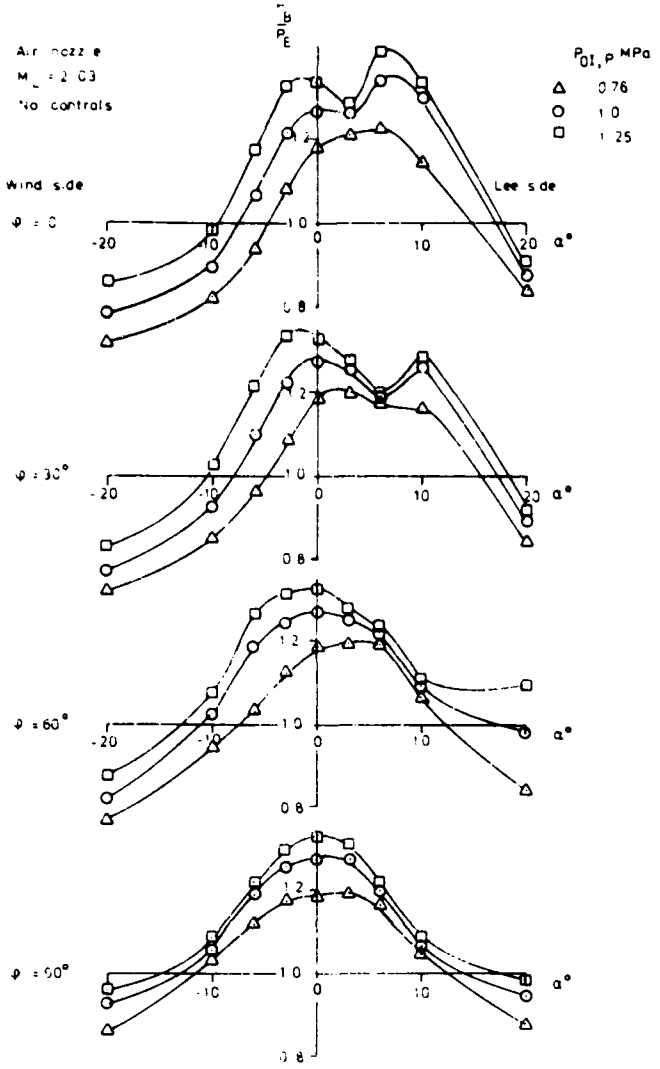

Fig. 16 Base Pressure Ratio for Air (Model) M_L = 2.03 Nozzle versus Angle of Attack α for Jet Stagnation Pressures P_{0I} and Circumferential Angles ϕ Investigated (Models without Controls)

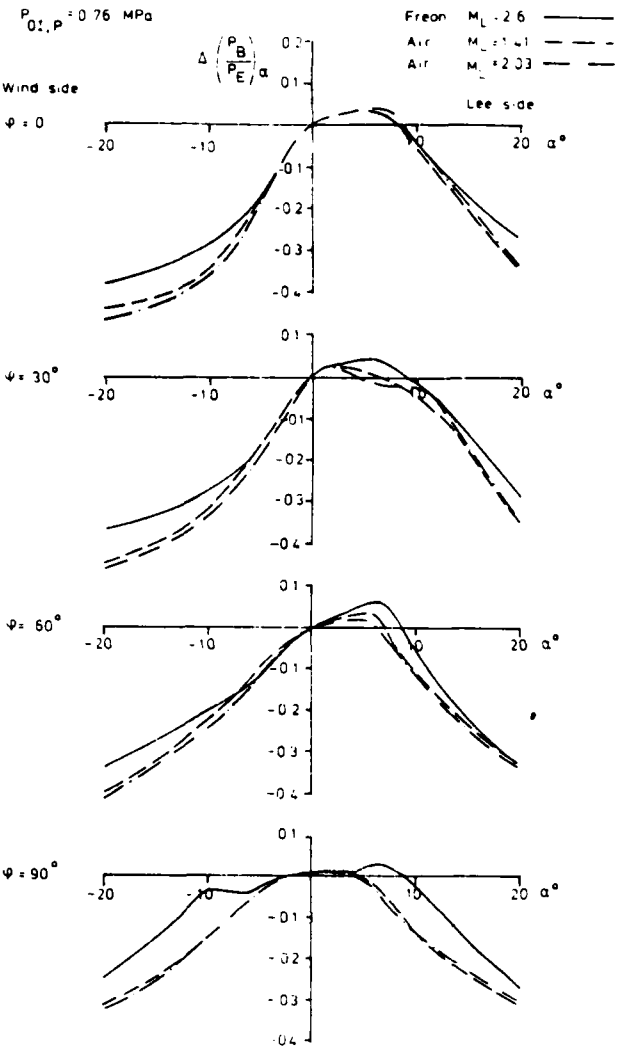

Fig. 17 Effect on Base Pressure Ratio of Angle of Attack $\Delta(P_B/P_E)_\alpha = (P_B/P_E)_\alpha - (P_B/P_E)_{\alpha=0}$ versus Angle of Attack α at Stagnation Pressure $P_{0I,P}$ = 0.76 MPa

proposed by Korst. During the first year, which this paper covers, an existing wind tunnel model and its support has been modified and wind tunnel tests have been carried out at Mach number M_E = 2.0 with one Freon (prototype) nozzle and two air (model) nozzles[11]. An analysis of the experimental results obtained allows the following conclusions:

1. The basic validity of the Korst modeling methodology, established in an earlier study, was confirmed. The concept correlates both base pressure and flow separation in the vicinity of the base of the prototype and modeled nozzles.
2. Although the total scatter in the correlation between Freon (prototype) and air (model) nozzles is the same as it was in the earlier tests[11], there are in the current test results indications of a minor systematic discrepancy between the Freon and the air results. Possible explanations are suggested and supplementary tests will be carried out.
3. The modeled results are good even if the jet stagnation pressure deviates ±25 percent from the design pressure.
4. The modeling scheme is satisfactory even at high angles of attack $\alpha \leq \pm 20^0$.
5. The effects of aft-mounted control fins are simulated satisfactorily. This includes cases where the controls are deflected ($\delta = \pm 10^0$) in combination with angle of attack ($-6^0 \leq \alpha \leq 6^0$).

The extreme limits of the applicability of modeling by congruent plumes for different gases are still being investigated and a future paper will report on additional results.

ACKNOWLEDGMENT

This research program is supported jointly by the European Research Office, U.S. Army, Contract No. DAJA37-81-C-1213, The Aeronautical Research Institute of Sweden (FFA), and the U.S. Army Research Office under Grant No. DAAG-29-F9-C-0184 to the University of Illinois. The authors also want to thank H. H. Korst for his continued interest, encouragement, and support during the investigation.

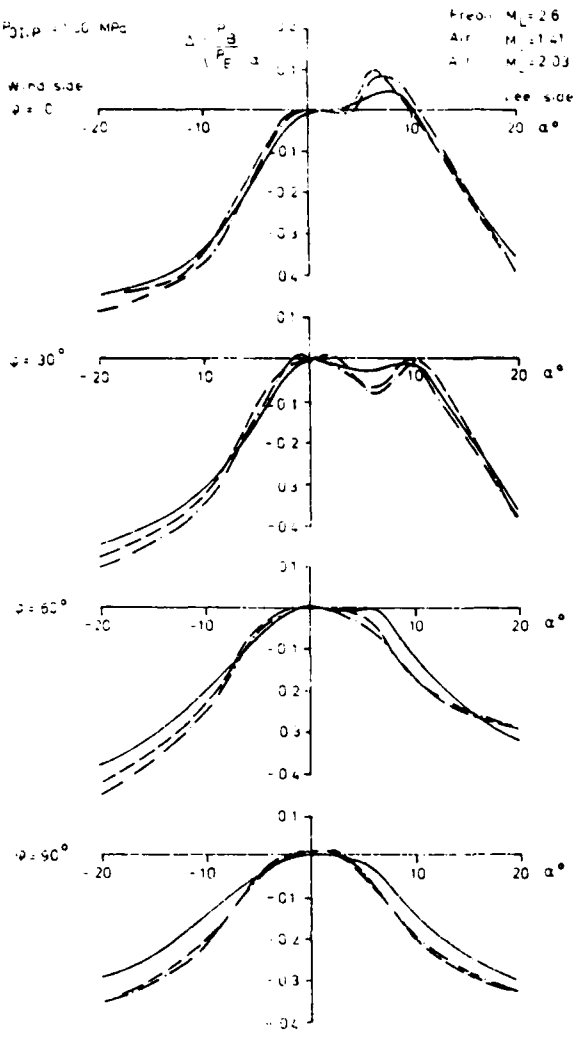

Fig. 18 Effect of Base Pressure Ratio of Angle of Attack $\Delta(P_B/P_E)_\alpha = (P_B/P_E)_\alpha - (P_B/P_E)_{\alpha=0}$ versus Angle of Attack α at Stagnation Pressure $P_{OI,P}$ = 1.00 MPa = Design Pressure

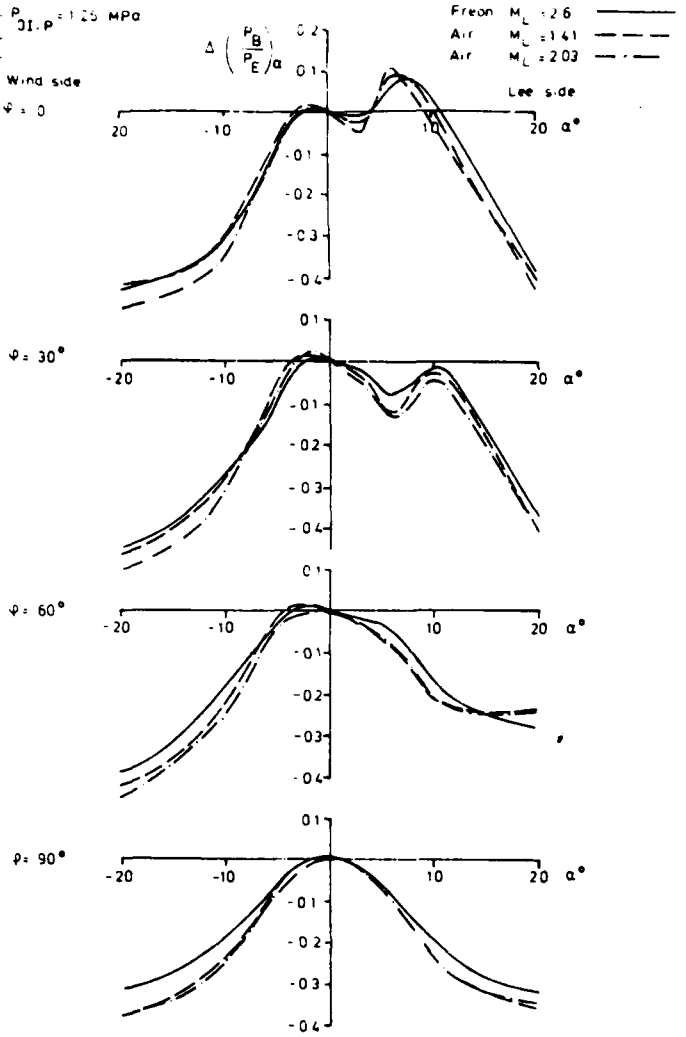

Fig. 19 Effect on Base Pressure Ratio of Angle of Attack $\Delta(P_B/P_E)_\alpha = (P_B/E)_\alpha - (P_B/P_E)_{\alpha=0}$ versus Angle of Attack α at Stagnation Pressure $P_{OI,P}$ = 1.25 MPa

REFERENCES

1. Addy, A. L., Korst, H. H., Walker, B. J., and White, R. A., "A Study of Flow Separation in the Base Region and its Effects during Powered Flight," AGARD-CP-124, AGARD Conference Proceedings No. 124 on Aerodynamic Drag, Specialists' Meeting, April 10-13, 1973 (available from NASA Langley Field, VA 23365, ATTN: Report Distribution and Storage Unit).
2. Alpinieri, L. J., and Adams, R. M., "Flow Separation due to Jet Pluming," AIAA Journal, Vol. 4, 1966, pp. 1865-1866.
3. Deep, R. A., Henderson, J. H., and Brazzel, C. E., "Thrust Effects on Missile Aerodynamics," U.S. Army Missile Command, RD-TR-71-9, May 1971.
4. Deiwert, G. S., "A Computational Investigation of Supersonic Axisymmetric Flow over Boattails containing a Centered Propulsive Jet," AIAA Paper 83-0462.
5. Blackwell, K. L., and Hair, L. M., "Space Shuttle Afterbody Aerodynamics/Plume Simulation Data Summary," NASA Technical Paper 1384, 1978.
6. "High Reynolds Number Research," NASA CP-2009, Oct. 27-28, 1976.
7. Korst, H. H., White, R. A., Nyberg, S.-E. and Agrell, J., "Simulation and Modeling of Jet Plumes in Wind Tunnel Facilities," Paper 80-0430, presented at AIAA 11th Aerodynamic Testing Conference, Colorado Springs, Col., USA, 18-20 March 1980; also published in J. Spacecraft and Rockets, Vol. 18, No. 5, Sept.-Oct. 1981, p. 427-434.
8. Korst, H. H., "Approximate Determination of Jet Contours near the Exit of Axially Symmetrical Nozzles as a Basis for Plume Modeling," TR-RD-72-14, Aug. 1972, U.S. Army Missile Command, Redstone Arsenal, Ala., USA.
9. Nyberg, S.-E., Agrell, J. and Hevreng, T., "Investigation of Modeling Concepts for Plume-Afterbody Flow Interactions," Grant DA-ERO-78-G-028, 1st Annual Technical Report, Feb. 1979.
10. Nyberg, S.-E., Agrell, J. and Hevreng, T., "Investigation of Modeling Concepts for Plume-Afterbody Flow Interactions," Grant DA-ERO-78-G-028, 2nd Annual Technical Report, Feb. 1980.

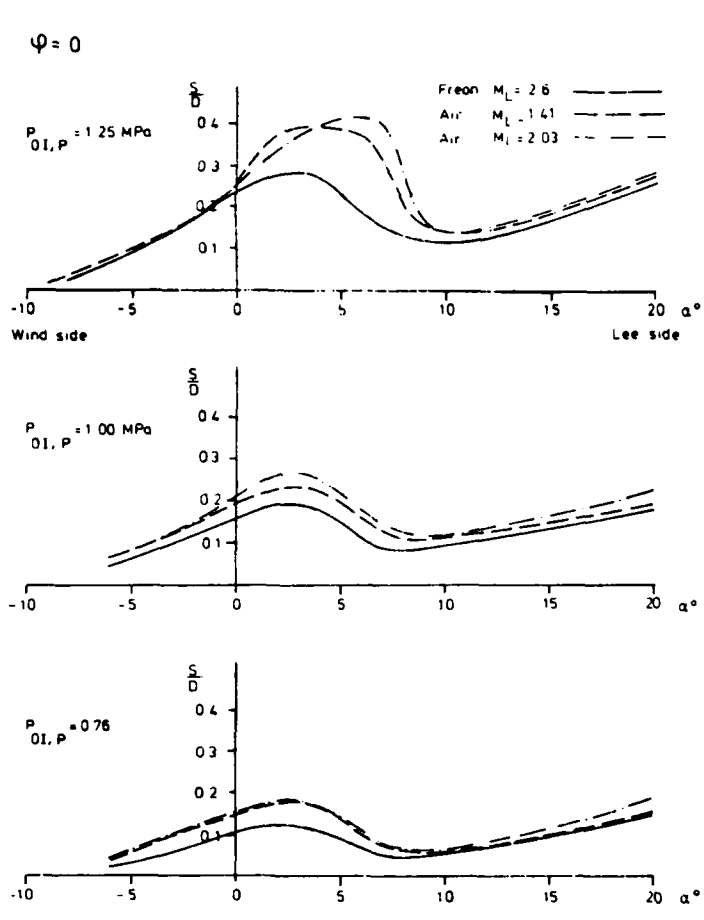

Fig. 20 Separation Location S/D at ϕ = 0 versus Angle of Attack α for Freon (Prototype) and Air (Model) Nozzles at Stagnation Pressures $P_{PO,P}$ = 0.76, 1.0 and 1.25 MPa

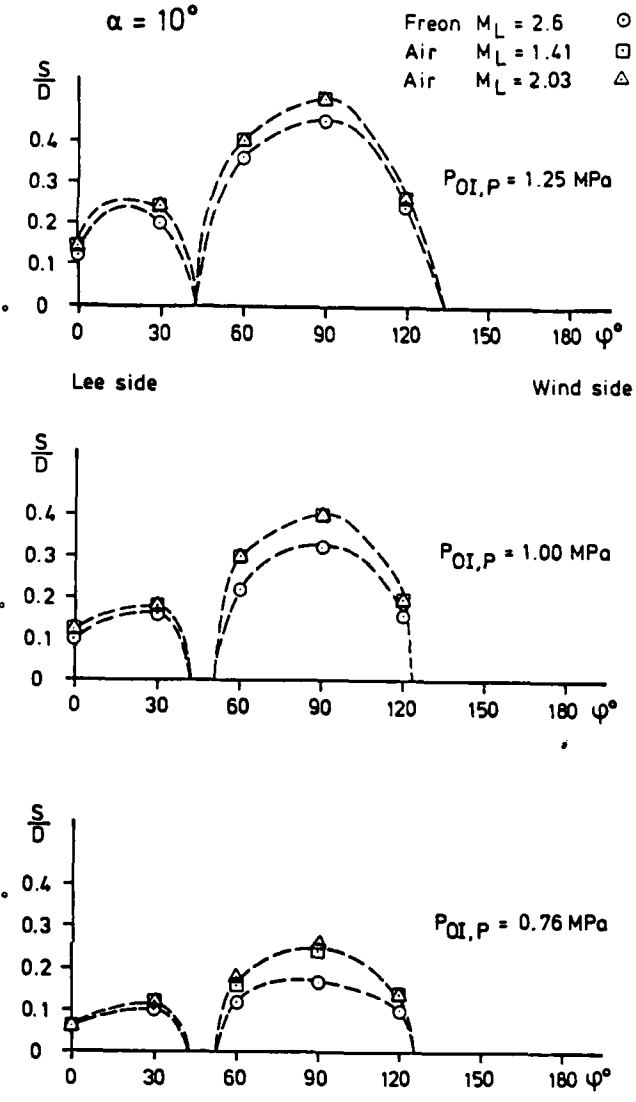

Fig. 21 Separation location S/D at α = 10° from pressure measurements versus circumferential angle φ for Freon (prototype) and air (model) nozzles at stagnation pressures $P_{OI,P}$=0.76, 1.00 and 1.25 MPa. The dotted lines show the separation line obtained from oil flow pictures as in Fig. 22.

11. Nyberg, S.-E., and Agrell, J., "Effects of Control Fins and Angle of Attack on Plume Afterbody Flow Simulation," Contract DAJA37-81-C-1213, Annual Tech. Report, FFA, Feb. 1983.
12. Korst, H. H., and Deep, R. A., "Modeling of Plume Induced Interference Problems in Missile Aerodynamics," AIAA Paper No. 79-0362, 17th Aerospace Sciences Meeting, New Orleans, La., Jan. 15-17, 1979.
13. Nyberg, S.-E., and Agrell, J., "Investigations of Modeling Concepts for Plume-Afterbody Flow Interactions," Grant DA-ERO-78-028, Final Technical Report, Nov. 1981.
14. Korst, H. H., Chow, W. L., and Zumwalt, G. W., "Research on Transonic Flwo of a Real Fluid at Abrupt Increases in Cross Section (with Special Consideration of Base Drag Problems)--Final Report," University of Illinois, ME-TN-392-5, Dec. 1959.
15. Sims, J. L., and Blackwell, K. L., "Base Pressure Correlation Parameters," Missile and Plume Interaction Flow Fields Workshop, Redstone Arsenal, Ala., June 7-8, 1977.
16. Goethert, B. H., and Barnes, L. T., "Some Studies of the Flow Pattern at the Base of Missiles with Rocket Exhaust Jets," Arnold Engineering Development Center, Tullahoma, Tenn., AEDC-TR-58-12, June 1960.
17. White, R. A., "Advanced Research/Analysis of Plume Induced Interference Flow," Proc. Symp. on "Rocket/Plume Fluid Dynamics Interactions," Huntsville, Ala., 1983.
18. Staff, F. F. A., "FFA Wind Tunnel Facilities, Part 2--Transonic-Supersonic Tunnels," The Aeronautical Research Institute of Sweden, (FFA), Memorandum 93, 1969.
19. Agrell, J., "An Experimental Investigation of Supersonic Flow over Axisymmetric Boattails with a Centered Propulsive Jet at Angles of Attack," FFA Technical Note (to be published).
20. Nyberg, S-E., and J. Agrell, "Wind Tunnel Simulations of Plume-Induced Interference Effects," Proc. Symp. on "Rocket/Plume Fluid Dynamics Interactions," Huntsville, Ala, April, 1983.

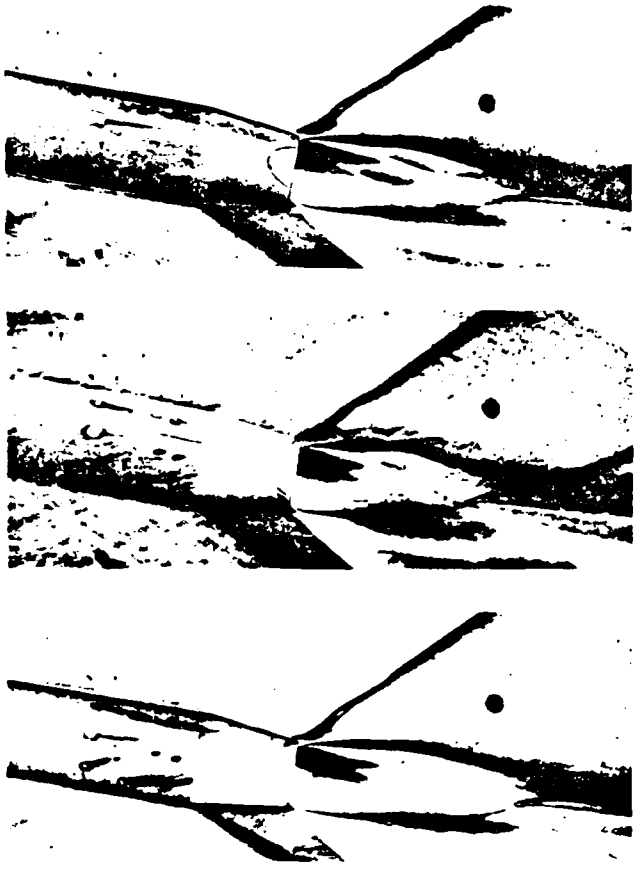

Fig. 22 Oil Flow and Schlieren Photographs at $\alpha = -10°$ and $P_{OI,P} = 1.00$ MPa for Freon (Prototype) and Air (Model) Nozzles

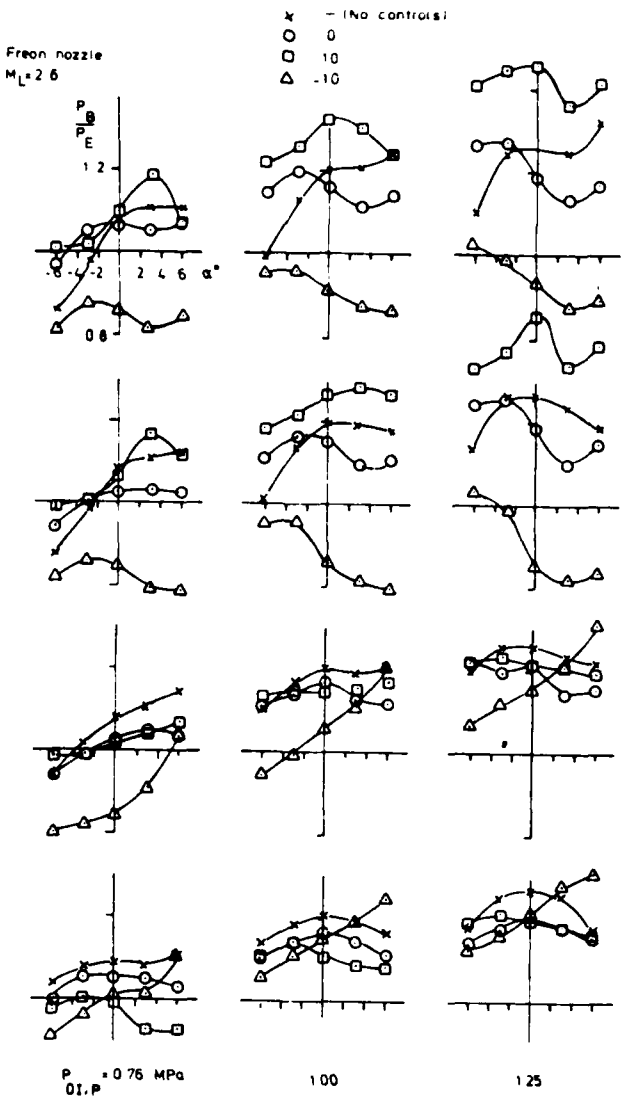

Fig. 23 Base Pressure Ratio for Freon (Prototype) $M_L = 2.6$ Nozzle versus Angle of Attack α for Different Control Angles δ, Jet Stagnation Pressures P_{OI} and Circumferential Angles ϕ

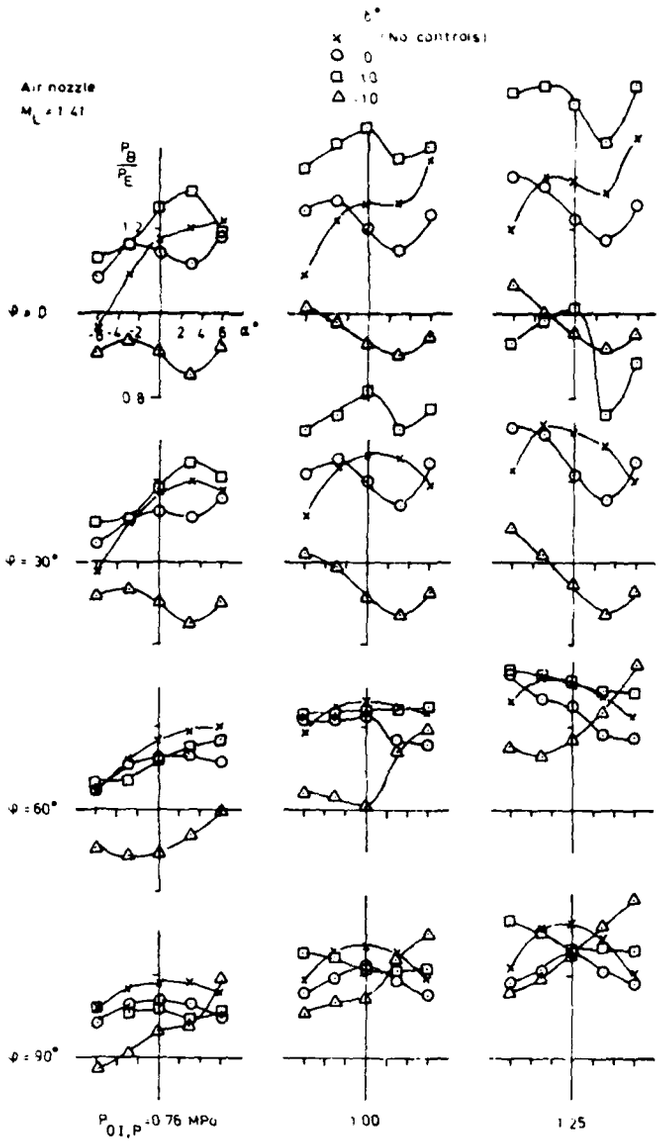

Fig. 24 Base Pressure Ratio for Air (Model) M_L = 1.41 Nozzle versus Angle of Attack α for Different Control Angles δ, Jet Stagnation Pressures P_{OI} and Circumferential Angles ϕ

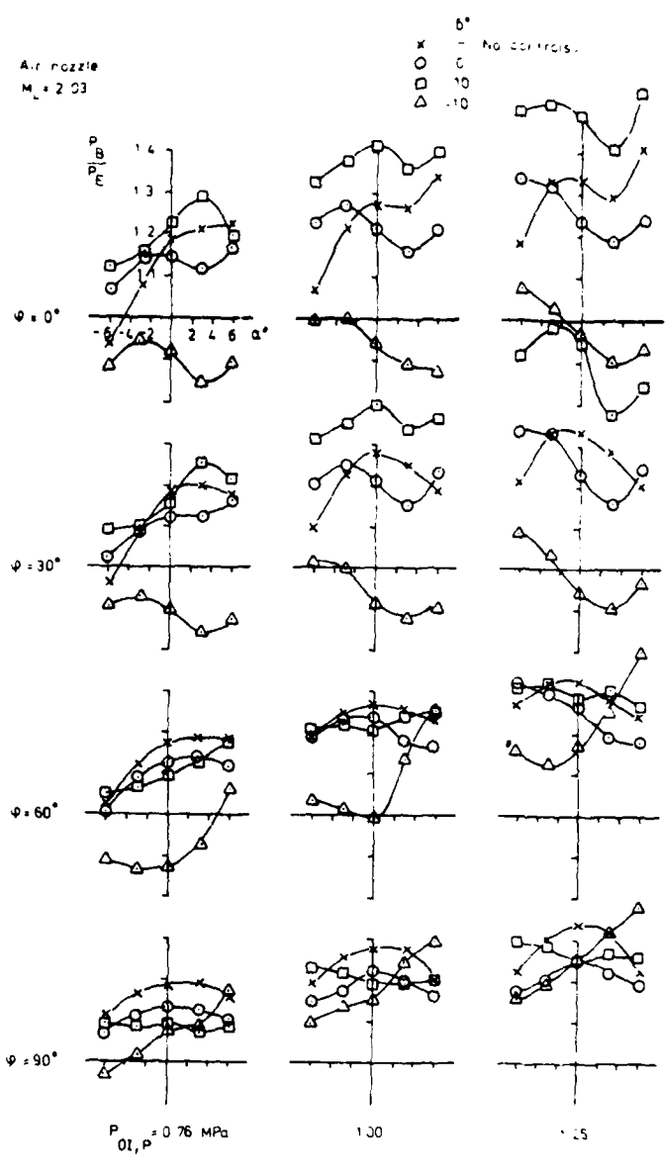

Fig. 25 Base Pressure Ratio for Air (Model) M_L = 2.03 Nozzle versus Angle of Attack α for Different Control Angles δ, Jet Stagnation Pressures P_{OI} and Circumferential Angles ϕ

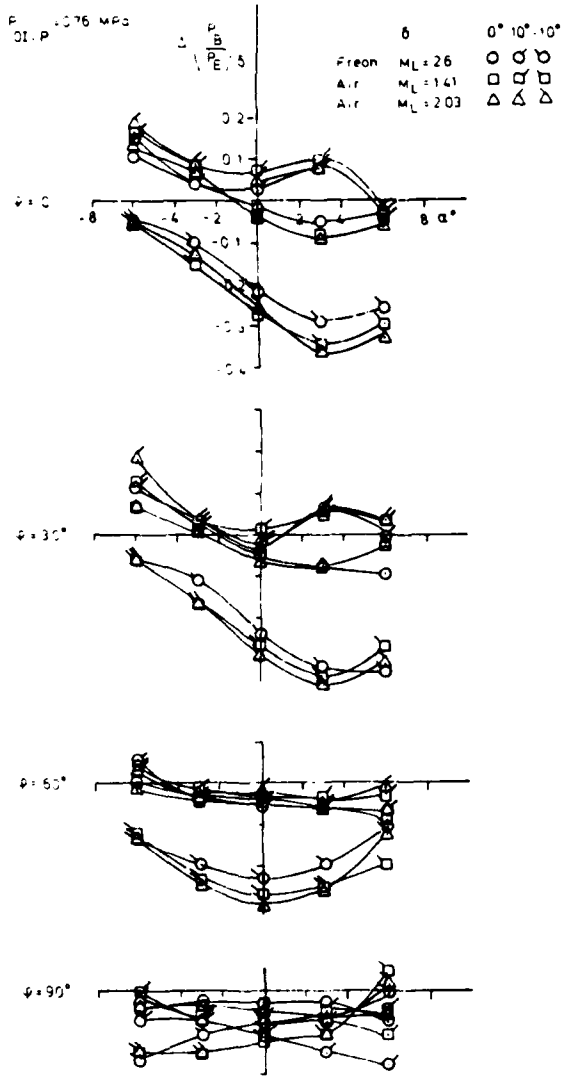

Fig. 26 Effect on Base Pressure Ratio of Controls $\Delta(P_B/P_E)_\delta = (P_B/P_E)_{\text{with controls}}$ minus $(P_B/P_E)_{\text{without controls}}$ versus Angle of Attack α at Stagnation Pressure $P_{OI,P} = 0.76$ MPa

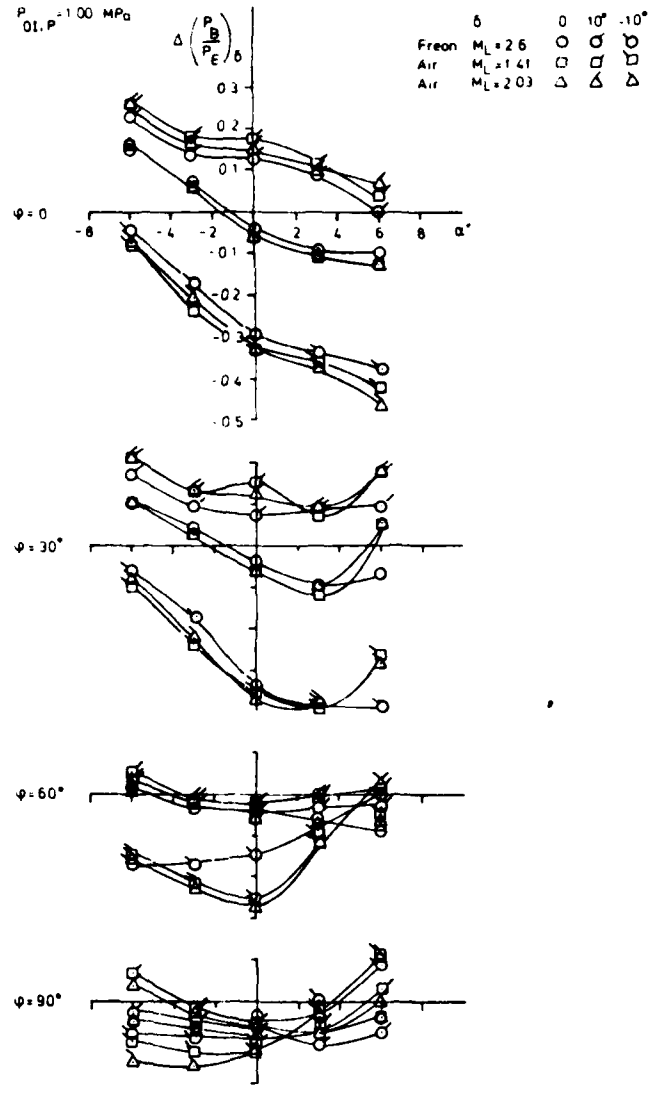

Fig. 27 Effect on Base Pressure Ratio of Controls $\Delta(P_B/P_E)_\delta = (P_B/P_E)_{\text{with controls}}$ minus $(P_B/P_E)_{\text{without controls}}$ versus Angle of Attack α at Stagnation Pressure $P_{OI,P} = 1.00$ MPa

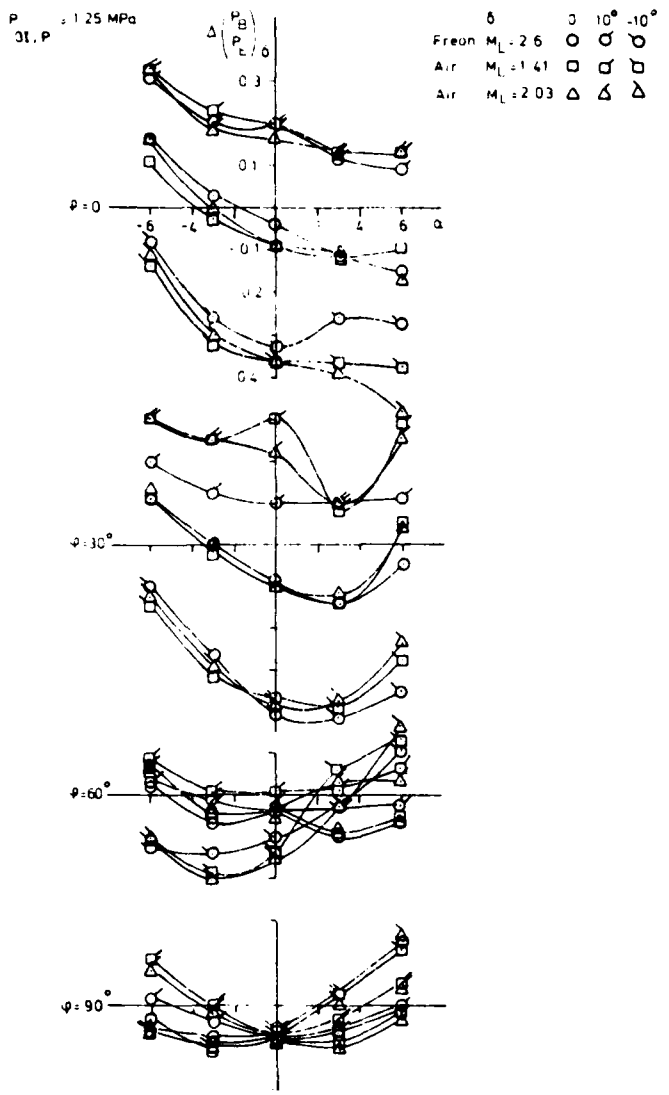

Fig. 28 Effect on Base Pressure Ratio of Controls $\Delta(P_B/P_E)_\delta = (P_B/P_E)_{\text{with controls}}$ minus $(P_B/P_E)_{\text{without controls}}$ versus Angle of Attack α at Stagnation Pressure $P_{OI,P} = 1.25$ MPa

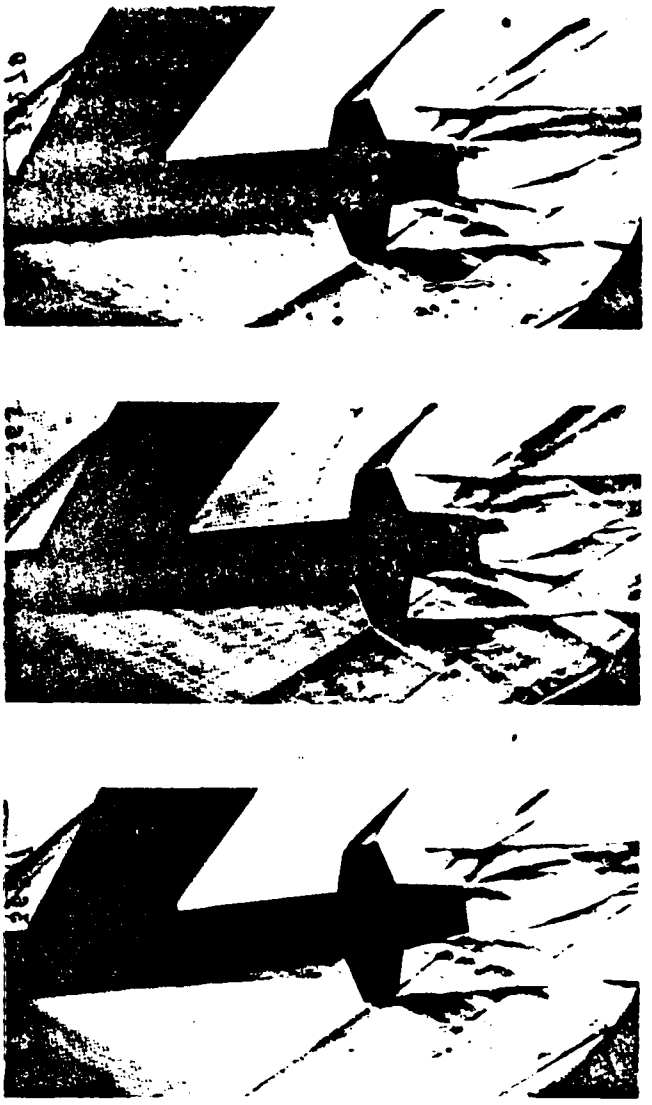

Fig. 29 Schlieren Photographs of Model with Controls: δ = -10° at α = 6° $P_{OI,P}$ = 1.00 MPa for Freon (Prototype) and Air (Model) Nozzles

APPENDIX E

RESEARCH CONTRACT RELATED PUBLICATIONS

APPENDIX E

RESEARCH CONTRACT RELATED PUBLICATIONS

Much of the research conducted under the sponsorship of this contract has produced significant results which have been reported in the literature. The following is a list of those publications:

THESES

Doerr, S. E., "Modeling of Propulsive Jet Plumes--Extension of Modeling Capabilities By Utilizing Wall Curvature Effects," M.S. Thesis, Department of Mechanical and Industrial Engineering, University of Illinois at Urbana-Champaign, Urbana, Illinois, 1984.

Gruber, E. L., "Numerical Analysis of Laminar Flow Past a Projectile Using Viscous-Inviscid Interaction," M.S. Thesis, Department of Mechanical and Industrial Engineering, University of Illinois at Urbana-Champaign, Urbana, Illinois, 1985.

Kuntz, D. W., "An Experimental Investigation of the Shock Wave-Turbulent Boundary Layer Interaction," Ph.D. Thesis, Department of Mechanical and Industrial Engineering, University of Illinois at Urbana-Champaign, Urbana, Illinois, 1985.

Marongiu, M. J., "Mechanisms Controlling Non-Steady Plume-Wall Interactions in Rocket Launch Tubes," Ph.D. Thesis, Department of Mechanical and Industrial Engineering, University of Illinois at Urbana-Champaign, Urbana, Illinois, 1985.

Moorehouse, J. A., "Correlation of Experimental Results for Turbulent Exchange Mechanisms in Supersonic, Compressible Free Shear Layers Based on a Transitional Two-Layer Model," M.S. Thesis, Department of Mechanical and Industrial Engineering, University of Illinois at Urbana-Champaign, Urbana, Illinois, 1985.

Petrie, H. L., "A Study of Compressible Turbulent Free Shear Layers Using Laser Doppler Velocimetry," Ph.D. Thesis, Department of Mechanical and Industrial Engineering, University of Illinois at Urbana-Champaign, Urbana, Illinois, 1984.

Samimy, M., "An Experimental Study of Compressible Turbulent Reattaching Free Shear Layers," Ph.D. Thesis, Department of Mechanical and Industrial Engineering, University of Illinois at Urbana-Champaign, Urbana, Illinois, 1984.

JOURNAL ARTICLES

Addy, A. L., Dutton, J. C., and Amatucci, V. A., "Nonuniform Nozzle Flow Effects on Base Pressure at Supersonic Flight Speeds," AIAA Journal, Vol. 24, No. 7, July 1986, pp. 1209-1212.

Chow, W. L., "Base Pressure of a Projectile Within the Transonic Flight Regime," AIAA Journal, Vol. 23, No. 3, March 1985, pp. 388-395.

Kuntz, D. W., Amatucci, V. A., and Addy, A. L., "The Turbulent Boundary Layer Properties Downstream of the Shock Wave-Boundary Layer Interaction," To be published in the AIAA Journal, 1986.

Petrie, H. L., Samimy, M., and Addy, A. L., "A Study of Compressible Separated Flows," To be published in the AIAA Journal, 1986.

Samimy, M., Petrie, H. L., and Addy, A. L., "A Study of Compressible Turbulent Reattaching Free Shear Layers," AIAA Journal, Vol. 24, No. 2, February 1986, pp. 261-267.

Wu, C. C. and Chow, W. L., "Study of an Asymmetric Flap Nozzle as a Thrust-Vectoring Device," Journal of Propulsion and Power, Vol. 1, No. 4, July-August 1985, pp. 286-291.

SYMPOSIUM PAPERS, CONFERENCE PROCEEDINGS, MEETING PAPERS, AND REPORTS

Addy, A. L., Amatucci, V. A., and Dutton, J. C., "An Investigation of the Effects of Non-Uniform Throat Flow on Base Pressure at Supersonic Flight Speed," Paper No. AIAA-84-0314, presented at the AIAA 22nd Aerospace Sciences Meeting, Reno, Nevada, January 9-12, 1984.

Chow, W. L., "Base Pressure of a Projectile Within the Transonic Flight Regime," Paper No. AIAA-84-0230, presented at the AIAA 22nd Aerospace Sciences Meeting, Reno, Nevada, January 9-12, 1984.

Chow, W. L., "The Effect of Boattailing of a Projectile in Transonic Flow," Proceedings of the Third Symposium on Numerical and Physical Aspects of Aerodynamic Flows, Long Beach, California, January 1985, pp. 9-15 to 9-22.

Chow, W. L., "Improvement on Numerical Computation of the Thin-Layer Navier-Stokes Equation--With Emphasis on the Turbulent Base Pressure of a Projectile in Transonic Flight Condition," Report for the U.S. Army Ballistic Research Laboratory, November 1985.

Kuntz, D. W., Amatucci, V. A., and Addy, A. L., "An Experimental Study of the Shock Wave-Turbulent Boundary Layer Interaction," paper presented at the Winter Annual Meeting of ASME as part of the International Symposium on Laser Anemometry, Miami Beach, Florida, November 17-22, 1985. (Also published as International Symposium on Laser Anemometry, FED-Vol. 33, New York, 1985, pp. 173-178.)

Kuntz, D. W., Amatucci, V. A., and Addy, A. L., "The Turbulent Boundary Layer Properties Downstream of the Shock Wave-Boundary Layer Interaction," Paper No. AIAA-86-0348, presented at the AIAA 24th Aerospace Sciences Meeting, Reno, Nevada, January 6-9, 1986.

Petrie, H. L., Samimy, M., and Addy, A. L., "A Study of Compressible Turbulent Free Shear Layers Using Laser Doppler Velocimetry," Paper No. AIAA-85-0177, presented at the AIAA 23rd Aerospace Sciences Meeting, Reno, Nevada, January 14-17, 1985.

Petrie, H. L., Samimy, M., and Addy, A. L., "An Evaluation of LDV Velocity and Fringe Bias Effects in Separated High Speed Turbulent Flows," ICIASF '85 Record, presented at the International Congress on Instrumentation in Aerospace Simulation Facilities, Stanford University, August 26-28, 1985. (Published as IEEE Publication 85CH2210-3, pp. 297-308.)

Samimy, M. and Addy, A. L., "Experimental Study of Supersonic Flow Over Backward-Facing Step Model," presented at the Symposium on Fluid Dynamics, University of Illinois at Urbana-Champaign, Urbana, Illinois, April 26-27, 1984, pp. 149-168.

Samimy, M. and Addy, A. L., "Effects of Expansion at the Step on Turbulence Characteristics of Compressible Free Shear Layers," presented at the 63rd Supersonic Tunnel Association Meeting, Dallas, Texas, April 14-16, 1985.

Samimy, M., Petrie, H. L., and Addy, A. L., "A Study of Compressible Turbulent Reattaching Free Shear Layers," Paper No. AIAA-85-1646, presented at the AIAA 18th Fluid Dynamics and Plasmadynamics and Lasers Conference, Cincinnati, Ohio, July 16-18, 1985.

Samimy, M., Petrie, H. L., and Addy, A. L., "Reattachment and Redevelopment of Compressible Turbulent Free Shear Layers," paper presented at the Winter Annual Meeting of ASME as part of the International Symposium on Laser Anemometry, Miami Beach, Florida, November 17-22, 1985. (Also published as International Symposium on Laser Anemometry, FED-Vol. 33, New York, 1985, pp. 159-166.)

Samimy, M. and Addy, A. L., "Interaction Between Two Compressible Turbulent Free Shear Layers," Paper No. AIAA-86-0443, presented at the AIAA 24th Aerospace Sciences Meeting, Reno, Nevada, January 6-9, 1986.

White, R. A., Agrell, J., and Nyberg, S.-E., "The Wind Tunnel Simulation of Propulsive Jets and Their Modeling by Congruent Plumes Including Limits of Applicability," Paper No. AIAA-84-0232, presented at the AIAA 22nd Aerospace Sciences Meeting, Reno, Nevada, January 9-12, 1984.

Agrell, J., Nyberg, S.-E., and White, R. A., "Wind Tunnel Investigations of the Plume-Modeling Methodology Suggested by Korst," presented at the Symposium on Fluid Dynamics, University of Illinois at Urbana-Champaign, Urbana, Illinois, April 26-27, 1984, pp. 49-62.

APPENDIX F

PARTICIPATING PERSONNEL

APPENDIX F

PARTICIPATING PERSONNEL

This appendix lists the faculty, graduate students, and support staff who participated on a part-time basis during the performance of this research contract.

FACULTY

A. L. Addy
Principal Investigator, Research Program Coordinator
Professor and Associate Head of Mechanical Engineering

W. L. Chow
Principal Investigator
Professor of Mechanical Engineering

J. C. Dutton
Principal Investigator
Associate Professor of Mechanical Engineering

H. H. Korst
Consultant
Emeritus Professor of Mechanical Engineering

R. A. White
Principal Investigator
Professor of Mechanical Engineering

GRADUATE STUDENTS

V. A. Amatucci
M.S. 1981
Ph.D. Candidate

S. E. Doerr
B.S. 1981
M.S. 1984
Member of Technical Staff
Sandia National Laboratories (Albuquerque, New Mexico)

E. L. Gruber
B.S. 1983
M.S. 1985
Research Engineer
Sundstrand Corporation (Rockford, Illinois)

D. W. Kuntz
M.S. 1981
Ph.D. 1985
Member of Technical Staff
Sandia National Laboratories (Albuquerque, New Mexico)

M. J. Marongiu
M.S. 1982
Ph.D. 1985

J. A. Moorehouse
B.S. 1982
M.S. 1985
Propulsion Engineer
General Dynamics (Fort Worth, Texas)

M. J. Morris
M.S. 1980
Ph.D. Candidate

H. L. Petrie
M.S. 1980
Ph.D. 1984
Research Associate
Pennsylvania State University (State College, Pennsylvania)

M. Samimy
M.S. 1981
Ph.D. 1984
Assistant Professor of Mechanical Engineering
The Ohio State University (Columbus, Ohio)

R. Shaw
M.S. 1986
Ph.D. Candidate

A. Ting
M.S. 1962
Ph.D. Candidate

P.-H. Tsai
M.S. 1985
Ph.D. Candidate

C. C. W. Wu
M.S. 1979
Ph.D. 1983
Assistant Professor of Mechanical Engineering
California State University at Los Angeles

SUPPORT STAFF

Karen K. Bryan
Staff Secretary

SHOP SERVICES

William E. Schaede
Shop Supervisor

Kathy L. Armer
Laboratory Mechanic

Gregory L. Cler
Instrument Maker

Donald R. Deschene
Electronics Technician II

Gerald Dickey
Instrument Maker

John Frizzell
Electronics Technician II

William D. Morfey
Instrument Maker

Leroy W. Westendorf
Instrument Maker

PUBLICATIONS OFFICE

June W. Kempka
Technical Editor

Suzanne F. Palmer
Draftsman-Illustrator I, Technical

END

11-86

DTIC